Advances in Wind Energy Conversion Technology

Springer

Environmental Science and Engineering

Environmental Engineering

For further volumes:
http://www.springer.com/series/7487

Sathyajith Mathew · Geeta Susan Philip
Editors

Advances in Wind Energy Conversion Technology

Springer

Editors
Dr. Sathyajith Mathew
Faculty of Science
University of Brunei Darussalam
Jalan Tungku Link
Gadong, BE1410 Negra
Brunei Darussalam
e-mail: windbook@gamil.com

Dr. Geeta Susan Philip
Faculty of Ag. Engg., KCAET
KAU, Tavanur, Malapuram, 679573
Kerala, India
e-mail: geetasusanphilip@yahoo.com

ISSN 1863-5520

ISBN 978-3-540-88257-2
e-ISBN 978-3-540-88258-9

DOI 10.1007/978-3-540-88258-9

Springer Heidelberg Dordrecht London New York

Cover design: deblik, Berlin

Printed on acid-free paper

Springer is part of Springer Science+Business Media (www.springer.com)

Preface

Growth of wind power during the recent years is highly impressive. Over the past decade, on an average, the global wind power capacity could be doubled by every 3 years. With the addition of 38 GW in 2009, the total global wind power installations could reach up to 158.5 GW, registering an annual growth rate of 31.7% during the year. As a result, wind is the fastest growing energy resource in the world today. Estimates by the Global Wind Energy Council (GWEC) indicate that this trend would continue during the next decade as well and even under the moderate growth scenario, the total wind power installations would reach up to 709 GW by 2020, contributing 8.2% of the world's electricity demand.

One of the major driving forces behind this rapid growth of wind power is the technological advances in wind energy conversion technology in the recent years. Wind turbines are getting bigger in size, efficient in performance and reliable even under adverse working environments. For example, advanced tools in fluid dynamics have made it easier for us to understand the aerodynamics of the wind turbines and thereby improve the efficiency and reliability of wind energy conversion systems. With an insight to the wind regimes characteristics, we could identify better locations for wind farm installations, yielding higher project capacity factors. Advanced forecasting methods empowered us to predict the availability of wind generated electricity even over short time scales, making wind energy more dependable and despatchable. Similarly, developments in the electrical and electronics technologies could provide wind turbines with better generation and regulation systems. Objective of this book is to share some of these recent advances with the wind energy students and researchers.

The book is divided in to eight chapters. The first chapter describes the aerodynamics of wind turbines, specifically applicable for the horizontal axis designs. At the beginning, the basic aerodynamic issues are discussed which is followed by the analysis based on the momentum theory. The blade element and the blade element momentum theories are then introduced followed by the vortex wake model for HAWTs. The chapter concludes with brief descriptions on advanced aerodynamic techniques applying Navier–Strokes, Euler and hybrid CFD methods.

The second chapter focuses on the wind energy resource analysis. Methods for characterising the wind regimes are explained and performance models for wind energy conversion systems are described. This is followed by the chapter on the offshore wind resource estimation which starts with the salient features of the offshore wind resource. Further, applications of LiDAR, SoDAR, SAR and scattometers in assessing offshore wind energy potential are demonstrated with examples from some offshore locations.

The fourth chapter discusses the methods for short term forecast of wind power. At first, various forecasting techniques are introduced followed by the details of different models used for the point forecasts. Some of the probabilistic forecast models are then considered and finally up-scaling of forecasts and evaluation of forecast quality are discussed.

The next chapter analyses the wind turbine loads under varying operating con-ditions. A general description of the origin of the loads is first presented to create the basis for the following load assessment methods and procedures. The design and certification perspectives of wind turbines are emphasized while developing this analysis.

The major characteristics, objectives and strategies of the control system of a wind turbine are described in the sixth chapter. Control strategies to attain effi-cient, stable and reliable operation of modern wind turbines are described and the classical control loops for the systematic regulation of the critical operating vari-ables are analysed. A dynamic model describing the dominant characteristics of a wind turbine is then introduced.

The seventh chapter discusses the basic issues in integrating the bulk power available from the offshore wind farms with the electrical grids. The basic re-quirements for the grid integration are first explained and various grid connection methods like HVAC, LCC HVDC and VSC HVDC are described. Alternate inte-gration strategies are also explored and at the end, various grid integration meth-ods are compared.

The last chapter of the book is devoted to the small wind turbines. The large and small systems are differentiated with respect to their design and operational requirements. Emphasis is given on the starting performance, yaw behaviour, gy-roscopic loads, over speed protection and control requirements.

The chapters of this book are contributed by experts working on different aspects of wind energy conversion technology. We would like to thank them for sharing their expertise with the readers through this project.

Sathyajith
Geetha

Contents

Aerodynamics of Horizontal Axis Wind Turbines

J. Gordon Leishman

List of Symbols

A	Area of the turbine disk, m^2
a	Axial induction factor, v_i/V_∞
C_d	Sectional drag coefficient
C_{d_0}	Sectional zero-lift drag coefficient
C_l	Sectional lift coefficient
C_{l_α}	Sectional lift curve slope, rad^{-1}
C_P	Turbine power coefficient, $P/0.5\rho A V_\infty^3$
C_T	Turbine thrust coefficient, $T/0.5\rho A V_\infty^3$
c	Airfoil chord, m
F	Prandtl tip loss factor
k	Reduced frequency, $\omega c/2V_\infty$
k_x	Longitudinal inflow weighting factor
k_y	Lateral inflow weighting factor
N_b	Number of turbine blades
P_W	Turbine power output, kW
R	Radius of turbine, m
Re	Chord Reynolds number, $\rho V_\infty c/\mu$
r	Position vector of vortex collocation point, m
r	Non-dimensional radial position on blade
r_0	Non-dimensional blade root cut-out
T	Rotor thrust, N
t	Time, s
V	Velocity vector, ms^{-1}

J. G. Leishman (✉)
Minta Martin Professor of Engineering, Department of Aerospace Engineering,
University of Maryland, College Park, MD 20742, USA
e-mail: leishman@umd.edu

S. Mathew and G. S. Philip (eds.), *Advances in Wind Energy Conversion Technology,* Environmental Science and Engineering,
DOI: 10.1007/978-3-540-88258-9_1,

V_{ex}	Perturbation or external velocity vector, ms^{-1}
V_{ind}	Induction velocity vector, ms^{-1}
V_{∞}	Free stream velocity vector, ms^{-1}
X_{TSR}	Tip speed ratio
x, y, z	Cartesian coordinates, (m, m, m)
α	Angle of attack, rad
γ	Yaw misalignment angle of turbine, deg
Γ_v	Vortex strength (circulation), $\text{m}^2\ \text{s}^{-1}$
ζ	Vortex wake age, rad
θ_{tip}	Blade tip pitch angle, deg
θ_{tw}	Blade twist rate, deg
κ	Induced loss factor
λ	Tip speed ratio, $\Omega\ R/V_{\infty}$
μ	Viscosity, $\text{kg m}^{-1}\ \text{s}^{-1}$
v	Kinematic viscosity, $\text{m}^2\ \text{s}^{-1}$
ρ	Air density, kg m^{-3}
σ	Solidity, $N_b c/\pi R$
φ	Induced angle of attack, rad
ψ	Azimuthal angle, rad
Ω	Rotational speed, rad s^{-1}

Abbreviations

BEM	Blade Element Momentum
CFD	Computational Fluid Dynamics
FVM	Free Vortex Method
NWS	Normal Working State
TSR	Tip Speed Ratio
TWS	Turbulent Wake State
VRS	Vortex Ring State
WBS	Windmill Brake State

This chapter reviews the aerodynamic characteristics of horizontal axis wind turbines (HAWTs). While the aerodynamics of wind turbine are relatively complicated in detail, the fundamental operational principle of a HAWT is that the action of the blowing wind produces aerodynamic forces on the turbine blades to rotate them, thereby capturing the kinetic energy contained in the wind and converting this energy into a rotation of the turbine's shaft. The captured energy is transferred through a gearbox to an electrical power generator, which sends the power into the electrical grid system and so eventually to the consumer.

A HAWT has an axis of rotation that is horizontal to the ground and will typically have two or three blades that are oriented either upwind or downwind of the vertical supporting tower. An example of a modern megawatt-capacity commercial HAWT is shown in Fig. 1, which is sited on a wind farm with several

Fig. 1 Modern, three-bladed, upwind-type of HAWT on a wind farm (In this case, the wind is blowing from right to left)

hundred other turbines. On average, a modern HAWT being installed today for commercial power generation will typically have an extraction capacity of between 1 and 5 MW. The other type of turbine, the vertical axis wind turbine (VAWT), the most common of which is the Darrieus turbine [1, 2], has slender curved blades with the axis of its rotation being vertical to the ground. The aerodynamics of VAWTs are not discussed here (despite VAWTs having some advantages), mainly because the type is aerodynamically less efficient, and so it is also less attractive when scaled-up to the sizes needed for commercial wind power production.

The primary purpose of this chapter is to describe the performance characteristics of HAWTs from an aerodynamics perspective, outline the fundamentals of the methods used for their aerodynamic analysis, discuss the effects of key design parameters on their performance, and show results of typical aerodynamic loads and power output characteristics. Emerging aerodynamic predictive capabilities such as Computational Fluid Dynamics (CFD), which will eventually lead to significantly improved aerodynamic predictive capabilities, are also briefly discussed. A general goal in this chapter is to expose the unique aerodynamic problems associated with HAWTs, and to explain why there are still many difficulties in predicting accurately their aerodynamic loads and in estimating their power output characteristics. In particular, understanding and predicting the effects of turbulent winds, the developing ground boundary layer, yawed flow effects, aerodynamic interference with the supporting tower (tower shadow), blade stall effects, and the influence of the unsteady vortical flow in the downstream wake behind the wind turbine, are just some of the technical challenges.

In an attempt to economically capture more wind energy, modern HAWTs have also become much bigger (often over 50 m in diameter). Such design trends have resulted in longer and much more flexible turbine blades, which can elastically bend and twist under the action of the aerodynamic and inertial loads. Therefore, improving the methods of coupling the aerodynamics to the structural dynamic response of the blades (and also with the support tower) has become an increasingly important engineering goal. In this regard, immediate problems are in developing suitable aerodynamic models for predicting the unsteady blade airloads under both attached and stalled conditions, and in tightly coupling these aerodynamic models with the structural dynamics (e.g., finite-element methods) as well as with wind models to give more accurate predictions of the loads and aeroelastic responses of the rotating blades. Only then will the performance characteristics of HAWTs be predicted as accurately as needed.

Overall, the ability to couple and properly integrate efficacious aerodynamic models into all other aspects of the design problem (i.e., the structural dynamics of the rotating blades, wind models, blade pitch and yaw controllers, drive train, electrical generator, etc.) remains fundamental for the improved design of HAWTs. To this end, several comprehensive computer models or design "codes" have been developed—see Manwell et al. [3] for a general outline of the approaches. However, the success of these codes in predicting blade loads and power outputs from a HAWT is not as good as would be desired. These deficiencies are reflected in a recent "blind" prediction of the loads and performance characteristics of a comprehensively instrumented HAWT that was tested in a large wind tunnel—see Fingersh et al. [4]. This experiment has provided an opportunity to obtain blade loads and power output measurements that are free of the high levels of uncertainty that are normally present in field experiments, and has provided a unique database that will help in eventually resolving outstanding modeling issues. Results from eight of the competing predictive methods in the blind study are shown in Fig. 2 (which includes several so-called "advanced" aerodynamic methods), and see Simms et al. [5] and Coton et al. [6] for further details. Clearly, the large spread in the results shown in the figure proves that there are still significant deficiencies in current modeling capabilities, even when a HAWT is operating in a steady wind without any yaw error.

It is not unexpected then, that current predictive capabilities for HAWTs in the field turn out to be as disappointing as these wind tunnel results, and are often much worse. The consequence has been that unexpected loads have been produced when wind turbines are sited, leading to structural fatigue problems, reduced mechanical reliability, compromised power output characteristics, and higher than desirable operating costs. For these reasons it has historically proven difficult for HAWTs to compete with other forms of widely available energy sources, especially fossil fuels such as coal, oil, and gas. There is still a clear need for much

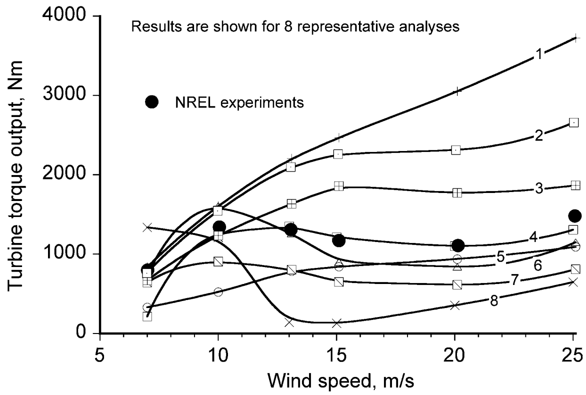

Fig. 2 Comparisons of several predictive methods versus measurements of torque output suggest that the overall capabilities of predicting the performance of HAWTs are still in need of improvement (Results are for an unyawed, 5-meter turbine operating in a steady flow in a large wind tunnel)

more foundational research into aerodynamic subcomponent methodologies (and their interdependent coupling effects) for HAWTs if modeling predictions are to be improved to the levels that they begin to agree better with the actual loads produced on HAWTs that are operating in the field.

The last decade, however, has seen many new developments in wind turbine technology, with several advances in the foundational understanding of the aerodynamic flows on turbine blades as well as in other disciplines such as wind characterization. As a result, the engineering field has now begun to see significantly improved predictive capabilities for blade loads and power output characteristics, so achieving better confidence in the ability to design improved HAWTs with higher aerodynamic efficiency and better mechanical reliability, and all this while still containing (and even reducing) costs. There is also an incentive to produce much better engineered wind turbines from the pressures brought on by the increased social awareness of limited global energy resources and the continued impact of burning fossil fuels on the environment, including pollution and the possibilities of global warming. As a result, wind turbines are playing an increasing role in the generation of net electrical power requirements, with average power capacity currently increasing at over 20% per annum [7–9]. Growth in the use of wind energy has been particularly significant in the United States, Germany, Spain, and India. However, wind energy production still constitutes only a relatively small portion of total world energy demands. This will change in the coming years as society increasingly focuses on conserving fossil fuels.

1 Basic Aerodynamic Issues

As discussed throughout this book, the design of a HAWT is very much an interdisciplinary one, and will involve the participation of aerodynamicists, structural dynamicists, material analysts, meteorologists, these specialists working along with control system analysts, electrical and electronic engineers, and civil engineers. However, the underpinning of the performance capabilities of a HAWT is its aerodynamic design, i.e., in making design decisions about the overall size of turbine, the amount and form of the blade twist, the chord distribution or planform shape, the type of airfoil section to be used, the expected loads and levels of efficiency, maximum required power output, etc. In this regard, the modeling of wind turbine aerodynamics has spanned the entire spectrum of traditional rotating-wing analyses, many of them built on (or adapted from) those used in the helicopter field [10].

The general approach to the aerodynamic modeling of HAWTs is one of synthesis where the aerodynamics of the composing elements of the problem is represented by the best available (and hopefully the most thoroughly validated) mathematical models. These types of analyses range from classical momentum theory, to models based on Blade Element (BE) and Blade Element-Momentum (BEM) theories, through to BE models combined with sophisticated unsteady aerodynamic models and either a Prescribed-Wake or a Free-Vortex Method (FVM). The resulting component models are then integrated together to predict the loads and performance characteristics of the wind turbine as a whole. However, efficacious coupling of all of these models is required; because the coupling process may not be uniquely defined, different predicted results (e.g., Fig. 2) have been shown when using essentially the same medley of component models. This outcome is obviously of major concern to the design community.

While a review of the extensive published technical literature on wind energy will show that all of the various technical problems of HAWTs have been addressed in some form or another, it is significant to note than many of the models used today for their engineering design are built on assumptions rooted firmly in empiricism. Unfortunately, empirically based approaches are often more postdictive than predictive in nature, and such models may be tuned to specific makes of wind turbines. Because of this shortcoming, they do not offer engineers the most flexible types of mathematical tools to help design new and better performing turbines. There are renewed research efforts underway to develop models that are much less postdictive in nature, such as using vortex wake theories and CFD models based on numerical solutions to the Euler and Navier–Stokes equations. As of yet, however, there has been only a limited impact of these types of models in the design of HAWTs, partly because of higher computational costs and longer turnaround times, but also because they are not yet accepted as “validated” or certified design tools. Numerical methods are maturing rapidly and computers continue to get faster and have more memory, so modern aerodynamic methods will eventually prevail as an integral part of design practice.

Meantime, an overarching goal for the immediate future must be to progressively improve upon (or remove) known limitations in all forms of predictive models through continued foundational research, and to reach better confidence levels in predicting blade loads and turbine performance characteristics through validation studies with carefully made measurements. Only then will wind energy reach and maintain a position as an economical source of environmentally friendly energy production.

1.1 Wind Power Density

To size a HAWT to meet the needed energy production requirements, a prerequisite is to evaluate the energy content of the winds at the proposed location where the turbine(s) will eventually be sited. This energy content depends on the geographical location, the average seasonal wind characteristics, the height of the turbine off the ground, the type of upstream terrain, and other factors such as the placement of the turbine relative to other turbines or to structures etc. To this end, detailed wind data must be measured in advance at proposed wind sites (often over years) so that sufficient information can be gathered to make informed engineering and economic decisions about the sizing and eventual placement of the turbines. Obviously, the best sites are those where a significant wind blows, on average, for much of the year.

The kinetic energy contained in a steady, uniform wind of velocity V_∞ can be easily evaluated. The mass flow rate will be $\dot{m} = \rho V_\infty$ per unit area, and so the kinetic energy per unit area per unit time contained in the wind is

$$\frac{KE}{dt} = \frac{1}{2}\dot{m}|V_\infty|^2 = \frac{1}{2}\rho|V_\infty|^3 \tag{1}$$

This previous result is called the wind power density, and it is equivalent to the power that could be extracted by assuming that all of the energy available in the wind could, in fact, be completely extracted by a turbine. For example, with a typical wind speed of 10 ms^{-1} (32.8 fts^{-1}) at standard sea level conditions, the wind power density is

$$\frac{1}{2}\rho|V_\infty|^3 = 0.5(1.225)(10)^3 \approx 0.6\,\text{kW/m}^2 \tag{2}$$

which is obviously rather modest. This result shows immediately that a HAWT will have to be relatively large in diameter (or smaller but more numerous) to extract sufficiently useful amounts of power at economical cost.

As a renewable energy resource, wind is usually classified according to wind power classes, which are based on typical average wind speeds and wind power densities. These classes range from Class 1 (the lowest) to Class 7 (the highest). Most of the economically successful wind farms have been sited in Class 4 areas and above, which will have wind power densities in the range of 0.4–0.5 kW/m^2 when measured at a fixed distance off the ground (typically this is defined as 50 m or about 164 feet).

Wind turbines can actually extract only a fraction of the available energy in the wind, even with aerodynamically and mechanically efficient designs, and especially when operating at sites that may be considered as less than ideal. While a wind turbine extracts power from the wind, it also consumes some of that power in the process, which is lost in overcoming the induced and profile losses of the rotating blades, as well as in losses from mechanical inefficiencies (transmission, gearbox, etc.). These losses can be minimized only so much through engineering design, and they typically will amount to between 20 and 30% of the maximum theoretical power extraction.

The average power extraction from the wind, $\bar{P}_W$, can be written as the equation

$$\bar{P}_W = \frac{1}{2}\rho A C_P \eta |\bar{V}_\infty|^3 \tag{3}$$

where A is the disk area swept out by the blades, C_P is a power coefficient (introduced later), and η is a mechanical efficiency (always less than unity). Equation 3 assumes that the wind blows consistently (on average) with a speed of $\bar{V}_\infty$ and it is turbulence-free and of uniform intensity over the plane of the turbine's disk. With typical values of C_P for a modern turbine reaching close to 0.5 (it will be shown that the theoretical maximum of C_P is 0.593) and η being about 0.90, a HAWT can extract only about 50% of the available wind energy in a best case scenario (extracting 20–40% of the wind energy over the course of an average year is more typical). This does not mean, however, that the machine is only 50% efficient, because compared to its theoretical ideal performance (see later), a modern HAWT can be 80% efficient (or more) when it is situated in isolation without interference from other turbines.

Equation 3 also shows that wind turbines must be located where the wind blows (on average) at high enough speeds. Even in windier sites (i.e., with Class 5 sites and above), the economics of wind energy production is such that HAWTs must usually be placed in farms with tens or even hundreds of other turbines to be economically attractive, although the placement of just a few large HAWTs together is not that uncommon in some rural areas. With the size of a modern commercial turbine for offshore use now reaching to nearly 150 m (492 feet) in diameter, which may produce up to 10 MW of power, just one large turbine may be enough to supply the needs of a small town of perhaps up to 2,000 homes. A technical challenge for the future is to continue to improve upon the performance and efficiency of all sizes of wind turbines so that they can operate over wider ranges of wind conditions at sites that may see lower average wind speeds (but are less remote and closer to electric grids), and also with greater reliability and at more economical cost.

1.2 Wind Speed Probability and Average Power

An important consideration in determining the aerodynamic performance of a HAWT is to recognize that the speed of the wind is never constant, and the wind also varies spatially and temporally over the turbine's disk—see Fig. 3. It is known that uncertainties in wind characterization (such as wind profile and turbulence content) can lead to a serious under-prediction of the highest expected structural loads on the turbine blades, the main shaft, support tower, gearbox and transmission system, etc., often leading to the premature failure of one or more of these

Fig. 3 A wind turbine operates in an atmospheric boundary layer with both spatial and temporal variations in wind velocity

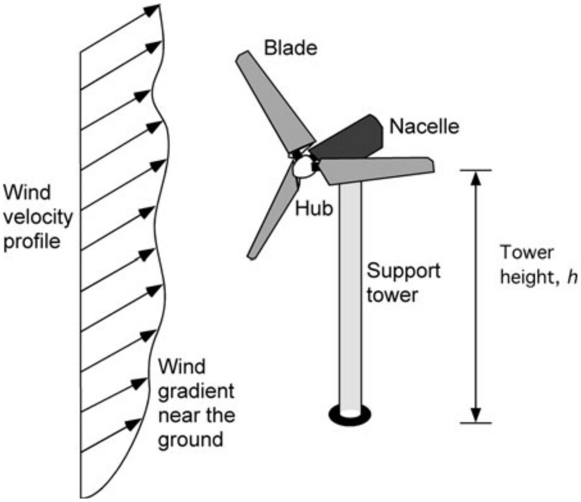

mechanical components. Historically, the reliability of wind turbines has not been good in this regard. However, over-designing the turbine in an attempt to minimize loads will significantly drive up the weight of the blades and increase manufacturing costs, with the result of making the turbine less economically attractive.

An unsteady (but spatially averaged) wind speed can be modeled using a statistical probability distribution $p(V_\infty)$, which will be based on long-term wind speed measurements at the proposed site of the wind turbine. These wind speed probabilities are usually expressed in functional form by curve-fitting to the measured data using either Rayleigh or Weibull equations. The simplest form is the Rayleigh probability equation, which is written as

$$p(V_\infty) = \frac{\pi}{2}\left(\frac{V_\infty}{\bar{V}_\infty^2}\right) \exp\left[-\frac{\pi}{4}\left(\frac{V_\infty}{\bar{V}_\infty}\right)^2\right] \tag{4}$$

where $\bar{V}_\infty$ is the specified average wind speed. This foregoing equation mimics the behavior of typical wind spectra, but it is not a complete description. Another representation, the Weibull equation, is a two-parameter equation [3, 11, 12] that gives a slightly better characterization of actual wind spectra.

With knowledge of $p(V_\infty)$, the power output equation can be written as

$$P_W = \frac{1}{2}\rho A \eta \int_0^\infty p(V_\infty) C_p V_\infty^3 \, dV_\infty \tag{5}$$

After integration, and by assuming in this case the simpler Rayleigh wind speed probability form in Eq. 4, the average power output becomes

$$\bar{P}_W = 3\rho C_P R^2 \bar{V}_\infty^3 \tag{6}$$

where R is the radius of the turbine disk, and C_P can be assumed to be an average operating power coefficient (although C_P will vary with several interdependent operating parameters, as shown later). Equation 6 is often called the "one-two-three" equation, in that it shows that the average power output is proportional to the air density, to the turbine disk radius squared, and to the wind speed cubed (see also Eq. 3). Notice that the altitude of the site (it may be high on a hill or plateau) and the air temperature will both affect the density of the air flowing through the turbine, so its actual power output will change from day-to-day and hour-to-hour, even with nominally the same probability of wind speed occurrence.

1.3 Wind Speed with Height off the Ground

The effect of the atmospheric boundary layer is to further reduce the average wind speed over the turbine's disk and so to reduce the average power output. The proper consideration of this effect is also important in selecting a site for the wind turbine, and in determining how high it needs to be placed off the ground to capture enough wind energy.

The spatial variation of wind speed with height is often modeled using the standard power law for a time-averaged turbulent boundary layer flow such that

$$V_\infty(h) = V_\infty(h_{\mathrm{ref}}) \left(\frac{h}{h_{\mathrm{ref}}} \right)^{1/7} \tag{7}$$

where h_{ref} is a defined reference height above the ground, which by convention is usually taken to be 10 m (32.8 feet). Because Eq. 6 shows that power output increases with $\bar{V}_\infty^3$, then this means that when operating in the boundary layer the power output from the HAWT will increase with $h^{3/7}$. In light of this result, it is obvious that placing the turbine higher up on a tower will capture more of the available wind energy. However, this goal must be traded off against several other issues, including the need to maintain sufficient tower strength and stiffness (a weight, erection, and cost issue), controlling the structural dynamic response of a rotor spinning on the top of a tall tower (a stiffness issue), and in the costs of construction and erection of the tower and the turbine blades at the site (which may need a large crane and a team of skilled workers).

A better model of the wind profile, the logarithmic law, includes a representation of a roughness length, z_0, representing the effects of the terrain on the upstream boundary layer development. In this case, the time-averaged wind profile can be written as

$$V_\infty(h) = V_\infty(h_{\mathrm{ref}}) \left(\frac{\ln\left(\frac{h}{z_0}\right)}{\ln\left(\frac{h_{\mathrm{ref}}}{z_0}\right)} \right) \tag{8}$$

Fig. 4 Representative, time-averaged wind velocity profiles after encountering different types of upstream terrain

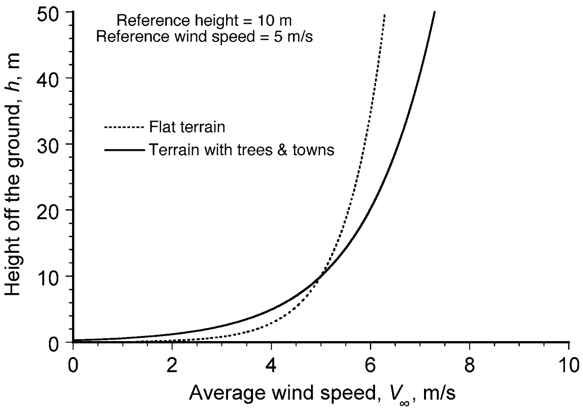

A representative set of wind profiles derived using this model is shown in Fig. 4. Standard values of z_0 have been defined and are available from several sources [3, 12], these values helping to account for the effects of trees or buildings (or any other upstream disturbances) on the evolving wind profile. There are other types of wind profiles that can be assumed for mountainous or ridge-top sites, where the terrain will tend to accelerate the wind flow and/or change its overall characteristics (i.e., it will change both its time-averaged velocity profile and its turbulence spectra), and also may account for the effects of other turbines that may be located nearby, i.e., a wake interference or an "array" effect.

1.4 Wake Array Effects

For the economical extraction of wind energy, several HAWTs are usually arranged together to form a wind farm—see Figs. 1 and 5. A typical farm may have from tens to several hundred turbines, depending on the energy extraction capacity needed. It is clear from the photograph in Fig. 5 that the downstream wake from turbines situated further upwind can affect the flow at the downstream turbines, typically producing significant distortion and turbulence in the approaching wind profile. This is called a wake array interference effect, and can lead to increased blade loads as well as a loss of energy capture.

The optimum placement of wind turbines on a site to minimize these adverse effects is one of the major challenges in designing an economically attractive wind farm; losses of up to 20% in capacity are possible from aerodynamic interference at farms that have small crosswind spacings between adjacent turbines. The total interference losses also depend on the directionality of the wind. Power losses from wake array effects are generally found to be less significant in a more omnidirectional wind compared to one where the wind blows more continuously from one direction or another, and so in this case the array interference effects are generally stronger and more persistent.

Fig. 5 An offshore farm of wind turbines with their array interference effects being identified by natural condensation of water vapor in their downstream wakes. Source: Uni-Fly A/S, Vattenfall windkraft, Erik Slot, BWEA Offshore 08, Westminster, June 4, 2008

An understanding of wake array effects requires an accurate understanding of the vortical wake downstream of the turbine, and how it ultimately affects the wind profile and increases the turbulence field as it approaches another wind turbine. This is a very difficult aerodynamic problem to model, but the motivation for becoming better at predicting such effects is clear because increased turbulence levels can lead to significant power output fluctuations and uncertainties in power production levels, not to mention the generation of undesirable unsteady blade loads and vibrations and so to the possibilities of decreasing the lives of mechanical components. For the future, the development of models that better represent lateral and vertical wind gradients with their appropriate turbulence contents are needed to better predict the various sources of loads on HAWTs.

1.5 Turbulent Wind Effects on Power

The turbulence characteristics of the wind are just one source of the unsteady loads that are ultimately produced on the turbine blades. However, turbulence-induced loads can be severe enough to cause undesirable fluctuations in electrical power output, as well as structural and drive train problems. Such turbulent wind variations have been measured at different sites using wind anemometers, and the acquired data have been developed into statistical models for use in various types of predictive analyses.

For a first level prediction to estimate the expected effects on power output from a HAWT, it is usual to represent the wind speed as an average (or mean) component $\bar{V}_\infty$ plus a temporal or fluctuating component $v(t)$, i.e.,

$$V_\infty(t) = \bar{V}_\infty + v(t) \tag{9}$$

The turbulence intensity I_v is written as a root-mean square of the fluctuating wind speed, as defined by

$$I_v = \frac{1}{\bar{V}_\infty}\left[\int_0^T v(t)^2 dt\right]^{1/2} \tag{10}$$

where T is the time interval (typically 10 min) over which the turbulence is measured. In practice, the value of I_v varies between $0.1\bar{V}_\infty$and $0.3\bar{V}_\infty$, with the higher values usually being found only when buildings, trees, or other obstacles are located upstream. The intensity of I_v also varies with height h above the ground, and typically decreases away from the ground surface. Furthermore, the magnitude of I_v is generally found to be larger at low wind speeds than at higher wind speeds. Because of these significant variations, measurement of actual turbulence spectra must often be used to better predict expected energy yields at the sites of proposed wind farms.

If it is assumed that the operating value of the power coefficient C_P is not substantially changed by the wind speed fluctuations during turbulent events, then an approximation for the power output in a turbulent wind can be found. It has already been shown that the power output varies with the cube of the wind speed, so with turbulence included this result becomes

$$\bar{V}_\infty^3 = \overline{(\bar{V}_\infty + v)^3} \tag{11}$$

where the overbar denotes the mean value. Expanding this equation in terms of I_v gives

$$\bar{V}_\infty^3 = \bar{V}_\infty^3\left(1 + 3I_v^2\right) \tag{12}$$

This result leads to the equivalent average power $\bar{P}_W$ with turbulent wind fluctuations as

$$\bar{P}_W = \frac{1}{2}\rho A C_P\left(1 + 3I_v^2\right)\bar{V}_\infty^3 \tag{13}$$

Therefore, with a typical value of $I_v = 0.1$, only a 3% change in the average power output from the turbine would be obtained if C_P is assumed to be constant.

While the foregoing analysis suggests relatively modest increases in power output resulting from turbulence in the wind, turbulence levels can still factor into decision-making about the potential economics of power production from specific wind farms. Some wind sites will statistically show larger levels of turbulence and different time-averaged wind velocity profiles than is measured at other sites, primarily because of the effects of upstream terrain, etc., and these must be factors that are properly included into the assessment of overall expected energy productivity levels. Turbulence will also be an important factor to consider when addressing the magnitudes of unsteady blade loads, overall vibration levels on the turbine and its tower, etc.

1.6 Capacity Factor and Specific Yield

The average power output, say $\bar{P}_W$, from all of the factors discussed above (aerodynamic efficiency, atmospheric boundary layer, wind turbulence, height off the ground, wake array effects, mechanical and electrical efficiency, etc.) is then used to derive a capacity factor defined by

$$\text{Capacity Factor} = \frac{\bar{P}_W(h, I_v, p, \text{etc.})}{\text{Rated power}} \tag{14}$$

This quantity is simply the ratio of the amount of power a turbine actually produces over a given time to the amount of power it could have produced if the turbine had operated at its fully rated capacity over that same time, i.e., at the best levels of expected energy yield and efficiency. However, a more precise measurement of net energy output is the specific yield, which gives the annual energy output from the turbine in terms of energy captured per unit area of the turbine's disk; this quantity is usually measured in kWh per square meter per year.

The accurate prediction of the capacity factor and the specific yield is particularly important in evaluating the overall economics of proposed wind farms. This process will include the need to size the turbine(s) appropriately based on the measured wind statistics at the proposed site [13]. Capacity factors generally need to be elevated to values of 0.5 or better to make a modern wind farm commercially viable, so this is where the turbine sizing and its expected power and efficiency characteristics come into the design and decision making cycle.

However, other factors such as the mechanical characteristics and reliability of the specific type and design of turbine, along with its maintenance costs, also enters into the overall economics of suitably locating and operating a wind farm. Perhaps a less obvious factor is the distance of the wind farm from the main electrical transmission lines and utility grid. Many suitable windy areas, especially in the USA, are just too far from the main electrical grid system to allow for the cost-effective development of wind farms in these areas.

2 Momentum Theory Analysis in Unyawed Flow

The aerodynamic analysis of a HAWT can first be approached by using an application of the classical "momentum" theory. This theory allows its maximum (ideal) performance limits to be defined in a uniform wind without turbulence, and also gives a first level estimate of the maximum power that could be produced by the wind turbine for any given wind speed. The momentum theory also forms the basis for many more advanced approaches used for wind turbine analysis, so the underlying principles of the theory (including its limitations) must be properly understood and appreciated.

The momentum theory for the analysis of a rotor system was first developed during the 1930s, mainly by Lock, Betz, and Glauert, for the analysis of autogiros, helicopter rotors and “windmills,” but the theory is usually attributed to Glauert [14, 15]. Because the momentum theory assumes an ideal, inviscid, incompressible flow, with no losses other than induced losses, it can also be used to determine the upper limits of energy conversion from the wind by a HAWT, i.e., for the purposes of defining and measuring its aerodynamic efficiency. The ability to define a baseline efficiency against which the performance levels of all types of wind turbines can be measured is clearly fundamental to the process of good engineering design.

2.1 Flow Model and Analysis

A flow model with the control volume surrounding a HAWT without any yaw misalignment is shown in Fig. 6. The average wind speed at the tower height is V_∞ and v_i is the average induced velocity (or the “induction” flow) in the plane of rotation. It is assumed that the velocity is defined as positive when measured in a downstream direction. Notice also, that because a wind turbine extracts energy from the flow, the average velocity downstream will decrease and so the wake boundary must expand to conserve mass flow.

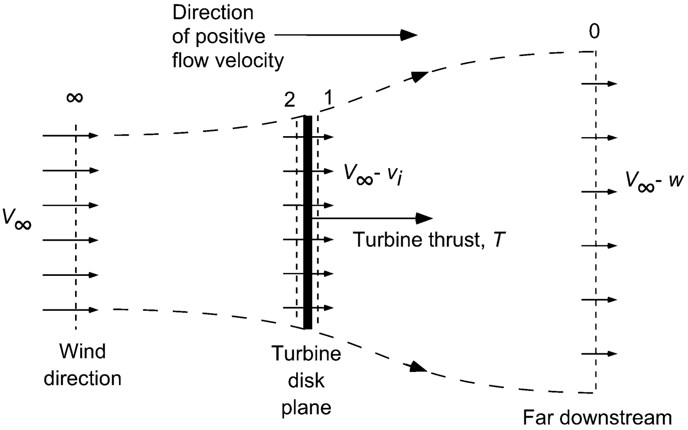

Fig. 6 Flow model used for the momentum theory analysis of a HAWT in normal aligned (unyawed) flow

At the plane of the turbine's disk, the net velocity is $V_\infty - v_i$. In the far wake downstream of the turbine, the corresponding velocity is $V_\infty - w$. The mass flow rate, $\dot{m}$, through the disk is

$$\dot{m} = \rho A (V_\infty - v_i) \tag{15}$$

The change in the momentum of the flow across the disk can be related to the thrust produced on the turbine using

$$T = \dot{m} V_\infty - \dot{m}(V_\infty - w) \tag{16}$$

Expanding out this equation gives a relationship for the thrust in terms of the velocity deficit in the wake, i.e.,

$$T = \dot{m} V_\infty - \dot{m} V_\infty + \dot{m} w = \dot{m} w \tag{17}$$

The power output from the HAWT can now be obtained by conducting an energy balance. The turbine, assuming no sources of viscous losses at this point, must extract all of the work done on the flow to reduce its downstream kinetic energy. The energy thus extracted goes into providing useful work at the shaft but also in overcoming aerodynamic losses, which in this present level of analysis are all induced losses. The work done by the air on the turbine per unit time, $\dot{W}$ is given by

$$\dot{W} = \frac{1}{2}\dot{m}(V_\infty - w)^2 - \frac{1}{2}\dot{m}V_\infty^2 = \frac{1}{2}\dot{m}w(w - 2V_\infty) = -\frac{1}{2}\dot{m}w(2V_\infty - w) \tag{18}$$

Notice that the HAWT "brakes" the flow and decreases its kinetic energy, and so the turbine extracts some of this energy per unit time (i.e., the power output); for obvious reasons this operating condition is known as the windmill brake state or WBS. The power output from the turbine is positive and so

$$P_W = T(V_\infty - v_i) = \frac{1}{2}\dot{m}w(2V_\infty - w) \tag{19}$$

Substituting Eq. 17 into Eq. 19 gives

$$\frac{1}{2}\dot{m}w(2V_\infty - w) = \dot{m}w(V_\infty - v_i) = \dot{m}w(V_\infty - w/2) \tag{20}$$

It is apparent then, that in the ideal case v_i and w are related such that $w = 2v_i$ or $v_i = w/2$. Furthermore, from mass conservation considerations the wake expands downstream as it is slowed down by the turbine; clearly it will expand to a value that depends on the induced velocity and, therefore, on the thrust (and power output) and overall operating state of the turbine.

Notice that for the assumed flow model in Fig. 6 to be valid, then $V_\infty - w > 0$ or alternatively that $V_\infty \geq |w| \geq 2|v_i|$. If this condition is violated, then two possible flow directions can exist, upstream and downstream, and so the wake boundary in this condition must expand beyond the limits defined by the edges of the turbine's disk. In this condition, a unique control volume is more difficult to define, in part because the flow naturally becomes somewhat unsteady (aperiodic). This operating condition is called the Turbulent Wake State (TWS), and the flow eventually progresses into the Vortex Ring State (VRS) as the wind speed is decreased. In the VRS, the average induced flow closely matches the wind speed, thereby making the flow very prone to recirculation, three-dimensionality, and unsteadiness in the disk plane. In either the TWS or the VRS, the flow model that has been assumed in Fig. 6 is invalid, and no exact solutions to the performance of a HAWT can be found using the momentum theory. Without empirical correction then, this is a fundamental limitation to the Glauert/Lock theory.

2.2 Thrust and Power Coefficients

The thrust and power coefficients for a wind turbine, C_T and C_P, respectively, can now be formally defined. The thrust coefficient is defined conventionally in terms of the wind speed and swept area of the turbine's disk such that

$$C_T = \frac{T}{\frac{1}{2}\rho A V_\infty^2} \tag{21}$$

and the corresponding power coefficient is defined as

$$C_P = \frac{P_W}{\frac{1}{2}\rho A V_\infty^3} \tag{22}$$

It is also conventional to define a non-dimensional inflow or induction ratio a as the independent parameter such that $a = v_i/V_\infty$ or that $v_i = aV_\infty$. The thrust variations and power output can then be established as functions of a. For example, using Eq. 19 with Eq. 15 and expanding out gives

$$C_P = \frac{2\rho A(V_\infty - v_i)^2 v_i}{\frac{1}{2}\rho A V_\infty^3} = \frac{4(V_\infty - v_i)^2 v_i}{V_\infty^3} = 4(1-a)^2 a \tag{23}$$

The relationship in Eq. 23 is shown graphically in Fig. 7 and, as previously mentioned, is strictly valid only for $0 \le a \le 1/2$ to avoid violating the flow model that has been assumed in Fig. 6. It will be apparent that the larger the value of the induction, a, the more the flow is slowed as it passes through the turbine. However, notice also that the peak power coefficient is not achieved when the flow is being slowed down by the most amount, a result perhaps initially counterintuitive.

The thrust coefficient can also be expressed in terms of a. Using Eq. 15 then

$$T = \dot{m}w = \rho A(V_\infty - v_i)w = 2\rho A(V_\infty - v_i)v_i \tag{24}$$

Fig. 7 Momentum theory solution for a HAWT in unyawed flow as a function of the induction ratio. Thrust and induction measurements derived from several published sources

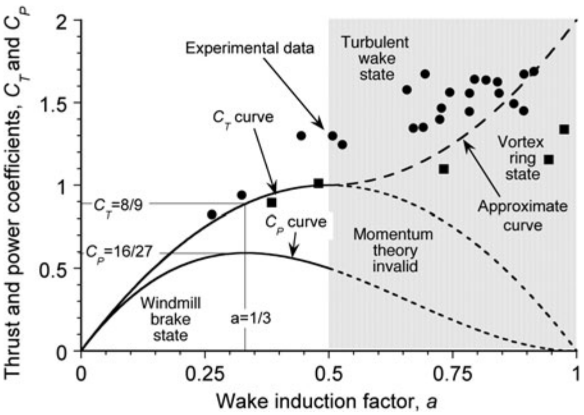

so that the thrust coefficient becomes

$$C_T = \frac{2\rho A(V_\infty - v_i)v_i}{\frac{1}{2}\rho A V_\infty^2} = \frac{4(V_\infty - v_i)v_i}{V_\infty^2} = 4(1-a)a \tag{25}$$

which is also shown in Fig. 7. Notice further that $C_P = (1 - a)C_T$ in this case. Alternatively, solving for a for a given (assumed) value of C_T (or C_P for that matter) by rearranging Eq. 25 gives the quadratic

$$4a^2 - 4a + C_T = 0 \tag{26}$$

The valid solution (i.e., the one that does not violate the assumed flow model) is

$$a = \frac{1}{2} - \frac{1}{2}\sqrt{1 - C_T} \quad \text{for} \quad C_T \leq 1.0 \tag{27}$$

This result gives the relationship between the thrust on the turbine and its average inflow (or induction) for ideal operating conditions (i.e., only induced losses).

2.3 Wake Expansion

The wake expansion downstream of the turbine can now be calculated. Based on continuity considerations, the mass flow is constant within the control volume, so referring to Fig. 6 gives

$$\rho A(v_\infty - v_i) = \rho A_0(V_\infty - w) = \rho A_0(V_\infty - 2v_i) \tag{28}$$

so that

$$\frac{A_0}{A} = \frac{1 - \frac{v_i}{V_\infty}}{1 - \frac{2v_i}{V_\infty}} = \frac{1-a}{1-2a} \tag{29}$$

In the case where the turbine produces no thrust, then $a = 0$ and $A_0/A = 1$ and the flow travels unimpeded through the turbine's disk. At the peak power condition (at $a = 1/3$ as shown in Fig. 6) then $A_0/A = 2$. In the limiting case where $a = 0.5$, then the wake downstream of the turbine ultimately expands to infinite cross-section, but this is not the most efficient operating state for energy extraction.

2.4 Turbulent Wake and Vortex Ring States

A result also shown in Fig. 7 is an empirical one for C_T in the range $1/2 \leq a \leq 1$ (i.e., turbulent wake state or TWS, which progresses to the vortex ring state or VRS)—see the discussion of this important point made by Glauert [16] and Lock [17]. Eggleston and Stoddard [11] and other authors give various empirical curves for $a > 1/2$, but a parsimonious curve (as also shown in Fig. 7) is

$$C_T = 4(a-1)a + 2 \quad \text{for}\, 2 \leq C_T \leq 1 \tag{30}$$

Clearly, there is much uncertainty and scatter with the so-called "measured" data in this TWS and VRS regime, and there is no universal engineering consensus about the most appropriate curve to fit to the available measurements—see Burton et al. [12] and Buhl [18] for a more detailed discussion. In any case, it should always be remembered that while Eq. 30 and other such equations mimic the average flow velocity (or as far as flow velocities can be determined indirectly from power and thrust measurements), they are not rigorous representations of the induction velocity in the VRS or TWS. In fact, they are only spatially and temporally averaged approximations to the average flow velocity in these complex operating regimes. Further details of the flow state in the TWS and the VRS are discussed later.

3 Momentum Theory Analysis with Yaw Misalignment

The out of wind (i.e., yaw misalignment) performance of the wind turbine is of fundamental importance in the process of design. HAWTs will operate much of the time with some amount of yaw misalignment to the relative wind, mainly because of temporal lags in the mechanics of yaw tracking. If the turbine is not pointed directly into the wind, then the velocity normal to the disk plane is reduced by a factor $V_\infty \cos \gamma$, where γ is the yaw misalignment (or error) angle—see Fig. 8. If the power coefficient for a given operating state is assumed to stay constant (although it generally does not and will decrease somewhat—see next), then according to Eq. 2 the power output from a HAWT will drop at least by $\cos^3\gamma$. This result shows that for a yaw misalignment of only 20°, the power output from the turbine decreases by about 20% at a minimum.

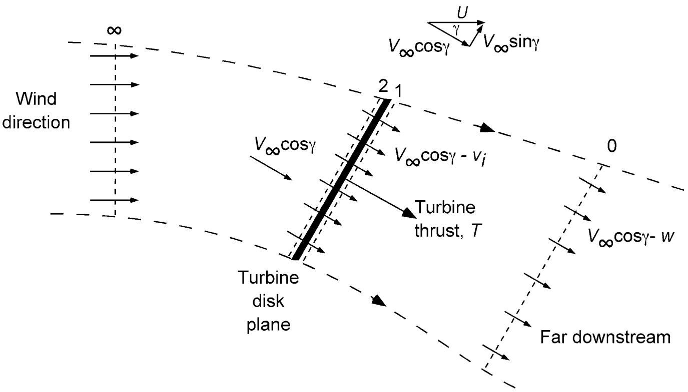

Fig. 8 Flow model for the momentum theory analysis of a HAWT in yawed (misaligned) flow

Therefore, it is clear that accurately controlling the orientation of the turbine relative to the wind direction is extremely important. Control must be performed through appropriate design, such as by using a downwind type of HAWT that will naturally want to weathervane into the wind, or by using an anemometer-based control device that senses changes in the wind speed and its direction and then drives a servo-motor to point the turbine more accurately into the wind. With the latter method, however, a primary problem is in measuring both the magnitude and direction of the wind, and also in turning the turbine sufficiently rapidly to achieve a better average yaw alignment. Larger turbines also have considerable rotational inertia and high gyroscopic forces, so it takes considerable torque and a finite time to re-orientate the turbine to a change in the wind direction.

The main problem, however, is that any form of yaw misalignment will be a source of high unsteady loads resulting from the in-component of wind velocity that is now produced in the plane of rotation (i.e., from the component $V_\infty \sin\gamma$). The subsequent unsteady airloads on the rotating blades can contribute to reducing mechanical reliability and may also lead to transients in the power output from the HAWT, neither of which is acceptable from an operational standpoint.

3.1 Flow Model and Analysis

A momentum theory flow model of wind turbine with a yaw misalignment angle γ is shown in Fig. 8. In this case, the turbine operates with components of flow velocity that are both perpendicular and parallel to the plane of rotation. Following Glauert [16], in this case the resultant flow velocity is defined as

$$U = \sqrt{(V_\infty \cos\gamma - v_i)^2 + (V_\infty \sin\gamma)^2} \tag{31}$$

The justification for this approach is based on the need for any yawed flow theory to reduce to the previous momentum theory results for unyawed flow. The net mass flow rate through the turbine is then

$$\dot{m} = \rho A U \tag{32}$$

The application of the conservation of momentum to the flow through the defined control volume gives

$$T = \dot{m} V_\infty \cos\gamma - \dot{m}(V_\infty \cos\gamma - w) = \dot{m} w \tag{33}$$

The power output from the HAWT in this case is

$$\begin{aligned} P_W &= \frac{1}{2}\dot{m}(V_\infty \cos\gamma - w)^2 - \frac{1}{2}\dot{m}V_\infty^2 \cos^2\gamma = \frac{1}{2}\dot{m}w(w - 2V_\infty \cos\gamma) \\ &= -\frac{1}{2}\dot{m}w(2V_\infty \cos\gamma - w) \end{aligned} \tag{34}$$

Again, using the result that $v_i = V_\infty a$, gives the thrust coefficient in the yawed case as

$$C_T = 4a\sqrt{(\cos\gamma - a)^2 + \sin^2\gamma} \tag{35}$$

and the corresponding power coefficient is

$$C_P = 4a\cos\gamma\sqrt{(\cos\gamma - a)^2 + \sin^2\gamma} = C_T \cos\gamma \tag{36}$$

Results are shown in Figs. 9 and 10 for various yaw misalignment angles. It is obvious that the theoretically attainable maximum power coefficient drops quickly with increasing yaw angle (see also Fig. 11), and that the operating conditions for maximum power coefficient also change. Notice that in the yawed case, the validity of these solutions will now be restricted to the condition that $a \leq 0.5 \cos\gamma$ to avoid the possibility of violating the assumed flow model shown in Fig. 8.

Fig. 9 Momentum theory solution for the thrust coefficient of a HAWT in misaligned yawed flow in terms of the induction ratio

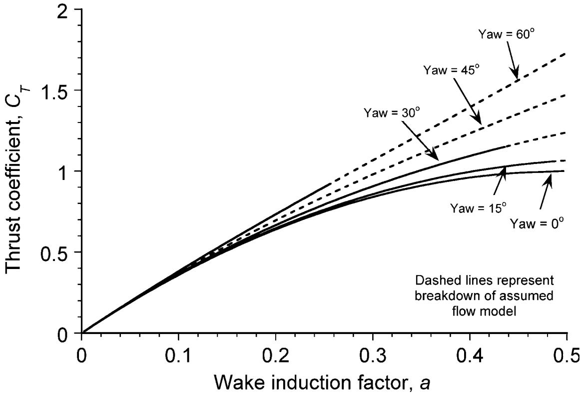

Fig. 10 Momentum theory solution for the power coefficient of a HAWT in misaligned yawed flow in terms of the induction ratio

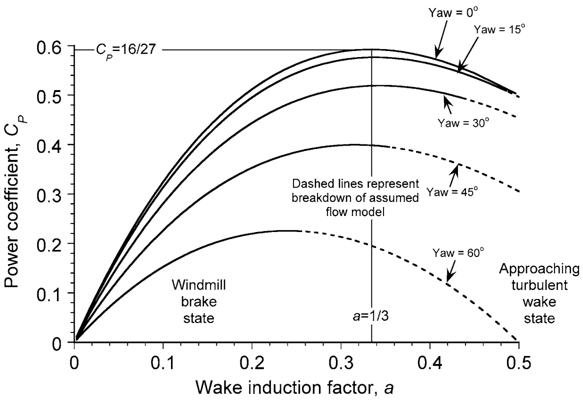

Fig. 11 The maximum power coefficient of a HAWT in misaligned yawed flow drops off quickly for larger yaw misalignment angles

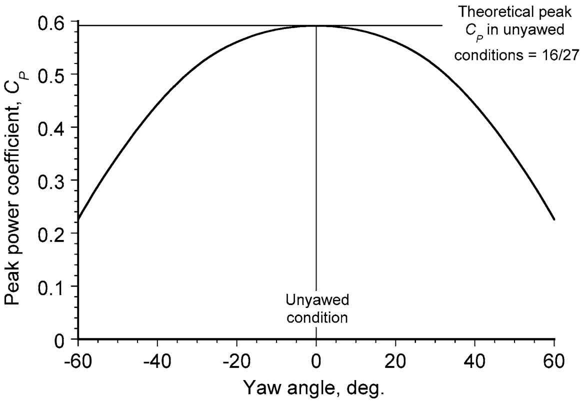

This means that the validity of these solutions become increasingly restrictive for larger yaw misalignment angles, and so placing further limits on the general applicability of the momentum theory at higher wind speeds, and certainly in its practical use without any modifications or empirical correction.

4 Maximum Wind Energy Conversion Efficiency

Because both the thrust and power coefficients on a HAWT are functions of the induction factor, a, it is useful to find the operating condition for maximum power output. Clearly, the foregoing results from the momentum theory analysis shows that this condition is obtained without any yaw misalignment angle. Therefore, differentiating Eq. 23 with respect to a gives

$$\frac{dC_P}{da} = 4(1 - 4a + 3a^2) = 0 \tag{37}$$

for a maximum. By inspection, this condition is met when the wake induction factor $a = 1/3$ in unyawed flow conditions, and the corresponding values of C_T and C_P are 8/9 and 16/27, respectively (see Fig. 7). This operating condition is called the Betz–Lanchester limit; see Glauert [14, 15] and Bergy [19]. It gives the upper theoretical limit to the operating condition of a HAWT such that it can extract the most amount of energy relative to the energy content of the wind when it blows at a given speed, assuming no viscous or other losses other than ideal induced losses.

Notice from Figs. 10 and 11 that the effects of yaw misalignment are to change the condition for the peak power coefficient, although these conditions would not necessarily be used as design points. Notice also that at the peak performance operating condition ($a = 0.5$ in unsaved condition) the wake area expansion is

$$\frac{A_0}{A} = \frac{1-a}{1-2a} = \frac{1-1/3}{1-2/3} = 2 \tag{38}$$

Therefore, in this case the downstream wake expands to twice the area of the turbine's disk. This issue of the downstream wake behavior is considered again later in this chapter.

5 Representative Power Curve for a HAWT

By now it will be apparent that the simple momentum theory does not allow a prediction of the overall power characteristics of a wind turbine at all speeds and at yaw misalignment angles. Therefore, to proceed any further first requires an examination of the actual measured output characteristics for a HAWT as a function of wind speed. A representative such power curve is shown in Fig. 12 for a variable speed turbine, which is one of the most common types of HAWT. Notice that no power is produced below a so-called "cut-in" wind speed; this is because of the need to overcome various types of losses, including aerodynamic,

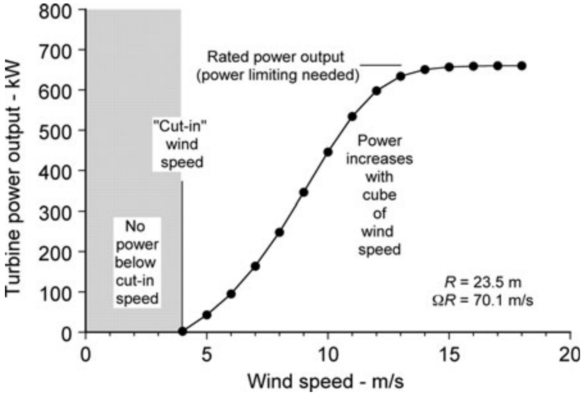

Fig. 12 Representative power output versus wind speed curve for a HAWT

Fig. 13 Representative power coefficient versus wind speed curves for constant rotational speed (variable pitch) and variable rotational speed types of HAWT

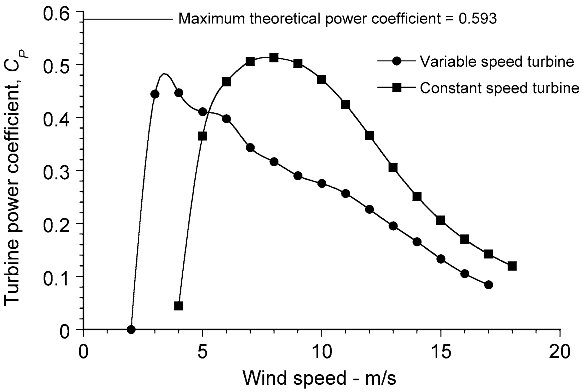

mechanical, and electrical losses with the generator. This characteristic means that a minimum wind speed is needed before the turbine will begin to rotate steadily, and so before any useful power is generated. After power is being produced, the output from the turbine increases rapidly with the cube of the oncoming wind speed, as would be expected according to Eq. 6.

Notice from Fig. 12 that the measured power curve then flattens out and approaches a limit; this limit is known as its rated power output. Power limiting is introduced by design and is always needed on a HAWT so that its rotational speed never exceeds values that might cause structural failure (i.e., avoiding a catastrophic over speed or "runaway" condition), or that the power being extracted stays below the rated capacity of the electrical generator and so not overload it.

One way of controlling the power output is to change the blade pitch angles (i.e., feathering), thereby controlling the driving aerodynamic forces being generated on the blades. Alternatively, some form of mechanical or aerodynamic brake (such as spoilers) can be used to limit power output, but such devices would normally be activated only at very high wind speeds.

Representative power coefficient versus wind speed curves for constant rotational speed (variable pitch) and variable rotational speed types of HAWTs are shown in Fig. 13. Notice that the variable speed type can operate efficiently over a wider range of wind speeds and can exhibit more efficient energy extraction at the lower wind speeds. The disadvantage of this type of HAWT, however, is that its aerodynamic efficiency decreases at the higher wind speeds, although such a characteristic is also desirable in that it eventually serves to automatically regulate the power output and prevents an overspeed condition.

For engineering analysis, the power curve for a wind turbine is usually plotted in a derived form as a power coefficient C_P (which has already been introduced) versus a non-dimensional wind speed parameter known as the tip speed ratio (TSR), X_{TSR}. The TSR is defined as

$$X_{\text{TSR}} = \frac{\text{turbine tip speed}}{\text{wind speed}} = \frac{\Omega R}{V_\infty} \tag{39}$$

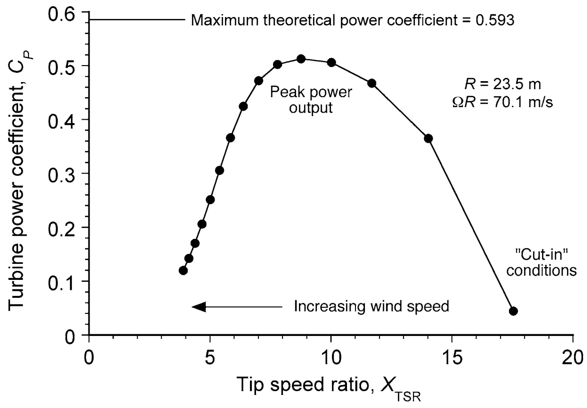

Fig. 14 Representative airpower coefficient versus tip speed ratio curve for a constant rotational speed HAWT

Notice that the value of X_{TSR} will change through either variations of wind speed and/or with variations in turbine speed. For the results of the constant rotational speed turbine shown in Fig. 13, the corresponding airpower C_P versus X_{TSR} curve is shown in Fig. 14 when correcting the power output measurements for a 90% electrical/mechanical conversion efficiency (i.e., assuming $\eta = 0.90$). In this case, the measured aerodynamic efficiency is seen to reach a peak that is almost 85% of the theoretical maximum that can be extracted from the wind by an ideal HAWT (i.e., one defined by the momentum theory solutions).

6 Blade Element Model for a HAWT

The foregoing results have shown the general flow characteristics of the power output from a HAWT and the momentum theory has exposed the maximum possible aerodynamic efficiencies under certain operating conditions. However, the simple momentum theory does not have the capabilities to predict the power curve as a function of wind speed because the operating state of the turbine (i.e., its thrust) must somehow be defined, and this value is generally not known a priori. The simple momentum theory also does not have the means to explain how to design the shape of the blades, or how to set their pitch angles to achieve the condition for the most useful (or most efficient) power generation.

These limitations can be circumvented to a large extent by the use of blade element (BE) methods coupled with inflow models that can predict the spatial distribution of “induction” flow velocities across the plane of the turbine’s disk. Included in this category of methods is the blade element momentum (BEM) theory. Incorporating estimates for the airfoil characteristics, along with the induction velocities in the BE method, allows the blade loads and performance characteristics of the HAWT to be estimated over a wide range of operating conditions. The main advantage of the blade element theories, in general, is that they allow the ready examination of the effects of the primary design variables (i.e., blade twist, blade planform, number of blades, airfoil sections, etc.) on energy extraction as a function of wind speed, blade pitch, tip speed, etc.

Needless to say, the potential flexibility offered by the BE- and BEM-based models have allowed them to be built up over the years into sophisticated engineering design tools, and they can also be coupled (with some additional effort) to structural dynamic models of the blades and the support tower. Typical comprehensive models of this type are embodied in the well-known computer codes AERODYN [20], BLADED [21], and ADAMS [22]. While these types of models have demonstrated many good predictive capabilities, they also have several intrinsic limitations in their aerodynamic fidelity and improvements are still needed.

6.1 Flow Model and Analysis

Initially, consider the BE theory and how the general analysis of a HAWT leads to a requirement for some mathematical representation of the induction velocities to fully solve the problem of predicting the blade loads and the power output. It will be shown later how this limitation is overcome to some extent with the use of the BEM model, which allows the spatial distribution of the induction velocity over the turbine's disk to be determined as part of the solution process.

As shown in Fig. 15, the local pitch angle of the blade element is θ so that the angle of attack at the blade element is $\alpha = \theta + \varphi$ where φ is called the inflow angle. The blade pitch is often measured from the position of full feathering (with the blade pointed directly into wind), but the convention used makes no difference to the final results. The physical effect of the inflow (or induction) angle is clear, in that the induction velocity modifies the direction of the resultant flow and so alters the angle of attack at each blade element. It will be apparent from Fig. 15, that it is the integrated effect of the forward inclination of the lift vector at each blade section that provides the necessary torque to drive the turbine and so produce a useful power output at its shaft.

Assume that the swirl component in the flow near the turbine and its wake is small and can be neglected. The resultant incremental lift *dL* and drag *dD* per unit span on the blade element are

$$dL = \frac{1}{2}\rho U^2 c C_l \, dy \tag{40}$$

and

$$dD = \frac{1}{2}\rho U^2 c C_d \, dy \tag{41}$$

where C_l and C_d are the airfoil section lift and drag coefficients, respectively, and the resultant flow velocity, U, is approximately Ωy. At each blade element, the lift

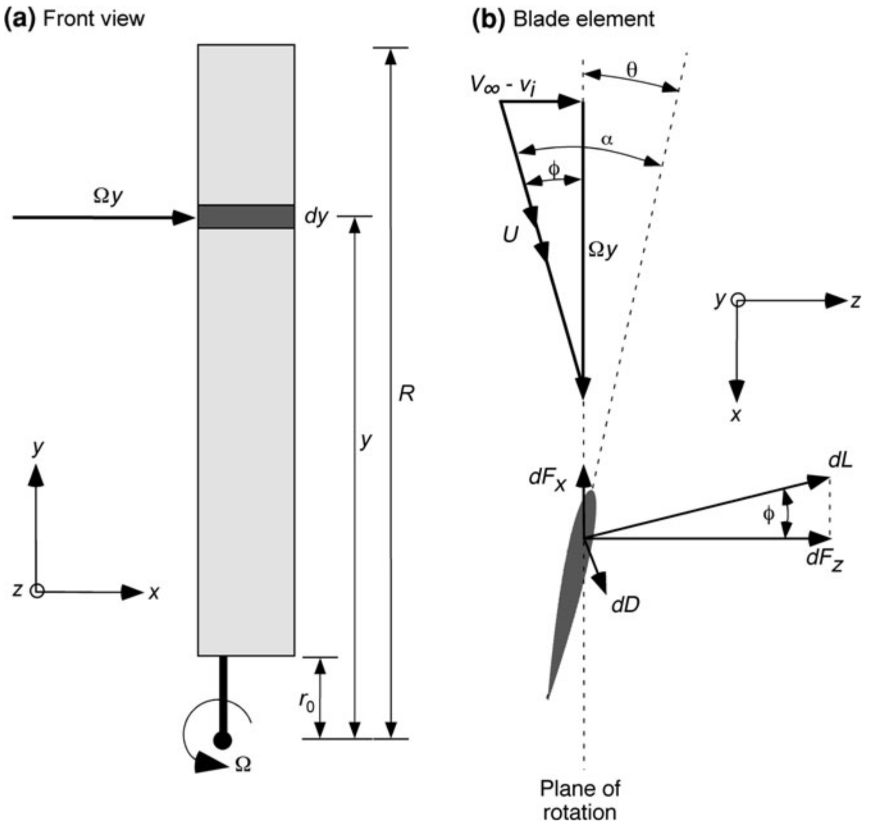

Fig. 15 Blade element model for a HAWT operating in axial (unyawed) flow

dL and drag *dD* will act perpendicular and parallel to the resultant flow velocity, respectively. Notice that the quantity *c* is the local blade chord, which will usually vary along the span on any modern HAWT. Wake swirl may be included into *U*, although this component is generally small and it is also hard to calculate accurately without invoking several other assumptions about the flow developments in the wake. In any practical sense, the contribution to the airloads from in-plane swirl can be considered as small, except perhaps if the blades operate near stall or at low tip speed ratios or other off-design conditions.

In Fig. 15 it is shown how the aerodynamic forces can be resolved perpendicular (into a thrust on the turbine, *T*) and parallel to the turbine's disk plane (the source of the torque and power output, P_W) giving

$$dF_z = dL \cos \phi + dD \sin \phi \tag{42}$$

and

$$F_x = dL \sin \phi - dD \cos \phi \tag{43}$$

The contributions to the thrust, shaft torque, and power output of the turbine are thus

$$dT = N_b \, dF_z \tag{44}$$

$$dQ = N_b y \, dF_x \tag{45}$$

$$dP_W = N_b \Omega y \, dF_x \tag{46}$$

where N_b is the number of blades comprising the turbine. Furthermore, notice that unless the turbine is yawed with respect to the wind and that there is no wind shear, the aerodynamic environment is (ideally) axisymmetric, and the airloads are independent of the blade position relative to the shaft (i.e., its azimuth angle).

Substituting the results for dF_x and dF_z from Eq. 42 and Eq. 43 gives

$$dT = N_b(dL \cos\phi + dD \sin\phi) \tag{47}$$

$$dQ = N_b(dL \sin\phi - dD \cos\phi)y \tag{48}$$

$$dP_W = N_b(dL \sin\phi - dD \cos\phi)\Omega y \tag{49}$$

Applying small angle simplifications to the preceding equations gives

$$dT = N_b(dL + \phi dD) \tag{50}$$

$$dQ = N_b(\phi dL - dD)y \tag{51}$$

$$dP_W = N_b\Omega(\phi dL - dD)y \tag{52}$$

The incremental thrust coefficient on the turbine blades is then

$$\begin{aligned} dC_T = \frac{N_b dL}{\frac{1}{2}\rho A V_\infty^2} &= \left(\frac{N_b c}{\pi R}\right)\left(\frac{\Omega y}{V_\infty}\right)^2 (C_l + \phi C_d)\, dr \\ &= \sigma X^2 (C_l + \phi C_d)\, dr \end{aligned} \tag{53}$$

where $r = y/R$, $\sigma = N_b c/\pi R$ is the local or chord solidity of the turbine, and $X = \Omega y/V_\infty$ is the local section speed ratio. It will be apparent that the local section speed ratio can be written as

$$X = \frac{\Omega y}{V_\infty} = \frac{\Omega R}{V_\infty}\left(\frac{\Omega y}{\Omega R}\right) = X_{\mathrm{TSR}}\, r \tag{54}$$

Therefore, the incremental thrust coefficient becomes simply

$$dC_T = \sigma X_{\mathrm{TSR}}^2 (C_l + \phi C_d) r^2 \, dr \tag{55}$$

Typically, the product φC_d is also small (C_d will typically be two orders of magnitude smaller than C_l when the blade operates in attached flow), so that the previous equation can be simplified to

$$dC_T = \sigma X_{\mathrm{TSR}}^2 C_l r^2 \, dr \tag{56}$$

Proceeding in a similar manner to find the incremental power output coefficient dC_P gives

$$dC_P = \sigma X_{\mathrm{TSR}}^3 (\phi C_l - C_d) r^3 \, dr \tag{57}$$

although in this case φC_l is not small compared to C_d. It will also be apparent that the inflow angle can be written as

$$\phi = \tan^{-1}\left(\frac{V_\infty - v_i}{\Omega y}\right) \approx \frac{V_\infty - v_i}{\Omega y} = \left(\frac{V_\infty - aV_\infty}{\Omega R}\right)\left(\frac{\Omega R}{\Omega y}\right) = \left(\frac{1-a}{r X_{\mathrm{TSR}}}\right) \tag{58}$$

6.2 *Solving for C_T and C_P*

In practice, the values of C_T and C_P can be solved by numerical integration, i.e., by numerically solving the equations

$$C_T = \int_{r=1}^{r=1} dC_T \quad \text{and} \quad C_P = \int_{r=1}^{r=1} dC_P \tag{59}$$

However, it will be seen from the forgoing development of the BE equations, that to accurately calculate the values of C_T and C_P, the spanwise variation in the wake induction ratio, a must be predicted too, along with providing a representation of the blade section aerodynamic force coefficients C_l and C_d in some form. Predicting both the wake induction and the blade section aerodynamic characteristics are both difficult problems, in general, although various mathematical approximations and numerical techniques may be used.

In the first instance, a can be related analytically to C_T by using Eq. 27. However, this assumes uniform inflow over the disk, a questionable assumption that will limit the ability of the BE theory to produce sufficiently accurate predictions of spanwise blade loads as a function of the design variables. Even with uniform inflow assumptions, the integrated power predictions are usually found to be in reasonable agreement with measurements, at least for conditions without blade stall, so the value of this approach for design purposes is not completely lost. However, for detailed design and loads predictions, the wake induction factors must be represented with sufficient fidelity such that the spanwise air-loads along the blades (and also their temporal variations) can be predicted more accurately.

7 Blade Element Momentum Theory for a HAWT

The Blade Element Momentum (BEM) theory has a significant advantage over the basic BE theory in that it allows the distribution of the induction factor along the blade span to be predicted from first principles, albeit still with several inherent assumptions. The BEM theory is a differential extension of the simple momentum theory that was discussed previously, and invokes the fundamental equivalence between the local circulation and momentum theories of lift. After the induction factor is determined using the BEM theory, then the loads and performance can be obtained following the same foundational principles of the BE theory.

The primary value of the BEM theory at a fundamental level is that it allows for a good understanding of the effects of varying geometrical and aerodynamic parameters on the overall performance characteristics of a HAWT, and without making ad hoc or otherwise empirical approximations about the magnitude and/or the distribution of the induction factors across the plane of the turbine's disk. More importantly, the BEM method helps in the determination of the blade shapes needed for maximum power generation at a given operating condition, hence better guiding the choices involved in design.

The principle of the BEM theory is based on satisfying a combination of a momentum balance on successive annuli of the turbine's disk with a blade element representation of the sectional aerodynamics. This approach implicitly assumes that the spanwise loading gradients are small, a reasonable assumption to make except at the tip and root of the blades. Just like the simple momentum theory, the BEM theory may also be restricted in terms of its applicability to certain ranges of wind speeds and to certain operating states of the turbine. In particular, and again just like the simple momentum theory, the BEM theory becomes increasingly invalid when the turbine is operating under yawed conditions, or when operating in the TWS or VRS. While the BEM theory includes several further inherent approximations and limitations, its validity may be extended with the use of certain empirical correction methods. When brought to this level, the value of the BEM theory to the engineer for the design of HAWTs has been fairly well established through correlation studies with measured loads and power output characteristics.

7.1 BEM Flow Model and Analysis

Referring to Fig. 16, the mass flow over an annulus of the turbine is

$$d\dot{m} = \rho dA(V_\infty - v_i) = 2\pi\rho(V_\infty - v_i)y\,dy \tag{60}$$

so that assuming the validity of the differential form of Eq. 24, the incremental thrust on the annulus is

$$dT = 2\rho(V_\infty - v_i)v_i dA = 4\pi\rho(V_\infty - v_i)v_i y\,dy \tag{61}$$

In coefficient form (again with $r = y/R$) this is simply

$$dC_T = 8\left(1 - \frac{v_i}{V_\infty}\right)\frac{v_i}{V_\infty} r\,dr = 8(1-a)ar\,dr \tag{62}$$

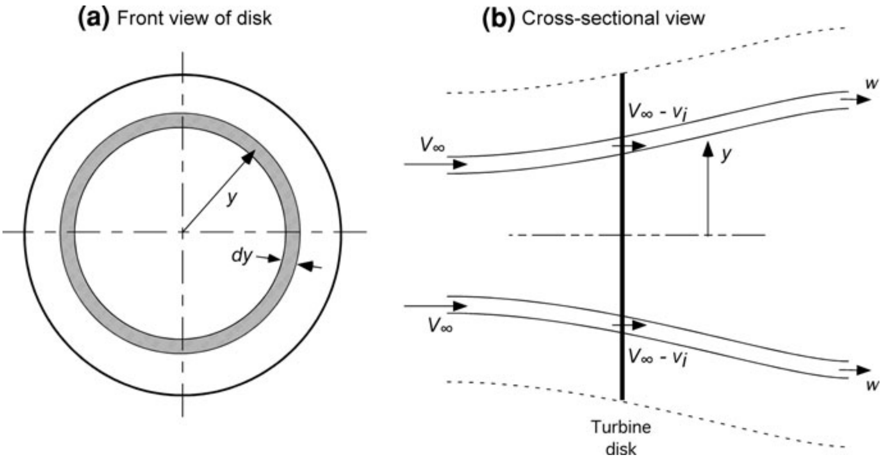

Fig. 16 Flow model used for the BEM analysis of a HAWT

This latter equation integrates to the correct result for C_T as given by the simple momentum theory in Eq. 25 under the assumption that the induction ratio, a, is constant over the turbine's disk, i.e.,

$$C_T = \int_0^1 8(1-a)ar\,dr = 4(1-a)a \tag{63}$$

The results for the differential momentum and blade element approaches can now be equated to get

$$dC_T = 8(1-a)ar\,dr = \sigma X_{\mathrm{TSR}}^2 (C_l + \phi C_d) r^2\,dr \tag{64}$$

thereby formally linking together the momentum and circulation theories of aerodynamic lift.

The next step is to relate C_l and C_d to the angle of attack of the blade sections. This can be done using a conventional "look-up" procedure from a set of tables of measured airfoil characteristics. However, a convenient and useful simplification of the equations at this point is obtained by recognizing that C_l/C_d is generally large and that the product φC_d is generally very small, so giving the thrust as

$$dC_T = \sigma X_{\mathrm{TSR}}^2 C_l r^2\,dr \tag{65}$$

without much loss of accuracy in the normal (windmill) state of operation. Furthermore, in the first instance the flow can be assumed to be fully attached to the blades, so that the relationship between C_l and α is linear, i.e.,

$$C_l = C_{l_\alpha}(\theta - \alpha_0 + \phi) \tag{66}$$

where φ is given by Eq. 58, and where α_0 is the zero-lift angle of attack of the airfoil used at that blade section. Then, in this case, the lift coefficient becomes

$$C_l = C_{l_\alpha}\left(\theta - \alpha_0 + \frac{1-a}{rX_{\text{TSR}}}\right) \tag{67}$$

Using this latter result (and assuming α_0 can be absorbed into θ if it is defined with respect to the zero-lift angle) gives

$$8\,(1-a)\,a = \sigma X_{\text{TSR}}^2\, C_l r = \sigma X_{\text{TSR}}\, C_{l_\alpha}(X_{\text{TSR}}\theta r + (1-a)) \tag{68}$$

After further manipulation, this equation can be expressed in the form

$$a^2 - \left(\frac{\sigma X_{\text{TSR}} C_{l_\alpha}}{8} + 1\right) a + \frac{\sigma X_{\text{TSR}} C_{l_\alpha}(X_{\text{TSR}}\theta r + 1)}{8} = 0 \tag{69}$$

where the induction factor, a, is the unknown. This equation has the solution

$$a(r, X_{\text{TSR}}) = -\sqrt{\left(\frac{\sigma X_{\text{TSR}} C_{l_\alpha}}{16} + \frac{1}{2}\right)^2 - \frac{\sigma X_{\text{TSR}} C_{l_\alpha}(X_{\text{TSR}}\theta r + 1)}{8}} + \left(\frac{\sigma X_{\text{TSR}} C_{l_\alpha}}{16} + \frac{1}{2}\right) \tag{70}$$

Equation 70 is valid for the range $0 \leq a \leq 0.5$; for higher values of a (considered later) the turbine approaches the TWS and then the VRS, for which no form of the momentum theory can give a rigorous solution to the actual flow state, a point explained previously.

Notice that Eq. 70 now allows the induction factor a to be solved for as a function of radial position on the blade for any given blade pitch, magnitude and distribution of blade twist, chord variation, and airfoil section distribution (through C_{l_α} and α_0). After the induction factor is obtained, the thrust and power from the turbine may then be found by integration across the disk using

$$C_T = \sigma X_{\text{TSR}}^2 \int_0^1 C_l r^2\, dr \quad \text{or} \quad C_T = 8 \int_0^1 (1-a) a r\, dr \tag{71}$$

and

$$C_P = \sigma X_{\text{TSR}}^3 \int_0^1 (\phi C_l - C_d) r^3\, dr \tag{72}$$

Notice that the first term represents the contribution of the lift forces on the blades that act to drive the turbine and produce a useful power output. In other words, the extraction of power from a HAWT depends on the ability of the blades to generate efficient lift forces over appropriate ranges of angles of attack. The second term is a profile power loss, which is a result of pressure forces and viscous shear drag contributions acting on the blades.

Furthermore, notice that while a greater blade area A_b (= σA) will increase the power output from the turbine (all other factors being equal), a greater blade area also increases profile losses and so can reduce the turbine's efficiency.

7.2 The Optimum HAWT: Ideal Blade Twist and Taper

There are several points of interest in Eq. 70. One is the distribution of blade twist that results in a uniform value of the induction factor over the turbine's disk, and so the condition for the best efficiency in energy extraction (i.e., what is assumed by the simple momentum theory). It will be apparent that for a given tip speed ratio this condition can only be obtained if the product $\theta r =$ constant, which, by analogy with helicopter rotors and propellers, is known as ideal twist, i.e., $\theta(r) = \theta_{\text{tip}}/r$. This form of hyperbolic blade twist will always give the lowest levels of induced losses on the turbine blades and, therefore, the best levels of energy extraction from the wind.

Notice that the form of the distribution of blade twist for maximum efficiency is independent of tip speed ratio, but that the magnitude of the needed twist does depend on the tip speed ratio (i.e., the amount of twist given to the blade and not just its form will affect the range of wind speeds and/or tip speeds over which the turbine can operate most efficiently). It has already been shown using the simple momentum theory that the average induction velocity is equal to 1/3 at the condition for maximum energy extraction from the wind. For variable pitch turbine blades, this result allows Eq. 70 to be solved for the blade pitch at any given tip speed ratio (or wind speed for a given blade tip speed) to reach the condition of maximum possible energy extraction.

Another point of interest in this development is that Eq. 67 shows that if rectangular blades are used on the turbine then the distribution of lift coefficient over the blade becomes high inboard, and so energy extraction will be non-optimal (i.e., the local sectional lift-to-drag ratios will not be at or near to their best values) and the broadest range of attainable efficiencies will eventually be limited by the onset of blade stall. If the blade is hyperbolically twisted to give uniform induction (i.e., with a being constant) then the spanwise distribution of lift coefficient is

$$C_l = C_{l_\alpha}\left(\frac{\theta_{\text{tip}}}{r} + \frac{1-a}{rX_{\text{TSR}}}\right) = \frac{C_{l_\alpha}\alpha_{\text{tip}}}{r} \tag{73}$$

where α_{tip} is defined as the angle of attack at the blade tip. Clearly, a rectangular blade will operate at higher lift coefficients at the inboard sections and will begin to more readily stall there, and so higher profile losses will be incurred compared to those otherwise be achieved without stall.

Control over the sectional lift coefficients (and hence the lift-to-drag ratios of the blade sections) can be achieved by using changes to the planform shape, although this must be done while also striving to maintain uniform inflow. From Eq. 65 that the thrust per unit span along the blade is

$$\frac{dC_T}{dr} = \sigma X_{\text{TSR}}^2 C_l r^2 \tag{74}$$

which is constant in the ideal case, i.e., the thrust varies linearly across the blade from zero at the rotational (shaft) axis and reaches a maximum at the blade tip. (Notice that it is easily shown that a linear thrust distribution is exactly equivalent to a uniform circulation distribution along the blade span). This result means that with ideal blade twist and minimum induced losses the grouping $\sigma\, C_l r^2$ must be constant at any given tip speed ratio, i.e.,

$$\sigma\left(\frac{C_{l_\alpha}\alpha_{\text{tip}}}{r}\right) r^2 = \sigma\, C_{l_\alpha}\, \alpha_{\text{tip}}\, r = \sigma\, C_l\, r = \text{constant} \tag{75}$$

If the lift coefficient is to be prescribed as constant, say at the appropriate value that will achieve the best lift-to-drag ratio of the airfoil sections, then the only way this condition is satisfied is if $\sigma r =$ constant and the local solidity is varied as

$$\sigma = \frac{\sigma_{\text{tip}}}{r} \tag{76}$$

Equivalently, the chord along the blade span must be varied as

$$c_{\text{tip}} = \frac{c_{\text{tip}}}{r} \tag{77}$$

which, of course, like the required twist distribution for optimum levels of output efficiency, is also of hyperbolic form.

Most commercial HAWTs use both hyperbolic blade twist and hyperbolically tapered blade planforms (or close approximations to these shapes) to help minimize aerodynamic losses on the blades and so to maximize the wind energy extraction and overall efficiency of the turbine. This type of blade design also gives the advantage of keeping the values of C_l inboard on the blade from operating too close to stall, and thereby keeping flow separation and increases in profile drag from limiting energy extraction efficiencies over a wider range of tip speed ratios.

The main benefit of blade taper, however, is that by getting more of the blade to operate at its best average lift-to-drag ratios, the profile losses on the blades will be minimized and power output maximized. In this regard, the behavior of the lift-to-drag ratio for the S809 airfoil is shown in Fig. 17, where it can be seen that the best lift-to-drag ratios are obtained only over a relatively small range of angles of attack (about a 4° spread). Hence, the importance of operating the turbine "on-design" near its maximum efficiency through not only its "optimum" blade shape design but also through precise pitch control at the appropriate wind speeds.

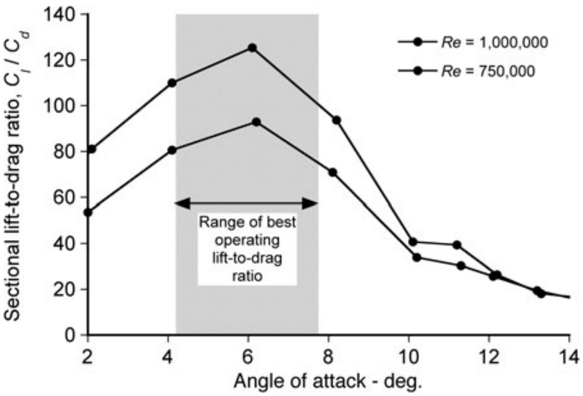

Fig. 17 Sectional lift-to-drag ratios for the S809 airfoil at two chord Reynolds numbers

8 Understanding Operational Interdependencies

It is clear that the BEM theory gives considerable insight into the design factors affecting loads and power output performance that are not available from simple momentum theory solutions. For example, the power output equation can now be expanded to give

$$C_P = \sigma X_{\mathrm{TSR}}^3 \int_0^1 \phi C_l r^3\,dr - \sigma X_{\mathrm{TSR}}^3 \int_0^1 C_d r^3\,dr \tag{78}$$

Proceeding further using the previously derived result for the inflow angle (Eq. 58) that

$$\phi = \frac{1-a}{r X_{\mathrm{TSR}}} \tag{79}$$

and for the incremental thrust on the blade element (Eq. 65) that

$$C_T = \sigma X_{\mathrm{TSR}}^2 C_l r^2\,dr \tag{80}$$

and if it is also assumed that $C_d = C_{l_0} C_d = C_{d_0}$ then the power output coefficient becomes

$$\begin{aligned} C_P &= \sigma X_{\mathrm{TSR}}^3 \int_0^1 \phi C_l r^3\,dr - \sigma X_{\mathrm{TSR}}^3 \int_0^1 C_{d_0} r^3\,dr \\ &= X_{\mathrm{TSR}} \int_{r=0}^{r=1} \phi\, r\, dC_T - \frac{\sigma X_{\mathrm{TSR}}^3}{4} C_{d_0} \\ &= \int_{r=0}^{r=1} (1-a) dC_T - \frac{\sigma X_{\mathrm{TSR}}^3 C_{d_0}}{4} \end{aligned} \tag{81}$$

In the ideal case, where a is uniformly distributed over the disk, then this equation becomes

$$\begin{aligned} C_P &= C_T(1-a) - \frac{\sigma X_{\mathrm{TSR}}^3 C_{d_0}}{4} \\ &= 4(1-a)^2 a - \frac{\sigma X_{\mathrm{TSR}}^3 C_{d_0}}{4} \end{aligned} \tag{82}$$

where the first term will now be recognized as the correct result for the power output as derived from the simple momentum theory. In this case, the maximum power coefficient of $C_P = 0.593$ is recovered from Eq. 82 when $a = 1/3$ and $C_{d_0} = 0$. In the real case, where a is non-uniformly distributed over the disk (and also $C_{d_0} > 0$), then this latter equation can be written as

$$C_P = C_T(1-\kappa a) - \frac{\sigma X_{\mathrm{TSR}}^3 C_{d_0}}{4} \tag{83}$$

where $\kappa \geq 1$ and accounts on average for an induced inflow that is higher than the ideal at any given operating condition. Typically, κ will be of the order of 1.1–1.2, and so the power output from the turbine will be reduced by some 10–20% relative to the ideal. The second term in Eq. 83 (which comes from the BE theory) depends on the blade area (solidity) and the drag coefficient of the airfoil section(s) comprising the blades, and acts to further reduce the power output. Notice that this second (profile) term can be written in dimensional form as

$$P_0 = -\frac{1}{2}\rho A V_\infty^3 \left(\frac{\sigma X_{\mathrm{TSR}}^3 C_{d_0}}{4}\right) = -\rho A (\Omega R)^3 \left(\frac{\sigma C_{d_0}}{8}\right) \tag{84}$$

where the negative sign indicates an energy loss relative to the ideal (no loss), which in this case is from the cumulative effect of the profile drag contributions on the rotating blades. Furthermore, it will be apparent that this energy loss is proportional to the cube of the blade tip speed, hence the importance of minimizing the tip speed of the turbine (all other factors being equal) to maximize its energy extraction and operating efficiency.

Representative performance characteristics for a HAWT (as predicted by the BEM theory) are shown in Figs. 18, 19, and 20 for blades with ideal twist when operating at different blade pitch angles. From these results, the power coefficient at a fixed rotational speed can be derived for different wind speeds. For variable pitch blades, a series of power coefficient curves can then be determined over a range of pitch angles and wind speeds, and the envelope of peak operational efficiency is then determined. This outcome would be the desired operating envelope for the turbine in the best-case scenario.

Several interesting (and fairly general) characteristics of a HAWT can be observed from these results. On one hand, it can be seen that the use of shallow blade pitch angles allows for good energy extraction over a significant range of wind speeds. On the other hand, clearly neither large positive nor negative pitch

Fig. 18 Representative thrust produced on a HAWT as a function of tip speed ratio using the BEM theory for various pitch angles (only ideal induced losses included)

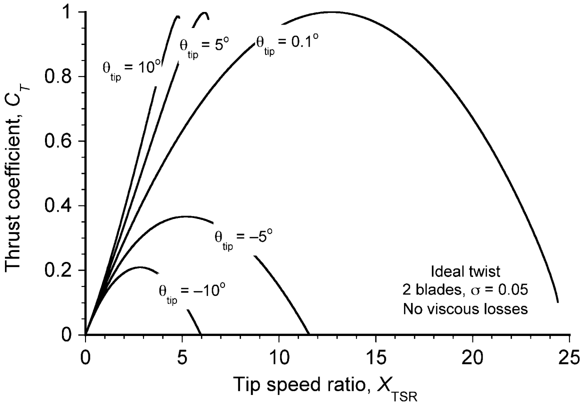

Fig. 19 Representative power output produced from a HAWT as a function of tip speed ratio using the BEM theory for various pitch angles (only ideal induced losses included)

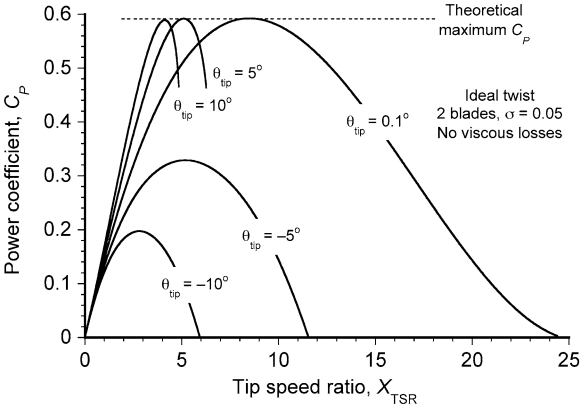

Fig. 20 Representative power output from a HAWT for airfoil sections with different assumed viscous drag coefficients as a function of tip speed ratio using the BEM theory (non-ideal losses included, but without tip losses)

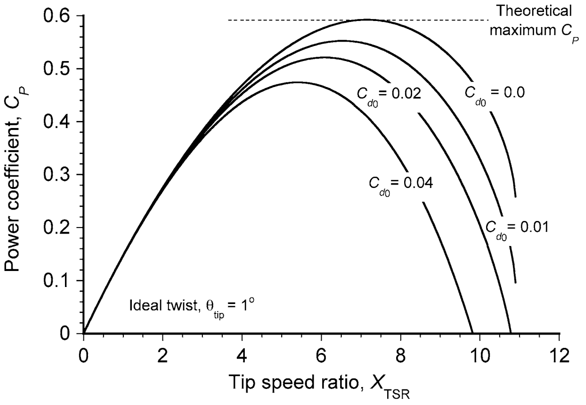

angles allow for efficient power extraction. Hence, the importance in matching precisely the blade pitch to the wind speed to maximize the energy capture. Recall that the BEM theory is strictly valid only for local induction values in the range $0 \leq a \leq 0.5$, so the power curves cannot be defined for all wind speeds and at all blade pitch angles unless empirical results are used to correct the basic theory (see later).

Figure 20 shows how the power output from a HAWT depends on the viscous drag of the airfoils used on the blades. As already shown using Eq. 82, achieving the best aerodynamic efficiency and the maximum energy extraction favors airfoils with lower average drag coefficients, all other factors considered constant. At the Reynolds numbers encountered on HAWTs most airfoils tend to have drag coefficients in the range $0.01 \leq C_{d_0} \leq 0.02$ unless their surface finish is further degraded by erosion, dead insects, frost, etc. (see later). Some airfoil sections are more sensitive to these effects than others, and so any expected sensitivity on airfoil lift and drag coefficients must be accounted for when estimating the efficiencies and potential power output of HAWTs. Overall, profile losses tend to reduce energy capture from a HAWT by about a further 10% when compared to the theoretical ideal.

9 Introducing Non-ideal Effects and Tip Losses

The physics of the rollup of the blade tip vortices and the non-uniform induced flow in the wake downstream of the turbine produces “non-ideal” induced losses that cause non-uniform spanwise gradients in aerodynamic loading near the tips of the blades. These non-ideal effects increase the average induction velocity at the turbine, and so act to increase induced losses and decrease energy extraction efficiency. In fact, the combined effects of higher induced flow acts to both decrease the thrust on the turbine and also to decrease its power output.

One clearly identifiable source of these higher induced losses is from “tip loss,” which is a loss that arises from the formation of the trailing vortex at the blade tips. Because most of the power generated by the turbine actually comes from stations out toward the blade tip, these tip loss effects must be modeled very accurately on HAWTs to avoid inaccurate power output predictions.

Unfortunately, tip loss effects are difficult to compute without resorting to vortex theory or some other more advanced aerodynamic method (see later). However, in the first instance tip loss effects can be approximated within the context of the BEMT by using the Prandtl tip loss correction method. Prandtl’s correction can account, albeit approximately, for a finite number of blades, and also for variations of blade planform and twist through the effect on the local inflow angle. The result is expressed in terms of a correction factor F to the change in momentum over the annulus of the disk such that Eq. 62 now becomes

$$C_T = 8F(1-a)a r \, dr \tag{85}$$

where

$$F = \left(\frac{2}{\pi}\right) \arccos(\exp(-f)) \tag{86}$$

and where the exponent f is given in terms of the number of blades and the radial position of the blade element r by

$$f = \frac{N_b}{2}\left(\frac{1-r}{r\phi}\right) = \frac{N_b}{2}\left(\frac{1-r}{1-a}\right) X_{\mathrm{TSR}} \tag{87}$$

If blade root losses are also to be modeled (from the finite cut-out where the blade attaches to the hub), then the corresponding equation for f is

$$f = \frac{N_b}{2}\left(\frac{r-r_0}{1-a}\right) X_{\mathrm{TSR}} \tag{88}$$

where r_0 represents the root cut-out distance. With the incorporation of tip and root loss effects into the BEM theory, the equation for the induction factor becomes

$$a(r, X_{\mathrm{TSR}}, F) = -\sqrt{\left(\frac{\sigma X_{\mathrm{TSR}} C_{l_\alpha}}{16F} + \frac{1}{2}\right)^2 - \frac{\sigma X_{\mathrm{TSR}} C_{l_\alpha} (X_{\mathrm{TSR}} \theta r + 1)}{8F}} + \left(\frac{\sigma X_{\mathrm{TSR}} C_{l_\alpha}}{16F} + \frac{1}{2}\right) \tag{89}$$

Because F is not known a priori, Eq. 89 must be solved iteratively. Notice that even in the case of ideal blade twist, the values of a will be larger on average than those obtained without tip loss effects, and so tip loss is a contributor to determining the net value of κ in Eq. 83.

Notice that the numerical processes to solve Eq. 89 when including Prandtl tip losses will fail if

$$\left(\frac{\sigma X_{\mathrm{TSR}} C_{l_\alpha} (X_{\mathrm{TSR}} \theta r + 1)}{8F}\right) > \left(\frac{\sigma X_{\mathrm{TSR}} C_{l_\alpha}}{16F} + \frac{1}{2}\right)^2 \tag{90}$$

This artifact of the numerical solution further limits the range of wind speeds and operating conditions over which the BEM theory can be considered valid. To some extent, this problem can be circumvented if the relationship between the induction flow and thrust produced is represented empirically for values of $a > 0.5$. This, however, assumes the validity of a differential equivalence of Eq. 30. In this case, the solution is

$$a(r, X_{\mathrm{TSR}}, F) = \sqrt{\left(\frac{\sigma X_{\mathrm{TSR}} C_{l_\alpha}}{16F} + \frac{1}{2}\right)^2 - \left(\frac{1}{2} - \frac{\sigma X_{\mathrm{TSR}} C_{l_\alpha} (X_{\mathrm{TSR}} \theta r + 1)}{8F}\right)} - \left(\frac{\sigma X_{\mathrm{TSR}} C_{l_\alpha}}{16F} - \frac{1}{2}\right) \tag{91}$$

Fig. 21 Representative spanwise distribution of blade thrust using the BEM and free-vortex methods

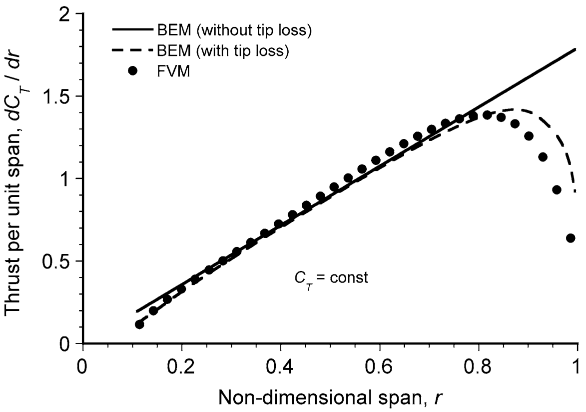

Fig. 22 Representative spanwise distribution of power using the BEM and free-vortex methods

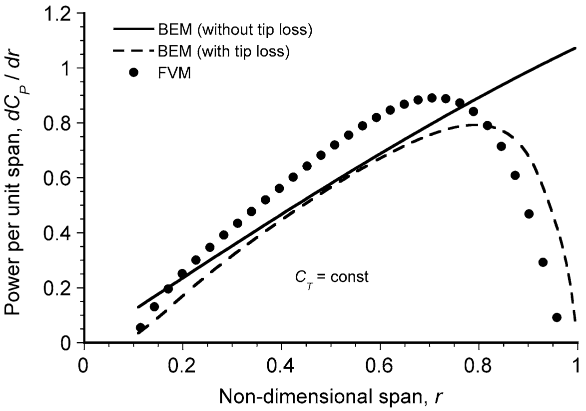

which can be considered valid for the extended range of $0.5 < a \leq 1.0$. However, it should be understood that the solution here is based on an underlying assumption that an empirically derived result developed from total thrust and power measurements also applies to a differential blade element. Nevertheless, in light of the reasonably good results obtained when compared to measurements and predictions made by more sophisticated methods such as the free-vortex method (FVM), this type of correction to the BEM theory seems appropriate. Caution, however, should be exercised in that the applicability of such a correlation may not be universal.

Representative examples of the predicted spanwise thrust and power distributions along the blade using the BEM method are given in Figs. 21 and 22, respectively. The FVM (see later) is used in this case as the basis for comparison. The results are compared at a constant total value of thrust on the turbine. Notice that the use of the Prandtl tip loss method gives a good approximation to the lift distribution at the blade tip compared to what would be obtained by using the standard BEM theory without any tip losses. While the power output tends to be

Fig. 23 Turbine power output as a function of TSR showing the separate effects of viscous drag and tip losses

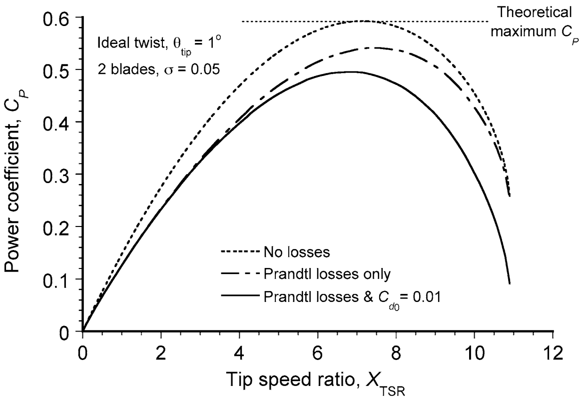

under-predicted in magnitude when using the BEM, the overall agreement of the spanwise form of the loading with the FVM results is actually quite good.

Representative results showing the separate effects of Prandtl tip losses and the viscous drag contributions to power output is shown in Fig. 23. Notice that both of types of losses tend to decrease the power output (and so decrease turbine efficiency), a point previously discussed. Taken together, in this case these effects comprise about a 15% loss of efficiency from the turbine relative to the ideal, which is fairly close to the measured performance levels of modern HAWTs at the conditions that do not involve any blade stall (see also Fig. 14).

10 Induction Factors in Yawed Flow Operation

While it is often convenient to think that a HAWT operates with the wind direction normal to its plane of rotation, this condition is never achieved in practice and there is always some yaw misalignment angle, γ, to the wind flow—see previously in Fig. 6. This effect manifests as a wind velocity component $V_\infty \sin \gamma$ that is parallel to the plane of rotation, thereby leading to a time-varying in-plane velocity component at the blade elements and so generating unsteady aerodynamic forces. Furthermore, a skewed wake is now produced downstream of the turbine's disk, which induces an inflow gradient. While these induction gradients are particularly important parallel to the direction of the wake skew, a small lateral induction gradient may also be produced in response to the asymmetric aerodynamic loading that now occurs over the disk. Clearly, any increase in the non-uniformity of the inflow will increase induced losses and so reduce power output.

While the origins of this induction gradient lie in the detailed structure of the down-stream wake and its resulting induced velocity field, several simplified mathematical models for the effects have been derived, mostly following the development of so-called "linear" inflow models for helicopter rotor applications. Snel [23] gives a review of the basic approach.

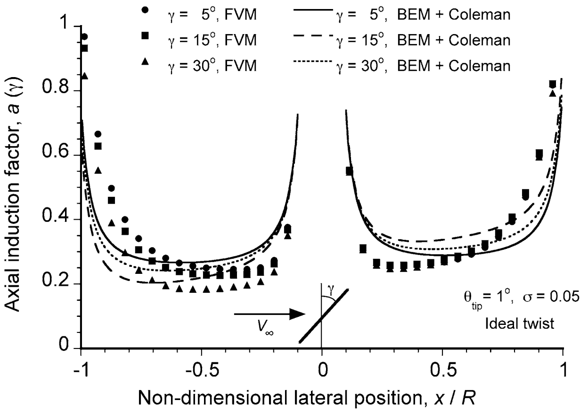

Fig. 24 Representative results of the lateral induction over the turbine's disk as predicted using BEM and free-vortex methods

The idea is to correct the value of the average induction ratio, a_{av}, predicted from the BEM theory by using an equation of the form

$$a_\gamma(r, \psi) = a_{\text{av}}(1 + K_s(\gamma) r \sin\psi + K_c(\gamma) r \cos\psi) \tag{92}$$

where a_γ is the "corrected" azimuthal value of the induction ratio. This correction technique changes the values of the induction based on the yaw misalignment angle, and an iterative series of momentum balances are conducted at each of the blade elements until the values for a_γ converge.

The values of K_s and K_c that have been used in design practice have been derived using various different assumptions and methods, including actual inflow measurements that have originated from subscale HAWTs tested in wind tunnels. For instance, the skewed cylindrical vortex wake model of Coleman et al. [24] has been used in some forms of analyses to calculate the K_s coefficient—see Burton et al. [12]. Several experiments have also been made to measure, not just the first harmonic, but also the higher harmonic inflow coefficients—see Schepers [25] for further details.

Predictions of the induction gradient achieved with this method when integrated into the BEM theory are shown in Fig. 24. Despite the somewhat crude assumptions and relative simplicity of the approach, there is seen to be good agreement in the results from the inflow model with the FVM. It would appear, therefore, that if these inflow effects are properly accounted for, then improvements in the prediction of the loads under yawed operations using the BEM theory seem possible, at least for small yaw misalignment angles. Nevertheless, the approach of "correcting" the induction ratio in this manner is not rigorous because it violates some of the principles under which the BEM theory equations were derived in the first place.

Engineering approaches based on vortex theory are probably the next best practical level for modeling accurately the induction velocities over the disk of a HAWT in a more general operational condition.

11 Airfoils for HAWTS

Even if the induction over the plane of the turbine's disk can be predicted accurately, the issue of determining power output is still not solved because a mathematical description of the airfoil section's force characteristics is also needed. These characteristics are generally nonlinear functions of angle of attack, and in some cases they may show significant Reynolds number dependencies. Static airfoil characteristics can be incorporated into the BE and BEM theories using a look-up table of measured force (and moment) coefficients, or by using another strategy such as curve-fitting to measured data, where in either case the measurements come from airfoil section tests made in the wind tunnel. The further modeling of unsteady effects on the aerodynamic response, however, including dynamic stall, is a much more difficult problem.

Like most types of rotating-wing machinery, the choice of airfoil section is clearly fundamental to the resulting efficiency and operational success of any HAWT. There have been many different types of airfoils used for HAWTs; a catalog of airfoil sections that may prove suitable has been compiled by Miley [26]—see Fig. 25 for just three airfoil shapes. There are, however, some special considerations in the design, selection, and modeling of the characteristics of airfoil sections for different types of HAWTs—see Tangler [27, 28]. Many airfoils designed for commercial-size turbines have their origin in standard NACA airfoils such as the NACA 4-digit series, which have been shown to give good levels of aerodynamic performance with low drag at the blade chord Reynolds numbers typical of those found on HAWTs.

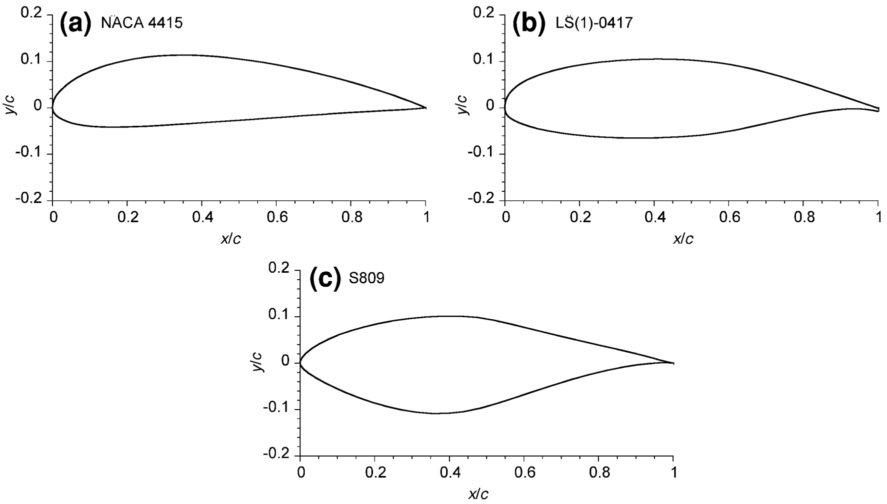

Fig. 25 Examples of airfoil sections that have been used for HAWTs: **a** NACA 4415, **b** LS(1)-0417, **c** NREL S809

Fig. 26 Representative aerodynamic characteristics for the S809 airfoil at several different chord Reynolds numbers

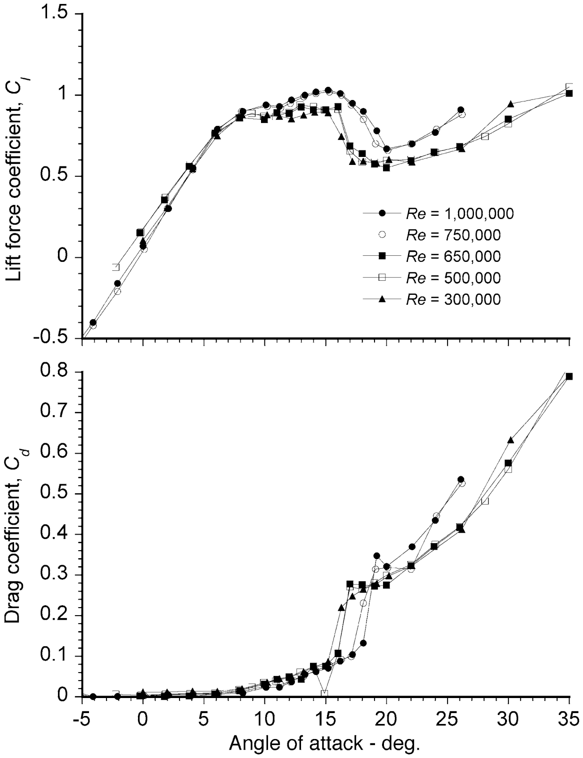

Representative 2-dimensional airfoil characteristics are shown in Fig. 26 for the S809 section. Because a turbine can operate with stall over some range of operational wind speeds, modeling the stall and post-stall airfoil characteristics will need special attention over that previously assumed in the development of the BEM theory; this is especially important if the turbine is of the stall-regulated type. The accurate modeling of Reynolds number effects on the aerodynamic characteristics will be important to predict accurately the blade loads and power output from the turbine. Because the local Reynolds number also varies significantly from section to section along the blades, then in the previous equations used in the BE and BEM theories it should be recognized that $C_l = C_l(\alpha, Re)$ and $C_d = C_d(\alpha, Re)$, where *Re* is the local chord Reynolds number. Unlike helicopter rotors and airplane propellers, compressibility effects are too low on HAWTs to have significant effects on the airloads.

Changes in effective Reynolds number as a result of surface finish or normal erosion on the blades is also an important consideration in airfoil selection and performance predictions. The normal operation of HAWTs in the low atmosphere tends to cause the progressive abrasion of the otherwise smooth surface finish of the blades when they leave the factory. The additional accumulation of dirt and dead insects or other foreign matter can act to further degrade levels of airfoil performance (i.e., producing higher drag and lower lift) and so reducing the aerodynamic efficiency and lowering the power output from the turbine—see Clark and Davis [29] and Eggleston [30]. The NASA LS-1 airfoil—see Fig. 25b—has been used on some HAWTs because of its known insensitivity to surface contaminants compared to some other airfoils.

For variable blade pitch or feathering turbines, the airfoil sections are generally designed to generate high values of maximum lift coefficient to avoid stall, while also producing good values of lift-to-drag ratios over a fairly wide range of angle of attack operation. The blade pitch control system on the turbine can be used to adjust the average operating angles of attack so that the best efficiency can obtained over a wide range of wind speeds, and hopefully up to the maximum rated power values. For fixed pitch stall-controlled HAWTs, however, the airfoil section(s) must be specifically designed to produce flow separation and stall onset at lower values of lift coefficient, and then to maintain a reduced value of lift over a further range of angle of attack with minimal increase in drag. One such example, in fact, is the NREL S809 airfoil, which has been previously discussed. Notice from Fig. 26 that the nonlinear range for the S809 airfoil starts at quite a low angle of attack. The lift coefficient then stays relatively constant for some range of angle of attack as trailing edge flow separation develops and the separation point stabilizes on the airfoil. This pre-stall flow separation helps regulate the power output from the turbine without significantly reducing its efficiency. Complete stall then occurs after the section reaches about 15° of angle of attack.

Representative results of power output from a HAWT showing the effects of nonlinear blade section aerodynamics and the effects of stall in particular, are given in Fig. 27. Notice that after peak efficiency is attained, a further increase in the wind speed tends to cause the power output to drop precipitously. This result is consistent with measured power output characteristics of HAWTs, and illustrates again the need for developing good mathematical descriptions of the airfoil section behavior in both the stalled and post-stalled operating regimes. However, the inherent difficulties of representing accurately 3-dimensional highly nonlinear aerodynamics

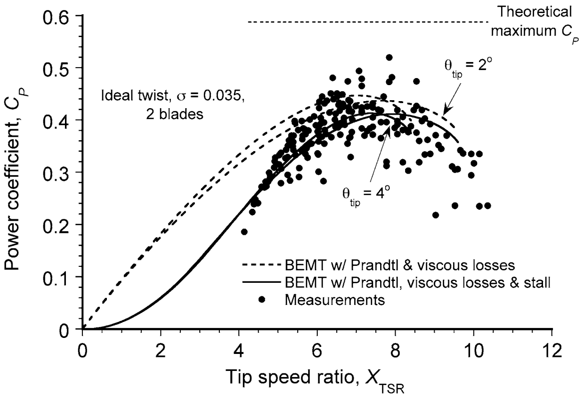

Fig. 27 Representative turbine power output as a function of TSR showing the effects of blade stall. Measurements courtesy of NREL

using a knowledge only of 2-dimensional sectional aerodynamics will always limit the predictive confidence obtained with BE methods. While several "correction" methods have been proposed, attempts to "reverse engineer" the 3-dimensional blade section aerodynamic characteristics from measured power curves it, is a process fraught with many issues and is certainly not one to be recommended

12 Vortex Wake Models for HAWTS

The motivation for developing better and more flexible mathematical models to describe the wake induced inflow or induction is now perhaps clearer, in that the flow at a HAWT is generally 3-dimensional and unsteady. Furthermore, there are operating conditions where the momentum and BEM theories fail, at least on a fundamental level without empirical correction. A significant source of the 3-dimensional induction is from the downstream vortical wake system. For example, a visualization of this wake is shown in Fig. 28. The blades produce significant lift forces at their maximum power output conditions, so the turbine wake is comprised of helicoidal like vortices that trail downstream from the tips of each blade.

Fig. 28 Photograph of the vortical wake behind a downwind type of HAWT rendered visible using smoke injection from smoke "bombs" placed at the blade tips (photo courtesy of NREL)

It is the strength and positions of these vortices that define much of the resulting induction field. Because a HAWT extracts energy from the wind, the helicoidal wake is seen to expand downstream of the turbine, a point previously discussed. The downstream wake may also distort because of the wind gradient, turbulence, or the yaw misalignment angle of the turbine, these factors all further complicating the problem of predicting the wake structure and so in predicting the resulting induction velocities in the plane of the turbine's disk. While flow visualization results showing the detailed wake structure that may exist downstream of a HAWT under different operating conditions is rather limited, a survey of nearly all known results is given by Vermeer et al. [31].

Calculating accurately the induction velocities from the downstream wake system requires a method that can represent the strengths (circulation) and spatial locations of the vortical elements that are trailed by each blade. This problem can be tackled (albeit still approximately compared to the overall complexity of the flow problem) by using vortex methods. These are methods based on the assumption that the wake vorticity is lumped into discrete, singular vortex filaments. The fundamental idea of a discretized vortex model applied to the wake of a HAWT is shown in Fig. 29. From the resulting strengths and positions of these vortex filaments (the determination of which requires the proper coupling to the

Fig. 29 Modeling the downstream wake of a HAWT using a vortex filament method, with discrete vortex filaments shown trailing from the tips of each blade

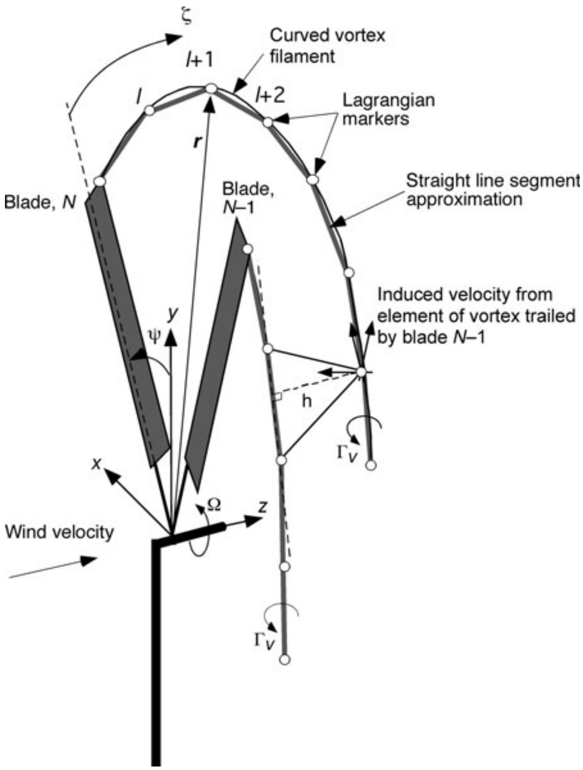

blade lift and its circulation distribution), the induction field can then be obtained through the application of the Biot–Savart law. While a disadvantage of all types of vortex methods for modeling the downstream wake is their relatively higher computational overhead compared to BEM methods, they do provide an inherently more appealing physical approach for modeling the wake than with the rather more crude prescription of the induction using inflow (or dynamic inflow) models.

Vortex methods are usually categorized into either “prescribed” or “free” vortex filament techniques. A prescribed vortex filament technique is where a discrete representation is made of the vorticity field, but the downstream positions of the vortical elements are specified a priori based on semi-empirical rules—see the methods developed by Kocurek [32], Robison et al. [33] and Coton [34]. Prescribed vortex methods use experimental measurements of wake geometries for formulation purposes, so they have only a postdictive capability. Developing more generalized prescribed wake models for HAWT applications requires data from a much wider range of test conditions, and a trade-off must be drawn between the costs of collecting such data versus any net gains that might eventually be achieved in a resulting modeling effectiveness, computational speed, and in predictive capability. Prescribed wake models are also limited in that they are unsuitable for application to unsteady flow conditions, which is by far the most common flow state in which a HAWT operates. While prescribed vortex wake models continue to be used in some types of design work (as are BEM methods), they are progressively being replaced by free-vortex models.

12.1 Governing Equations

Free-vortex methods are based on a discretized, finite-difference representation of the governing equations for the wake behavior and, when properly solved, track the actual evolution of discrete vortex filaments through the flow field under the imposed flow and operating conditions [35]. Unfortunately, the vortex wake tracking process is memory intensive and computationally much more demanding than when using BEM methods. However, with the computational speeds available today, the approach is well within the bounds of being practical for routine design-type performance evaluations.

The derivation of the FVM assumes an inviscid flow field in which case the Navier–Stokes equations can be reduced to the form

$$\frac{D\vec{\omega}}{Dt} = (\vec{\omega} \cdot \vec{\nabla})\mathbf{V} \tag{93}$$

Under the further assumptions of an incompressible and irrotational flow, vortex lines will convect with the fluid particles, so that the rate of change of the position vector of an element on a vortex filament (i.e., a discrete wake marker) is equal to its local velocity. With these assumptions, Eq. 93 reduces to a simpler convection equation. However, the positions of the wake markers are a function of both the blade position and the time it was trailed into the wake. This means that the convection of the wake can be described by the equation

$$\frac{d\mathbf{r}(\psi,\zeta)}{dt} = \mathbf{V}(\mathbf{r}(\psi,\zeta),t), \quad \mathbf{r}(t_0) = \mathbf{r}_0 \tag{94}$$

where ψ is the azimuthal position of a blade defined from a reference datum, and ζ is the time (or “age”) of the vortex filament since it was trailed into the wake; see Fig. 29. The vector $\mathbf{r}$ represents the position of a marker lying on a vortex filament that is trailed from any blade located at an azimuth ψ at time t, $\mathbf{V}$ is the local velocity of that marker, and $\mathbf{r}_0$ is the initial position vector. If t_0 denotes the time when the vortex element was first formed and the blade was located at $(\psi - \zeta)$, i.e., $(\psi - \zeta) = \Omega t_0$. Because $\psi = \Omega t$, then $\zeta = \Omega(t - t_0)$. Equation 94 can be written in terms of ψ, ζ and Ω as [36, 37]

$$\frac{d\mathbf{r}(\psi,\zeta)}{dt} = \Omega\left(\frac{\partial\mathbf{r}(\psi,\zeta)}{\partial\psi} + \frac{\partial\mathbf{r}(\psi,\zeta)}{\partial\zeta}\right) \tag{95}$$

In blade fixed coordinates, this latter equation can be written as the partial differential equation

$$\frac{\partial\mathbf{r}(\psi,\zeta)}{\partial\psi} + \frac{\partial\mathbf{r}(\psi,\zeta)}{\partial\zeta} = \frac{\mathbf{V}(\mathbf{r})(\psi,\zeta)}{\Omega} \tag{96}$$

The velocity term on the right-hand side of the above equation is the sum of the free stream velocity V_∞, any external sources of perturbation V_{ex}, such as the atmospheric boundary layer, turbulence in the wind, etc., and the wake induction V_{ind}. Therefore, V in totality can be written as

$$\mathbf{V} = \mathbf{V}_\infty + \mathbf{V}_{\text{ex}} + \mathbf{V}_{\text{ind}} \tag{97}$$

The induction velocity term, $\mathbf{V}_{\text{ind}}$, is a highly nonlinear function of the spatial and temporal locations of the wake vortices, which must be computed using the repeated application of the Biot–Savart law to all of the filaments. This calculation comprises most of the computer expense in solving any type of vortex wake problem. The left-hand side of the governing equation can be solved numerically using finite difference approximations, for which there are various schemes available—see Leishman et al. [35], Bhagwat and Leishman [38] and Gupta and Leishman [39].

12.2 Linking to the Blade Solution

One further problem is that the free-vortex wake method must also be supplied with boundary conditions that relate the lift (i.e., the bound circulation) on the blades to the strengths (i.e., the trailed circulation) of the vortex filaments. This is usually done by using a lifting line or a lifting surface model, for which there are several types of possible implementations. The vortex wake may also be linked to a CFD solution for the blade aerodynamics (see later), thereby forming a so-called "hybrid" wake scheme. In fact, it is here that the application of CFD methods may make a more significant shorter-term impact on wind turbine design.

In a typical lifting line approach, the blade span is divided into discrete spanwise segments. A bound vortex is placed along the 1/4-chord of the blades, and control points are located the 3/4-chord; the bound circulation and lift are assumed to be constant over each segment. This circulation is then uniquely determined by imposing flow tangency at the control points. Because of the unequal bound vortex strengths on the adjacent segments, circulation must be trailed between each segment; the strength of each trailer is equal to the difference between the bound vortex strengths of any two adjacent segments. This near wake is typically truncated at some small distance behind the blade. A connectivity between the near wake and the rolled-up tip vortex is made by assuming that the vorticity outboard of the maximum bound vorticity over the blade span forms a tip vortex of strength Γ_v. The tip vortex can be released at the blade tip or at the appropriate centroid of vorticity. After the blade inflow and lift distribution has been determined consistently with the vortex wake solution, the thrust and power on the turbine can be calculated using the conventional BE approach, as previously outlined.

12.3 Representative Results from the FVM

Representative examples of time-accurate FVM wake calculations are shown in the set of Fig. 30 for a two-bladed HAWT operating in a steady wind of different speeds. The predicted wake structure and the corresponding time-averaged streamtraces are shown for a blade pitch angle of $\theta_{\text{tip}} = 4°$. At 2 ms^{-1} the turbine operates in the VRS—see Fig. 30a. As previously explained, this is an operating state where the BEM model breaks down because under these conditions the flow can potentially proceed in multiple directions (i.e., simultaneously both downstream and upstream) at the plane of rotation, and so the wake boundary must extend beyond the geometric limits encompassed by the turbine's disk. The flow under these conditions also tends to become more aperiodic in that the wake has a slightly different structure during each revolution of the turbine. The corresponding streamtraces at a wind speed of 2 ms^{-1} clearly shows a form of flow recirculation region near the turbine's disk.

At a wind speed of 2.5 ms^{-1} the turbine operates more in what would be classified as a turbulent wake state or TWS—see Fig. 30b. Here, the flow recirculation zone moves downstream somewhat, and a significant mixing region exists in the downstream wake. Of course, the actual "turbulence" in the flow per se is not modeled in the FVM, but the predicted flow state is still representative of this operating condition.

At a wind speed of 4 ms^{-1} ($X_{\text{TSR}} = 8.33$) the wake is more stable (and periodic), but for the last wake turn of the tip vortices interact to produce a form of aperiodic behavior. The corresponding streamtraces show the wake expansion region and then a wake contraction where the wake becomes aperiodic.

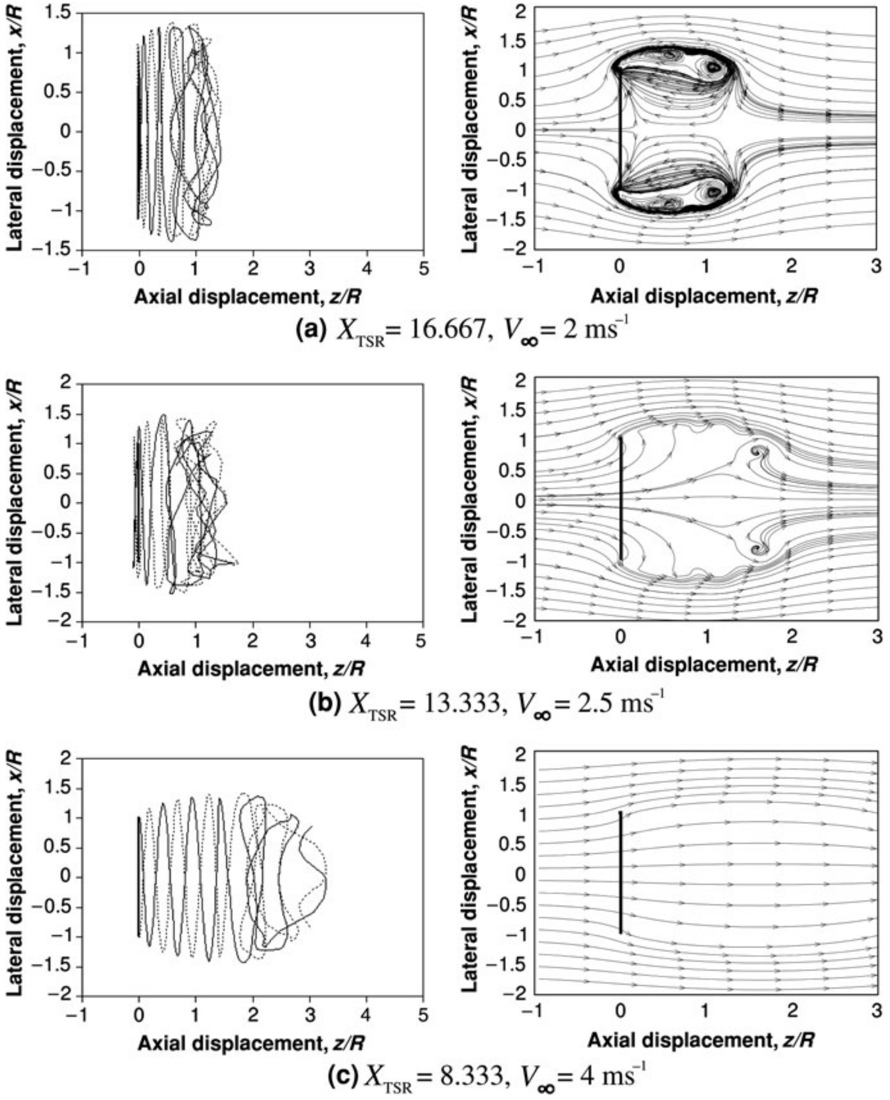

(a) $X_{TSR} = 16.667$, $V_{\infty} = 2\ \text{ms}^{-1}$

(b) $X_{TSR} = 13.333$, $V_{\infty} = 2.5\ \text{ms}^{-1}$

(c) $X_{TSR} = 8.333$, $V_{\infty} = 4\ \text{ms}^{-1}$

Fig. 30 Top view of the wake geometry and the time-averaged streamtraces behind a HAWT for various tip speed ratios for blades with ideal twist and $\theta_{\text{tip}} = 4$ deg

At higher wind speeds (lower values of TSR), the vortex wake structure now becomes almost perfectly helicoidal—see Figs. 30d–f; the streamtraces in this case pass smoothly through the turbine and the resulting patterns are consistent with the flow models previously assumed by using the momentum theory approaches. The maximum expansion of the wake (corresponding closely to the conditions for maximum power extraction, which is when the approximate average induction is 1/3) is obtained for $X_{TSR} = 6.66$ in this particular case. For the highest

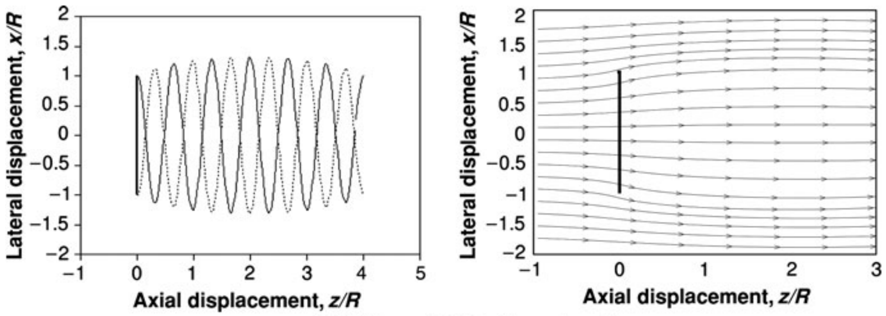

(d) $X_{\text{TSR}} = 6.667$, $V_\infty = 5$ ms^{-1}

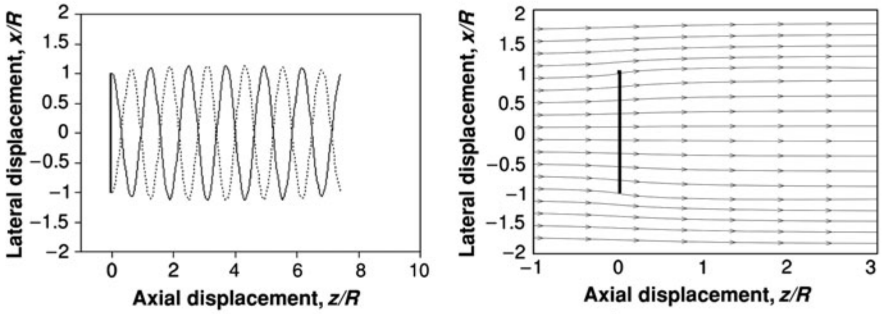

(e) $X_{\text{TSR}} = 4.1667$, $V_\infty = 8$ ms^{-1}

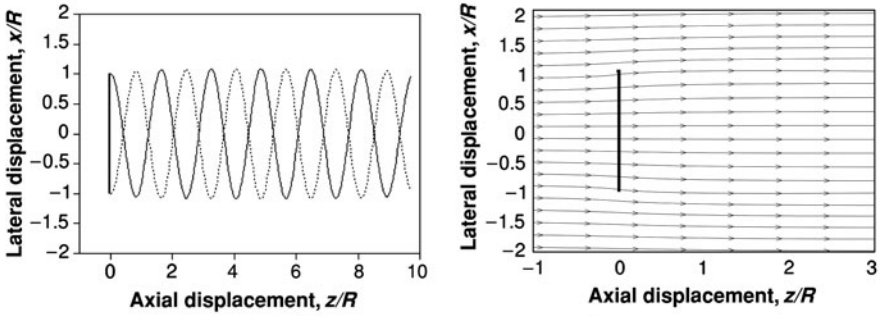

(f) $X_{\text{TSR}} = 3.333$, $V_\infty = 10$ ms^{-1}

Fig. 30 (continued)

wind speeds the wake is periodic and almost purely helicoidal, but the wake expansion reduces and so the power output from the turbine decreases.

Figure 31 shows the comparison of the predicted variation of power coefficient, C_P, versus TSR from the BEM analysis and the FVM calculations for a blade tip pitch angle of 4°. As the TSR is increased, an optimum tip speed ratio is reached where the power coefficient reaches its maximum. For the BEM method with no viscous losses, a maximum theoretical power coefficient of 0.593 is obtained, which corresponds to the Lanchester–Betz limit in ideal flow. When tip losses and

Fig. 31 Comparison of the variation of the predicted power coefficient with tip speed ratio for $\theta_{tip} = 4°$ using the BEM and FVM

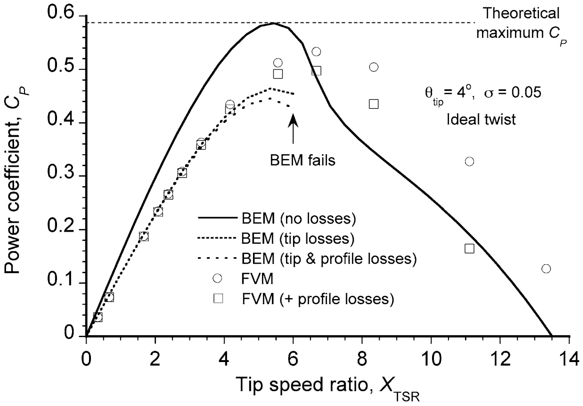

profile losses are included into the calculations, the maximum C_P is reduced, as would be expected. In this case, the maximum C_P is achieved for a TSR of around 5.75, and this agrees with the predictions made by the FVM. From the BEM theory results, clearly the addition of tip losses causes significant change in the predicted power output, whereas the addition of the viscous losses does not significantly reduce power output in this case. For low values of TSR, there is no significant difference in the predicted power with and without viscous losses in the FVM calculations. The addition of viscous losses, however, reduces the power output at moderate to high values of TSR.

The overall agreement between the predicted power coefficient from the FVM and the BEM theory is seen to be very good for low values of TSR. As the TSR is increased further, however, the TWS and the VRS are encountered, and predictions become more difficult for the BEM to handle. The BEM results shown here include the correction for $a > 0.5$ as given by Eq. 30, despite its empirical origin. The variation of the thrust coefficient with TSR is almost linear—see Fig. 32. Again, the BEM method and the FVM predictions are seen to be in good agreement up to a TSR of 6. For higher values of the TSR, the modified BEM theory with the inclusion of tip losses also breaks down, and in fact the BEM generally does not converge for blades sections near the tip where the induction ratio becomes larger. The BEM method also generally underpredicts the thrust coefficient here, hence showing a fundamental limit to this type of theory.

13 Unsteady Aerodynamic Effects on HAWTS

Unquestionably, HAWTs operate in a relatively unsteady flow environment for much of their time—see Robinson et al. [40], Huyer et al. [41], Schreck et al. [42], and Leishman [43]. The airloads on each blade element vary in time because of yawed flow, gradients and shear in the ambient wind, turbulence, blade flapping and bending, vibratory displacements, and other factors such as tower shadow

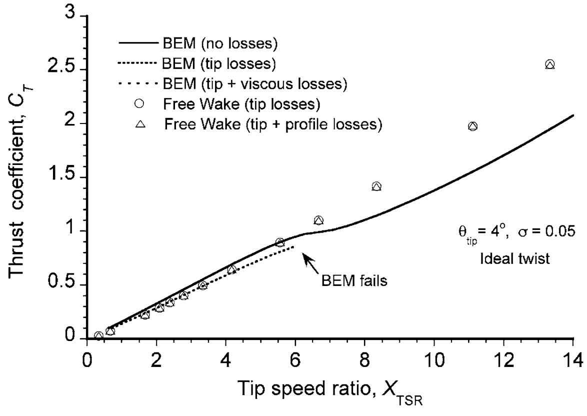

Fig. 32 Comparison of the variation of the predicted thrust coefficient with tip speed ratio for $\theta_{tip} = 4°$ using the BEM and FVM

(a transitory phenomenon where the blades pass through the downstream wake of the support tower). In the yawed (out of wind) case, the component of the wind speed produced in the plane of the turbine (V_∞ sin γ) results in unsteady aerodynamic excitation that is a multiple of the number of blades. Because of the relatively low rotational velocity of HAWTs (they will turn at about 20 revs per minute on large turbines up to about 800 revs per minute on small turbines) and their low tip speeds, gusts in the wind speed (and turbulent fluctuations) can result in significant changes in the angles of attack at the blade element level.

13.1 Reduced Frequency

A quantification of the degree of unsteadiness of the flow at a HAWT can be performed using the reduced frequency, k. While many flow disturbances or unsteady aerodynamic events may be transient or aperiodic in nature, it is convenient to characterize unsteady problems, in terms of the k parameter. Because of the typically low rotational velocities of HAWTs, perturbations at the blade elements may experience quite high effective values of reduced frequency, and especially so when moving inward along the blade from its tip; reduced frequencies exceeding 0.1 are not untypical and considerably higher effective reduced frequencies will be associated with more transitory events such a tower shadow. Only for $k < 0.05$ can the flow be assumed to be steady, or at least quasi-steady. The analysis of unsteady flow problems is considerably more difficult than if steady flow was assumed in the formulation, and requires the consideration of unsteady effects on the blade as well as in the downstream wake.

13.2 Unsteady Airfoil Theory

Representing the unsteady aerodynamic effects at the blade sections is a difficult problem for which there are no exact mathematical solutions that can be easily included into the BE method. However, there are several approaches that can be used to make assessments of the changes to the magnitudes and phasing of the aerodynamic response resulting from unsteady flow conditions. In fact, the "classical" unsteady aerodynamic theories describing the observed behavior have formed the basis for models used in rotating-wing analyses, including helicopter and wind turbine applications—see Leishman [10] for a summary.

While the classical theories assume linearity in the airloads, this assumption can probably be justified a good number of the conditions of practical interest on HAWTs. Advanced CFD solutions to unsteady airfoil problems have shown the validity of these linearized theories, but also have exposed their fundamental limitations. Compressibility effects do not need to be included for HAWT problems, so such unsteady aerodynamic models can be used in considerably more simplified forms than would be needed for helicopter problems.

Overall, it has been shown throughout the literature on the subject that incorporating some basic representation of unsteady aerodynamic effects in the aerodynamic simulation of the HAWT generally gives better results for blade loads and power output than if no representation of these effects were to be included at all. However, any such models must be used with considerable care, appreciating that only time-domain simulations will have the best flexibility to deal with the types of aperiodic flow problems that are found on HAWTs.

13.3 Dynamic Stall

The excursions in angles of attack seen at the blade element on a HAWT in yawed flow operation are often large enough to produce some form of blade stall. As previously mentioned, the power output from a HAWT can also be regulated deliberately by promoting blade stall, either by pitch regulation or through suitable airfoil design. However, stall generally has a deleterious effect if it occurs at other operating conditions because it will adversely affect blade loads and also significantly decrease power output.

As a result of the generally unsteady flow environment at the blades on a HAWT, the stall when it occurs is rather dynamic in nature and so is normally referred to as dynamic stall—see Fig. 33 for a schematic of the process. Dynamic stall manifests as a welcome delay in the onset of flow separation to higher angles of attack than occurs under static conditions, but this is then followed by abrupt and less than welcome catastrophic flow separation from the leading edge region of the airfoil (or blade section). This separation is quickly followed by the formation of a concentrated vortical flow that is then swept over the airfoil section by the local flow velocity. The main problem with the vortex shedding phenomenon during dynamic stall is that it tends to produce very large lift, drag, and pitching moment overshoots compared to the maximum values of the airloads that could have been obtained under quasi-steady conditions—see the results in Fig. 34. Dynamic stall, when it occurs on a HAWT, is known to be a particularly

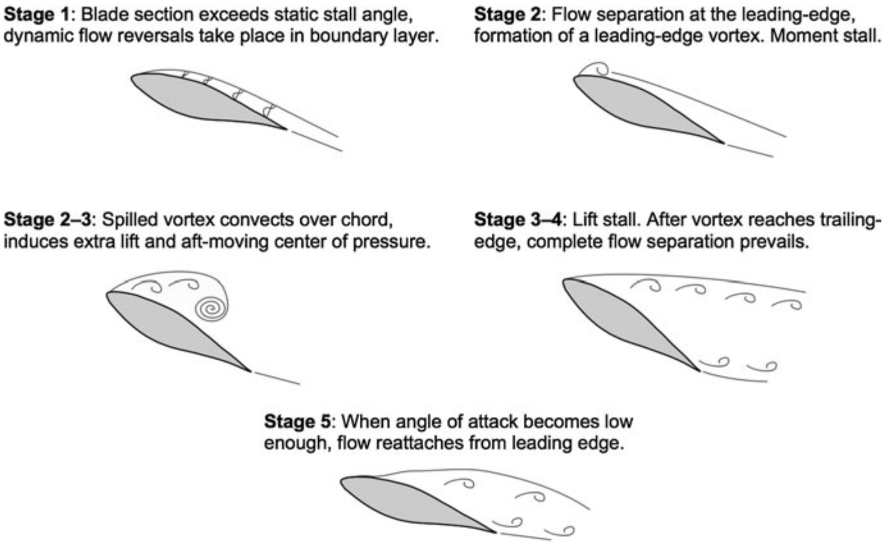

Fig. 33 The process of dynamic stall involves several distinct stages, but the shedding of a concentrated vortical disturbance from the leading edge of the airfoil is a distinguishing feature of the phenomenon

significant source of unsteady blade airloads that can be responsible for structural and/or mechanical damage.

Unfortunately, the prediction of dynamic stall events has not yet been very successful on HAWTs. Because of the high 3-dimensionality and nonlinearity of the aerodynamic problem (which involves hysteresis effects), the development of suitable mathematical models (even semi-empirical ones) has proved very difficult. In summary, the underlying physical problems can be divided into three main areas: (1) Defining stall onset by representing the unsteady pressure gradient reduction effects on the blade resulting from unsteady changes in angle of attack. This is needed because unsteady effects lead to delays or lags in the development of the boundary layer compared to those obtained under quasi-steady conditions; (2) Representing coupled influences of the centrifugal and Coriolis effects acting on the boundary layer in the rotating flow environment (i.e., a radial flow effect); (3) Representing the effects of leading edge vortex shedding during the dynamic stall process.

Needless to say, the interdependent combination of factors that can affect the problem of dynamic stall has made it difficult to understand exactly what is happening aerodynamically on wind turbine blades. While some of the predictive issues that have arisen are because of the imprecise modeling of the delayed onset of flow separation resulting from unsteady aerodynamic effects, there are also subtle 3-dimensional effects unique to the rotating blade environment that seem to be particularly pronounced on HAWTs and these effects are very difficult to predict.

A prerequisite to predicting dynamic stall and its onset, is first to predict adequately the unsteady airloads under attached flow conditions. Despite its

Fig. 34 The vortex shedding process during dynamic stall will produce significant overshoots in the values of the airloads. Unsteady airfoil data are for an oscillating S809 airfoil

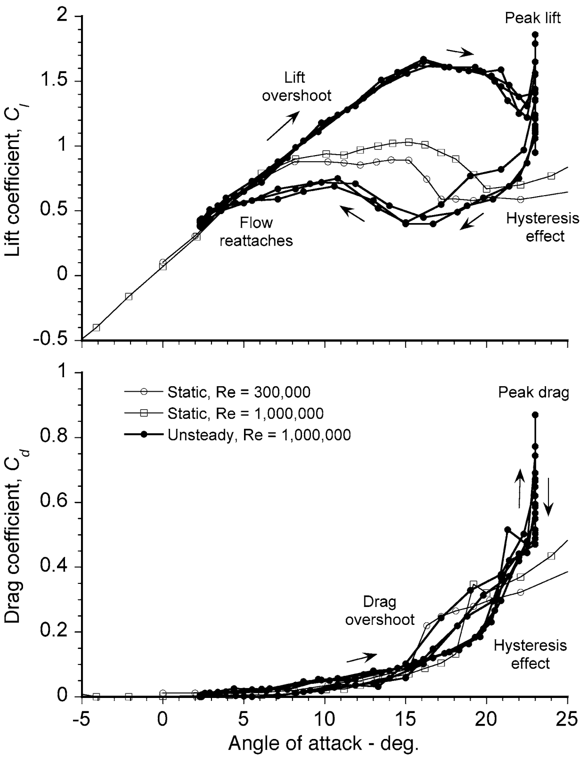

apparent simplicity compared to the stalled case, however, this is a nontrivial problem for which the development of general models that are valid for the wind turbine environment is still a major challenge [10, 43]. The motivation for the development of more efficacious models is very clear in that they must remain in a mathematical form that is compatible with the structure of BE and BEM type models. To this end, several relatively parsimonious semi-empirical models have been developed or adapted for wind turbine use. Several design analyses use the method developed by Leishman and Beddoes [44], which has been modified by Pierce and Hansen [45] and Gupta and Leishman [46]. However, while often giving good results such models are not strictly predictive tools (i.e., they are fundamentally postdictive) and they must be applied with a good application of common sense, especially for airfoils that are substantially different to those used to originally develop the model.

A better integrated modeling capability for dynamic stall clearly depends on foundational understanding of the resulting 3-dimensional boundary layer developments that are found on rotating blades. Several experimental and modeling studies have provided at least some insight into these effects—see Himmelskamp [47], Young and Williams [48], Madsen and Christensen [49], Snel [50], Narramore and Vermeland [51], Dwyer and McCroskey [52], Robinson et al. [53], Schreck et al. [42] and Schreck et al. [54]. Snel [50] has speculated that the Coriolis acceleration terms act to alleviate adverse pressure gradients and so delay the onset of flow separation and stall, but this is an assumption questioned by others—see Corten [55]. Fogarty [56] has calculated the radial or spanwise development of the boundary layer flow on the blade and has shown that for helicopter rotors at least, these effects are small, except near the inboard part of the blade. It is exactly here, however, where the blades of HAWTs (because of their design) generally tend to exhibit higher values of lift coefficients compared to those produced on helicopter rotors, and therefore the effects of radial flow on the developing airloads can be more important here.

Similar observations of the 3-dimensional flow state have been found using CFD methods, such as in the work of Narramore [51], although confidence in these types of analyses to represent fully stalled flows is not yet very good because of deficiencies in the turbulence models used for separated flows. Approximate methods have also been developed to model the so-called 3-dimensional “stall delay” effects—see Corrigan [57] and Du and Selig [58]. However, a rigorous approach to represent these effects is still lacking because such models have questionable validity under unsteady flow conditions or for situations where dynamic stall may occur. This is an area where more foundational research is needed if better 3-dimensional models of unsteady airfoil behavior and dynamic stall are to be developed and used confidently for the analysis of improved HAWTs.

14 Transitory Yaw Effects

As already discussed in this chapter, significant once-per-revolution unsteady variations in the local velocity at the blade elements will be produced whenever the plane of rotation of a HAWT is misaligned (yawed) relative to the wind. The mechanical systems used for yaw control cannot track the wind to give perfect alignment at all times, so some yaw misalignment angle must always be expected. Combined with the low tip speeds of HAWTs, this can produce large excursions in relative flow velocity, which can amplify unsteady effects even although the blade pitch and angle of attack may remain relatively low and/or constant. Amplitude and phase changes of the local forces are then produced on the blades compared to those loads that might be obtained if only quasi-steady aerodynamics had been assumed, and this can be a significant source of predictive deficiency.

Another source of unsteady effects can be traced to the actual direction of the incident flow velocities at each element on the rotating blades as they are approaching stall. Because of the relatively low rotational velocity of HAWTs, the local sweep angle of the flow with respect to the leading edge of the blade can become relatively large when the turbine is yawed by even a few degrees. With fully attached flows the independence principle of aerodynamic loads applies, and insignificant changes in airloads will be expected. However, as already discussed the radial flow component can affect the development of the 3-dimensional boundary layer on the blade, and so also alter the conditions that eventually may lead to the onset of dynamic stall. This is just one more reason why the prediction of stall on HAWTs is so difficult to represent by using parsimonious mathematical models.

Furthermore, there is an additional unsteady aerodynamic lag in the development of the wake induction in response to the changing downstream flow structure with changes in the yaw misalignment angle. These are complicated effects to represent from a modeling perspective, and vortex theory (previously discussed) probably offers one of the better approaches without making too many assumptions. A representative calculation using a FVM is shown in Fig. 35 for a HAWT that progressively yaws out of wind over the course of two revolutions of the turbine. Notice that power output drops quickly as the yaw misalignment increases, but there is also a significant transitory response. In this case, the power produced decreases before recovering to approach a more steady state value. The residual fluctuations in the power output, which are undesirable from an electrical power generation standpoint, are a result of the in-plane component of the wind velocity combined with a dynamic response of the downstream wake; such wake adjustments may take place over many revolutions before the aerodynamics stabilize and the turbine produces a nominally steady-state output.

The equations describing the distribution of induction over the turbine's disk have also been modified for use under unsteady conditions; in this case they are usually written in the form of a set of ordinary differential equations. The time constant (or constants) in the equations represent the dynamic lag in the build-up of the induction flow to the changing operating conditions. Specific values of the wake time constants for wind turbine analyses are used based on empirical evidence of the so-called "induction lag." This mathematical form is appealing for many of the structural dynamic and aeroelastic analyses of the wind turbine that use the comprehensive design models—see Bierbooms [59], Snel and Schepers [60], Hansen and Butterfield [61] and Snel [23]. However, this is an area of modeling capability that needs substantially more development if the resulting

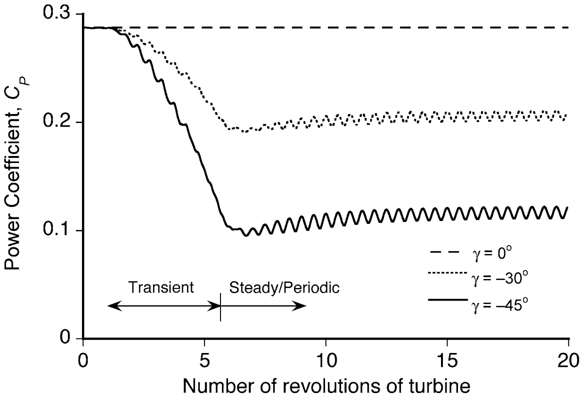

Fig. 35 Representative predictions of transient power output for a change in yaw misalignment angle relative to the wind direction

effects on inflow and loads are to be predicted as confidently as could be obtained, for example, by using vortex theory.

15 Tower Interference Effects

Tower interference effects on the turbine blades are experienced with both the downwind and upwind types of HAWT. While the interference issue on loads is more important for the downstream type of HAWT, an interference effect with the upwind type of HAWT can occur as the blades pass in front of the tower. Tower "shadow" inevitably manifests as a region of velocity deficit in the downstream wake behind the support tower—see Fig. 36. Because a body of cross-section that is circular shape (or otherwise bluff in form) generates this wake, the wake is manifest by a notable reduction in flow velocity and significant levels of turbulence. As the blade passes into the downstream velocity deficit region, there is a sudden reduction in the net lift and torque produced by the blade. Because this is a transitory phenomenon with high effective values of reduced frequency, there are significant unsteady aerodynamic forces produced; in fact, it is the modeling of the unsteady aerodynamic effects that is critical if the effects on the blade

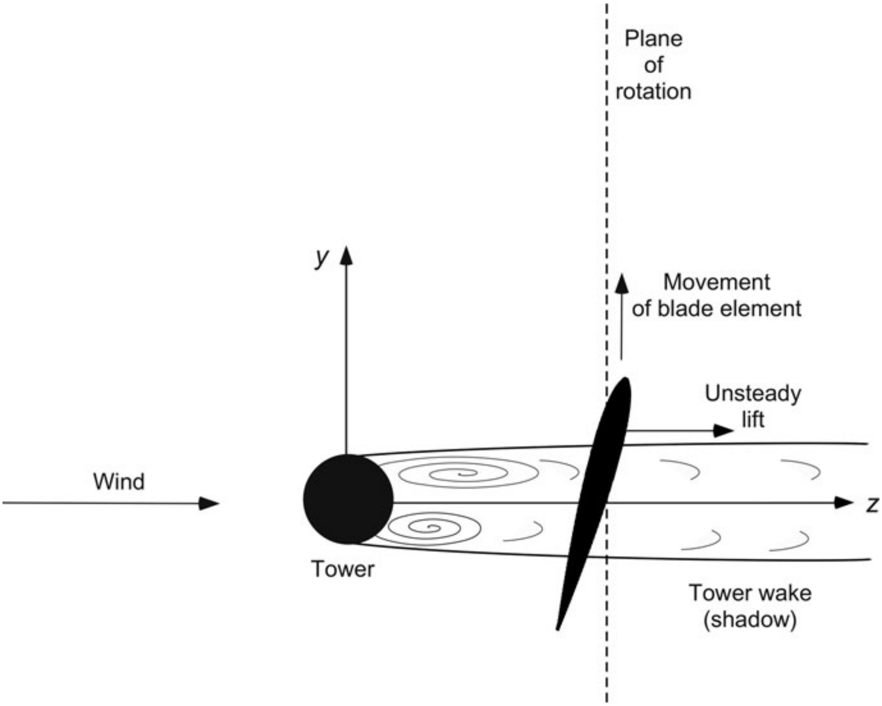

Fig. 36 Schematic of a blade element interacting with the wake shadow produced by the support tower

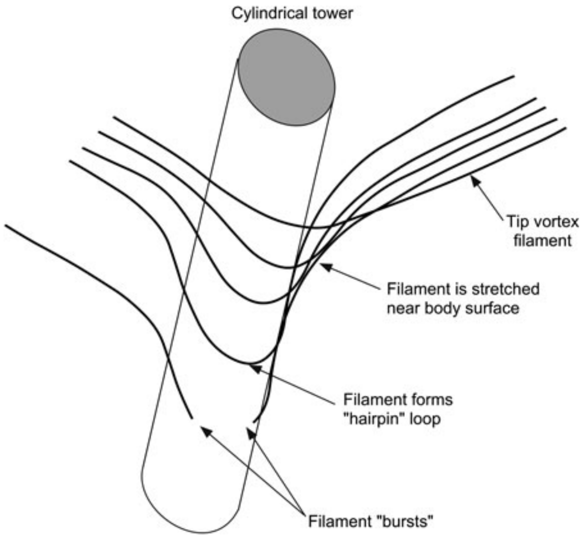

Fig. 37 Schematic of the blade tip vortices generated in the wake of the turbine impinging on the support tower

aerodynamics are to be faithfully represented in this regime. As a consequence, the downwind type of HAWT also tends to generate more noise than the upwind type as the blades periodically intersect this tower wake.

In most forms of engineering analysis, the tower shadow effect is modeled as a velocity deficit normal to the plane of rotation, although other models have also been used. The velocity deficit is determined empirically, and so it will be specific to different types and shapes of towers. The effect of this change in the velocity field on the resulting lift and torque on the blade as a function of its azimuthal location is then calculated, such as using the BE model. While reasonable results have been obtained with this approach, fundamentally the method is only postdictive in nature—see Munduate et al. [62] and Wang and Coton [63]. Further work on the tower shadow problem is still needed to better characterize the unsteady wake structure behind the tower and so to develop suitable mathematical models for the effects on blade loads and power output.

With an upwind type of HAWT, the blade itself is relatively free of the interference effects associated with the support tower. A perturbation in loading may still be produced as each blade passes in front of the tower, albeit this will be of relatively small magnitude compared to the downwind type. In this case, however, the turbine and its wake produce a more important effect on the support tower. As shown previously, the downstream wake is comprised, in part, of vortices that trail from the tips of the blades, which then impinge on the tower; a schematic of the behavior is shown in Fig. 37. The process of vortex impingement, stretching, and finally bursting, is a relatively complicated one from a fundamental fluid dynamics standpoint. The net effect of this process, however, is that a transient aerodynamic loading is produced on the tower, and although a local event, the unsteady loads produced can still be of sufficient magnitude to produce notable vibrations levels and noise.

16 Advanced Aerodynamic Modeling Requirements

Advanced computational fluid dynamic (CFD) methods based on numerical solutions to the Euler and Navier–Stokes (N–S) equations have begun to see some significant use for the analysis of HAWTs [64–66]. This class of methods has the potential to provide a consistent and physically realistic simulation of the turbine flow field without the layers of empiricism that are typical of contemporary design methods. However, it is not possible to solve the N–S equations without invoking at least some levels of numerical approximation. Furthermore, CFD methods in general, although giving a very sophisticated modeling capability, are computationally expensive and have large computer memory requirements. These requirements well-exceed those of the BEM or FVM methods, for example.

In addition to their high cost, the numerical issues associated with CFD methods include grid sensitivity, turbulence modeling, artificial (i.e., unrealistic) wake diffusion, etc., which have prevented the use of these methods for many practical problems of interest, even in a research context. In particular, problems involving flow separation on the blades and dynamic stall have proved extremely challenging for N–S based methods, in part because of the deficiencies with current turbulence models. The prediction of the 3-dimensional vortical wake behind a turbine has also proved to be extremely challenging for CFD methods to solve. This is because the vortical wake is a consequence of complex 3-dimensional, viscous, separated flow effects, and also because the various numerical methods used in solving the discretized form of the equations have difficulty in preserving the coherent wake structure as it is convected into the downstream flow.

16.1 Navier–Stokes Equations

The N–S equations are the fundamental equations governing fluid dynamic behavior. These equations invoke the principles of the conservation of mass, and momentum and energy interchange. A further reduction to the N–S equations can be made to obtain the Reynolds Averaged N–S or RANS equations, and this form has proved very useful in aerodynamic studies. Several researchers have used RANS methods for computing flow field around HAWTs [67–69]. However, the resolution of the turbulence scales requires extremely fine grids with fine numerical discretization, and hence the very biggest and fastest computers are needed to solve even the RANS equations. The RANS equations also require turbulence closure models for their solution, for which several types have been developed—see, for example, the popular models devised by Baldwin and Lomax [70], Baldwin and Barth [71], and Spalart and Allmaras [72], although these models are not suitable for representing turbulence in a vortical wake.

Reasonable levels of success has been demonstrated using RANS methods for predicting the flows on the rotating blades under fully attached flow conditions, but not unexpectedly several issues have been discovered when attempting to solve problems involving separated flow and in deep stall regimes. Wolfe and Ochs [73] noted that poor predictions of the maximum lift coefficient for the S809 airfoil was probably caused by the deficiencies in the turbulence model. Chaviaropolous [74] also noted problems with turbulence models. Langtry et al. [75] discuss the use of transition model for general CFD methods used for airfoil studies and wind turbine performance predictions. A more thorough evaluation of turbulence models for wind turbine aerodynamics is discussed by Benjanirat et al. [76].

While the computational costs for RANS solutions, at least for now, are high and turnaround time for typical VAWT problems is long, they have great potential to help improve the understanding of wind turbine problems. However, they also have the disadvantage that the dependencies affecting the design of the turbine are harder to expose because of uncertainties in prediction and long turnaround times. Therefore, the practical use of the RANS models in the engineering design of new wind turbines still lies some way in the future.

16.2 Euler and Hybrid CFD Methods

Numerical solutions to the Euler equations have also seen some use for HAWT problems. These equations are an inviscid form of the N–S equations, so they cannot represent the creation, diffusion, or dissipation of vorticity. Because of higher Reynolds numbers in the global flow, and the absence of solid boundaries except near the blades, the Euler approximation is somewhat justified, as are free-vortex methods. However, the viscous and turbulent diffusion of vorticity in the downstream wake of the turbine, and the creation of turbulence and mixing of the tip vortices are not accounted for. A discussion of such methods for wind turbine applications is given by Madsen [77]. Another approach, effectively also an Euler approach, uses the asymptotic acceleration method [78]. Although adapted for helicopter applications initially, the method has been extended to study HAWTs by van Bussel [79].

The use of so-called "hybrid" CFD methods have also been explored. Hybrid methods combine the use of direct CFD for the blades (i.e., RANS methods) with free-vortex models for the wake, or perhaps N–S method for the wake and an actuator disk to represent the turbine blades. Coupling strategies must be developed to link information between the different numerical methods.

Sørenson and colleagues have developed the Ellipsys2D/3D code [80], which is a N–S approach. The flow on the blades themselves, however, is solved by the solution of the RANS equations; an example of the results from such an analysis is shown in Fig. 38. Sankar and co-workers [81–83] have developed a hybrid N–S/full potential/free-wake method for predicting the flow at a HAWT. This hybrid approach seems one of the more promising shorter-term approaches for the application of CFD to solving real aerodynamic problems with HAWTs, including the problems associated with unsteady aerodynamic effects and dynamic stall.

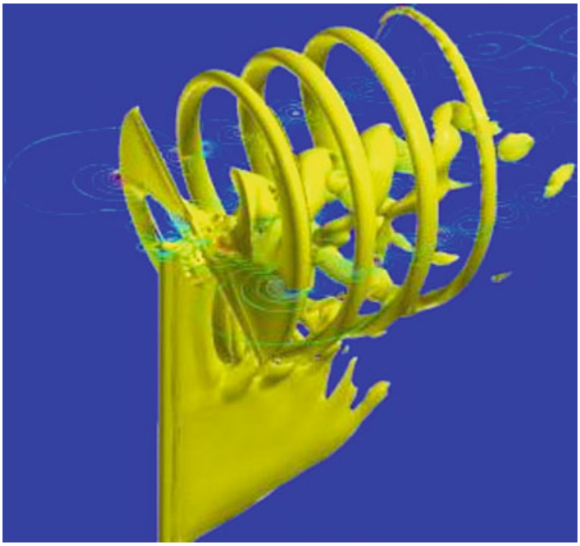

Fig. 38 Example of a CFD solution of the flow about a HAWT (NREL Phase IV turbine). The primary flow is solved using the EllipSys2D/3D code, which is an incompressible finite volume, N–S method [80]

17 Chapter Review

Unquestionably, many strides have been made in the understanding and in the mathematical modeling of the aerodynamics HAWTs, especially over the last decade or so. In this chapter, the fundamental methods of HAWT aerodynamics have been reviewed, mainly from the perspective of the classic momentum theory, blade element momentum (BEM) theory, and blade element (BE) theory combined with vortex wake models. Despite the various assumptions and approximations in the BEM theory, it still remains a standard method for analyzing the performance of HAWTs. The BEM method gives good predictions of the effects key design parameters, but its predictive confidence levels are significantly reduced in high wind conditions or when the turbine is yawed with respect to the wind. Today, newer engineering methods that are used for wind turbine analyses are based on blade element theory combined with either inflow models or vortex models to represent the non-uniform induction velocity that has its source in the vortical wake downstream of the turbine. This type of approach gives much more flexibility compared to the BEM theory, and also offers the analyst the options of including a wide range of validated subcomponent models that represent physical phenomena but are difficult to represent from first principles. These methods can also be combined with structural dynamic models of the blades, the support tower, and the power generation system, so as to produce comprehensive mathematical tools to help in the detailed design of HAWTs.

It has also been emphasized in this chapter why significant unsteady effects may be produced on HAWTs by the phenomenon of dynamic stall, and this problem still remains a serious concern to analysts from a loads perspective. In higher winds, when much of the blade can be stalled, current methods of analysis tend to predict blade loads and power outputs that are considerably different (i.e., higher or lower) to those actually measured. For the future, there is a need to refine and expand upon existing aerodynamic models especially for more general operating conditions, and in some cases the goal will be to develop completely new models that can encompass a wider range of operating conditions for use in wind turbine applications.

While it is also clear that the challenges of modeling HAWT problems using CFD have been taken up, the capabilities of these methods have not yet been sufficiently elevated to be assigned the confidence levels that are necessary for design purposes. With faster computers and with improved numerical algorithms, CFD methods will ultimately prevail and will become increasingly used in the design of better and more efficient types of HAWTs. However, sustained validation of all of these approaches against experimental measurements remains essential, and good measurements continue to be needed from both wind tunnel tests on wind turbines and also in the field. This improved modeling capability will then allow adverse loads or other undesirable effects to be predicted well in advance, and so to allow more efficient and reliable wind turbines to be designed in the future.

References

1. Paraschivoiu I (2002) Wind Turbine Design: With Emphasis on Darrieus Concept, Ecole Polytechnique de Montréal
2. Darrieus FM (1931) Turbine Having its Rotating Shaft Transverse to the Flow of Current. US Patent No. 1,834,018
3. Manwell FJ, McGowan JG, and Rogers AL (2002) Wind Energy Explained, John Wiley & Sons, New York, NY
4. Fingersh LJ, Simms D, Hand M, Jager, D, Cotrell J, Robinson M, Schreck S, Larwood S (2001) Wind Tunnel Testing of NREL's Unsteady Aerodynamics Experiment. AIAA Paper 2001-0035, 20th ASME Wind Energy Symposium and the 39th Aerospace Sciences Meeting, Reno, NV
5. Simms D, Schreck S, Hand M, Fingersh L (2001) NREL Unsteady Aerodynamics Experiment in the NASA-Ames Wind Tunnel: A Comparison of Predictions to Measurements. National Renewable Energy Laboratory Report NREL/TP-500-29494
6. Coton FN, Wang T, Galbraith RAMcD (2002) An Examination of Key Aerodynamic Modeling Issues Raised by the NREL Blind Comparison. AIAA Paper 2002-0038, 21st ASME Wind Energy Symposium and the 40th AIAA Aerospace Sciences Meeting, Reno, NV
7. Thresher R (2002) State of the Wind Industry: Technology, Economics & Future Evolution. Presentation by the National Renewable Energy Laboratory
8. Global Wind Energy Council (2007) Global Wind 2005 Report, 2006
9. US Department of Energy (2007) Annual Report on US Wind Power Installation, Cost, and Performance Trends: 2006
10. Leishman JG (2006). Principles of Helicopter Aerodynamics, Cambridge University Press, 2nd Edition, New York, NY

11. Eggleston DM, Stoddard DM (1987) Wind Turbine Engineering Design, Van Norstrand Reinhold Co., New York, NY
12. Burton T, Sharpe D, Jenkins N, Bossanyi, E (2001) Wind Energy Handbook. John Wiley & Sons, Ltd., Chichester, England
13. Frost W, Long BH, Turner RE (1978) Engineering Handbook on the Atmospheric Environment Guidelines for Use in Wind Turbine Generator Development. NASA Technical Paper 1359
14. Glauert H (1976) Airplane Propellers. In Division L of Aerodynamic Theory, Edited by WF Durand, Springer–Verlag, Berlin, Germany, 1935. Reprinted by Peter Smith, Glouster, MA
15. Glauert H (1983) Elements of Aerofoil and Airscrew Theory. Cambridge University Press, New York, NY
16. Glauert H (1926) The Analysis of Experimental Results in the Windmill Brake and Vortex Ring States of an Airscrew. British ARC R & M 1026
17. Lock CNH, Bateman H, Townend H (1925) An Extension of the Vortex Theory of Airscrews with Applications to Airscrews of Small Pitch and Including Experimental Results. British ARC R & M 1014
18. Buhl, ML (2004) A New Empirical Relationship Between Thrust Coefficient and Induction Factor for the Turbulent Windmill State. NREL/TP-500-36834
19. Bergy KH (1974) The Lanchester–Betz Limit. Journal of Energy 3(6):382–384
20. Hansen AC, Laino DJ (1977) Validation Study for AeroDyn and YawDyn Using Phase II Combined Experiment Data. Proceedings of the 16th ASME Wind Energy Symposium and the 35th AIAA Aerospace Sciences Meeting, Reno, NV
21. Bossanyi EA (2003) GH Bladed Version 3.6 User Manual. Garrad Hassan and Partners Limited Document 2.82/BR/010 Issue 12
22. McCoy T (2004) Wind Turbine ADAMS Model Linearization Including Rotational and Aerodynamic Effects. Proceedings of 23rd Wind Energy Symposium and the 42nd AIAA Aerospace Sciences Meeting, Reno, NV
23. Snel H (2001) Survey of Induction Dynamics Modeling with BEM-Like Codes: Dynamic Inflow and Yawed Flow Modeling Revisited. 20th ASME Wind Energy Symposium and the 39th AIAA Aerospace Sciences Meeting, Reno, NV
24. Coleman RP, Feingold AM, and Stempin, CW (1945) Evaluation of the Induced Velocity Fields of an Idealized Helicopter Rotor. NACA ARR L5E10, 1945
25. Schepers JG (1999) An Engineering Model for Yawed Conditions Developed on the Basis of Wind Tunnel Measurements. Report ECN DE: ECN-RX–98-057, Energy Research Center of the Netherlands
26. Miley SJ (1982) A Catalog of Low Reynolds Number Airfoil Data for Wind Turbines Applications. Rockwell International, Rocky Flats Plant, RFP-3387
27. Tangler JL (1987) Status of the Special Purpose Airfoil Families. Solar Energy Research Institute, SERI/TP-217-3264
28. Tangler JL, Somers DM (1995) NREL Airfoil Families for HAWTs. American Wind Energy Association, Windpower '95, Washington DC
29. Clark RN, Davis RG (1991) Performance Changes Caused by Rotor Blade Surface Debris. American Wind Energy Association, Windpower '91, Palm Springs, CA
30. Eggleston DM (1991) Wind Turbine Bug Roughness Sampling and Power Degradation. American Wind Energy Association, Windpower '91, Palm Springs, CA
31. Vermeer LJ, Sørensen JN, Crespo, A (2003) Wind Turbine Wake Aerodynamics. Progress in Aerospace Sciences 39: 467–510
32. Kocurek D (1987) Lifting Surface Performance Analysis for Horizontal Wind Axis Turbines. Solar Energy Research Institute, SERI/STR-217-3163
33. Robison DJ, Coton FN, Galbraith RA McD, Vezza, M (1995) Application of a Prescribed Wake Aerodynamic Prediction Scheme to Horizontal Axis Wind Turbines in Axial Flow. Wind Engineering, 19(1):41–51

34. Coton FN, Wang T (1999) The Prediction of Horizontal Wind Turbine Performance in Yawed Flow Using an Unsteady Prescribed Wake Model. Institute of Mechanical Engineers, Part A, Journal of Power and Energy 213:33–43
35. Leishman JG, Bhagwat MJ, Bagai A (2003) Free Vortex Methods for Helicopter Rotor Wake Analyses. Journal of Aircraft, 39(5):759–775
36. Crouse GL, Leishman, JG (1993) A New Method for Improved Free-Wake Convergence in Hover and Low-Speed Forward Flight. 21st Aerospace Sciences Meeting & Exhibit, Reno, NV
37. Bagai A Leishman JG (1994) Rotor Free-Wake Modeling using a Relaxation Technique – Including Comparisons with Experimental Data. Proceedings of the 50th Annual National Forum of the American Helicopter Society, Washington, DC
38. Bhagwat MJ, Leishman JG (2001). Stability, Consistency and Convergence of Time-Marching Free-Vortex Rotor Wake Algorithms. Journal of the American Helicopter Society 46(1):59–70
39. Gupta S. Leishman JG (2004) Stability of Methods in the Free-Vortex Wake Analysis of Wind Turbines. Proceedings of the 23rd ASME Wind Energy Symposium and the 42nd AIAA Aerospace Sciences Meeting, Reno, NV
40. Robinson MC, Galbraith RAMcD, Shipley D, Miller M (1995) Unsteady Aerodynamics of Wind Turbines. AIAA Paper 95-0526, 14th ASME Wind Energy Symposium and the 33rd Aerospace Sciences Meeting, Reno, NV
41. Huyer SA, Simms DA, Robinson MC (1996). Unsteady Aerodynamics Associated with a Horizontal-Axis Wind Turbine. AIAA Journal, 34(7):1410–1419
42. Schreck S, Robinson M, Hand M, Simms D (2000) HAWT Dynamic Stall Response Asymmetries Under Yawed Flow Conditions. AIAA Paper 2000-0040, 19th ASME Wind Energy Symposium and the 38th AIAA Aerospace Sciences Meeting, Reno, NV
43. Leishman JG (2002) Challenges in Modeling the Unsteady Aerodynamics of Wind Turbines. Wind Energy 5:86–132
44. Leishman JG, Beddoes TS (1989) A Semi-Empirical Model for Dynamic Stall. Journal of the American Helicopter Society 34(3):3–17
45. Pierce K, Hansen AC (1995) Prediction of Wind Turbine Rotor Loads Using the Beddoes-Leishman Model for Dynamic Stall. Journal of Solar Energy Engineering, 117:200–204
46. Gupta S, Leishman JG (2006) Dynamic Stall Modeling of the S809 Aerofoil and Comparison with Experiments. Wind Energy 9(6):521–547
47. Himmelskamp H (1950) Profile Investigations on a Rotating Propeller. Max-Plank Institut für Stromungsforschung Göttingen, Germany
48. Young WH, Williams JC (1972) Boundary-Layer Separation on Rotating Blades in Forward Flight. AIAA Journal, 10(12):1613–1619
49. Madsen H, Christensen H (1990) On the Relative Importance of Rotational, Unsteady and Three-Dimensional Effects on the HAWT Rotor Aerodynamics. Wind Engineering 14 (6):405–415
50. Snel H (1991) Scaling Laws for the Boundary Layer Flow on Rotating Wind Turbine Blades. 4th IEA Symposium on Aerodynamics for Wind Turbines, Rome
51. Narramore JC, Vermeland R (1992) Navier–Stokes Calculations of Inboard Stall Delay Due to Rotation. Journal of Aircraft, 29(1):73–78
52. Dwyer HA, McCroskey WJ (1971) Crossflow and Unsteady Boundary-Layer Effects on Rotating Blades. AIAA Journal, 9(8):1498–1505
53. Robinson MC, Simms DA, Hand MM, Schreck SJ (1999) Horizontal Axis Wind Turbine Aerodynamics: Three Dimensional, Unsteady and Separated Flow Influences. 3rd ASME/JSME Joint Fluids Engineering Conference, San Francisco, CA
54. Schreck SJ, Robinson MC, Hand MM, and Simms DA (2001) Blade Dynamic Stall Vortex Kinematics for a Horizontal Wind Axis Turbine in Yawed Conditions. Journal of Solar Energy Engineering 123:272–281
55. Corten GP (2000) Inviscid Stall Model. 13th IEA Symposium on Aerodynamics of Wind Turbines, Golden, CO

56. Fogarty LE (1951) The Laminar Boundary Layer On a Rotating Blade. Journal of the Aeronautical Sciences 18(3):247–252
57. Corrigan J (1994) Empirical Model for Stall Delay Due to Rotation. American Helicopter Society Aeromechanics Specialist Meeting, San Francisco, CA
58. Du ZH, Selig MS (1998) A 3-dimensional Stall Delay Model for HAWT Performance Prediction. AIAA Paper 89-0021, 36th AIAA Aerospace Sciences Meeting and Exhibit and 1998 ASME Wind Energy Symposium, Reno, NV
59. Bierbooms W (1991) A Comparison Between Unsteady Aerodynamic Models. European Wind Energy Conference, Amsterdam, The Netherlands
60. Snel H, Schepers JG (1991) Engineering Models for Dynamic Inflow Phenomena. European Wind Energy Conference, Amsterdam, The Netherlands
61. Hansen AC, Butterfield CP (1993) Aerodynamics of Horizontal-Axis Wind Turbines. Annual Review of Fluid Mechanics 25:115–149
62. Munduate X, Coton FN, Galbraith RA McD (2003) An Investigation of the Aerodynamic Response of a Wind Turbine to Tower Shadow. 4th ASME-JSME Joint Fluids Engineering Conference, Honolulu, HI
63. Wang T, Coton FN (2001) A High Resolution Tower Shadow Model for Downwind Wind Turbines. Journal of Wind Engineering and Industrial Aerodynamics 89:873–892
64. Duque EPN, van Dam CP, Brodeur RR, Chao DD (1999) Navier–Stokes Analysis of Time-Dependent Flows About a Wind Turbine. 3rd ASME/JSME Joint Fluids Engineering Conference
65. Duque EPN, Johnson W, van Dam CP, Cortes R, Yee K (2000) Numerical Prediction of Wind Turbine Power and Aerodynamic Loads for the NREL Phase II Combined Experiment Rotor. AIAA Paper 2000-0038, 19th ASME Wind Energy Symposium and the 38th AIAA Aerospace Sciences Meeting, Reno, NV
66. Duque EPN, Burkland MD, Johnson W (2003) Navier–Stokes and Comprehensive Performance Predictions of the NREL Phase IV Experiment. AIAA Paper 2003-0355, 22nd ASME Wind Energy Symposium and the 41st AIAA Aerospace Sciences Meeting, Reno, NV
67. Ekaterinaris JA (1997) Numerical Simulation of Incompressible Two-Bladed Rotor Flow Field. Proceedings of 16th ASME Wind Energy Symposium and the 35th AIAA Aerospace Sciences Meeting, Reno, NV
68. Duque EPN, van Dam CP, Hughes SC (1999) Navier–Stokes Simulations of the NREL Combined Experiment Phase II Rotor. Proceedings of 18th ASME Wind Energy Symposium and the 37th AIAA Aerospace Sciences Meeting, Reno, NV
69. Sørenson, NN, Michelsen JA (2000) Aerodynamic Predictions for the Unsteady Aerodynamics Experiment Phase-II at the National Renewable Energy Laboratory. Proceedings of 19th ASME Wind Energy Symposium and the 38th AIAA Aerospace Sciences Meeting, Reno, NV
70. Baldwin BS, Lomax H (1978) Thin Layer Approximation and Algebraic Model for Separated Turbulent Flows. AIAA Paper 78-257, 16th AIAA Aerospace Sciences Meeting, Huntsville, Alabama
71. Baldwin BS, Barth TJ (1990) A One-Equation Turbulence Transport Model for High Reynolds Number Wall-Bounded Flows. NASA TM 102847
72. Spalart PR, Allamaras SR (1992) A One-Equation Turbulence Model for Aerodynamic Flows. AIAA Paper 92-0439, 30th AIAA Aerospace Sciences Meeting & Exhibit, Reno, NV
73. Wolfe WP, Ochs SS (1997) Predicting Aerodynamic Characteristics of Typical Wind Turbine Airfoils Using CFD. Sandia National Laboratories SAND96-2345
74. Chaviaropolous PK (1996) Investigating Dynamic Stall, 3-D and Rotational Effects on Wind Turbine Blades by Means of an Unsteady Quasi-3D Navier–Stokes Solver. Proceedings of 10th IEA Symposium on Aerodynamics of Wind Turbines, Edinburgh, Scotland, pp. 175–182
75. Langtry R, Gola, J, Menter F (2006) Predicting 2D Airfoil and 3D Wind Turbine Rotor Performance using a Transition Model for General CFD Codes. Proceedings of 25th Wind Energy Symposium and the 44th AIAA Aerospace Sciences Meeting, Reno, NV

76. Benjanirat S, Sankar L, Xu G (2003) Evaluation of Turbulence Models for the Prediction of Wind Turbine Aerodynamics. Proceedings of 22nd ASME Wind Energy Symposium and the 41st AIAA Aerospace Sciences Meeting, Reno, NV
77. Madsen HA (1998) Application of Actuator Surface Theory on Wind Turbines. Proceedings of the 2nd IEA Symposium on Aerodynamics of Wind Turbines, Lyngby, Denmark
78. van Holten T (1977) On the Validity of the Lifting Line Concepts in Rotor Analysis. Vertica, vol:1 pp 239–254
79. van Bussel, GJW (1995) The Aerodynamics of Horizontal Axis Wind Turbine Rotors Explored with Asymptotic Expansion Methods, Ph.D. thesis, Delft University
80. Hansen MOL, Sørenson NN, Sørenson JN, Michelsen, JA (1997) A Global Navier Stokes Rotor Prediction Model. AIAA Paper 97-0970, 35th Aerospace Sciences Meeting and Exhibit, Reno, NV
81. Xu G (2001) Computational Studies of Horizontal Axis Wind Turbines. Ph.D. Dissertation, Department of Aerospace Engineering, Georgia Institute of Technology
82. Benjanirat S, Sankar L (2004) Recent Improvements to a Combined Navier-Stokes Full Potential Methodology for Modeling Horizontal Axis Wind Turbines. Proceedings of 23rd ASME Wind Energy Symposium and the 42nd AIAA Aerospace Sciences Meeting, Reno, NV, pp. 378–385
83. Tongchitpakdee C, Benjanirat S, Sankar L (2005) Numerical Simulation of the Aerodynamics of Horizontal Axis Wind Turbines Under Yawed Flow Conditions. Proceedings of 24th ASME Wind Energy Symposium and the 43rd AIAA Aerospace Sciences Meeting, Reno, NV
84. Menter FR (1993) Zonal Two Equation k–ω Model for Aerodynamic Flows. AIAA Paper 93-2906, 24th Fluid Dynamics Conference, Orlando, FL

Author Biography

Prof. J. Gordon Leishman is the Minta Martin Professor of Engineering in the Department of Aerospace Engineering at the University of Maryland. Dr. Leishman holds D.Sc.(Eng), Ph.D., and B.Sc (1st Class Honors) degrees in Aeronautics and Fluid Mechanics and in Aerospace Engineering from the University of Glasgow in the UK. He joined the University of Maryland in 1986. Dr. Leishman is an internationally recognized specialist in rotorcraft aerodynamics whose work has spanned the gamut of experimental, theoretical, and numerical approaches. Formally an aerodynamicist for Westland Helicopters Ltd., Dr. Leishman has authored over 300 papers on rotorcraft aerodynamics, wind energy, and topics in fluid mechanics and experimental aerodynamics. Dr. Leishman is the author of two books, including Principles of Helicopter Aerodynamics, first published in 2000 by Cambridge University Press and adopted as a course text for many colleges and universities worldwide. He has served as the Editor-in-Chief of the Journal of the American Helicopter Society. Dr. Leishman is an Associate Fellow of the AIAA, a Fellow of the Royal Aeronautical Society, and a Technical Fellow of the American Helicopter Society.

Analysis of Wind Regimes and Performance of Wind Turbines

Sathyajith Mathew, Geetha Susan Philip and Chee Ming Lim

With the present day's energy crisis and growing environmental consciousness, the global perspective in energy conversion and consumption is shifting towards sustainable resources and technologies. This resulted in an appreciable increase in the renewable energy installations in different part of the world. For example, Wind power could register an annual growth rate over 25% for the past 7 years, making it the fastest growing energy source in the world. The global wind power capacity has crossed well above 160 GW today [1] and several Multi-Megawatt projects-both on shore and offshore-are in the pipeline. Hence, wind energy is going to be the major player in realizing our dream of meeting at least 20% of the global energy demand by new-renewables by 2020.

Assessing the wind energy potential at a candidate site and understanding how a wind turbine would respond to the resource fluctuations are the initial steps in the planning and development of a wind farm project. Energy yield from the Wind Energy Conversion System (WECS) at a given site depends on (1) strength and distribution of wind spectra available at the site (2) performance characteristics of the wind turbine to be installed at the site and more importantly (3) the interaction between the wind spectra and the turbine under fluctuating conditions of the wind regime.

Thus, models which integrate the wind resource as well as the turbine performance parameters are to be used in estimating the system performance. Based on the above parameters, methods for assessing the available wind energy resource at

---

S. Mathew (✉) and C. M. Lim
Faculty of Science, University of Brunei Darussalam, Jalan Tungku Link, Gadong, BE1410 Negra, Brunei Darussalam
e-mail: windbook@gmail.com

G. S. Philip
Faculty of Engineering, KAU, Kerala, India

S. Mathew and G. S. Philip (eds.), *Advances in Wind Energy Conversion Technology,* Environmental Science and Engineering,
DOI: 10.1007/978-3-540-88258-9_2,

a candidate site and the performance expected from a wind turbine installed at this site are presented in this chapter.

1 Wind Regime Characteristics

In this section we will discuss how the characteristics of the wind regimes can be incorporated in assessing the wind energy potential as well as estimating the output from a wind energy conversion system.

1.1 Boundary Layer Effects

The first factor to be considered while estimating the wind resource and wind turbine performance at a given site is the variations in wind velocity due to the boundary layer effect. Due to the frictional resistance offered by the earth surface (caused by roughness of the ground, vegetations etc.) to the wind flow, the wind velocity may vary significantly with the height above the ground. For example, wind profile at a site is shown in Fig. 1. Variations in the wind velocity with height are quite evident in the figure. Thus, if the wind data available are not collected from the hub height of the turbine, the data are to be corrected for the boundary layer effect.

Ground resistance against the wind flow is represented by the roughness class or the roughness height (Z_0). The roughness height of a surface may be close to zero (surface of the sea) or even as high as 2 (town centers).

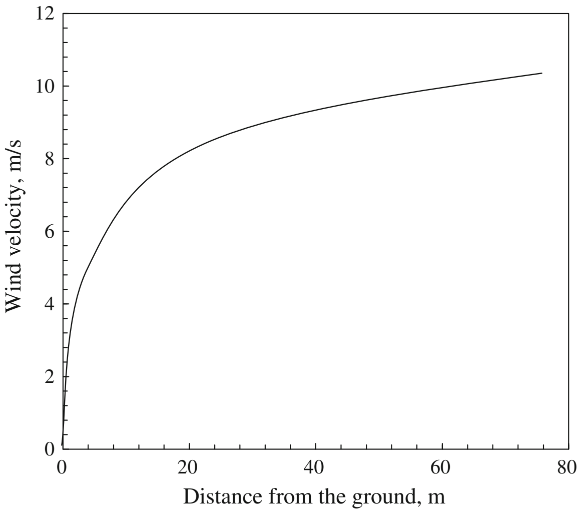

Fig. 1 Variation of wind velocity with height [2]

Some typical values for the roughness heights are 0.005 for flat and smooth terrains, 0.025–0.1 for open grass lands, 0.2–0.3 for row crops, 0.5–1 for orchards and shrubs and 1–2 for forests, town centers etc. On the basis of the roughness height of the terrain, wind data collected at different heights are to be extrapolated to the hub height of the turbine. If the wind data are available at a height Z and the roughness height is Z_0, then the velocity at a height Z_R is given by [3, 4].

$$V(Z_R) = V(Z)\frac{\ln\left(Z_R/Z_0\right)}{\ln\left(Z/Z_0\right)} \tag{1}$$

where $V(Z_R)$ and $V(Z)$ are the velocities at heights Z_R and Z respectively. Thus, if the velocity of wind measured at a height of 10 m is 7 m/s and the roughness height is 0.1, the velocity at the hub height—say 100 m—is 10.5 m/s. It should be noted that the power available at 100 m would be 3.4 times higher than at 10 m.

In some cases, we may have data from a reference location (meteorological station for example) at a certain height. This data is to be transformed to a different height at another location with similar wind profile but different roughness height (for example, the wind turbine site). Under such situations, it is logical to assume that the wind velocity is not significantly affected by the surface characteristics beyond a certain height. This height may be taken as 60 m from the ground level [5]. With this assumption and equating the velocities at 60 m height at both the sites as per Eq. 1, we get

$$V(Z) = V(Z_R)\left(\frac{\ln\left(60/Z_{OR}\right)\,\ln\left(Z/Z_O\right)}{\ln\left(60/Z_O\right)\,\ln\left(Z_R/Z_{OR}\right)}\right) \tag{2}$$

where Z_{OR} is the roughness height at the reference location.

1.2 Wind Velocity Distribution

Being a stochastic phenomena, speed and direction of wind varies widely with time. Apart from the seasonal variations, the differences can be considerable even within a short span of time. These variations can significantly affect the energy yield from the turbine at a given site. For example, a turbine may deliver entirely different amount of energy when it is installed in two sites with the same average wind velocity but different velocity distributions. Similarly, two wind turbines with the same output rating but different in the cut-in, rated and cut-out velocities may behave differently at the same site. Statistical distributions are used to take care of these variations in wind energy calculations.

Several attempts were made to identify the statistical distribution most suitable for defining the characteristics of wind regime. A wide range of distributions are being tried by the researchers. The Weibull distribution, which is a special case of Pierson class III distribution, is well accepted and commonly used for the wind energy analysis as it can represent the wind variations with an acceptable level of accuracy [6–9]. In some situations, Rayleigh distribution—which is a simplified form of Weibull distribution—is also being used. It is worth mentioning that some innovative attempts are also been made by applying the Minimum Cross Entropy (MinxEnt) [10] and Maximum Entropy (ME) [11] principles in wind energy analysis. However, a recent study comparing various statistical distributions in wind energy analysis has established the acceptability of Weibull distribution [9]. Hence we will follow the Weibull distribution in our analysis.

The Weibull distribution can be defined by its probability density function *f(V)* and cumulative distribution function *F(V)* where:

$$f(V) = \frac{k}{c}\left(\frac{V}{c}\right)^{k-1} e^{-(V/c)^k} \tag{3}$$

and

$$F(V) = \int f(V)\,dV = 1 - e^{-(V/c)^k} \tag{4}$$

where *k* is the Weibull shape factor, *c* the scale factor and *V* is the velocity of interest. Here, *f(V)* represents the fraction of time (or probability) for which the wind blows with a velocity *V* and *F(V)* indicates the fraction of time (or probability) that the wind velocity is equal or lower than *V*.

From Eqs. 3 and 4, it is evident that *k* and *c* are the factors determining the nature of the wind spectra within a given regime. Effects *k* and *c* on the probability density and cumulative distribution of wind velocity are demonstrated using the wind data from three potential wind farm sites in Figs. 2 and 3. The site wind velocities are represented in Table 1.

Fig. 2 Effect of Weibull shape factor on the probability density of wind velocity of some potential sites

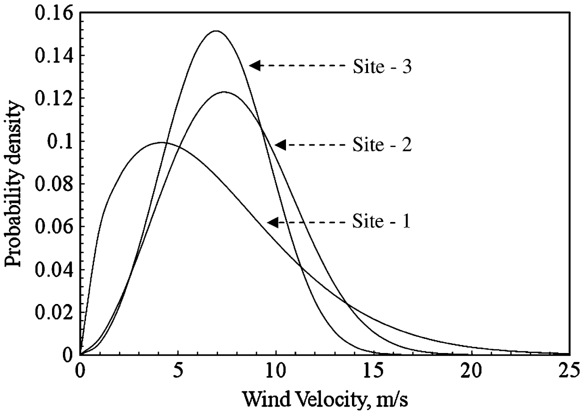

Fig. 3 Effect Weibull shape factor on the cumulative distribution of wind velocity at some potential sites

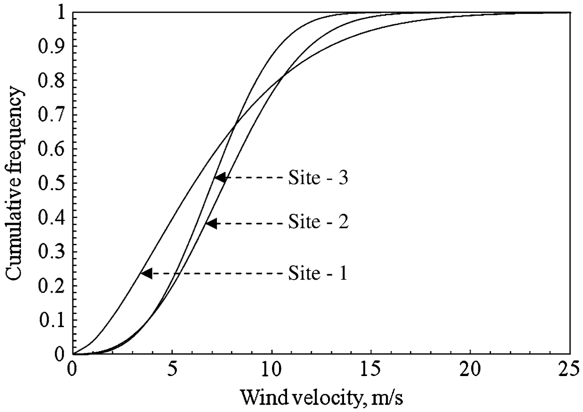

Table 1 Weibull shape and scale factors of some wind farm sites

Site no.	Mean wind velocity, m/s	Standard deviation, m/s	k	c, m/s
1	6.79	4.11	1.6	7.66
2	7.75	3.11	2.7	8.74
3	6.99	2.50	3.06	7.89

There are several methods for determining k and c from the site wind data. Some of the common methods are the graphical method, moment method, maximum likelihood method, energy pattern factor method and the standard deviation method [2]. For example, in the standard deviation approach, the relationship between the mean (V_m) and standard deviation (σ_V) of the wind velocities and k are correlated as

$$\left(\frac{\sigma_V}{V_m}\right)^2 = \frac{\Gamma\left(1+\frac{2}{k}\right)}{\Gamma^2\left(1+\frac{1}{k}\right)} - 1 \tag{5}$$

Once Vm and σ_V are calculated for a given data set, then k can be determined by solving the above expression numerically. Once k is determined, c is given by

$$c = \frac{V_m}{\Gamma\left(1+\frac{1}{k}\right)} \tag{6}$$

In a simpler approach, an acceptable approximation for k can be made as [7, 12]

$$k = \left(\frac{\sigma_V}{V_m}\right)^{-1.090} \tag{7}$$

and c can be approximated as

$$c = \frac{2\,V_m}{\sqrt{\pi}} \tag{8}$$

1.3 Energy Density

The power available in a wind stream of velocity *V*, per unit rotor area, is given by

$$P_V = \frac{1}{2}\rho_a V^3 \tag{9}$$

where P_V is the power and ρ_a is the density of air. The fraction of time for which this velocity *V* prevails in the regime is given by the probability density function *f(V)*. Thus, the energy contributed by *V*, per unit time and unit rotor area, is $P_V\, f(V)$. Hence, the total energy contributed by all possible velocities in the wind regime, available for unit rotor area in unit time (that is energy density, E_D) may be expressed as

$$E_D = \int_0^\infty P_V f(V)\, dV \tag{10}$$

Substituting for *P(V)* and *f(V)* in the above expression and simplifying, we get

$$E_D = \frac{1}{2}\rho_a \frac{k}{c^k}\int_0^\infty V^{(k+2)} e^{-\,(V/c)^k}\, dV \tag{11}$$

This can further be simplified as [2]

$$E_D = \frac{3}{2}\rho_a \frac{c^3}{k}\,\Gamma\left(\frac{3}{k}\right) \tag{12}$$

2 Velocity–Power Response of the Turbine

Power curve of a 2 MW pitch controlled wind turbine is shown in Fig. 4. The turbine has cut-in, rated and cut-out velocities 3.5, 13.5 and 25 m/s respectively. The given curve is a theoretical one and in practice we may observe the velocity power variation in a rather scattered pattern.

In this curve, we can observe that the turbine has four distinct performance regions.

1. For velocities from 0 to the cut-in (V_I), the turbine does not yield any power.
2. Between the cut-in and rated velocities (V_I to V_R), the power increases with the wind velocity. Though, theoretically, this increase should be cubic in nature, in practice it can be linear, quadratic, cubic and even higher powers and its combinations, depending upon the design of the turbine.
3. From the rated to cut-out wind speed (V_R to V_O), the power is constant at the rated power P_R, irrespective of the change in wind velocity.
4. Beyond the cut-out velocity, the turbine is shut down due to safety reasons.

Fig. 4 Theoretical power curve of a 2 MW wind turbine

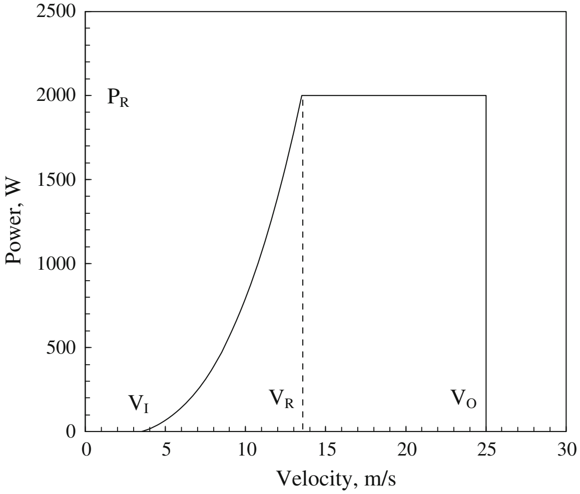

So, the wind turbine is 'productive' only between the velocities V_I and V_O. For any wind velocity between V_I and V_R, the power P_V can generally be expressed as

$$P_V = aV^n + b \tag{13}$$

where a and b are constants and n is the velocity–power proportionality. Now consider the performance of the system at V_I and V_R. At $V_{I,}$ the power developed by the turbine is zero. Thus

$$aV_I^n + b = 0 \tag{14}$$

At V_R power generated is P_R. That is:

$$aV_R^n + b = P_R \tag{15}$$

Solving Eqs. 14 and 15 for a and b and substituting in Eq. 13 yields

$$P_V = P_R\left(\frac{V^n - V_I^n}{V_R^n - V_I^n}\right) \tag{16}$$

Above equation gives us the power response of the turbine between the cut-in and rated wind speeds. Obviously, the power between V_R and V_O is P_R.

In the above expression, the major factor deciding the variations in power with velocity in the cut-into rated wind speed region is n. Value of n differs from turbine to turbine, depending on the design features. For example, Fig. 5 compares the power responses of two commercial wind turbines in this performance region. The curves are derived from data available from the manufactures. It should be noted that, although both the turbines are of the same 2 MW rated capacity, their power responses in the 'cut-into rated' velocity region differ significantly.

For a specific turbine, n can be calculated from its power curve data, available from the manufacturer. For example, the cut-in, rated and cut-out wind velocities

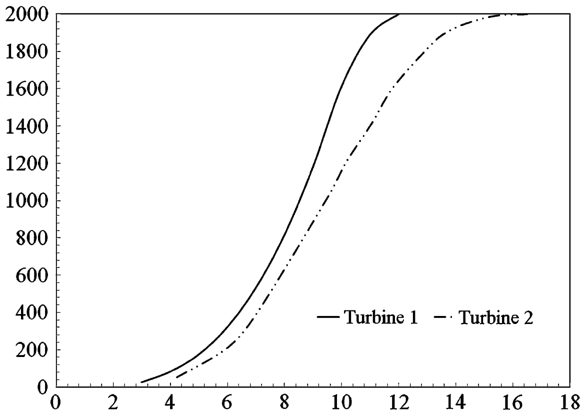

Fig. 5 Variations in output power from cut-into cut-out velocities for two wind turbines of 2 MW rated capacity

Table 2 Cut-in, rated and cut-out wind velocities of the turbines

Turbine no.	Cut-in velocity, m/s	Rated velocity, m/s	Cut-out velocity, m/s
1	3	12	28
2	4	16	25

of the two turbines compared above are shown in Table 2. Putting these values in Eq. 16 we get

$$P_V[T1] = 2000 \times \left(\frac{V^n - 3^n}{12^n - 3^n}\right) \text{ and } P_V[T2] = 2000 \times \left(\frac{V^n - 4^n}{16^n - 4^n}\right)$$

where T1 and T2 represents the turbines 1 and 2 respectively. Solving the above relationship with the velocity power data for the turbines (available from the manufacturer or obtained by digitizing the power curve) we can find out the value of n. Any standard curve fitting package can be used for the solution. Following this method, n for the turbines T1 and T2 are 1.8 ($R^2 = 0.97$) and 0.6 ($R^2 = 0.95$) respectively.

Instantaneous values of wind velocity and corresponding power were recorded from a 225 kW wind turbine installed at a wind farm and are plotted in Fig. 6. Cut-in and rated wind velocities of this turbine are 3.5 and 14.5 m/s respectively. Scattered points represent the measured power where as the continuous line represents the power computed using Eq. 16. Reasonable agreement could be observed between measured and computed values.

3 The Energy Model

To estimate the energy generated by the turbine at a given site over a period, the power characteristics of the turbine is to be integrated with the probabilities of different wind velocities expected at the site. For example, power curve of a wind

Fig. 6 Field performance of a 225 kW wind turbine

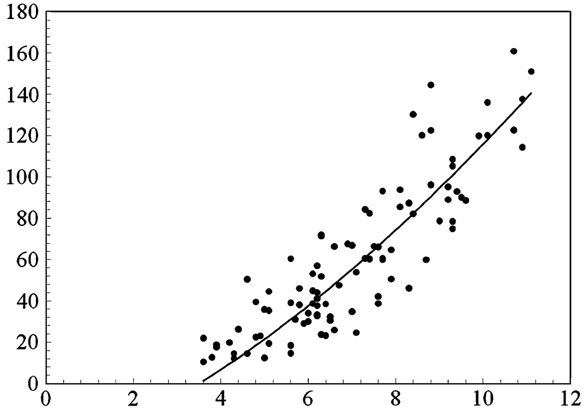

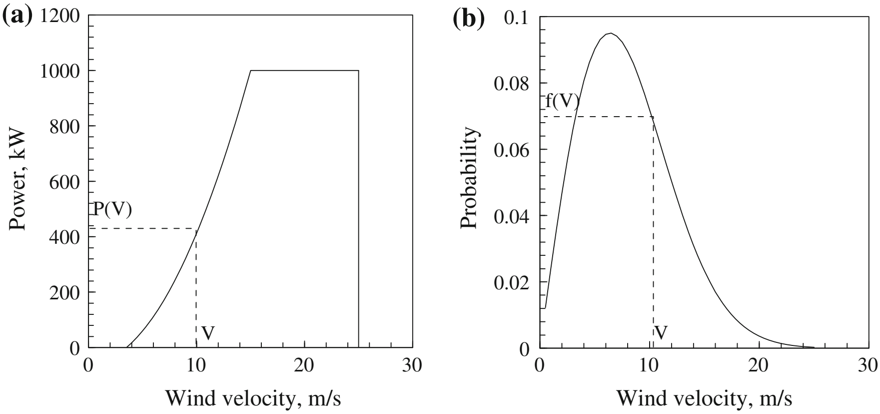

Fig. 7 Integrating the power (**a**) and probability (**b**) curves to derive the energy yield

turbine is shown in Fig. 7a whereas Fig. 7b presents the Weibull probability density function of a candidate site. In the wind regime, the fraction of energy contributed by any wind velocity *V* is the product of power corresponding to *V* in the power curve, that is *P(V)* and the probability of *V* in the probability density curve, which is *f(V)*. Thus, at this site, the total energy generated by the turbine *E*, over a period *T*, can be estimated by

$$E = T \int_{V_i}^{V_o} P_V f(V)\, dV \tag{17}$$

As we have discussed, the power curve has two distinct productive regions—from V_I to V_R and V_R to V_O. Thus, let us take

$$E = E_{IR} + E_{RO} \tag{18}$$

where E_{IR} and E_{RO} are the energy yield corresponding to V_I to V_R and V_R to V_O respectively. From the foregoing discussions, we have

$$E_{IR} = T \int_{V_i}^{V_R} P_V f(V)\, dV \tag{19}$$

and

$$E_{RO} = T\, P_R \int_{V_R}^{V_O} f(V) dV \tag{20}$$

Substituting for *f(V)* and *P(V)* from Eqs. 3 and 16 in Eq. 19, we get

$$\begin{aligned} E_{IR} &= P_R\, T \int_{V_I}^{V_R} \left[\frac{V^n - V_I^n}{V_R^n - V_I^n}\right] \frac{k}{c} \left(\frac{V}{c}\right)^{k-1} e^{-(V/c)^k}\, dV \\ &= \left(\frac{P_R\, T}{V_R^n - V_I^n}\right) \int_{V_I}^{V_R} \left(V^n - V_I^n\right) \frac{k}{c} \left(\frac{V}{c}\right)^{k-1} e^{-(V/c)^k} dV \end{aligned} \tag{21}$$

For simplifying the above expression and bringing it to a resolvable form, let us introduce the variable X such that

$$X = \left(\frac{V}{c}\right)^k \tag{22}$$

Then,

$$dX = \frac{k}{c}\left(\frac{V}{c}\right)^{k-1} \text{ and } V = cX^{\frac{1}{k}} \tag{23}$$

With Eq. 22, we have

$$X_I = \left(\frac{V_I}{c}\right)^k, X_R = \left(\frac{V_R}{c}\right)^k \text{ and } X_O = \left(\frac{V_O}{c}\right)^k \tag{24}$$

With this substitution, and simplification thereafter, E_{IR} can be expressed as

$$\begin{aligned} E_{IR} = &\frac{P_R\, T\, c^n}{(V_R^n - V_I^n)} \int_{X_I}^{X_R} X^{n/k}\, e^{-X}\, dX \\ &- \frac{P_R\; T\; V_I^n}{(V_R^n - V_I^n)} \left[e^{-X_I} - e^{-X_R}\right] \end{aligned} \tag{25}$$

Now consider the second performance region. From Eq. 20, E_{RO} may be represented as

$$E_{RO} = P_R\, T \int_{V_R}^{V_O} \frac{k}{c} \left(\frac{V}{c}\right)^{k-1} e^{-(V/c)^k}\, dV \tag{26}$$

As $\int f(V)\, dV = F(V)$, from Eqs. 4 and 16, the above equation can be simplified as

$$E_{RO} = T\, P_R \left(e^{-X_R} - e^{-X_O}\right) \tag{27}$$

The above expressions can be evaluated numerically.

The capacity factor C_F—which is the ratio of the energy actually produced by the turbine to the energy that could have been produced by it, if the machine would have operated at its rated power throughout the time period—is given by

$$C_F = \frac{E}{P_R\, T} = \frac{E_{IR} + E_{RO}}{P_R T} \tag{28}$$

Thus,

$$\begin{aligned} CF = {} & \frac{c^n}{V_R^n - V_I^n} \int_{X_I}^{X_R} X^{n/k}\, e^{-X}\, dX \\ & - \frac{V_I^n}{V_R^n - V_I^n}\left[e^{-X_I} - e^{-X_R}\right] + \left(e^{-X_R} - e^{-X_O}\right) \end{aligned} \tag{29}$$

The energy model discussed above is validated with the field performance of a 10 kW wind turbine [13] in Fig. 8. The turbine considered here has cut-in, rated and cut-out wind speeds of 3.0, 13.5 and 25 m/s respectively. From the manufacturer's power curve, the velocity–power proportionality for the design was

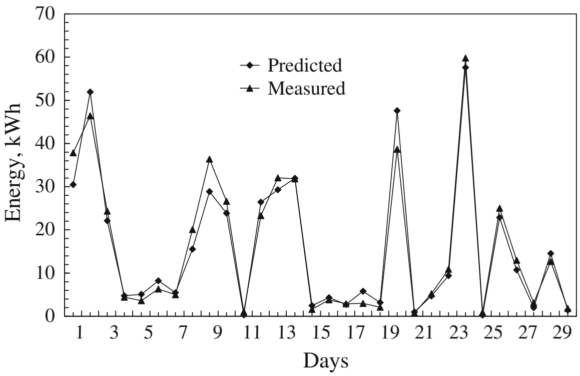

Fig. 8 Comparison between estimated and measured daily energy yield from a 10 KW wind turbine

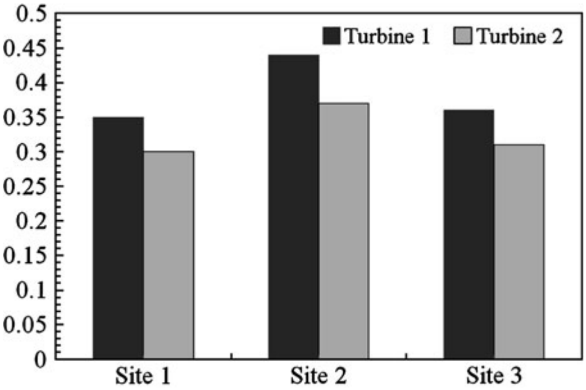

Fig. 9 Comparative performance of two 2 MW wind turbines in different wind regimes

found to be 2.16. It can be observed that the predicted performance closely follows the measured values throughout the period.

4 Conclusion

A method for assessing the wind energy resource available at a potential wind farm site has been presented in the above sections. Model for simulating the performance of wind turbines at a given site has also been discussed.

For example, the performances expected from the turbines given in Table 2, when installed at the sites described in Table 1 are compared in Fig. 9. Though both the turbines have the same rated power of 2 MW, the first turbine is expected to generate more energy from all the three sites. This is obvious as (1) the first turbine has lower cut-in and higher cut-out velocities, making it capable of exploiting a broader range of wind spectra available at the site (2) The first turbine shows better power response between the cut-into rated wind speeds as seen from Fig. 5.

The methods described above can be useful in the preliminary planning of wind power project. However, for a final investment decision, apart from a more rigorous technical analysis, economical and environmental dimensions of the project should be investigated.

References

1. Renewable Energy World (2010) Global Wind Installations Boom, Up 31% in 2009. Retrieved from http://www.renewableenergyworld.com/rea/news/article/2010/02/global-wind-installations-boom-up-31-in-2009
2. Mathew S (2006) Wind Energy: Fundamentals, Resource Analysis and Economics. Springer-Verlag, Berlin Heidelberg

3. Machias AV, Skikos, GD (1992) Fuzzy risk index for wind sites. IEEE Transactions on Energy Conversion 7(4):638–643
4. Mathew S, Pandey KP, Anil KV (2002) Analysis of wind regimes for energy estimation. Renewable Energy 25:381–399
5. Lysen EH (1983) Introduction to wind energy. CWD, Amersfoort, Netherlands
6. Hennessey JP (1977) Some aspects of wind power statistics. J Applied Meteorology 16: 119-128
7. Justus CG, Hargraves WR, Mikhail A, Graber D (1978) Methods of estimating wind speed frequency distribution. J Applied Meteorology 17:350–353
8. Stevens MJM, Smulders PT (1979) The estimation of parameters of the Weibull wind speed distribution for wind energy utilization purposes. Wind Engineering 3(2):132–145
9. Carta J A P. Ramírez P Velázquez S (2009) A review of wind speed probability distributions used in wind energy analysis: Case studies in the Canary Islands. Renewable and Sustainable Energy Reviews 13(5):933–955
10. Yeliz MK, Ilhan U (2008) Analysis of wind speed distributions: Wind distribution function derived from minimum cross entropy principles as better alternative to Weibull function Energy Conversion and Management 49(5):962–973
11. Meishen L, Xianguo Li (2005) MEP-type distribution function: a better alternative to Weibull function for wind speed distributions Renewable Energy 30(8):1221–1240
12. Boweden GJ, Barker PR, Shestopal VO, Twidell JW (1983) The Weibull distribution function and wind statistics. Wind Engineering 7:85–98
13. The Vermont Small-Scale Wind Energy Demonstration Program (2010) Retrieved from http://www.vtwindprogram.org/performancedata/

Author Biography

Dr. Sathyajith Mathew is an Associate Professor at the Faculty of Engineering, KAU and holds a concurrent faculty position at the University of Brunei Darussalam. He has more than 15 years of teaching, research and development experience on Wind Energy Conversion Systems in different parts of the world. Dr. Mathew has published extensively in this area of research. His recent book “Wind Energy: Fundamentals, Resource Analysis and Economics” which is published by Springer has been adopted as the text book for wind energy programmes in Universities around the world. Dr. Mathew is also a freelance wind energy consultant and serves as a resource person to several International Training Programmes on Wind Energy.

Advances in Offshore Wind Resource Estimation

Charlotte Bay Hasager, Merete Bruun Badger, Alfredo Peña, Jake Badger, Ioannis Antoniou, Morten Nielsen, Poul Astrup, Mike Courtney and Torben Mikkelsen

Wind resource mapping is basically a meteorological time-series statistical analysis, to which the features of the landscape such as roughness, topography and local obstacles are integrated. The normal procedure is to use the WAsP program which is de facto standard for wind turbine siting [1, 2]. The basic principle of the program is to solve the atmospheric flow equation using the logarithmic wind profile law and then to include the effects of the terrain. The optimal situation is to have accurate, long-term wind and turbulence observations from the height in the atmospheric boundary layer at the site where a wind farm is envisioned. This information provides the basis for wind resource mapping, identifying extreme conditions and wind load on the turbines.

The current total capacity of offshore wind farms is around 3 GW and EWEA predicts an offshore capacity of 40 GW by year 2020 [3]. Thus the growth is fast and the unit size of wind turbines are increasing. Multi-MW turbines are being installed in offshore applications since year 2000. Turbines of 12 MW size are expected to be developed under the EU IP UPWIND project by 2013 [4] and the atmospheric conditions relevant for this turbine are investigated under the Danish project [5]. There is a need for observing and modeling offshore winds at very high heights for these Multi-MW turbines.

C. B. Hasager (✉) · M. B. Badger · A. Peña · J. Badger · M. Nielsen · P. Astrup ·
M. Courtney · T. Mikkelsen
Risø National Laboratory for Sustainable Energy, Wind Energy Division,
Risø DTU, VEA-118, P.O. Box 49, Frederiksborgvej 399, 4000 Roskilde, Denmark
e-mail: cbha@risoe.dtu.dk

I. Antoniou
Siemens Wind Power A/S, Lyngby, Denmark

S. Mathew and G. S. Philip (eds.), *Advances in Wind Energy Conversion Technology,* Environmental Science and Engineering,
DOI: 10.1007/978-3-540-88258-9_3,

The most significant development in offshore wind resource estimation is the application of new remote sensing observation technologies. So far these are not fully implemented, but are obviously relevant in future observational offshore programs. Reasons for the new trend on using remote sensing methods are the difficulty and cost of erecting and maintaining very tall meteorological masts under offshore conditions. Ground-based remote sensing provides observations at high levels in the atmosphere. Satellite remote sensing provides maps of ocean winds with high spatial detail.

In this Chapter, new developments that are of particular interest for the offshore wind energy segment are discussed. These include new observation methods and mesoscale modeling of wind resources. The remote sensing technologies like ground-based LiDAR (Light Detection And Ranging) and SoDAR (Sound Detection And Ranging) are described along with the satellite-based SAR (Synthetic Aperture Radar) and scatterometer observations.

1 Offshore Observations at High Levels

The major need for advanced techniques in offshore wind resource estimation is reliable wind observations at very high heights. Ground-based remote sensing techniques appear as promising replacement solution to tall offshore meteorological masts. The use of LiDAR and SoDAR for wind resource estimation at high heights are described in the following sections. A typical installation of LiDAR and SoDAR is shown in Fig. 1.

The ZephIR wind LiDAR consists of a coherent wave laser beam operating at 1.55 μm. It is an eye-safe wavelength. It measures the Doppler-shift of radiations scattered by aerosols in the air and it is assumed that these particles flow with the same velocity as the wind. The particles can be dust, water droplets, pollution, pollen or salt crystals. The LiDAR scans conically into the atmosphere at an angle of 30.6°

Fig. 1 The Zephir wind LiDAR in the centre of the image and the AQ500 SoDAR in the front right installed at the Horns Rev platform in 2006

from the azimuth. It is possible to select five scanning heights up to 200 m. The observation spectra are produced in the circular scanning pattern $\sim 50\ \mathrm{s}^{-1}$. Hence there are 50 points of observation per revolution and each revolution takes 1 s. The LiDAR is operated with 3 revolutions per scanning height. The resolution (scanning volume) varies as a function of observational height [6, 7].

The AQ500 SoDAR uses three parabolic dishes and three horns, tilted to the vertical at 15° and having an azimuth separation of 120°. It operates at 3100 Hz. Another type of SoDAR, the AV4000, is a phased array system and its antenna consists of 50 piezoelectric speakers. The array steers the sound beam in three directions, one vertical and two beams at a tilt angle of 17°, separated by an azimuth angle of 90°. It operates at 4,500 Hz. The backscattered sound measured by a SoDAR is a function of the scatter angle of return, the wave number, the ambient temperature, and the temperature and velocity structure functions. The observation resolution heights from SoDARs can be selected and in contrast to the LiDAR, the observational volume is constant at all heights. SoDARs can observe up to 300 m [6, 8, 9].

The LiDAR and SoDARs have been tested in several experiments. Recent results are reported here from the following three experimental campaigns: [6, 8–11].

1. Høvsøre (December 2006 to January 2007) at the National Danish Test Site for Large Wind Turbines at Høvsøre located near the coast of the North Sea (DK);
2. Horns Rev (May to October 2006) in the North Sea at the transformer platform at the Horns Rev offshore wind farm (DK);
3. Nysted (June to September 2005) in the Baltic Sea at the transformer platform at the Nysted offshore wind farm (DK).

1.1 Results from the Coastal Station at Høvsøre

The Høvsøre site is operated by Risø DTU and the site is characterized by installation of one 116 m and another 165 m tall meteorological masts, heavily equipped with meteorological instruments like cup and sonic anemometers, thermometers, etc. The landscape is flat and observations were collected 1.5 km inland from the North Sea. The site is ideal for comparison of instrument performance and inter-calibration. The main purpose of the test site is the power curve observation for new large wind turbines.

An example of observations from cup anemometer and LiDAR both observing at 116 m above ground are presented in Fig. 2. Rain-data have been omitted in the graph. The 10-min mean values are very well correlated with bias $\sim 0\ \mathrm{ms}^{-1}$ and slope $\sim 1\ \mathrm{ms}^{-1}$. The data availability was 99% during the observational period.

Only data from the prevailing wind sector (240–300°) are included to avoid influence from the mast itself, other masts and turbines.

In another experiment, LiDAR, SoDAR (AV4000) and cup anemometers were observing partly in parallel for the power curve of a wind turbine. The results are

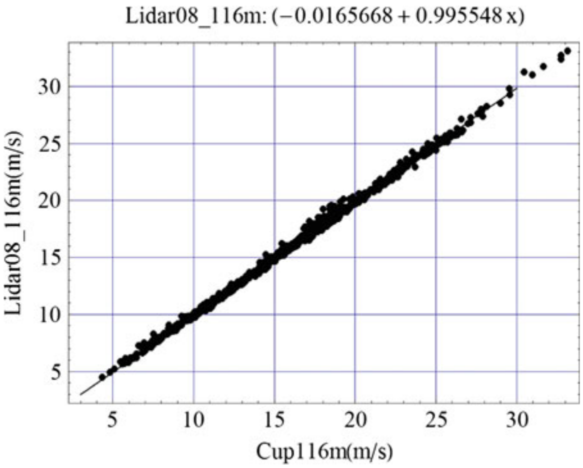

Fig. 2 Comparison of 10-minute mean wind speed observed by cup anemometer and LiDAR at 116 m above ground at Høvsøre, Denmark in December 2006 and January 2007 in the prevailing wind sector from 240 to 300°

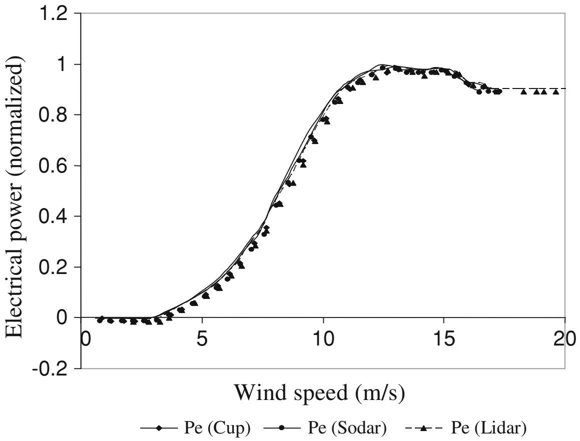

Fig. 3 The power curve, shown as a function of the wind speeds measured by cup anemometer, LiDAR and SoDAR (AV4000) [9]

presented in Fig. 3. The power curve is normalized and only observed for two different nominal power configurations. Hence the power curve is not truly representative of the specific wind turbine. The results indicate that remote sensing wind data can also be used for power performance. Further work in this direction is progressing [8].

1.2 Results from Offshore at Horns Rev

The Horns Rev site in the North Sea is characterized by the offshore distance to the nearest coastline of ∼12 km. At the site there are three well-equipped meteorological masts observing winds up to 70 m above mean sea level operated by DONG Energy. Both LiDAR and SoDAR (AQ500) were installed at the

Table 1 Comparison of 10-min wind speeds observed by cup anemometer at three masts and LiDAR

Name	Height (m)	Distance (km)	Slope (ms^{-1})	Bias (ms^{-1})	R^2	Data (#)
Mast 2	62	5.6	0.96	+0.15	0.97	4,236
Mast 6	60	3.4	0.99	+0.12	0.98	1,937
Mast 7	60	5.2	0.99	+0.15	0.97	3,264

LiDAR data at 63 m above mean sea level. The height of the mast observations, the distance between LiDAR and masts, and the linear regression results are listed. All data are from free stream conditions (no wake influence)

transformer platform, 20 m above mean sea level, in close cooperation with DONG Energy from May to October 2006. The Horns Rev wind farm with 80 wind turbines is in the vicinity. Therefore, at certain wind directions (135–270°), the influence of the wind turbines to the wind field (wake effect) is observed by the LiDAR and SoDAR [12].

Comparison between the results from LiDAR and cup anemometers at the nearby masts is reported in [12]. Summary of linear regression results between cup anemometers at three masts (called Mast 2, Mast 6 and Mast 7) and LiDAR are shown in Table 1. All the data are 10-min mean values observed ~60 m above mean sea level in the free stream sectors of all masts and LiDAR.

At Horns Rev, the LiDAR was mainly operated at four selected heights viz. 63, 91, 121 and 161 m above mean sea level. The lower level was chosen for comparison with the three meteorological masts (see above). The other heights were chosen to identify winds at higher levels. Figure 4 shows some of these results.

The profile observations are separated into two main groups, wind profiles from open-ocean, and wind profiles from land sectors, where the closest fetch is 12 km. The profiles are the averages of all 10-min profiles from the campaign in each sector. It is seen that strong winds are from the open-ocean sectors (westerly to north) while the fetch-influenced sectors have less wind (southeasterly to northeast).

At Horns Rev, the SoDAR AQ500 was observing winds in parallel with the LiDAR during the campaign. Results from LiDAR and SoDAR at three levels are compared in Table 2. All data are from the same free stream sectors, i.e. northwesterly sectors (no wake influence). The number of data decreases with height due to the increase of the signal to noise ratio in the SoDAR measurements. This is explained by the fixed echoes detected from the platform and the crane surrounding the SoDAR, and to the noise originating from the platform to scare birds away (that otherwise pollute the helipad next to the instruments; for safety reasons this pollution is avoided).

The differences in wind speed (Table 2) can be explained from the measuring volume: in the LiDAR, the conical scanning is done with an angle of ~30° with the azimuth, whereas the SoDAR does it with ~15°. Despite of the high flow homogeneity of offshore winds, the platform can influence the wind streamlines.

From both LiDAR and SoDAR, it is possible to observe the turbulence intensity [6, 11]. The (longitudinal) turbulence intensity is defined as the ratio between the

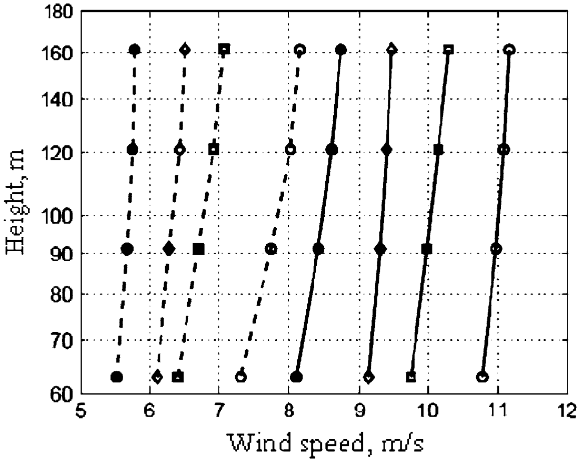

Fig. 4 Mean wind speed profiles from LiDAR measurements at heights: 63, 91, 121 and 161 m at the offshore transformer platform at Horns Rev. The solid lines correspond to profiles of open-sea sectors while the dash lines represent profiles corresponding to winds influenced by land. The open sea sectors (sectors 9–12 using WaSP sector classification) show higher winds than the land ones. The profile with less energy content corresponds to the sector where the land is closest to the platform

Table 2 Comparison of 10-min wind speed observed by LiDAR and SoDAR

LiDAR (m)	SoDAR (m)	Slope (ms^{-1})	Bias (ms^{-1})	R^2	Data (#)
91	95	0.89	+1.41	0.94	2,557
121	125	0.86	+1.02	0.93	863
161	155	0.83	+0.95	0.94	277

The height of the LiDAR and SoDAR observations and the linear regression results are listed. All data are from free stream conditions (no wake influence)

standard deviation of the wind speed longitudinal component and the longitudinal mean wind speed averaged over 10 min.

An example of turbulence intensity observed from LiDAR at four heights above mean sea level is presented in Fig. 5. The figure shows the turbulence intensity as a function of wind speed. It is known that LiDAR turbulence measurements are attenuated due to its measuring volume around 20% [11].

Nevertheless, from the LiDAR data, it is possible to follow the behavior of offshore turbulence with height, i.e. the result shows an increment on the turbulence intensity for high wind speeds due to an increasing sea roughness length. For higher heights, the wind speed needs to be higher in order to "feel" the ground and increase the turbulence levels. Comparison between LiDAR and cup anemometer observed turbulence intensities at the three masts at Horns Rev show good correspondence [11].

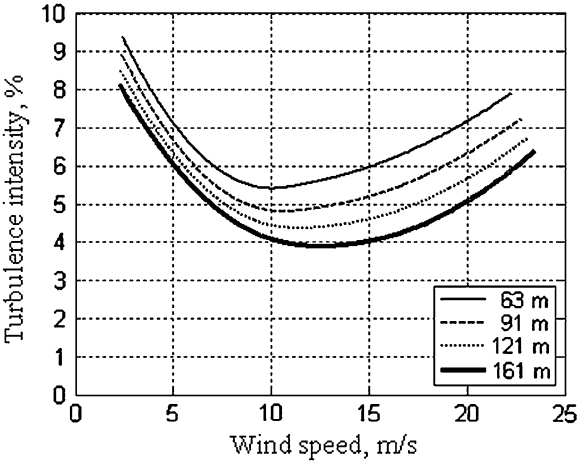

Fig. 5 Turbulence intensity from the longitudinal component of the wind speed measured by the LiDAR at different heights at Horns Rev as a function of wind speed. The lines show locally weighted smooth plots of the scatter data

Table 3 Comparison of 10-min wind speed observed by LiDAR and SoDARs AQ500 and AV4000 at 110 m above mean sea level

SoDAR (m)	Slope (ms^{-1})	Bias (ms^{-1})
AV4000	1.00	−0.15
AQ500	0.99	−0.02

The linear regression results are listed. All data are from free stream conditions (no wake influence) [6]

1.3 Results from Offshore at Nysted

The Nysted site is located in the Baltic Sea ~10 km south of the island Lolland. At the site the LiDAR and two SoDARs—AQ500 and AV4000—were installed on the transformer platform in close collaboration with E2. The instruments were mounted 20 m above mean sea level. The AV4000 observed at every 15 m up to 200 m range and the AQ500 observed at every 15 m up to 300 m range. Observations from five offshore masts belonging to E2, up to 69 m above mean sea level, were used for comparison. Comparison between the LiDAR and SoDARs observations are listed in Table 3 [6].

Selected wind profile results from SoDAR AQ500 are presented in Figs. 6 and 7. The data are binned into three wind speed levels (5–7; 7–9; 9–11 m/s) in the figure and only stable conditions are included from the northeasterly sector (10–70°). The selection is based on observations from the meteorological mast 3 at 69 m above sea level (MM3_69) [6]. The atmospheric profiles from 50 to 220 m above mean sea level in the figure show different behaviors. For high winds, the speed continuously increases with the height whereas for lower winds a maximum in wind speed is observed at 150 m (medium wind) and 100 m (low wind).

The offshore wind conditions in free stream are relevant in wind resource estimation. However, it is necessary to stress that the wake effects are also important [10, 12–15]. The turbulence intensity typically is lower in offshore than on land. Hence, the recovery of winds downstream of a wind farm may be slower.

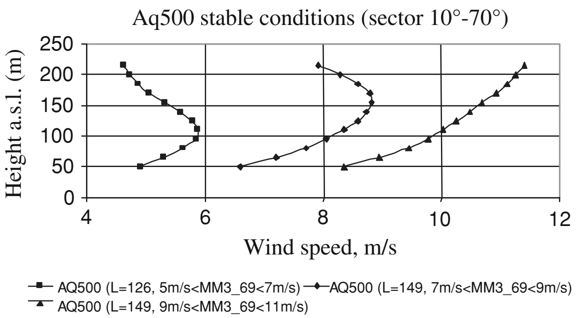

Fig. 6 Mean wind profiles observed with SoDAR AQ500 at Nysted. The selected data are binned into wind speed levels observed at meteorological mast (mast 3) for stable conditions and winds from the free stream sector 10–70° (no wake influence)

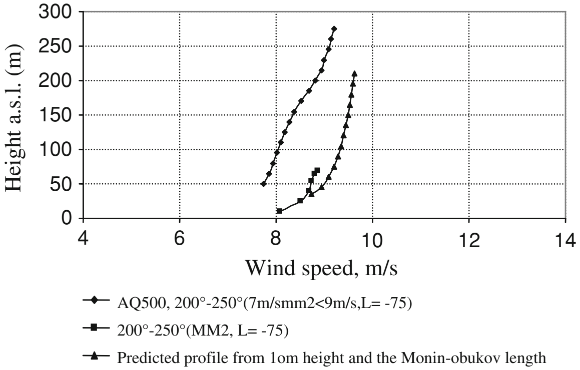

Fig. 7 Mean wake wind profile observed with SoDAR AQ500 at Nysted. The selected data are observed during conditions of 7–9 m/s at meteorological mast (mast 2) for unstable conditions and winds from 200 to 250°. The SoDAR is in the wake whereas mast 2 is in free stream. The mean free stream wind profile observed at mast 2 from 10 to 69 m above mean sea level and a hypothetical logarithmic profile at higher levels are included [8]

Wake effects have been investigated by cup anemometers at masts near Vindeby, Horns Rev and Nysted. Results from LiDAR and SoDAR provide new insights to wake behavior in offshore [6, 7, 10–12]. As an example, Fig. 7 shows offshore winds in the wake observed by SoDAR AQ500 at Nysted and it is compared to a logarithmic profile. It is the average wake profile for winds observed by the SoDAR when winds were between 7 and 9 m/s in the sector 200–250° at the meteorological mast 2 (MM2) and the atmospheric stratification was unstable. It is clear that a wake deficit (reduced mean wind speed) is found in the entire profile from 50 to 270 m above mean sea level.

2 Offshore Observations with Spatial Detail

Offshore winds can be observed from the space through Earth observing satellites. The satellites provide instantaneous maps of ocean wind conditions and hence spatial variations could be observed. The remote sensing techniques for ocean wind mapping from Synthetic Aperture Radar (SAR) and scatterometer are described in the following sections.

2.1 Ocean Winds from Synthetic Aperture Radar

Synthetic Aperture Radars (SAR) are active microwave sensors. The CMOD functions developed for scatterometer wind retrievals have been successfully applied to C-band SAR imagery too. A comprehensive overview on this is given in [16]. Advantages of SAR data include a high spatial resolution (around 1 km for derived wind products) and full coverage in near-shore areas. This makes SAR the most suitable satellite data type for offshore wind resource mapping. SAR data are not acquired routinely in the same manner as scatterometer data. Due to a narrower swath of SAR, a given point on the Earth surface is covered less frequently. This is a major disadvantage in terms of offshore wind resource mapping where the highest possible number of samples are required.

SAR measurements are obtained from a single look angle. As a consequence, several wind speed and direction pairs may correspond to a given backscatter coefficient (i.e. the radar backscatter per area). To select the appropriate wind speed, the wind direction must be known a *priori*. Wind directions may be obtained from in situ measurements [17–21] or atmospheric models interpolated in time and space to match the SAR data acquisition [22, 23]. Directions may also be retrieved with a 180° ambiguity from km-scale streaks found in most SAR images [24–26]. The streaks are aligned approximately with the wind direction and originate from atmospheric roll vortices impacting the sea surface. SAR winds have been retrieved to an accuracy of 1.1 m/s compared to high-quality in situ measurements from an offshore mast at Horns Rev, Denmark [27–29].

The environmental satellite Envisat, operated by the European Space Agency (ESA), has an advanced C-band SAR (ASAR). The mission is a follow-up on the successful ERS-1/2 missions. Another C-band SAR is flown on board the Canadian Radarsat-1/-2. Today, SAR imagery is generally available in near-real time from the data processing facilities and several software packages exist for operational SAR wind retrieval.

In the following, the APL/NOAA SAR Wind Retrieval System (ANSWRS) developed at the Johns Hopkins University, Applied Physics Laboratory will be used for demonstration [23]. The software uses, as default input, wind directions from the Navy Operational Global Atmospheric Predictions System (NOGAPS) on a 1° latitude/longitude grid. The wind directions are interpolated in time and space to match a given SAR data acquisition.

An example wind field over the Danish Seas (400 km by 500 km) is shown in Fig. 8. The wind map is based on Envisat data from 15 January 2007 at 20:54 UTC. Winds were blowing from the southwest—the prevailing wind direction

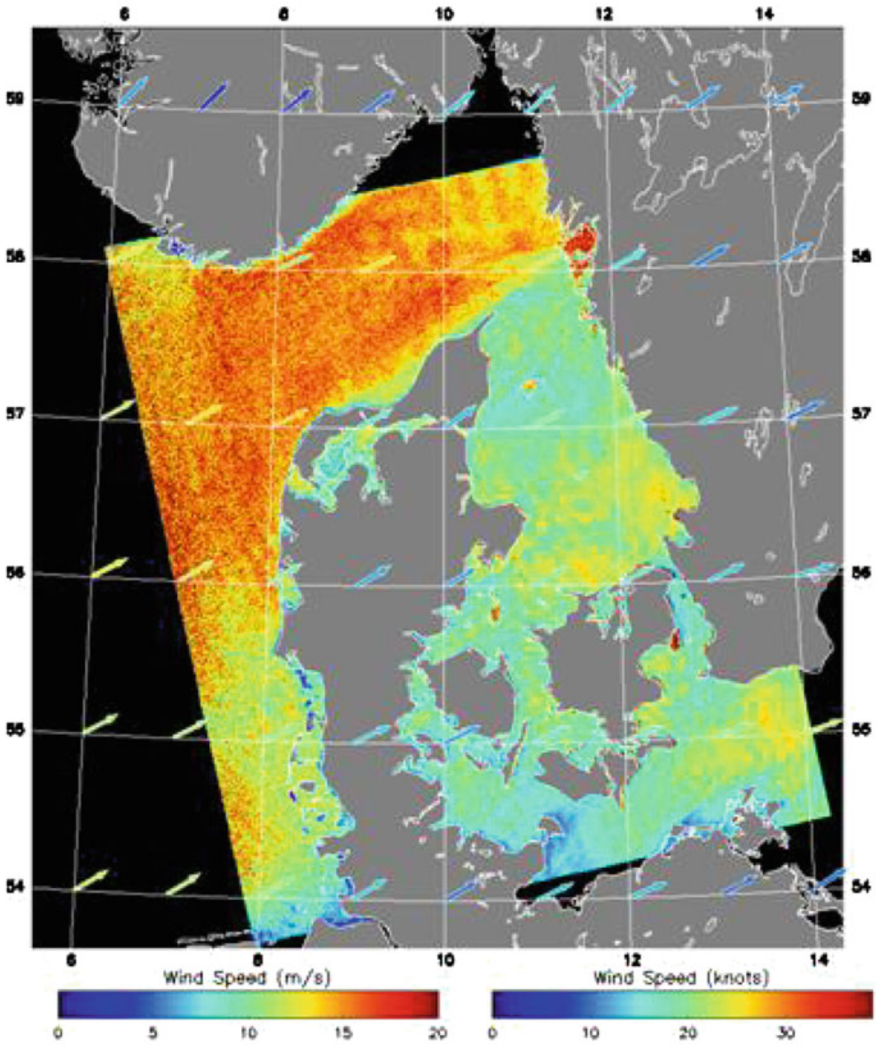

Fig. 8 Map showing winds over the Danish Seas retrieved from an Envisat ASAR image of 15 January 2007 at 20:54 UTC. Arrows indicate NOGAPS model wind speeds and directions

in Denmark. The map illustrates how the wind speed decreases from the North Sea (west) to the enclosed seas (east).

Figure 9 shows a wind map over the North Sea (400 km by 1,100 km). This map is based on Envisat ASAR data acquired on 24 February 2007 with winds from the south and southeast. A compression of the wind field is seen around the headland of Norway, which causes a significant increase of the wind speed. On the lee side of Norway, winds are much calmer. The calm zone extends up to 200 km offshore. Calm zones have also been identified downwind of existing offshore wind farms

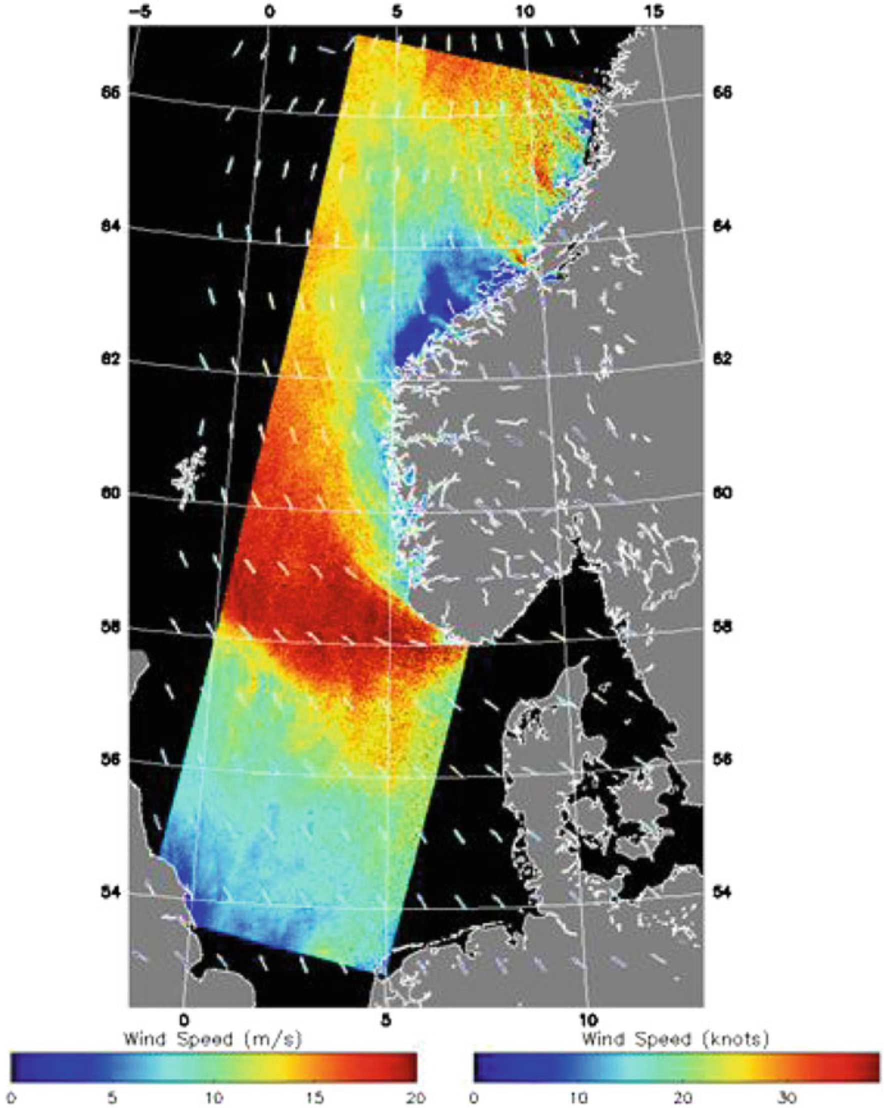

Fig. 9 Map showing winds over the North Sea retrieved from an Envisat ASAR image of 24 February 2007 at 10.09 UTC. Arrows indicate NOGAPS model wind speeds and directions

using airborne and satellite SAR data [28, 30]. SAR based wind maps over the two large wind farms Horns Rev and Nysted in Denmark have revealed that wind farm wake effects can extend as far as 20 km downwind [30]. State-of-the art wake models predict a maximum wake extend of 15 km [14]. Satellite observations have thus contributed to our understanding of the wind climate around existing offshore wind farms and other aerodynamic obstacles, e.g. islands or mountains.

Single satellite wind maps are valuable for understanding local wind speed variations at existing and potential wind farm sites. In addition, wind resource assessment studies may be performed using a series of satellite wind fields accordingly to assessments from on-site time series measurements.

Wind fields derived from SAR images need processing before statistical analysis. First step is to screen out areas with false data, e.g. from land surfaces, offshore constructions, tidal currents in shallow water, and surfaces affected by heavy rain or algae bloom. It is practical to transform the wind fields to a common frame of reference.

The boundary-layer response to new conditions is fast near the surface and delayed at elevated positions. Satellite observations reflect surface conditions so the wind estimate at turbine hub height relates to the signal upwind of the turbine position. The response function is known as the flux footprint and it is available from boundary-layer theory [31].

A positive side effect of spatial averaging is that it reduces speckle noise in the image. If the wind speed and direction do not vary much over the image, then the response function is uniform and the footprint averaging can be calculated efficiently by Fast Fourier Transformation. The pixel sizes in images from wide-swath SAR may be so large that footprint averaging becomes unnecessary.

Generally wind climates are described by the frequency of occurrence in a number of wind-direction sectors and a Weibull distribution of the wind speed in each of these. The directional distribution is needed to model the acceleration when the wind blows off the coast and to correct for effects of wakes from neighbour turbines.

Maximum-likelihood is the preferred method for fitting Weibull distributions to sparse data sets, as it has little bias and scatter [32]. The limited range of SAR calibration implies that, winds less than a certain threshold are not mapped. Simply to reject this information would be wrong, but fortunately maximum-likelihood has an extension which yields unbiased estimates for censored data sets [33]. The limited number of observations introduces uncertainty, and it may be necessary to simplify the statistical model, e.g. by setting the Weibull shape parameter equal in all wind direction sectors. Another approach would be to correlate SAR observations with wind data from a reference mast and use the correlation to correct long-term statistics from the reference station for systematic differences at offshore positions—a method known as measure-correlate-predict [34].

At Risø DTU, the described method has been developed to compute wind statistics such as the mean wind speed, the energy density (E), and the Weibull shape (k) and scale (a) parameters from satellite wind fields. The method has been tested at Horns Rev in the North Sea using 91 satellite samples [29]. The test showed very good agreement between energy densities computed from SAR ($E = 421$ W/m^2) and in situ data ($E = 422$ W/m^2). This was also true when 18 years of measurements from a nearby lightship were used for comparison ($E = 456$ W/m^2). Errors on the SAR-based energy density were related to uncertainties of the retrieved mean wind speeds. These uncertainties were, in turn, caused by erroneous wind directions and, presumably, by non-neutral stability, internal boundary layers from the land, and wake effects of the large offshore wind farm operating at Horns Rev.

A major advantage of using SAR in offshore wind resource assessment is that spatial variability of the statistical parameters may be identified within a given area of interest. A severe limitation of the method is the restricted number of available satellite samples. However, the amount of samples will increase as the SAR data archive continues to grow. Another limitation is that, satellite overpasses occur at fixed times of the day (i.e. one morning and one evening overpass) [35]. Diurnal variations in the wind climate are not taken into account but such variations are considerably smaller at offshore locations compared to land sites. Finally, SAR based wind fields are valid at the height 10 m, whereas wind turbines of today operate at much higher levels above the surface. To really make use of the SAR observations for wind energy planning, an interpolation to the turbine hub height is necessary.

In addition to the C-band SAR sensors described above, a new generation of SAR instruments has been launched with the Japanese L-band sensor ALOS PALSAR and the German X-band sensor TerraSAR-X. Work is ongoing to tune the current wind retrieval algorithms for both longer and shorter radar wavelengths. The new sensors may also provide information about other parameters relevant for wind engineering such as bathymetry and waves. Further, the combination of several radar frequencies is expected to improve wind retrieval algorithms through a separation of different contributors to the radar backscatter over a given area.

2.2 Ocean Winds from Scatterometer

Scatterometers are real aperture radars operating in the microwave spectrum. The American/Japanese scatterometer SeaWinds on-board the QuikSCAT satellite works at Ku-band. The scatterometer transmits pulses. The pulses are echoed back to the instrument and received. The normalized backscatter per resolution cell in slant range (across track) and ground range (along flight track) are the key information used for wind vector retrieval. Variations in the magnitude of the Normalized Radar Cross Section (NRCS) are functions of the centimeter-sized, wind-driven waves of the ocean surface. The geophysical model function relates the NRCS to the wind vector through empirical coefficients. The coefficients are found from collocated in situ wind data and NRCS values, or a combination of in situ wind data, meteorological model data and NRCS values [36]. QuikSCAT data are available from 19 July 1999 to November 2009. QuikSCAT ocean wind maps cover 90% of the globe twice daily (fewest observations near the Equator, more near the poles).

Two examples of QuikSCAT wind data used for offshore wind resource estimation are provided here. One example is from the Horns Rev site and the other is from Cape Verde. Hence the meteorological conditions are contrasting. Results are presented in Fig. 10. The wind climatology in Cape Verde is governed by the trade winds. These are nearly constantly blowing from the northeast. In contrast, the

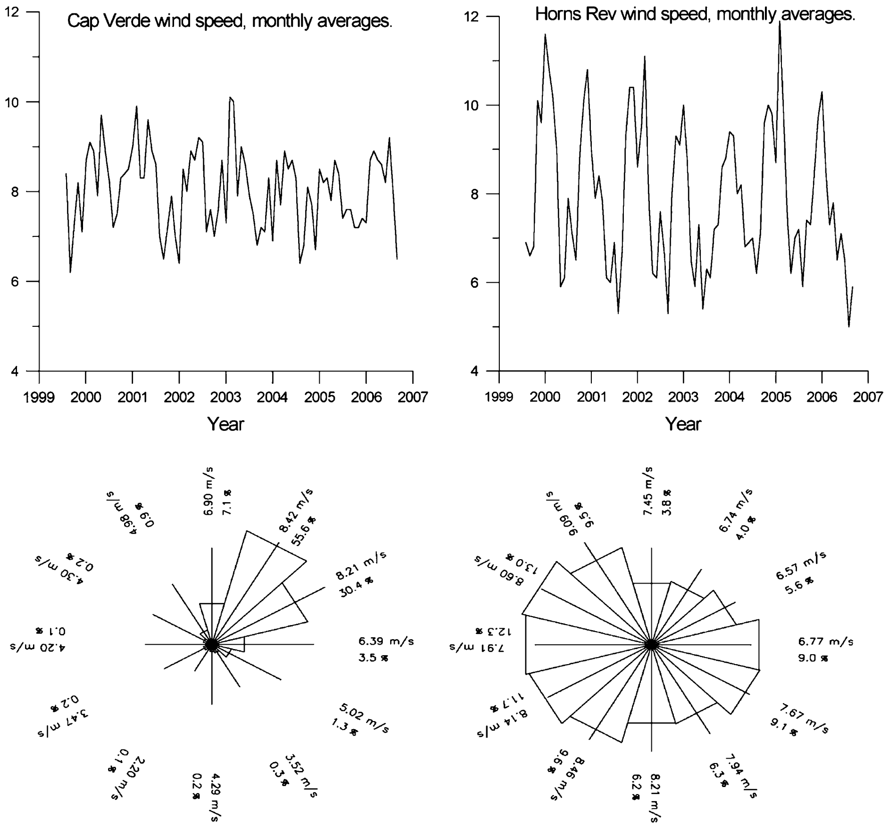

Fig. 10 Offshore mean wind statistics from Cape Verde at 334.25 E, 16.75 N (*left panels*) and Horns Rev at 7.75 E, 55.50 N, Denmark (*right panels*) observed from QuikSCAT from 7 years, twice daily, i.e. ~5,000 observations. The *upper panels* show monthly mean wind speed and the lower panels display the wind roses

wind climate in Denmark is characterized by synoptic frontal systems passing from different directions. The mean wind speed, Weibull scale and shape factors are calculated for Cape Verde as 8.04 m/s, 8.86 m/s and 4.57, respectively. For Horns Rev corresponding values are 7.95 m/s, 9.06 m/s and 2.0, based on the QuikSCAT observations.

2.3 Mesoscale Modeling for Offshore

The atmospheric flow over coastal regions is complicated. This is because the coastal region represents a transition of two distinct surface types, land and sea. For homogeneous surface condition, there is a much better understanding of, for example, the wind velocity profiles within the boundary layer, compared to profiles for the coastal regions. The distinction between the two surface types in the coastal region may be described using at least three different properties, namely surface aerodynamic roughness length, surface temperature, and surface elevation.

The surface aerodynamic roughness length describes a property that determines how, according to the logarithmic wind profile, the wind speed increases with increasing height above the surface. However, the logarithmic wind profile is only a good approximation for homogeneous roughness and neutral conditions. For a hypothetical simple coastal zone, where the only distinction between land and sea is the surface aerodynamic roughness length (i.e. flat, level, land at same temperature and approximate height temperature as sea), there will be a region where the wind profile will be in transition, where for upwind there is a combination of land and sea roughness lengths. This transition behavior is described by roughness induced internal boundary layer development [37].

Now, imagine a slightly more complicated coastal zone where land and sea have different temperatures, as well as different roughness. This new complication introduces a change in the surface heat flux into the atmosphere when air flows from land to sea or vice versa. The impact of the surface heat flux on surface profiles for homogeneous conditions is described by Monin–Obukhov similarity theory [38]. However, for heterogeneous conditions, the transition of the wind profile is less well understood. Refer [39], where the response of wind profile to abrupt changes in surface heat fluxes are described using analytical, numerical simulation and experimental methods.

The next complication to be introduced to the hypothetical coastal zone is heterogeneous surface elevation (orography) of the land surface. Orography has a large impact on the surface winds, not just at the location of the orographic feature itself (for instance, strong winds at a hill top), but also some distance from the feature. This is strongly related to the stability of the atmosphere. For more stably stratified conditions, flow tends to be steered more laterally around orography obstacles such as hills and mountains. The range at which the flow can be modified by orography can be in the order of hundreds of kilometers (Fig. 9). Therefore, onshore orography can impact the offshore wind properties. High orography along the coast can lead to flow damming, or the creation of barrier jets enhancing flow parallel to the coast. Where islands with high orography are present, the deflection of flow around the island can increase winds on the flanks of the island, including offshore areas. Similarly, flow can be enhanced in the gaps between islands. For examples of these phenomena as seen from SAR satellite imagery, see [40].

There are further distinctions that can be made between land and sea surfaces in a coastal region such as moisture fluxes that are not covered here. However, considering just dry processes between surface and atmosphere alone has created challenging problems to be addressed.

Mesoscale models can be used to model the wind flow in coastal regions and are able-to some extent-to model the influence of the heterogeneous surface aerodynamic roughness, surface heat fluxes, and orography [41, 42]. As an example of an offshore mesoscale study, a summary of an investigation for the Nysted Wind Farm in Denmark is discussed here. The objective was to determine the variation of wind conditions over the extent of the offshore wind farm. The wind farm is large and therefore, the horizontal gradient of wind speed found in coastal zones can have a greater impact. More details of the study can be found in [13].

The model used was Karlsruhe Atmospheric Mesoscale Model (KAMM) [43]. The model has been used extensively in wind energy applications, mostly in the calculation of numerical wind atlases in the KAMM/WAsP methodology [44, 45]. In this study KAMM was run with a uniform 2 km horizontal resolution in a domain of 200 × 200 km. In the vertical, 25 model levels using a terrain following coordinate were used from the surface to 5,500 m. The spacing between vertical levels is not uniform; levels close to the surface have the smallest interval.

The mesoscale requires a description of the surface elevation (orography), surface aerodynamic roughness, profiles of geostrophic wind speed, direction, and potential temperature. The orography for computational domain was derived from the Shuttle Radar Topography Mission (SRTM), dataset available for download at 30 arc second resolution. A similar gridded dataset is created for the surface roughness in the computation domain, derived from the Global Land Cover Classification (GLCC) dataset from the United States Geological Survey.

The atmospheric profiles were based on the means derived from NCEP/NCAR reanalysis temperature and geo-potential height gradient data determined for years 1965 to 1998 for the heights 0 m, 1,500 m, 3,000 m and 5,500 m above sea level. Based on the mean wind speeds at these heights, a set of 12 wind directions were used from 0° to 330° with a constant 30° interval, with no variation of direction with height.

In KAMM, the land and sea surface temperatures can be set by a constant offset relative to the lowest model level air temperature at initialization. In the first set of integrations (set A), the offset temperature was set to 0 K for both land and sea surfaces. That is to say that the surface temperature is set to the lowest model level air temperature at initialization everywhere in the domain. The surface temperatures do not change during the model integration.

In the second set of integrations (set B), the surface temperature offset relative to the lowest model level air temperature is +5 K for sea surfaces and −5 K for land surfaces. That is, the sea surface is warm and the land surface is cold. In the third set of integrations (set C) the surface temperature offset was −5 K for sea surfaces and +5 K for land surfaces, meaning a cold sea surface and a warm land surface.

Figure 11 shows the modeled winds at 70 m above surface level for the 150° wind forcing in case C (the cool sea, warm land configuration), next to a SAR image derived winds for a similar large-scale forcing situation. A similar spatial variation of the wind speed is seen in the modeled winds and those derived from the SAR image, especially in the streaky higher wind regions formed in the gaps between islands.

Figure 12 shows the winds at 70 m above surface level for the three surface configurations using the 60° wind forcing. It is from this direction that a large range of wind speeds are experienced over the wind farm extent.

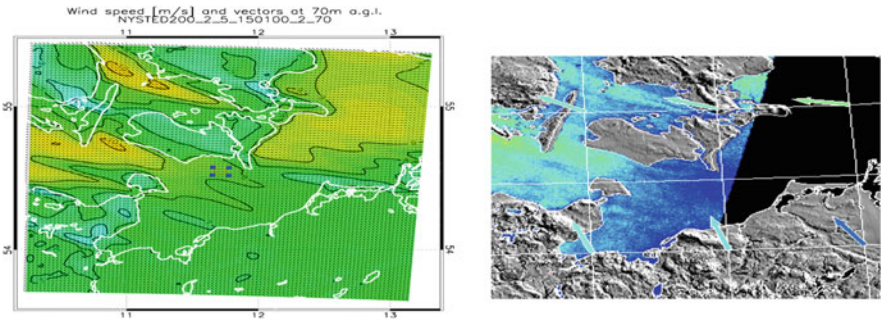

Fig. 11 Comparison of mesoscale model winds at 70 m above surface level using a large-scale wind forcing from 150 degree (*left*) and wind derived from a SAR image during similar large-scale wind conditions (*right*)

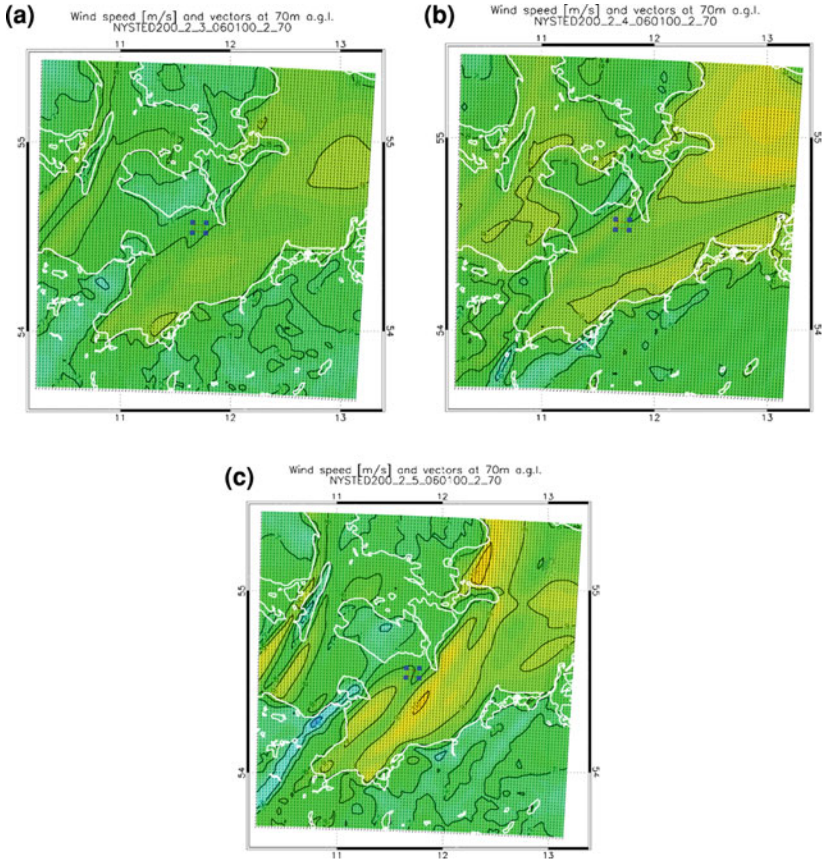

Fig. 12 The winds at 70 m above surface level for a large-scale forcing from 60 degrees, using three different surface temperature configurations: **a** configuration A: land and sea same temperature, **b** configuration B: warm sea, cool land, **c** configuration C: cool sea, warm land

It can also be seen that the wind field at 70 m above surface level is sensitive to the different surface temperature configurations. For the warm sea cases there is a tendency for the winds blowing offshore to increase speed over a shorter distance, and then remain rather uniform. For the cool sea cases, the tendency of the wind blowing offshore is to increase the speed over a longer distance and to create more elongated narrow jet features with higher wind.

This mesoscale study demonstrates the complexity of offshore winds and the sensitivity of the winds to the surface heat flux conditions that influence the stability of the boundary layer. This complexity and sensitivity can have impacts on the wind characteristics over the extent of wind farm site. Thus, mesoscale modeling provides a valuable tool for investigating the flow behavior in coastal regions.

3 Discussion and Conclusion

Offshore winds observed from meteorological masts are still used in offshore wind resource mapping. New approaches in offshore wind resource estimation using LiDAR, SoDAR, SAR and scatterometer are discussed in the above sections. The ability of each of these observing technologies to provide relevant information on offshore wind is also demonstrated.

LiDAR observations give good comparison with the wind measured using cup anemometers as demonstrated at the Høvsøre site (where the instruments were spaced with a few meters) and the offshore site (where the instruments were spaced at a few kilometers). Furthermore, very recent results at Høvsøre show that LiDAR is able to cope in conditions of frost and snow storm where cup anemometers were not working properly. LiDAR also have very high data availability, close to 100%.

SoDAR works well on land sites. When used in wind resource mapping, a short (e.g. 40 m) mast is used in combination with SoDAR for part of the observational period, for the calibration. A similar procedure could be used when it is used in offshore measurements. However, SoDAR may have less data availability under offshore conditions. Further, the reliability of these instruments may be affected by fixed echoes from structures, noise from bird, bird scaring devices, and transformers appeared. All of these may potentially be circumvented with ideal mounting.

Both LiDAR and SoDAR provide wind observations at much higher levels than any offshore meteorological mast (at present). Therefore the accuracy at the highest levels is impossible to verify from comparison to cup anemometers. As a consequence, the interesting wind and wake profiles observed from LiDAR and SoDAR are the state-of-the-art observations. At these heights, modeling results of winds and wakes are the only information available. But, as modeling of winds in the coastal zone and offshore wakes are challenging, no conclusions can be drawn. It is comforting that observations from LiDAR and SoDAR agree well in spite of some differences like in case of observational volumes.

Satellite-based ocean wind observations can provide spatial details. This is in contrast to vertical detail from ground-based LiDAR, SoDAR and meteorological masts. Satellite SAR and scatterometer observe the capillary and short gravity waves on the ocean formed instantaneous by wind interaction with the sea surface. The pattern of capillary waves is non-linearly proportional to ocean winds at 10 m above sea level. The relationship is found from empirical fitting, and the accuracy is $\sim 1.1\ \mathrm{ms}^{-1}$ rms error. This error is one order of magnitude larger than necessary in wind resource mapping. Therefore this type of information is relevant in pre-feasibility studies. One advantage is that the information is readily available; it is not necessary to wait for an year for the observations to be recorded as multi-year data are available in archives with global coverage. In satellite remote sensing there is a trade-off between frequent observation (twice daily) with low spatial resolution (25 km) and infrequent observations (some per month) with high spatial resolution (0.5–1 km) from scatterometer and SAR, respectively.

Mesoscale modeling of flow in the coastal zone is relevant in the case of non-sufficient offshore observations. In other words, wind climate modeling with microscale models in the coastal zone is possible only for short distances as the atmosphere is much affected by mountains, land roughness and thermal properties of land and sea. Satellite wind maps are valuable in evaluation of offshore mesoscale wind resource model results. Similarly offshore wind observations from LiDAR and SoDAR are valuable for evaluation of mesoscale model results at elevated heights within the atmospheric boundary layer.

Methods of offshore wind resource analysis using LiDAR and SoDAR mounted on the ground are highly promising as observations can be made at the relevant heights of the expected very large wind turbines. Further, the data quality and data availability are also high. Hence, it is realistic to use remote sensing in offshore wind resource mapping in the future. Satellite observations and mesoscale modeling provide spatial details. It is clear from both observations and model results that great spatial variability exists in the atmospheric boundary layer in the coastal zones. Further investigation is needed in this direction, yet the present results are very promising.

Acknowledgments Funding from the Danish Research Academy for the SAT-WIND project (Sagsnr. 2058-03-0006), SAT-WIND-SMV (Sagsnr. 2104-05-0084), 12 MW project (Sagsnr. 2104-05-0013), the Danish PSO project Large Wind Farms Shadow Effects (PSO F&U 4103), European Space Agency (ESA) EO-windfarm (contract 17736/03/I-IW) and the EU WISE project (NNE5-2201-297) are acknowledged. Cooperation with Paul B. Sørensen at DONG Energy (DK), Frank Monaldo and Don Thompson at Johns Hopkins University, Applied Physics Laboratory (USA) and Lars Boye Hansen at GRAS (DK) are acknowledged. Envisat ASAR images from ESA Cat. 1 EO-1356 and EO-3644 projects are acknowledged. KAMM is used with kind permission from Karlsruhe University, Germany. NCEP/NCAR reanalysis data were provided by the National Center for Environmental Prediction (NCEP), USA and the National Center for Atmospheric Research (NCAR), USA. SRTM data were provided by the National Geospatial-Intelligence Agency (NGA), USA and the National Aeronautics and Space Administration (NASA), USA. The GLCC dataset was provided by the United States Geological Survey (USGS).

References

1. Mortensen N, Heathfield DN, Landberg L, Rathmann O, Troen I, Petersen EL (2000) Wind Atlas Analysis and Wind Atlas Analysis and Application program:WAsP 7.0 Help Facility. ISBN 87-550-2667-2, Risø National Laboratory, Roskilde
2. Jimenez B, Durante F, Lange B, Kreutzer T, Tambke J (2007) Offshore wind resource assessment with WAsP and MM5: comparative study for the German Bight. Wind Energy 10 (2):121–134
3. http://www.ewea.org
4. http://www.ewea.org/?id=47
5. Hasager CB, Peña A, Mikkelsen T, Courtney M, Antoniou I, Gryning SE, Hansen P, Sørensen PB (2007) 12 MW Horns Rev Experiment. Risø-R-1506 (EN), Roskilde
6. Antoniou I, Jørgensen HE, Mikkelsen T, Frandsen S, Barthelmie R, Perstrup C, Hurtig M (2006) Offshore wind profile measurements from remote sensing instruments. European Wind Energy Conference and Exhibition 2007, Athens, Brussels: European Wind Energy Association
7. Peña A, Hasager CB, Gryning SE, Courtney M (2007) Offshore wind profiling using LiDAR measurements
8. Antoniou I, Jørgensen HE, Mikkelsen T, Pedersen TF, Warmbier G, Smith D (2004) Comparison of wind speed and power curve measurements using a cup anemometer, a LIDAR and a SODAR. European Wind Energy Conference and Exhibition, London (GB) 2004, Brussels: European Wind Energy Association, pp. 47–51
9. Antoniou I, Jørgensen HE, Bradley SG, Hunerbein SV, Cutler N, Kindler D, Noord M, Warmbier G (2004) The Profiler Intercomparison Experiment (PIE). European Wind Energy Conference and Exhibition, London (GB) 2004, Brussels: European Wind Energy Association pp. 1–7
10. Barthelmie R, Pryor S (2006) Challenges in predicting power output from offshore wind. J.Energy Eng. 132:91–103
11. Jørgensen HE, Mikkelsen T, Mann J, Bryce D, Coffey A, Harris M, Smith D (2004) Site wind field determination using a CW Doppler LIDAR - comparison with cup anemometers at Risø. Special Topic Conference. The science of making torque from wind, Delft (NL), 2004, Brussels: European Wind energy Association, pp. 261–266
12. Frandsen S, Barthelmie R, Pryor S, Rathmann O, Larsen S, Højstrup J, Thøgersen M (2006) Analytical modelling of wind speed deficit in large offshore wind forms. Wind Energy 9: 39–53
13. Badger J, Barthelmie R, Frandsen S, Christiansen MB (2006) Mesoscale modelling for an offshore wind farm. European Wind Energy Conference and Exhibition. European Wind Energy Association, Athens Brussels, pp. 1–6
14. Barthelmie RJ, Pryor SC, Frandsen S, Larsen S (2004) Analytical and empirical modelling of flow downwind of large wind farm clusters. The science of making torque from wind, Delft: pp. 292–303
15. Barthelmie R, Folkerts L, Larsen SE, Rados K, Pryor S, Frandsen S, Lange B, Schepers G (2006) Comparison of wake model simulations with offshore wind turbine wake profiles measured by sodar. J.Atmos.Ocean.Technol. 23:888–901
16. Monaldo F, Kerbaol V, Clemente-Colón P, Furevik B, Horstmann J, Johannessen J, Li X, Pichel W, Sikora TD, Thomson DJ, Wackerman C (2003) The SAR measurement of ocean surface winds:an overview. Proceedings of the Second Workshop Coastal and Marine Applications of SAR, Svalbard, Norway, ESA: pp. 15–32
17. Hasager CB, Dellwik E, Nielsen M, Furevik B (2004) Validation of ERS-2 SAR offshore wind-speed maps in the North Sea. International Journal of Remote Sensing 25 (19):3817–41
18. Hasager CB, Nielsen M, Astrup P, Barthelmie RJ, Dellwik E, Jensen NO, Jørgensen BH, Pryor SC, Rathmann O, Furevik B (2005) Offshore wind resource estimation from satellite SAR wind field maps. Wind Energy 8:403–19

19. Hasager CB, Barthelmie RJ, Christiansen MB, Nielsen M, Pryor SC (2006). Quantifying offshore wind resources from satellite wind maps: study area the North Sea. Wind Energy 9:63–74
20. Hasager CB, Astrup P, Nielsen M, Barthelmie RJ, Christiansen MB, Pryor SC, Nielsen P, Sørensen PB (2005). SAT-WIND project. First yearly report. Risø National Laboratory, Roskilde, Denmark
21. Monaldo F, Thompson DR, Pichel W, Clemente-Colón P (2004) A systematic comparison of QuickSCAT and SAR ocean surface wind speeds. IEEE Transactions on Geoscience and Remote Sensing 42 (2):283–91
22. Monaldo FM, Thompson DR, Beal RC, Pichel WG, Clemente-Colón P (2001). Comparison of SAR-derived wind speed with model predictions and ocean byou measurements. IEEE Transactions on Geoscience and Remote Sensing 39:2587–600
23. Monaldo F (2000) The Alaska SAR demonstration and near-real-time synthetic aperture radar winds. John Hopkins APL Technical Digest 21:75–79
24. Du Y, Vachon PW, Wolfe J (2002) Wind direction estimation from SAR images of the ocean using wavelet analysis. Canadian Journal of Remote Sensing 28 (3):498–509
25. Fichaux N, Ranchin T (2002) Combined extraction of high spatial resolution wind speed and direction from SAR images: a new approach using wavelet transform. Canadian Journal of Remote Sensing 28 (3):510–16
26. Koch W (2004) Directional analysis of SAR images aiming at wind direction. IEEE Transactions on Geoscience and Remote Sensing 42 (4):702–10
27. Christiansen MB, Hasager CB, Monaldo F (2006) Offshore winds observed from space. Issues for planning of offshore wind farms. WindTech Int. 2 (5):6–9
28. Christiansen MB, Hasager CB (2006) Using airborne and satellite SAR for wake mapping offshore. Wind Energy 9:437–55
29. Christiansen MB, Koch W, Horstmann J, Hasager CB (2006) Wind resource assessment from C-band SAR." Remote Sensing of Environment 105:68–81
30. Christiansen MB, Hasager CB (2005) Wake effects of large offshore wind farms identified from satellite SAR. Remote Sensing of Environment 98:251–68
31. Gash JHC (1986) A note on estimating the effect of a limited fetch on micrometeorological evaporation measurements. Boundary-Layer Meteorology 35:409–13
32. Pryor SC, Nielsen M, Barthelmie RJ,.Mann J (2004) Can satellite sampling of offshore wind speeds realistically represent wind speed distributions? Part II Quantifying uncertainties associated with sampling strategy and distribution fitting methods. Journal of Applied Meteorology 43:739–50
33. Cohen AC (1965) Maximum-likelihood estimation in the Weibull distribution based on complete and on censored samples. Technometrics 6:579–88
34. Rodgers AL, Rodgers JW, Manwell JF (2005) Comparison of the performance of four measure-correlate-predict algorithms. Journal of Wind Engineering and Industrial Aerodynamics 93:243–64
35. Barthelmie RJ, Pryor SC (2003) Can satellite sampling of offshore wind speeds realistically represent wind speed distributions. Journal of Applied Meteorology 42 (1):83–94
36. Stoffelen A, Anderson DLT (1997) Scatterometer data interpretation: Estimation and validation of the transfer fuction CMOD4. Journal of Geophysical Research 102 (C3):5767–5780
37. Sempreviva AM, Larsen SE, Mortensen NG, and Troen I (1990) Response of Neutral Boundary-Layers to Changes of Roughness. Boundary-Layer Meteorology 50 (1-4):205–225
38. Dyer A (1974) A review of flux-profile relationships. Boundary-Layer Meteorology. Boundary-Layer Meteorology 7:363–72
39. Owinoh AZ, Hunt JCR, Orr A, Clark PKR, Fernando HJS, Nieuwstadt FTM (2005). Effects of changing surface heat flux on atmospheric boundary-layer flow over flat terrain. Boundary-Layer Meteorology 116:331–361
40. Beal B, Young GS, Monaldo F, Thompson DR, Winstead NS, Scott C (2004) High Resolution Wind Monitoring with Wide Swath SAR: A User's Guide

41. Smedman A, Högström U, Bergstrom H Low level jets – a decisive factor for offshore wind energy siting in the Baltic Sea. Wind Engineering 20:137–147
42. Bergstrom H (2001). Boundary-Layer Modelling for Wind Climate Estimates. Boundary-Layer Meteorology 25:289–299
43. Adrian G, Fiedler F (1991). Simulation of unstationary wind and temperature fields over complex terrain and comparison with observations. Beitrage Physical Atmosphere 64:27–48
44. Frank H P, Landberg L (1997) Modelling the wind climate of Ireland. Boundary-Layer Meteorology 85:359–378
45. Mortensen N G, Hansen J C, Badger J, Jørgensen B H, Hasager C B, Georgy Youssef L, Said U, Abd El-Salam A, Akmal Mahmoud M, El Sayed Yousef A, Mahmoud Awad A,.Amd-El Raheem Ahmed M, Sayed M A M, Hussein Korany M, Adb-El Baky Tarad M (2005). Wind Atlas for Egypt, Measurements and Modelling 1991–2005. New and Renewable Energy Authority, Egyptian Meteorological Authority and Risø National Laboratory.

Author Biography

Dr. Charlotte Bay Hasager is a senior scientist at the Wind Energy Division, Risø National Laboratory for Sustainable Energy, Technical University of Denmark, Roskilde, Denmark. Dr. Hasager received M.Sc. and Ph.D. from University of Copenhagen, Institute of Geography in 1992 and 1996 respectively. Her area of specialization is satellite remote sensing, micrometeorology, turbulence and wind energy—in particular offshore and wind at high levels. Dr. Hasager has been employed at Risø since 1993 and was a visiting scholar at Department of Meteorology, Pennsylvania State University, USA in 1995. She has been involved in the international projects EU-Norsewind, EU-WEMSAR, EU-WATERMED, EU-MEAD and ESA EOMD EO-Windfarm. Dr. Hasager is the PI of the national projects SAT-MAP-CLIMATE, SAR-WAKE, SAT-WIND, 12MW, Satellite Eye for Galathea 3 and VirtuelGalathea3. She has been elected as the president of the Atmospheric Sciences Division at the European Geosciences Union 2007–2011, Co-Chair for Wind Energy Community of Practice (WECP) at the Global Earth Observation (GEOSS) 2005 and the member of the steering committee of the Danish Space Consortium 2003–2010. She has more than 200 publications in this area.

Short Term Forecast of Wind Power

Henrik Aalborg Nielsen

With the fast growth of wind energy worldwide, owners and operators of wind farms, transmission system operators, and energy traders need reliable forecasts of wind energy production covering some horizon into the future. The length of the horizon depends on the type of decisions which need to be taken on the basis of the forecast. Typically, focus has been on horizons from 12 to 36 h, at least when the production is traded on a day ahead market. However, other horizons are also relevant. For example, horizons up to 1 week are relevant for unit commitment. Shorter horizons, down to hours or minutes, are also relevant for wind farm operation.

Often wind power is dispatched when available. From a simple economics point of view this makes sense because, when available, the marginal production cost of wind power is very low, if not zero. However, this point of view may be somewhat naive. For example, consider the case where an unexpected high wind power production will require conventional plants to be shut down. Since these cannot be restarted instantly, such a decision may prove economically sub-optimal and it might have been better to limit the actual production from the wind turbines. Other cases where limiting the production may be required or beneficial are in case of limited capacity of the grid or when using the wind turbines as regulating power. However, the market and the energy tax structure should encourage that wind power is dispatched when available. It is better to use the electricity for heating or cooling than to limit the wind energy production. Technically, this requires that the end users are able to react on on-line price signals.

In this chapter various aspects of wind power forecasting are addressed. When building or selecting a forecast system, the data available for the system must be

---

H. A. Nielsen (✉)
Department of Informatics and Mathematical Modelling, Technical University of Denmark, 2800 Kongens, Lyngby, Denmark
e-mail: han@enfor.dk

S. Mathew and G. S. Philip (eds.), *Advances in Wind Energy Conversion Technology,* Environmental Science and Engineering,
DOI: 10.1007/978-3-540-88258-9_4,

specified. For very short-term forecasting *persistence*, where the future is forecasted as the latest power production, might perform quite well. However, on-line measurements of the wind power production may not be available, and in this case the simple predictor mentioned is not realizable in practice. Other types of data includes (i) other on-line measurements of, e.g. wind speed, (ii) meteorological forecast data, (iii) physical site data, and (iv) data used for up-scaling. Throughout this chapter, the type of data required by the methods mentioned will be described. It is noted that, if the production of a wind farm is limited during some periods, it is important to have access to not only the actual production but also (and more importantly) to the potential production.

The chapter starts by introducing various types of forecast. Hereafter, various models producing point forecasts are described which is followed by some probabilistic forecast models. Finally, up-scaling of forecasts and evaluation of forecast quality are considered. Generally, the number of references mentioned throughout the chapter is limited and instead the chapter ends with some bibliographical notes.

1 Types of Forecasts

The traditional notion of a forecast is a single value, representing the expectation, e.g. for each hour within the horizon. Here, such a forecast will be termed a point forecast. Usually, a point forecast is supplemented with error bands based on the

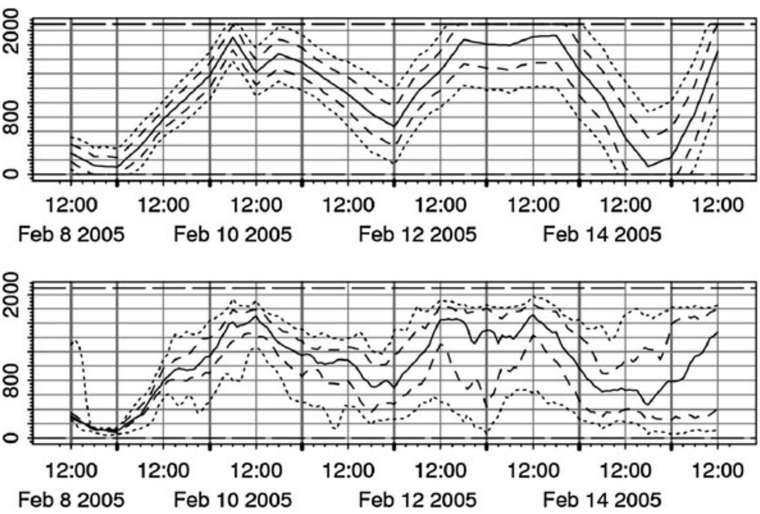

Fig. 1 Point forecast (*top*, *full line*) with error bands found using the observed standard deviation of the forecast errors and probabilistic forecast (*bottom*) represented by 10% (*dotted*), 25% (*dashed*), 50% (*full*), 75% (*dashed*), and 90% (*dotted*) quantiles. The error bands represent the central 50 and 80%

standard deviation of the forecast error and an assumed Gaussian distribution of the forecast error. When the error bands exceed the possible values, they are simply truncated. Instead of a single value for each time point in the future, probabilistic forecasts, in principle, contain the conditional distribution of wind power production for each time point within the horizon. The distribution is represented by a set of quantiles.

Figure 1 shows examples of a point forecast with error bands and a probabilistic forecast, represented by a few quantiles. While the error bands of the point forecast are based solely on an observed standard deviation of historical forecast errors, the probabilistic forecast aims at modeling the full distribution conditional on the information available at forecast time. While the certainty by which the future wind power production can be forecasted depends upon the horizon, it may also depend on the overall meteorological situation. This implies that, for a specific forecast, it cannot be assumed that, e.g. the distance between 25 and 75% quantiles will increase with the horizon. Also, given the horizon, the distance mentioned may change markedly over forecast time points.

While a probabilistic forecast includes much more information about the future than a point forecast, the probabilistic forecast by no means contains all relevant information. In order to construct possible scenarios of future wind power production, the auto-correlation of the data must be respected. This implies that independent samples from each of the conditional distributions will not produce realistic scenarios.

Figure 2 shows ten future scenarios for the case where the correlation is appropriately modeled and ten scenarios generated using independent sampling.

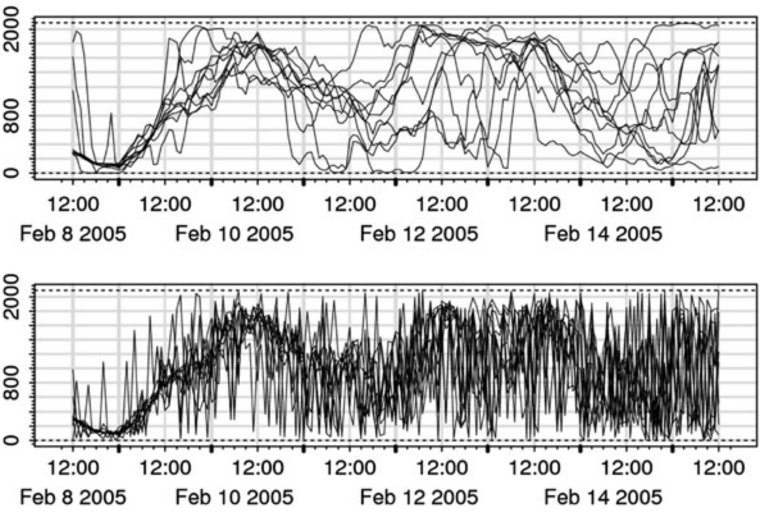

Fig. 2 Ten simulations corresponding to the probabilistic forecast in Fig. 1 respecting the correlation observed in the data (*top*) and ten simulations for which independent sampling is used (*bottom*)

The difference is evident, but the question remains if this should affect the decisions taken by the users of the forecasts. If any kind of storage is available, it is evident that the correlation will be important. This is also true when planning unit commitment. As opposed to that, when only trading on a day-ahead market and for each hour separately, the correlation will not be important in the long run, but the day-to-day risk will be influenced by the correlation.

2 Point Forecast Models

Given the current time *t,* point forecast models supply a single value for each time step in the near future $t + k$; $k = 1, 2, \ldots, K$. Denote the future power production by p_{t+k}, the point forecast of this value is denoted by

$$\hat{p}_{t+k|t} \tag{1}$$

The corresponding prediction error is defined as

$$e_{t+k|t} = p_{t+k} - \hat{p}_{t+k|t} \tag{2}$$

and can be observed at time $t + k$. The point forecast should have low bias and variance, i.e. the mean and variance of the random variable should be low. To summarize both bias and variance as a single quantity, the second moment, i.e. $E[e^2_{t+k|t}]$, is often used. Note that the measures of performance have to be estimated on the basis of a test period. This is discussed in a separate section later in this chapter.

2.1 Models Based on Measurements of Power Production Only

Models based solely on measurements of power production will produce a forecast based on the observed power productions available at forecast time. Consequently, on-line measurements are essential for these types of models.

In very general terms the *k*-step forecast produced at time t can be formulated as

$$\hat{p}_{t+k|t} = f_t(t + k, p_t, p_{t-1}, p_{t-2}, \ldots) \tag{3}$$

where the function f_t, in most cases, must be estimated from data. The time index t indicates that the function may change over time and in this case the estimation procedure should reflect this, i.e. the estimates should be time-adaptive.

2.1.1 Simple Forecast Models

The simplest example of the above case is *persistence*, which forecasts the future as the most recent observation. In this case no estimation is involved in the procedure:

$$\hat{p}_{t+k|t} = p_t \tag{4}$$

If the time series representing the wind power production has a high positive autocorrelation in lag k then Eq. 4 will perform well.

However when the autocorrelation for the horizon considered is low, the performance of Eq. 4 is poor. This can be illustrated by the case where p_t and p_{t+k} are independent. In this case, the second moment (and the variance) of the prediction error equals twice the variance σ_p^2 of the time series of wind power production measurements. In contrast to the predictor just mentioned, predicting p_{t+k} as the mean of the time series results in $E[e_{t+k|t}^2] = \sigma_p^2$ for all horizons. These observations have led to the suggestion of a simple forecast which mixes the two forecasts considered above in an optimal way. The forecast is defined as

$$\hat{p}_{t+k|t} = a_k p_t + (1 - a_k)\mu \tag{5}$$

where μ is the mean wind power production estimated as the average of all historical measurements available at time t, and a_k is the estimated autocorrelation in lag k based on observations available at time t, i.e.

$$a_k = \frac{\sum_{s=1}^{t-k}(p_s - \mu)(p_{s+k} - \mu)}{\sum_{s=1}^{t}(p_s - \mu)^2} \tag{6}$$

2.1.2 Recursive and Adaptive Estimation

The forecast model consisting of Eqs. 5 and 6 uses estimates of the mean of the series and of the autocorrelation corresponding to the horizon considered, in order to produce the forecast. In general, it is beneficial to consider the model structure and estimation of model parameters separately. As an example, Eq. 5 can be formulated as

$$\hat{p}_{t+k|t} = \phi_k p_t + \mu_k \tag{7}$$

and the coefficients (ϕ_k and μ_k) of the model can be estimated by minimizing the criterion

$$\sum_{s=1}^{t-k}(p_{s+k} - \hat{p}_{s+k|s})^2 = \sum_{s=1}^{t-k}(p_{s+k} - \phi_k p_s - \mu_k)^2 \tag{8}$$

i.e. the sum of squared prediction errors using the data available at time t. Since the model in Eq. 7 is linear in the parameters, the values of ϕ_k and μ_k which minimize Eq. 8 can be obtained by linear regression, treating p_s as the independent variable and p_{s+k} as the dependent variable.

In real operation, the forecast system will receive new information with a prespecified sampling interval, e.g. hourly. In order to utilize all information optimally, the estimates should be recalculated when new information arrives. The Recursive Least Squares (RLS) algorithm provides an efficient update of the estimates valid at time $t - 1$ to the estimates valid at time t:

$$\hat{\theta}_t = \hat{\theta}_{t-1} + R_t^{-1} x_t \left(y_t - x_t' \hat{\theta}_{t-1} \right) \tag{9}$$

$$R_t = R_{t-1} + x_t x_t' \tag{10}$$

The algorithm is initialized by setting all elements of R to zero and not calculating the estimates until R is invertible. Above, the algorithm has been formulated for the general regression case:

$$y_t = x_t' \theta + e_t \tag{11}$$

where y_t is the dependent variable, x_t is a vector of explanatory variables, θ is a vector containing the coefficients of the model, and e_t is the noise term. To implement Eq. 7, $y_t = p_t$, $x_t = [1 \; p_{t-k}]'$, $\hat{\theta}_t = [\hat{\mu}_{k,t} \; \hat{\phi}_{k,t}]'$ can be used.

Often, improved performance can be obtained by forgetting old data. Possible reasons include (i) wear and tear of the turbines, (ii) seasonal variations in the mean and autocorrelation of the wind power production data, (iii) changes in the surroundings of the wind farm, and, for regional forecasting, (iv) changes in the number and type of wind turbines installed. Old data can be forgotten by a small modification of the RLS-algorithm, in that only Eq. 10 must be changed to

$$R_t = \lambda R_{t-1} + x_t x_t' \tag{12}$$

where $0 < \lambda < 1$ is called the forgetting factor and controls the speed by which old information is disregarded. At time t the resulting estimates minimize the exponentially weighted least squares criterion, i.e.

$$\sum_{s=1}^{t-k} \lambda^{t-k-s} \left(p_{s+k} - \hat{p}_{s+k|s} \right)^2 \tag{13}$$

from which it is seen that starting with the most recent observation the sequence of weights is 1, λ, λ^2, λ^3, λ^4, …

2.1.3 Other Model Structures

The model represented by Eq. 7 does not include a term representing the diurnal variation. It is however easy to extend the model by replacing the overall mean with a mean for every hour of the day. Formally, such a model can be written

$$\hat{p}_{t+k|t} = \mu_{k,[t+k]} + a_k p_t \tag{14}$$

where $[t + k]$ is the time of the day, as a full hour, for the running time $t + k$ and $\mu_{k,[t+k]}$ is an offset adjusting for the diurnal variation.

To implement this model in the RLS-algorithm, a number of indicator variables must be defined. Let $I()$ be the indicator function returning 1 if its argument is true and 0 otherwise. For every full hour of the day $h = 0, 1, 2, \ldots, 23$, an indicator variable $z_{h,t} = I([t] = h)$ is defined and the vector x_t in the RLS algorithm is then defined as

$$x_t = \left[z_{0,t}\ z_{1,t}\ \ldots\ z_{23,t}\ p_{t-k}\right]' \tag{15}$$

Using the exponentially weighted criterion, this procedure will track the average diurnal variation over time. To obtain a fast response on the most recent diurnal variation the model

$$\hat{p}_{t+k|t} = a_k p_t + a_d p_{t+k-24} \tag{16}$$

can be used, if hourly data is considered and if the horizon k is less than 24 h. The coefficients a_k and a_d can be estimated as described above.

2.2 *Models Based on Physical Relations*

Models based on physical relations basically consider the task of forecasting wind power production from a deductive point of view. The forecasts are based on meteorological forecasts, wind farm layout, and the physical characteristics of the wind turbines.

The meteorological forecasts are produced using Numerical Weather Prediction (NWP) models, the details of which are far beyond the scope of this text. The NWP models are run by metrological offices and the forecasts are obtained electronically; typically via the Internet. Depending on the domain of the NWP model, the grid size can be approximately 100 km for a global model down to approximately 5 km, or even less, for a high resolution model with limited domain, but still covering several thousand kilometers. The meteorological office will typically offer forecasts for the actual site of the wind farm, but these are usually produced using a relatively simple interpolation scheme. Also, the NWP models operate with a number of vertical layers, which are defined by pressure levels. Therefore, the wind speed at hub height is usually not directly obtainable.

For the reasons mentioned above, wind power forecasting techniques based on physical modeling start by correcting the meteorological forecast to take local and height effects into account. This can be done using Meso-scale models or less computationally demanding models applying a direction-dependent correction for height, roughness, and orography. The resulting output is the wind speed at a certain location and height, but assuming that the wind farm has not been established. Following this, the layout of the wind farm and the power and C_t curves of the turbines are used to calculate the actual production of the individual turbines.

As examples, Fig. 3 shows the power and C_t curves for a Vestas V44 turbine and Fig. 4 shows the wind speed and power production as function of NWP speed and direction forecasts for a wind farm in Denmark. It is notable that given the forecasted wind direction, the farm wind speed is proportional to the forecasted wind speed.

2.3 Models Applying Both Measurements and Physical Information

The physical modeling approach outlined in the previous section requires detailed information regarding the wind farm and the surroundings. Inaccuracies in this information, together with seasonal variations and, e.g., wear and tear of the turbines suggest that, prediction performance can often be improved using measurements of wind speed and/or power.

One approach is to use a procedure called Model Output Statistics (MOS) which corrects for bias by postulating a linear relationship between the forecasted output from the physical model $\hat{p}_{\text{phys}}$ and the expected wind power production $\hat{p}$

$$\hat{p} = \beta_0 + \beta_1 \hat{p}_{\text{phys}} \tag{17}$$

where coefficients β_0 and β_1 are estimated from data using the least squares criterion. To track changes in the coefficients the RLS-algorithm with exponential forgetting can be applied.

Fig. 3 Power (*full*) and C_t (*dotted*) curves of a Vestas V44 turbine. The curves are valid for an air density of 1.225 kg/m^3

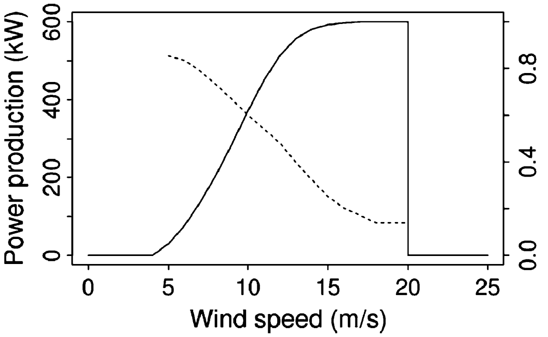

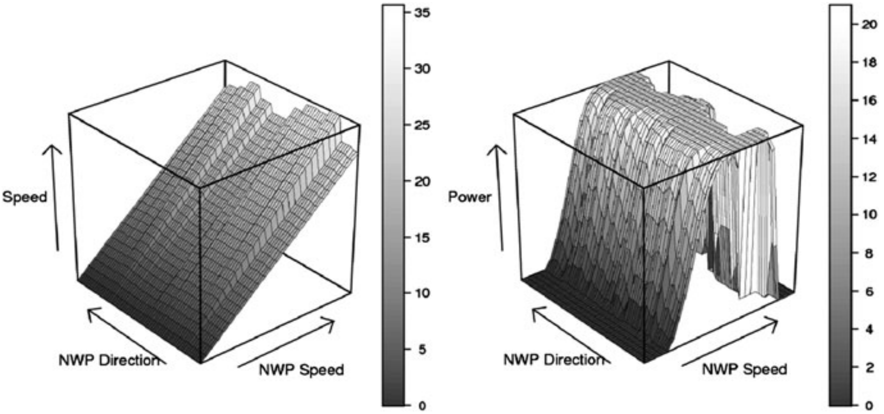

Fig. 4 Farm wind speed (*left*) and farm power (*right*) curve as derived from WAsP and as used in Zephyr/Prediktor (both from Risø National Laboratory/DTU, see also www.prediktor.dk) for the wind farm Klim in the north-west of Denmark. The wind farm consists of 35 Vestas V44 turbines

Often the MOS is performed separately for sectors defined by the forecasted wind direction ($\hat{d}_{\text{NWP}}$). This is equivalent to including direction-dependent coefficients in Eq. 17, using the relationship

$$\hat{p} = \beta_0(\hat{d}_{\text{NWP}}) + \beta_1(\hat{d}_{\text{NWP}})\hat{p}_{\text{phys}} \tag{18}$$

In the statistical literature, models such as Eq. 18 are called varying coefficient models or conditional parametric models and a general theory for estimation of the coefficient *functions* exists.

Given measurements of wind speed, the MOS procedure can also be performed on the physically corrected local wind. While this can be beneficial due to the nonlinearity of the power curve, it essentially eliminates the calculations based on roughness and orography. However, this is only true when the modeled relationship between the NWP and local wind speeds is linear as in Fig. 4.

If the detailed information required by the physical modeling is not available or if it is unreliable, the structure of the physical model might still be used to suggest a model structure which is then estimated directly from data. As an example, consider the physical model which led to the direction-dependent wind farm power curve in Fig. 4. Based on this, it can be assumed that, we can express the power curve model of the wind farm as

$$\hat{p} = f(\hat{w}_{\text{NWP}}, \hat{d}_{\text{NWP}}) \tag{19}$$

where $\hat{w}_{\text{NWP}}$ and $\hat{d}_{\text{NWP}}$ are the meteorological forecast of wind speed and direction, $\hat{p}$ is the forecasted power production, and f is a *function* representing the wind farm power curve. This function can be estimated directly from data, which also implies that the model can easily be used on power production data originating from a region.

Several methods exist for estimation in models such as (19), including artificial neural networks, fuzzy-neural networks, and local regression, all of which have been applied to wind power forecasting. The full list of possible estimation methods is too extensive to cover in this text and special attention is therefore paid to one method, in this case the local regression.

In local regression, the function *f* is estimated at a number of distinct points called the fitting points. For each of these points, the function is approximated by a low order polynomial, the coefficients of which are estimated using only data near the fitting point. Evaluating the polynomial with the estimated coefficients at the fitting points produces the estimate of the function value. The procedure is repeated for all relevant fitting points.

It is customary to place the fitting points close to each other, allowing simple interpolation methods to be used for points not originally considered. The selection of data to be used for a particular fitting point is often based on the nearest-neighbor principle, where a certain proportion of the data are used. In practice, a weighted least squares solution is used and the weights are chosen so that the observations enter the neighborhood smoothly as the fitting point moves over the relevant region.

For the wind farm at Klim in north-west Denmark, the physical-based power response is shown in Fig. 4. In Fig. 5, this power curve is shown together with an estimated power curve. The estimate is based on data from 2003 and the power curves are only shown for forecasted values of wind speed and direction occurring in this year.

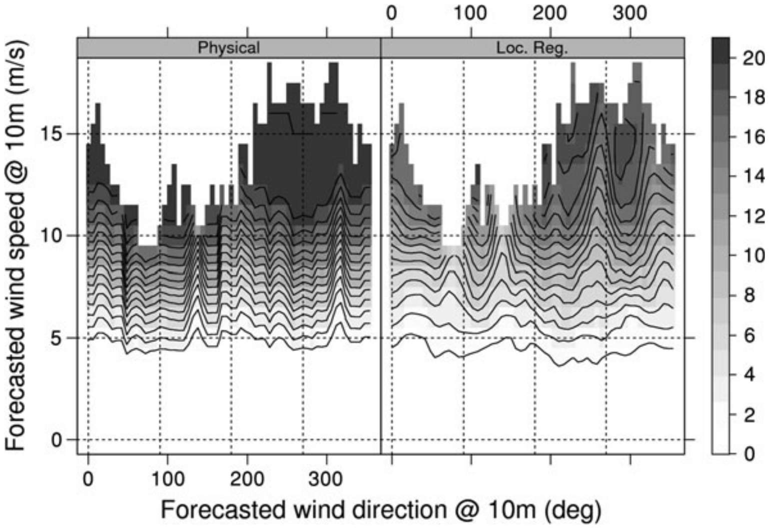

Fig. 5 Power curve for the wind farm at Klim. The *left panel* shows the physical power curve also shown in Fig. 4. The *right panel* shows a 5% nearest neighbor local quadratic regression estimate based on data from data from 2003 and meteorological forecasts corresponding to horizons of 12–18 h, updated four times daily

For some wind directions, the two power curves are similar. One example is the valley at approximately 135° (SE). For other wind directions, e.g. just below 270° (W), the two power curves are quite different. Also, it is seen that the estimated power curve is smoother than the physically based power curve. This is partly due to differences between the methods; the physical based method operates on sectors defined by the forecasted wind direction and the method underlying the estimated power curve assumes that the function *f* is smooth, implying that it can be locally approximated by low order polynomials. While, from a physical point of view, it may be very plausible that the wind farm power curve is smooth, there are additional reasons why it should be smooth when used for forecasting. To realize this, consider the meteorological forecast of the wind direction. The physical power curve suggests that an infinitesimal change in the forecast can cause a jump in the forecasted wind power production. However, since the actual wind direction will deviate from the forecasted wind direction, the performance of the wind power forecast can be improved by using a smooth transition.

It is often possible to improve the wind power forecasts generated by models such as Eq. 19 or a corresponding physical model. As an example, consider the residuals, or in-sample forecast errors, of the estimated power curve mentioned above. Figure 6 shows the mean residual versus the time of day for each month in 2003. It is seen that the mean error is up to near 10% of the installed capacity of 21 MW and this occurs around 15:00 for 2 months (April and May). For the

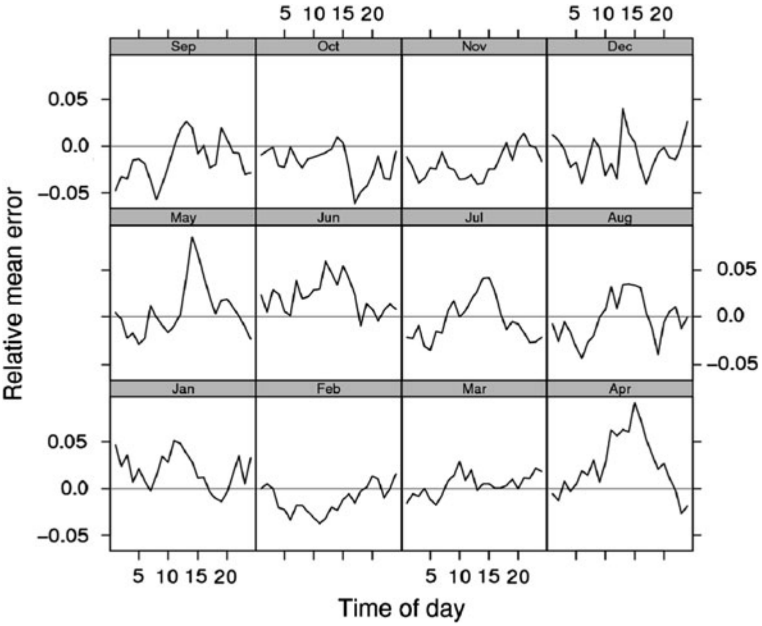

Fig. 6 Mean error relative to the installed capacity for the data from 2003 for the estimated power curve shown in the right panel of Fig. 5

geographical location of the wind farm, this corresponds to the time of year at which the sea is still relatively cold, while solar radiation is relatively high.

The most plausible explanation of this is that the diurnal variation is not fully accounted for in the meteorological forecast. This can be corrected by including a term for adjusting the diurnal variation in the power curve model. Alternatively, a two-step procedure, where a model like Eq. 14 is applied to the forecast errors of the power curve model, can be used. In this case the second model layer will adjust for the auto-correlation of the forecast errors as well.

The models considered so far only use meteorological forecasts of wind speed and direction at a certain level in the meteorological model. Some improvement can be possible by selecting the most appropriate model level. Given a record of power productions and meteorological forecasts, this can be investigated before actually putting a particular wind power forecasting system into operation.

Possibly, other aspects of the meteorological forecast than wind speed and direction can be important. For instance the forecasts may be improved by including information about atmospheric stability in the models used. While the topic is too large to cover in this chapter, this seems to be a promising area for further development of wind power forecasting systems and an area where the combination of meteorological insight and statistical modeling can further improve short-term forecasting.

Combining forecasts is another possible method by which point forecasts can be improved. Investigations have shown that the wind power forecasts driven by different meteorological forecasts can have similar performance, while the forecast errors are only moderately correlated between forecast systems. For this reason a weighted average of the forecasts will perform better than any of the individual forecasts.

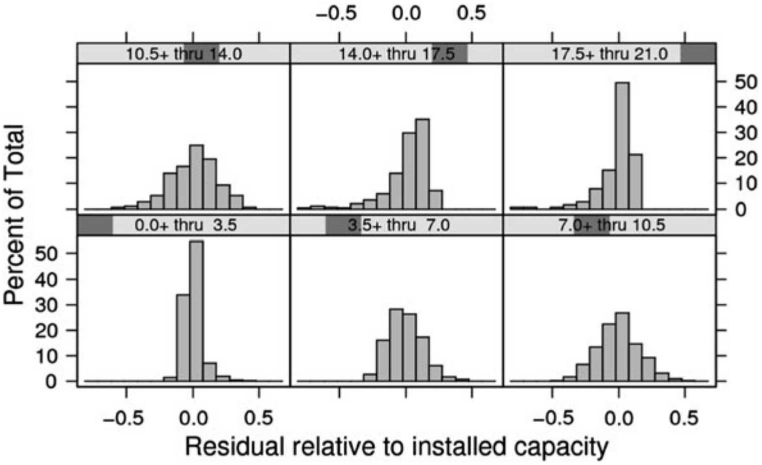

Fig. 7 Histograms of the residuals from the estimated power curve shown in Fig. 5 for different levels of the power forecast as given by the model. The installed capacity is 21 MW

3 Probabilistic Forecast Models

So far the chapter has mainly been concerned with point forecasts. As discussed in the beginning of the chapter, we can use the estimated standard deviation of the forecast errors and add error-bands to the point forecasts. However, due to the bounded nature of possible wind power productions, it is unlikely that such error bands will be representative for the situation. As an example, consider Fig. 7 which shows histograms of the residuals mentioned in the previous section for various levels of the forecasted wind power production. It is seen that the distribution is quite narrow for low values of the forecasted power production. As the level of the forecasted power production increases, the distribution gets wider and changes shape. Near the maximum production, the distribution is again somewhat narrower. This clearly indicates that the simple error bands as mentioned above are inappropriate. Instead we might directly consider the problem of forecasting the conditional density of wind power production at time $t + k$ given information available up to time t.

Formally, this density function will be denoted $f_{t+k|t}(p)$ and is known to be zero outside the interval of possible productions. If a parametric form of the density function can be specified, the parameters collected in the vector θ_k, of the density can be modeled as a function of, e.g. the point forecast $\hat{p}_{t+k|t}$. Formally, this may be written $f_{t+k|t}\left(p;\ \theta_k\left(\hat{p}_{t+k|t}\right)\right)$. With an appropriate parameterization of the density function, it should be possible to model each of the elements of θ_k as a linear regression model. This observation also directly points towards the possibility of including more explanatory variables and enables the possibility of modeling situation-specific uncertainties.

Apparently, experience with the approach outlined is limited within the wind energy forecasting community. A similar approach based on fuzzy-logic and resampling, essentially allowing sampling from a time-adaptive estimate of $f_{t+k|t}\left(p;\ \theta_k\left(\hat{p}_{t+k|t}\right)\right)$, has been developed at Ecole des Mines de Paris [1]. Below some alternatives will be outlined.

3.1 Quantile Regression

A relatively well-established method within statistics is quantile regression. With this approach *one* quantile of the conditional distribution is modeled as a linear regression-type model. Running several such models in parallel, the full distribution can be well approximated.

Considering a random variable Y, the median is the most well known quantile and is characterized as the value $Q(1/2)$ for which the probability of obtaining values of Y above or below $Q(1/2)$ both equals 1/2.

Let $Q(\tau)$ be the τ-quantile of, e.g. the wind power forecast error, i.e., the value at which the probability is τ of the actual forecast error being lower than this value. In quantile regression $Q(\tau)$, $0 < \tau < 1$, is expressed as a linear combination of some known regressors and unknown coefficients, exactly as the mean is modeled in (multiple) linear regression. Thus, the τ-quantile is modeled as

$$Q(\tau) = \beta_0(\tau) + \beta_1(\tau)x_1 + \beta_2(\tau)x_2 + \cdots + \beta_p(\tau)x_m \tag{20}$$

where $x_.$ are the m known regressors, also called explanatory variables and $\beta_.(\tau)$ are unknown coefficients, depending on τ, to be determined from observations $(y_i, x_{i,1}, \ldots, x_{i,p})$; $i = 1, \ldots, N$. Following, the beginning of this section x_1 may be the point forecast of the power production and x_2 may be the forecasted wind direction, which has been shown to have some influence on some quantiles [2].

Given the check function

$$\rho_\tau(e) = \begin{cases} \tau e, & e \geq 0 \\ (\tau - 1)e, & e < 0 \end{cases} \tag{21}$$

the sample τ-quantile can be found by minimizing $\sum_{i=1}^{N} \rho_\tau(y_i - q)$ with respect to q. Figure 8 shows the check function for two values of τ. Replacing q with the right-hand side of Eq. 20 leads to the estimates

$$\hat{\beta}(\tau) = \underset{\beta}{\operatorname{argmin}} \sum_{i=1}^{N} \rho_\tau(y_i - (\beta_0 + \beta_1 x_{i,1} + \cdots + \beta_m x_{i,m})) \tag{22}$$

where $\beta(\tau)$ is a vector containing the unknown coefficients. The method by which the coefficients of quantile models are estimated is based on linear programming and thus is much more demanding than for linear regression. However, software for quantile regression is readily available.

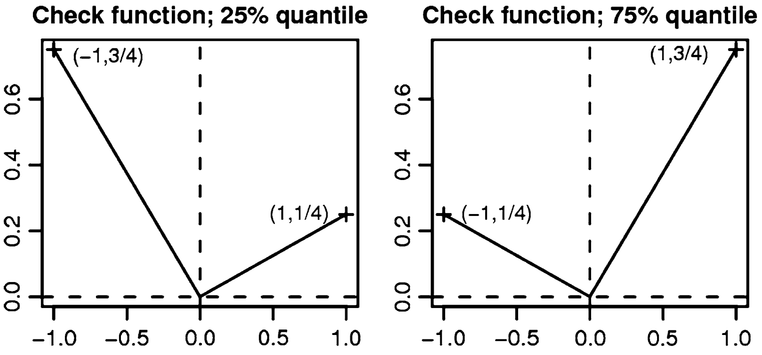

Fig. 8 The check function $\rho_\tau(e)$, for $\tau = 0.25$ (*left*) and for $\tau = 0.75$ (*right*)

3.2 Meteorological Ensemble Forecasts

It may be argued that the driving force of the situation-dependent uncertainty is the overall state of the atmosphere in a large region surrounding the area of interest. This has led to the development of meteorological ensemble forecast products, where the most well known global models are the Ensemble Prediction System from the European Centre for Medium-Range Weather Forecasts (ECMWF) and the GFS-based Ensemble forecast system from the National Centers for Environmental Prediction (NCEP) in the United States.

The basis of numerical weather prediction models is a large set of coupled differential equations describing the processes in the atmosphere. Given a set of initial conditions, the future development of the atmosphere can then be forecasted by numerical solution of the differential equations. The initial conditions are obtained trough a process called *data assimilation* in which measurements are assimilated into the model in order to estimate the current state of the atmosphere. Due to the chaotic nature of the atmosphere, the forecasts are more sensitive to some initial conditions than others. Ensemble prediction systems essentially explore the sensitivity of the model to changes in the initial conditions. Following this the initial conditions are perturbed in directions for which high sensitivity is expected.

Apparently, the directions in which the initial conditions are perturbed are only linked to the sensitivity of the model and not to the variance–covariance matrix of the measurement error. For this reason ensemble predictions cannot be expected to directly reflect the future development of the weather in a probabilistic sense. Hence, quantiles, derived directly from ensemble forecasts cannot be expected to be correct. Nevertheless, ensemble forecasts contain information regarding the current predictability and may be valuable in determining the conditional densities of future power productions; $f_{t+k|t}(p)$.

Due to the heavy computational demand of meteorological models, the number of members in the ensemble is limited and the models are not run as frequently as normal meteorological models. As an example, the ensemble from ECMWF consists of one unperturbed member (the control) and 50 members for which the initial values are perturbed. The calculations are initiated daily at 12:00 UTC and take 17–18 h to complete. Figure 9 shows an example of such an ensemble of the wind speed.

An approach to the application of ensemble forecasts in order to produce forecasts of the conditional density is to use the control forecast in order to estimate the power curve of the wind farm or region under consideration. Using this power curve, it is possible to produce wind power ensembles for the period considered during estimation. For each wind power ensemble the nomial quantiles of the distribution can readily be found. Given a grouping of the data, e.g., by horizon, it is then possible to compare the nomial probabilities with the actual frequency. If the nomial probability and the actual frequencies are approximately equal the power ensemble can be used directly.

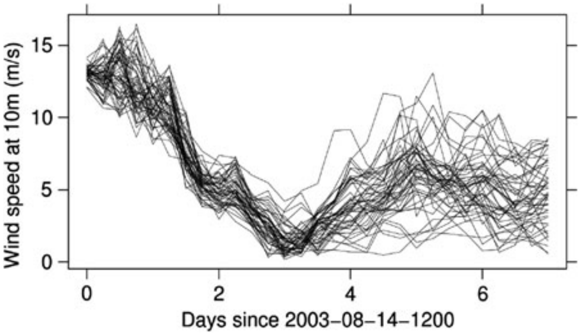

Fig. 9 An example of a wind speed ensemble from ECMWF for the location of the Klim wind farm

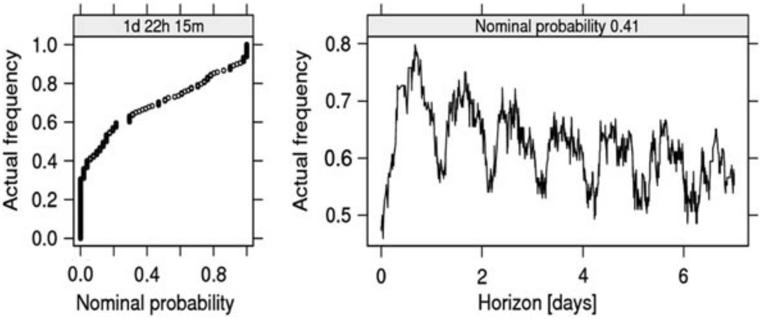

Fig. 10 Examples of dependence of the actual observed frequencies on the nominal probability given a specific horizon (*left*) and on the horizon given a specific nominal probability (*right*). The example originates from [4], where data from a small offshore wind farm is used

Figure 10 shows an example of the relationship between nomial probability and the actual frequencies, when using ECMWF ensembles and an estimated power curve for the total wind power production in western Denmark [3]. A clear discrepancy is observed and further investigations show that the same behavior is seen for all horizons and probabilities. As a consequence, a model correcting these probabilities is needed.

The smooth relationship between the nominal p_n and actual p_a probabilities can be modeled using a spline basis expansion [5]. The fluctuating behavior over the horizon τ indicates that the coefficients of the expansion vary with the horizon τ. The resulting model is

$$\log \frac{p_a}{1-p_a} = b'(p_n)\theta(\tau) + \epsilon \tag{23}$$

where ϵ is an error term, $b(p_n)$ is a column vector representing the spline expansion, $\theta(\tau)$ is a column vector containing the coefficient functions. The logit-transformation of p_a is used to ensure that the forecasted p_a will be between 0 and 1.

On the basis of a (training) data set consisting of the actual power production and meteorological ensemble forecasts, another data set containing all combinations of τ, p_n, and p_a can be constructed as outlined above. Estimation in the model represented by Eq. 23 can then be accomplished using a local regression technique.

Finally, it is mentioned that the ensembles considered so far are *initial value ensembles*. Another approach to ensemble forecasting is the *parametrization ensembles* in which members are generated by altering different aspects of the meteorological model. This essentially amounts to running several meteorological models in parallel. While the information contained in parametrization ensembles can be valuable when modeling $f_{t+k|t}(p)$, it is important to note the conceptual difference between the approaches. Bayesian Model Averaging has been used by researchers at the University of Washington to produce probabilistic forecasts of rainfall [6]. Apparently, the method has not yet been applied to wind power forecasting.

3.3 Scenario Generation

While a probabilistic forecast as described above contains more detailed information than a point forecast, it does not contain all information required to produce realistic scenarios of future wind power production within the forecast horizon. The reason for this is that the probabilistic forecast consists of marginal densities $f_{t+k|t}(p)$; $k = 1, \ldots, K$ and in order to produce realistic scenarios, the joint density of future wind power production $p_{t+1}, \ldots, \mathrm{p}_{t+K}$, conditional on information at forecast time t, is required.

Based on the probabilistic forecast $f_{t+k|t}(p)$ and the corresponding observed wind power production p_{t+k}, an artificial observation $z_{t+k|t}$ from a standard Gaussian distribution can be generated. Based on a data set, the correlations of $z_{t+k|t}$; $k = 1, \ldots, K$ can then be estimated under the assumption that the correlations are constant across time. Assuming the joint distribution of $z_{t+k|t}$; $k = 1, \ldots, K$ to be multivariate Gaussian, it is then easy to produce pseudo random samples from this distribution. Using the inverse of the cumulative distributions corresponding to the probabilistic forecast, the random samples from the multivariate Gaussian can then be transformed back to the scale of the wind power production. The plot in the top panel of Fig. 2 shows ten scenarios generated as just described. Comparing with the scenarios obtained using independent sampling in the bottom panel of the same figure, the potential importance of correct modeling of the joint distribution can be verified. It is easy to extend the method to allow adaptive estimation of the correlations, see also [7].

Comparing the figure just mentioned with the wind speed ensemble in Fig. 9, it is seen that the same kind of information is contained in the ensemble forecast as in the statistically generated scenarios. The advantage of the latter is that several thousands of scenarios can be generated on the fly and furthermore it can be ensured that the probabilistic forecasts forming the basis of the scenarios are correct in a probabilistic sense.

4 Upscaling

Upscaling is concerned with the issue of forecasting the total production of a region when on-line measurements of the total are not available. Instead the forecast of the total is based on a forecast for a subset of the wind turbines in the region.

First, consider a point forecast for a subset of the wind farms. Precisely how to perform the upscaling depends on the type of data available. When only the installed capacity of the region is known, the straightforward approach is to upscale by multiplying the point forecast by the ratio between the installed capacity of the region and the installed capacity of the turbines for which the forecast is valid. Assuming the turbines for which on-line forecasts are available is a representative sample from the population of turbines, this procedure is valid and by analysing the spatial correlation, the standard deviation of the upscaled forecast can be calculated [8].

However, the turbines/farms for which on-line measurements are available typically differ in character from the turbines/farms for which such measurements are not available. For this reason, if relevant data are available, it can be advantageous to use other methods. Typically, for accounting purposes, readings with a relatively high time-resolution (in Denmark; 15 min) are available for all points in the transmission grid at which turbines are connected. These data are typically available as batches on a monthly basis. Assuming that there is no, or very limited, consumption on the secondary side of these connection points, these data are valuable for upscaling purposes.

Essentially, such data allow models of the relationship between the forecasted values for the on-line turbines and the total production to be identified. However, model updates can only be performed each time a batch of measurements are available. Given measurements of the total $\hat{p}_{\text{total}}$, the sum of the on-line forecasts $\hat{p}_{\text{online}}$ and meteorological forecasts for of wind speed and direction for the region of interest, $\hat{w}_{\text{NWP}}^{(\text{reg})}$ and $\hat{d}_{\text{NWP}}^{(\text{reg})}$, respectively, a possible upscaling model is

$$\hat{p}_{\text{total}} = \theta\left(\hat{w}_{\text{NWP}}^{(\text{reg})}, \hat{d}_{\text{NWP}}^{(\text{reg})}\right)\hat{p}_{\text{online}} \tag{24}$$

That is, the upscaling-factor is modeled as a function of the NWP forecast of the wind speed and direction for the region. These would usually be defined as spatial averages over some NWP grid points. The model is a varying coefficients model. As for the power curve model, other approaches such as artificial or fuzzy neural networks, can be applied.

Due to the assumed non-representativeness of the on-line turbines, upscaling of probabilistic forecasts is not possible. Even if the on-line turbines could be considered representative for the full population of turbines, upscaling would be difficult without unrealistic assumptions about the parametric form of the joint distribution of future power production. As a consequence, if a probabilistic forecast of the total of a region is to be produced, it is required that measurements of the total wind power production in the region are available. It is however not required that these data are available on-line, batch wise availability is sufficient.

5 Evaluation

The model building process starts off by selecting one or more data sets. The models considered during the process are often compared with the data. Such comparisons include:

- Model estimation; i.e. estimation of coefficients or coefficient functions.
- Selection of tuning parameters such as forgetting factors and bandwidths.
- Comparison of different model structures.

In principle, it is therefore possible to identify models which fit the particular data arbitrarily well, especially when many explanatory variables are available. By such *over-fitting* the resulting model loses its ability to *generalize* to new data. Furthermore, the estimate of performance will be over-optimistic.

In order to limit over-fitting, standard statistical disciplines such as significance testing and comparison of models via, e.g., cross-validation should be applied during the model building process. Still, to obtain an unbiased estimate of the model performance, it is recommended that the selected model is applied to a new data set. It should be noted that there can be some site effects on the ranking of models [9].

In summary when sufficient data are available, these should be split into:

Training data: The data on which the model is built, estimation is performed, and tuning parameters selected.

Test data: The data on which the performance of the selected model is estimated and compared to competing models.

For time-adaptive estimation, the forgetting factor should be selected based on the training data, but the model will be estimated adaptively when applied to the test data. The re-estimation must closely mimic the real on-line situation.

The measures used to summarize model performance depend on whether point forecasts or probabilistic forecasts are considered. These measures will be briefly described below. For point forecasts, the measures and additional information which is reasonable to present in the case of wind power forecasting is well defined and as part of the ANEMOS project on short-term wind power forecasting, a protocol for model evaluation has recently been published [10]. Probabilistic forecasts are relatively new within the field of wind power and therefore a similar document does not exist for probabilistic forecasts. More work has been done on the subject within the field of econometrics; see [11] and the references therein.

5.1 Point Forecasts

Let the forecast error $e_{t+k|t}$; $t = 1, ..., N - k$ on the test data $t = 1,\ldots, N$ be defined as in Eq. 2. Also, for comparison, it is beneficial to assume that the observations and the forecasts are all normalized by dividing with the installed capacity of the farm or region under consideration. The following set of performance measures should be considered:

- The Normalized Root Mean Squared Error for horizon k:

$$\mathrm{NRMSE}_k = \sqrt{\frac{1}{N_s}\sum e_{t+k|t}^2} \tag{25}$$

- The Normalized Absolute Mean Error for horizon k:

$$\mathrm{NMAE}_k = \frac{1}{N_s}\sum |e_{t+k|t}| \tag{26}$$

- The Normalized Bias for horizon k:

$$\mathrm{NB}_k = \frac{1}{N_s}\sum e_{t+k|t} \tag{27}$$

Here N_s is the number of terms in the sum, which might be slightly lower than N because all horizons should be compared on the basis of the same time points and missing values might exist in the test data. Furthermore, to simulate steady online operation, adaptive methods might require an initialization period to be excluded when calculating the performance measures. The measures NRMSE and NMAE include both variability and bias. Due to the squared forecast error, NRMSE assigns more penalty on large errors than NMAE, similarly NRMSE assigns little penalty to small errors.

If markedly different forecast methods are compared, these may not all be able to generate forecasts at all time points, possibly because different meteorological forecasts are used. In this case, it is important that the performance measures are based on the intersect of time points for which forecasts are available. Here, the fraction of the time with non-missing forecasts is probably the most important performance measure to the end-user.

Other performance measures are sometimes used. One example is $R^2 = 1 - \sum e_{t+k|t}^2 \Big/ \Sigma(p_{t+k} - \bar{p})^2$, where $\bar{p}$ is the average power production over the test data. Hence, R^2 is the ratio between the variability explained by the model $\Sigma(p_{t+k} - \bar{p})^2 - e^2_{t+k|t}$ and the overall variability.

Another example is the empirical correlation coefficient r_k for horizon k. Except for the sign, this performance measure is invariant to linear transformations of the forecast, i.e. using r_k the forecasts $\hat{p}_{t+k|t}$ and $a + b\hat{p}_{t+k|t}$, where a and b are arbitrary constants, are considered equally good. For this reason r_k cannot be recommended as a performance measure when comparing competing models.

5.2 Probabilistic Forecasts

When evaluating the performance of a probabilistic forecasting system, it is important to consider to what extent the system is actually producing correct quantiles, e.g. it must be verified that in 75% of the cases the actual production is below the 75% quantile in the forecasted distribution. This property is called the *reliability* of the system. As an example, Fig. 11 displays *reliability diagrams* obtained from the results of an actual probabilistic forecast application.

Besides the reliability, the precision of the forecast must be addressed. *Sharpness* measures the average precision, e.g. the average of the distance between 25 and 75% quantiles. *Resolution* measures the variation in precision, e.g. the standard deviation of the distance between 25 and 75% quantiles. High resolution indicates that the system is able to differentiate between situations with low and high predictability. The concept originates from meteorology [12], but for models identified using data, some part of the resolution will be artificial in the sense that it originates from random estimation error. Generally, this error has zero mean and therefore, it will not influence sharpness in a systematic way.

When comparing several forecast systems, these should only be compared with respect to sharpness and resolution if they are all reliable to some accepted degree.

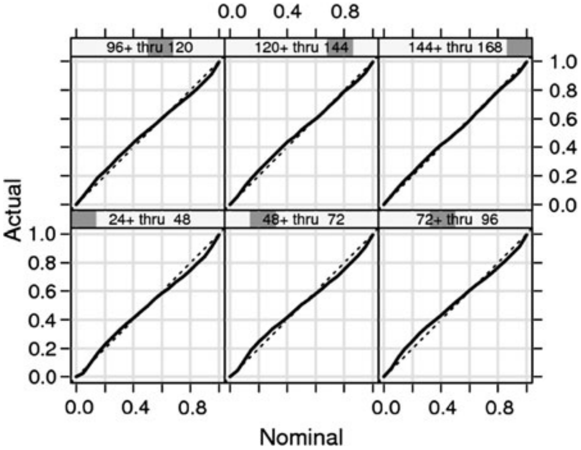

Fig. 11 Actual frequencies versus nominal probabilities when grouping by horizon in hours as indicated on top of each plot. The example originates from [3], where the results of an actual application is analysed. The results are based on 8 months of data

One difficulty with such an approach is that exact reliability can probably not be achieved in practice. It should also be noted that the observed frequency is an uncertain estimate, for which the variance cannot easily be estimated due to the inherent correlation between consecutive multi step ($k > 1$) forecasts. Hence, in practice, some degree of non-reliability must be accepted. In turn, this may affect other performance measures, e.g. a slightly too narrow distribution might be accepted as approximately reliable and in terms of sharpness this will be rewarded.

Also, reliability can only be investigated by grouping the data, e.g. by horizon, in bins defined by the forecasted wind speed or direction, or other explanatory variables. In principle the bins can also be defined in multiple dimensions. Unless the test data set is very large, in practice, this will thin the number of observations in each bin to an extend, where the uncertainty on the estimated probabilities is too large.

As an alternative, a *skill-score* can be used. In [13], desired properties of a skill-score are discussed and the concept of a proper scoring rule is defined. It is shown that for a probabilistic forecast and the resulting quantiles $q_1, q_2, \ldots, q_\ell$ with nominal levels $\tau_1, \tau_2, \ldots, \tau_\ell$ the following form of a skill-score is proper

$$\sum_{i=1}^{\ell} \left(\tau_i s_i(q_i) + (s_i(p) - s_i(q_i)) I[p \leq q_i] + f(p)\right) \tag{28}$$

where p is the actual power production, $I[]$ is the indicator function which takes the value 1 if its argument is true, and 0 otherwise, s_i are non-decreasing functions and f is an arbitrary function. The skill-score defined by Eq. 28 is positively rewarding. Considering a single quantile τ, the score in Eq. 28 is equal to $\tau s(q)(s(p) - s(q)) I[p \leq q] + f(p)$. Selecting the function s to identity and $f(p) = \tau p$, the score $-(\tau - 1)(p - q)$ is obtained if $p \leq q$ and the score $-\tau(p - q)$ is obtained if $p > q$. Comparing with the estimation criterion used in quantile regression, and especially with the check function Eq. 21 $\rho_\tau(p - q)$, reveals that the check function is a negative skill-score.

A skill-score, as defined above, is valid for one observation p and a corresponding forecast. To apply the method to a test data set, we will sum the scores over the test data set and, e.g. group by horizon. The score summarizes both reliability and sharpness and therefore, in principle, the reliability assessment is not required. However, due to the absolute nature of the requirement of reliability, it is recommended that this is addressed separately.

To further verify the appropriateness of the quantile forecasting system, the *spread/skill relationship* is often considered. Here the relationship between the magnitude of the observed forecast error of a point forecast and the uncertainty indicated by the quantile forecast system is analysed. The point forecast could be the forecast originating from the unperturbed scenario or it could be the 50% quantile forecast.

As examples of how these methods are applied to actual evaluation of probabilistic forecasts generated over a test period, the reader is referred to [3], where the results of an actual application based on meteorological ensemble forecasts is evaluated, and to [14] where skill scores are also considered.

The precision by which the reliability is estimated has not yet been addressed. Assuming independence between time points, exact or approximate confidence intervals based on the Binomial distribution can be constructed. Similarly, χ^2-tests can be applied in order to test the correctness of the probabilistic forecasts. However, for multi step forecasts, the assumption of independence is unattainable, thus completely violating the assumptions underlying standard statistical procedures. As a result, due to correlation, the uncertainty of the estimates of reliability is higher than expected from the assumption of independence. This is demonstrated in [11].

At the current stage, no definitive recommendation can be made regarding the handling of correlation. It is however clear that, if the correlation is removed by considering only a small random sample from the data, the results would be inconclusive. A far more promising procedure seems to be block-wise bootstrapping [15] or smooth spectrum resampling as suggested in [16].

6 Bibliographical Notes

The plots shown in the introduction of this chapter are based on the probabilistic forecast system and the data described in [3]. The point forecast is based on the unperturbed member in the ECMWF ensemble and the direction-dependent power curve estimated as described in the reference. The standard deviations forming the basis of the error bands of the point forecast are calculated from the entire data set in the reference. This also holds for the variance–covariance matrix illustrating the conditional scenarios.

The simple point forecast which mix persistence and mean predictors was originally suggested in [17]. The RLS-algorithm with and without forgetting is described in [18]. In [8], a detailed account for physically based short-term forecasting of wind power is given, see also [19] and the references therein. Details regarding Prediktor can be found in [20, 21] and on the homepage mentioned above.

The main paper on varying coefficient models is [22] which addresses a class of models somewhat larger than considered in this chapter. Considering conditional parametric models where all coefficient functions depend on the same external variables, a comprehensive description can be found in [23]. Adaptive and recursive estimation in such models is described in [24]. Combined forecasting was originally suggested by Bates and Granger [25]. With respect to wind power forecasting see [26, 27] and the references therein.

Overviews of some short-term point prediction systems and methods can be found in [28–30] and as part of the ANEMOS project on short-term wind power forecasting an interesting comparison of different forecasting systems across sites with markedly different characteristics has been published in [9].

Quantile regression is described in [31] and application to wind power forecasting is described in [2], where the non-linearities are modeled using spline basis expansions. The benefit of adaptive quantile estimation is demonstrated in [32]. A similar method based on re-sampling is described in [33] and the two methods are compared in [14]. The method based on meteorological ensembles is briefly described in [3], more details can be found in [4, 34].

The upscaling model (Eq. 24) is used in Zephyr/WPPT (Wind Power Prediction Tool), see e.g., [35] and http://www.risoe.dk/zephyr. Other approaches to the upscaling problem include [36, 37].

As part of the ANEMOS project mentioned above, a protocol on evaluation of wind power forecasts has been published [10]. Evaluation the evaluation of probabilistic forecasts follows the ideas used in meteorology [38]. The application to wind power forecasting is discussed in [14]. The inappropriateness of, e.g., χ^2-tests is demonstrated in [11], see also [39].

References

1. Pinson P (2006) Estimation of the uncertainty in wind power forecasting. PhD thesis, Ecole des Mines de Paris, Paris, France
2. Nielsen H Aa, Madsen H, Nielsen TS (2006) Using quantile regression to extend an existing wind power forecasting system with probabilistic forecasts. Wind Energy, 9(2):95–108
3. Nielsen H Aa, Nielsen TS, Madsen H, Giebel G, Badger J, Landberg L, Sattler K, Voulund L, Tøfting J (2006) From wind ensembles to probabilistic information about future wind power production—results from an actual application. In Proceedings of the 9th International Conference on Probabilistic Methods Applied to Power Systems
4. Nielsen H Aa, Madsen H, Nielsen TS, Badger J, Giebel G, Landberg L, Sattler K, Feddersen H (2005) Wind Power Ensemble Forecasting Using Wind Speed and Direction Ensembles from ECMWF or NCEP. Technical report, Informatics and Mathematical Modelling, 2005. Prepared under PSO-project FU2101, URL: http://www.risoe.dk/zephyr/publ.htm
5. Boor C (1978) A Practical Guide to Splines. Springer, Berlin
6. Sloughter JM, Raftery AE, Gneiting T (2006) Probabilistic quantitative precipitation forecasting using bayesian model averaging. Technical Report 496, Department of Statistics, University of Washington, Seattle, Washington
7. Pinson P, Papaefthymiou G, Klockl B, Nielsen H Aa (2007) Generation of statistical scenarios of short-term wind power production. In Proceedings of the IEEE PowerTech Conference, Lausanne, Switzerland
8. Lange M, Focken U (2005) Physical Approach to Short-Term Wind Power Prediction. Springer, Berlin
9. Martí I, Kariniotakis G, Pinson P, Sanchez L, Nielsen HMTS, Giebel G, Usaola J, Palomares A, Brownsword JTR, Focken U, Lange M, Sideratos G, Descombes G (2006) Evaluation of advanced wind power forecasting models—results of the ANEMOS project. In Proceedings of the European Wind Energy Conference, Athens, Greece
10. Madsen H, Pinson P, Kariniotakis G, Nielsen H Aa, Nielsen TS (2005) Standardizing the performance evaluation of short-term wind prediction models. Wind Engineering, 29(6): 475–489
11. Pinson P, Kariniotakis G, Nielsen H Aa, Nielsen TS, Madsen H (2006). Properties of quantile and interval forecasts of wind generation and their evaluation. In Proceedings of the European Wind Energy Conference & Exhibition, Athens, http://www.ewea.org

12. Jolliffe IT, Stephenson DB (2003). Forecast verification—a practitioner's guide in atmospheric science. Wiley, Chichester
13. Gneiting T, Raftery AE (2004) Strictly proper scoring rules, prediction, and estimation. Technical Report 463, University of Washington, Department of Statistics
14. Pinson P, Nielsen H Aa, Møller JK, Madsen H, Kariniotakis G (2007). Non-parametric probabilistic forecasts of wind power: Required properties and evaluation. Wind Energy, 10(6):497–587
15. Efron B, Tibshirani RJ (1993) An Introduction to the Bootstrap. Chapman & Hall, London
16. Pinson P, McSharry P, Madsen H (2010) Reliability disgrams for nonparametric density forecasts of continuous variables: accounting for serial correlation. Quarterly Journal of the Royal Meteorological Society, 136(646):77–90
17. Nielsen TS, Joensen A, Madsen H, Landberg L, Giebel G (1998) A new reference for predicting wind power. Wind Energy, 1(1):29–34
18. Ljung L (1999) System Identification—Theory for the User. Prentice Hall, Upper Saddle River
19. Landberg L (1998) A mathematical look at a physical power prediction model. Wind Energy, 1(1):23–30
20. Landberg L (2001) Short-term prediction of the power production from wind farms. Journal of Wind Engineering & Industrial Aerodynamics, 80:207–220
21. Landberg L (2001) Short-term prediction of local wind conditions. Journal of Wind Engineering & Industrial Aerodynamics, 89:235–245
22. Hastie T, Tibshirani R (1993) Varying-coefficient models. Journal of the Royal Statistical Society, Series B, Methodological, 55:757–796
23. Cleveland W (1994) Multivariate Analysis and Its Applications, chapter Coplots, Nonparametric Regression, and conditionally Parametric Fits, pages 21–36. Institute of Mathematical Statistics, Hayward
24. Nielsen H Aa, Nielsen TS, Joensen AK, Madsen H, Holst J (2000) Tracking time-varying coefficient-functions. Int. J. of Adaptive Control and Signal Processing, 14(8):813–828
25. Bates JM, Granger CWJ (1969) The combination of forecasts. Operational Research Quarterly, 20(4):451–468
26. Nielsen H Aa, Nielsen TS, Madsen H, Pindado MJSI., Martí I (2007) Optimal combination of wind power forecasts. Wind Energy, 10(5):471–482
27. Sánchez I (2006) Adaptive combination of forecast with application to wind energy forecast. In 9th International Conference on Probabilistic Methods Applied to Power Systems, KTH, Stockholm, Sweden, Power Engineering Society, IEEE
28. Giebel G, Brownsword R, Kariniotakis G (2003). The state-of-the-art in short-term prediction of wind power; a literature overview. Technical report, Project ANEMOS public document http://anemos.cma.fr/download/ANEMOS_D1.1_StateOfTheArt_v1.1.pdf
29. Giebel G, Landberg L, Madsen H, Nielsen TS, Nielsen H Aa (2006). Introduction to Wind Technology, chapter Short-term (30 min–72 hrs) prediction for power output from wind farms, pages 1–19. Lecture Series 2006–02. von Karman Institute for Fluid Dynamics. ISSN 0377-8312, ISBN 2-930389-64-8, VKI LS 2006-02
30. Landberg L, Giebel G, Nielsen H Aa, Nielsen T, Madsen H (2003) Short-term prediction—an overview. Wind Energy, 6(3):273–280
31. Koenker R (2005) Quantile Regression. Cambridge University Press, New York
32. Møller JK, Nielsen H Aa, Madsen H (2008) Time adaptive quantile regression. Computational Statistics & Data Analysis, 52(3):1292–1303
33. Pinson P, Kariniotakis G (2004) On-line assessment of prediction risk for wind power production forecasts. Wind Energy, 7(2):119–132
34. Nielsen H, Madsen H, Nielsen T, Badger J, Giebel G, Landberg L, Sattler K, Feddersen H (2004). Wind power ensemble forecasting. In Proceedings of the 2004 Global Windpower Conference and Exhibition, Chicago, Illinois, USA. http://www.awea.org
35. Madsen H, Nielsen H Aa, Nielsen TS (2005) A tool for predicting the wind power production of off-shore wind plants. In Proceedings of the Copenhagen Offshore Wind Conference &

Exhibition, Copenhagen, Danish Wind Industry Association. http://www.windpower.org/en/core.htm

36. Focken U, Lange M, Waldl HP (2001). Previento—a wind power prediction system with an innovative upscaling algorithm. In Proceedings of the European Wind Energy Conference and Exhibition, Copenhagen, Denmark
37. Pinson P, Siebert N, Kariniotakis G (2003). Forecasting of regional wind generation by a dynamic fuzzy-neural networks based upscaling approach. In Proceedings of the European Wind Energy Conference & Exhibition, Madrid, Spain. http://www.ewea.org
38. Toth Z, Talagrand O, Candille G, Zhu Y (2003) In IT. Jolliffe and DB. Stephenson, editors, Forecast verification—a practitioner's guide in atmospheric science, chapter Probability and ensemble forecasts. Wiley, New York
39. Hamill TM (2001) Interpretation of rank histograms for verifying ensemble forecasts. Monthly Weather Review, 129(3):550–560

Author Biography

Henrik Aalborg Nielsen holds a position as Associate Professor at Department of Informatics and Mathematical Modelling, Technical University of Denmark. Henrik has been working within the field of wind power forecasting for approximately 15 years and was one of the main developers of the core mathematical and statistical method used in WPPT (Wind Power Prediction Tool). Henrik is currently (summer 2009) on leave and working at ENFOR A/S, a company working within the field of optimization and forecasting for the energy sector, which he founded together with Torben Skov Nielsen, Henrik Madsen, and Kim Knudsen in 2006.

Analysis of Wind Turbine Loads

Helge Aagaard Madsen and Kenneth Thomsen

The analysis of wind turbine loads is an important discipline within wind turbine technology. Though it is performed widely by the wind turbine industry and wind turbine certification institutes, it also plays an important role in wind energy research. The objectives of such an analysis can be quite different, as for example exploration of system dynamics, verification of design loads and validation of aerodynamic and aeroelastic models.

Generation of the loads on a wind turbine is schematically shown in Fig. 1. Wind is the main input to the system but often there are other site parameters which contribute to the loads. For example there are wave loads on the foundation for an off-shore installation. As most wind turbines are within wind farms, wake generated loads are also important. Additional input is control parameters, shown here as separate input to the wind turbine for clarity, although the control system normally is fully integrated in the wind turbine. The output from the wind turbine is mechanical or electrical power accompanied with loads on the system.

Analysis of the loads is the main subject of the present chapter but to have a firm basis for interpretation of the loads, a description of the origin of the loads is presented first. Then follows the loads analysis methods and procedures which are used for certification purposes.

H. A. Madsen (✉)
Wind Energy Division, Risø National Laboratory for Sustainable Energy,
Technical University of Denmark, P.O. Box 49, Building 118, 4000 Roskilde, Denmark
e-mail: helge.aagaard.madsen@risoe.dk

K. Thomsen
Siemens Wind Power A/S, Borupvej 16, 7330 Brande, Denmark

S. Mathew and G. S. Philip (eds.), *Advances in Wind Energy Conversion Technology,* Environmental Science and Engineering,
DOI: 10.1007/978-3-540-88258-9_5,

1 The Origin of Wind Turbine Loads

Loads can either be measured on a turbine or simulated with a numerical code. Nowadays, design of MW turbines relies heavily on simulations with so-called aeroelastic models as building different prototypes would be too costly. Different aeroelastic codes are used by the industry. Some examples are FLEX4 [1], HAWC [2], BLADED [3] and HAWC2 [4].

Such codes can in principle simulate the complete wind turbine system as shown in Fig. 1. The codes have separate modules for simulation of the wind and of the waves and also complete modules for the whole wind turbine control system.

Simulated loads will mainly be used in the present chapter as it has the advantage that the input parameters can fully be controlled. This enables, for example, the load response from the different input parameters to be clearly illustrated. However, a few examples with measured loads from operation in wakes will also be presented. The loads analysis will mainly be from simulations on the three-bladed turbine concept with an upwind rotor. A few cases from a two-bladed downwind rotor also would be presented to illustrate the loading from the tower shadow.

Most of the results for the three-bladed concept will specifically be from simulations on a 5 MW reference wind turbine (RWT) [5] with design parameters set up only for the purpose of aerodynamic and aeroelastic simulations. However, the turbine design parameters are typical for modern MW turbines of a similar size.

2 Influence of the Mean Wind Speed

The primary parameter influencing the turbine mean loads is the mean wind speed. A typical operational range for a turbine is from 3 to 25 m/s, at which wind speed the turbine is shut down. The variations of the turbine electrical power output P_e and some load components are shown in Fig. 2.

Fig. 1 Schematic illustration of the loads on a wind turbine

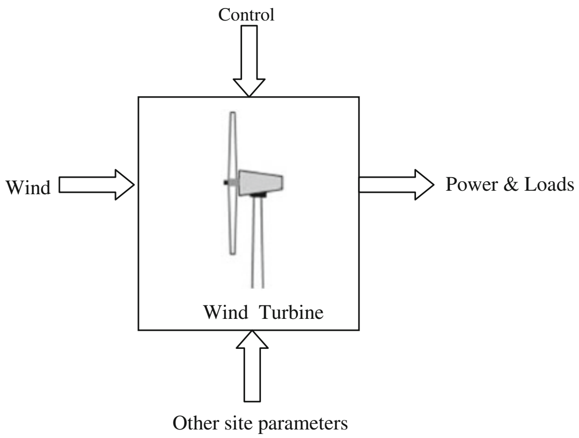

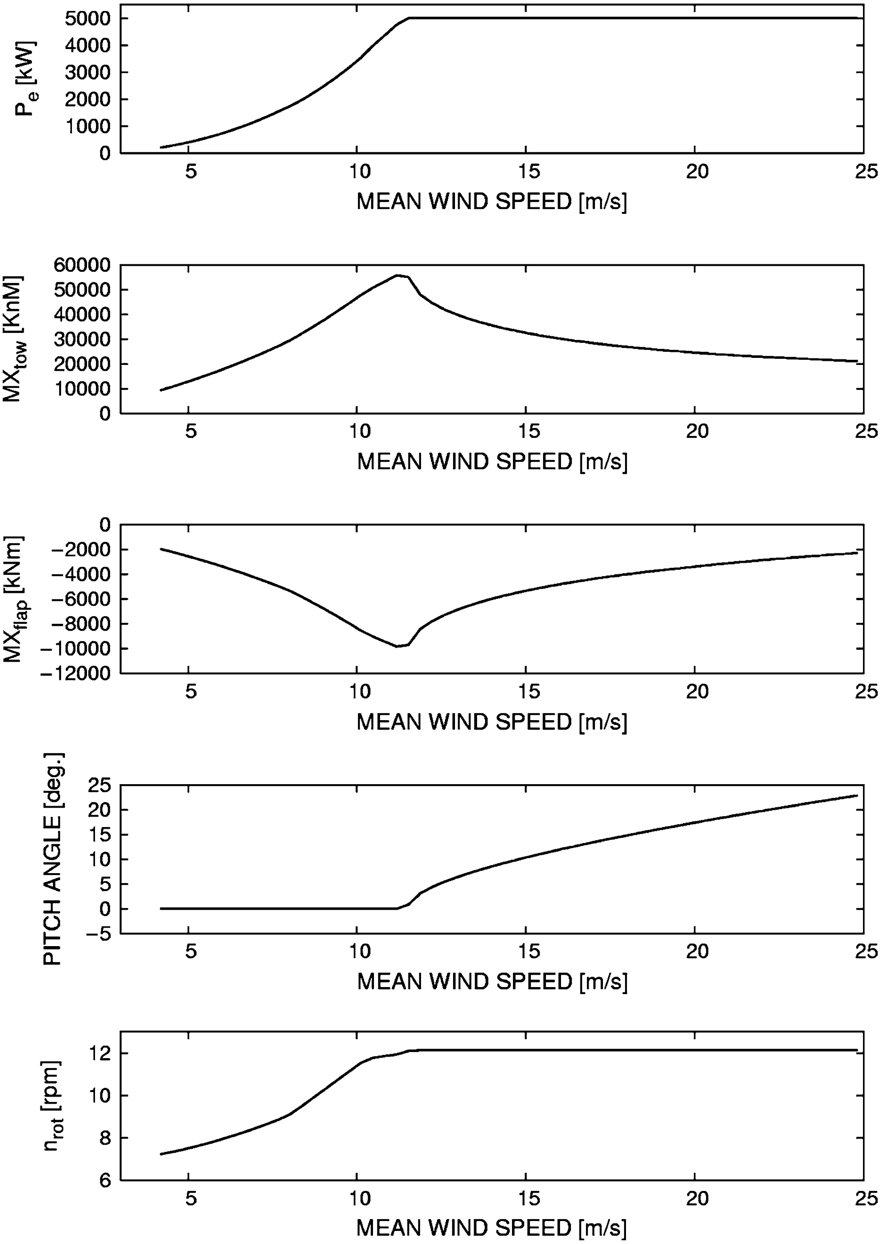

Fig. 2 Different loads and control parameters as function of mean wind speed

Between 11 and 12 m/s the turbine reaches its nominal electrical power output of 5 MW and above this wind speed, P_e is kept constant by pitching the blades so that the effective angle of attack is reduced. Below rated power the rotor rotational speed n_{rot} increases as function of wind speed in order to track a constant, maximum rotor power coefficient $C_{P.}$ The tower bottom bending moment MX_{tow} reaches a maximum at rated power and then decreases considerably for higher wind speeds due to the pitching of the blades. The same trend is seen for the flapwise blade root bending moment MX_{flap} in Fig. 2.

3 Loads from Wind Shear

For smaller rotors, the wind shear does not contribute much to the total loading. But for bigger rotors with rotor diameters now exceeding 120 m, the variation in average wind speed for the blade in bottom position to the blade in top position can be considerable and thus cause important dynamic loading. The wind shear depends heavily on the atmospheric stability conditions which often show a 24 h cycle. During the night the conditions are stable due to cooling of the surface and a strong shear is developing. However during daytime the surface will be heated again and a mixing in the boundary layer will reduce the shear.

As an example, the wind speed measured over a period of 1 day at six different heights at the test site for MW turbines at Høvsøre [6] in Denmark is shown in Fig. 3. At around 18:00 o'clock, a strong wind shear developed with a maximum difference in wind speed of about 5 m/s from height 40 to 116 m, which is within the typical span of vertical position for the tip of a MW turbine. In the lower part of the graph, the wind direction measurements at three heights show that a considerable change in wind direction as function of height is linked to the strong wind shear. During daytime the wind shear almost disappears.

The dynamic loading from wind shear is mainly seen on the blades and in particular on the flapwise blade root moment MX_{flap} (Fig. 4). A simulation was run with a specified strong shear in the inflow and compared with a simulation with no shear. The shear causes a 1p variation in the flapwise moment, but still the amplitudes are small when compared with the variations in the edgewise moment due to the gravity of the blades.

4 Loads from Blades Passing the Tower

Almost all of the new turbines build today have a cylindrical tower and have the rotor on the upwind side of the tower. In this case, the load changes from the small distortion of the flow from the tower are of minor importance compared with the other types of loads. Most aerodynamic and aeroelastic models use a tower flow model based on the potential flow solution for flow around a cylinder. An example of a simulation using such model for the 5 MW RWT turbine at 8 m/s is shown in Fig. 5. It is seen that there is a maximum flow distortion about 1 m/s, but the influence on the variation of the lift on the blade is seen to be small. In some

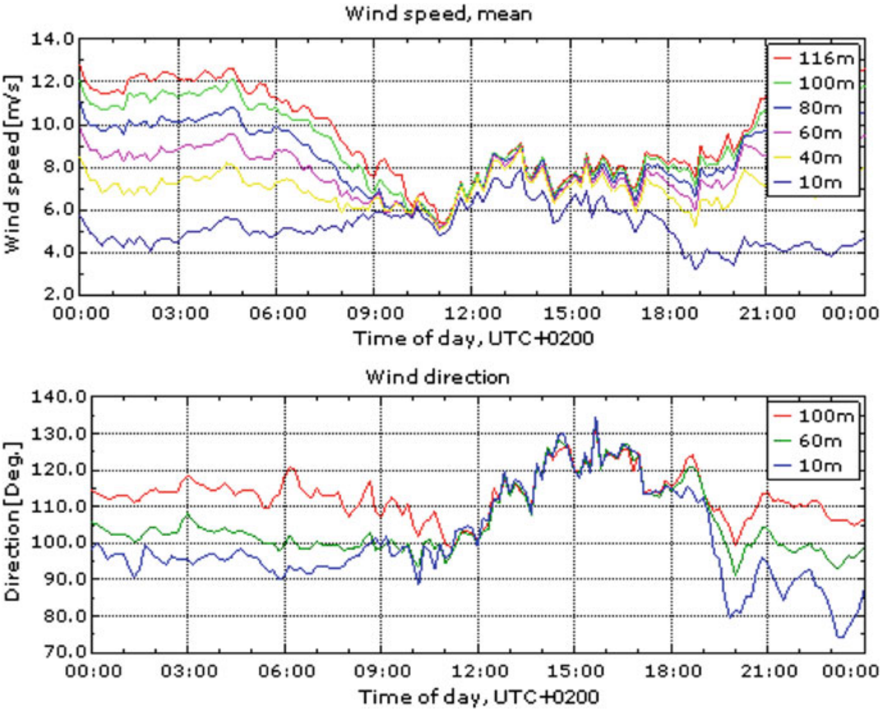

Fig. 3 Measured wind data at the Høvsøre Test site for MW turbines in Jutland, Denmark [6]

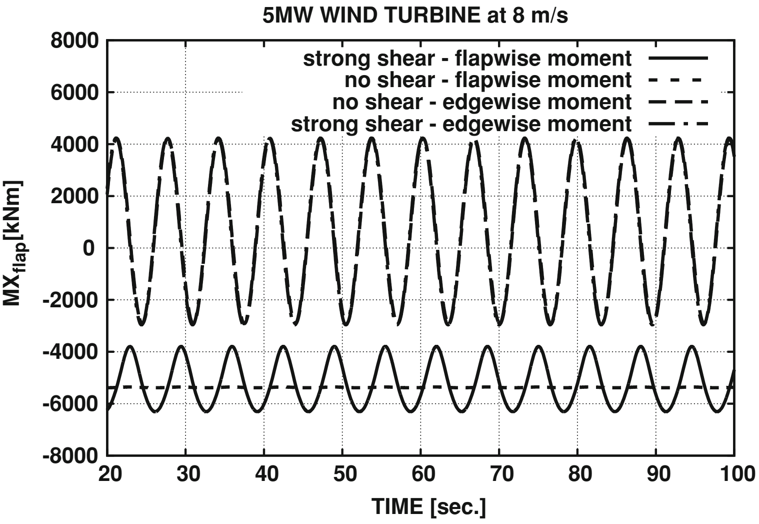

Fig. 4 Influence of wind shear on the flapwise and the edgewise blade root moment

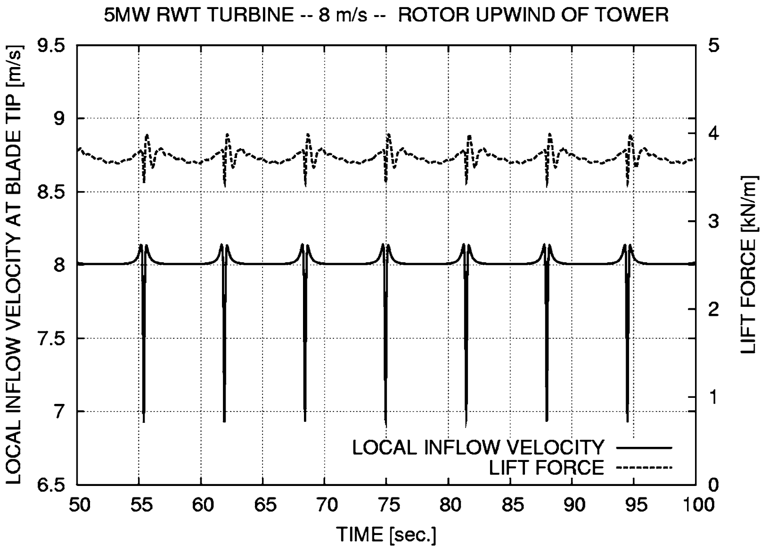

Fig. 5 Influence of the tower distortion of the flow for an upwind rotor, 5 MW RWT turbine, at 8 m/s with flexible blades. Data for the tip of the blade

situations with complex inflow to the rotor and where the blades bend considerably and thus are much closer to the tower, the influence from the tower on the loads can be more important.

However, for a rotor on the down wind side of the tower, the influence of tower on the loads is much more severe. For such turbine concepts as in the two-bladed teetering rotor (which has the rotor on the downwind side of the tower in order to increase the blade to tower clearance), direct loading on the structure from the blades passing the wake of the tower is more important. Another aspect is the generation of low frequency noise as investigated in a recent paper [7] for a two-bladed, downwind version of the 5 MW RWT turbine.

In this paper two different methods were used to compute the flow behind the tower. One model was a simple engineering model computing the steady deficit based on the boundary layer equations for a jet (named JET wake model). The other model was a 3D Navier–Stokes Solver EllipSys3D [8–10] computing the flow around a 16 m section of the tower. The iso-vorticity surface plot in Fig. 6 shows clearly the unsteady flow behind the tower due to the vortex shedding. The time trace of the computed thrust using the two different tower wake simulation models is shown in Fig. 7. The importance of modeling the unsteadiness in the wake flow from vortex shedding is clear, when comparing the thrust with the steady JET wake model. Details of the local aerodynamics on the outer part of the blade in Fig. 8 reveal the strong variation in lift coefficient. In general, it can be concluded that, for a down wind turbine the dynamic loading from the blade passing the tower deficit can be of major importance for the turbine response and generation of low frequency noise.

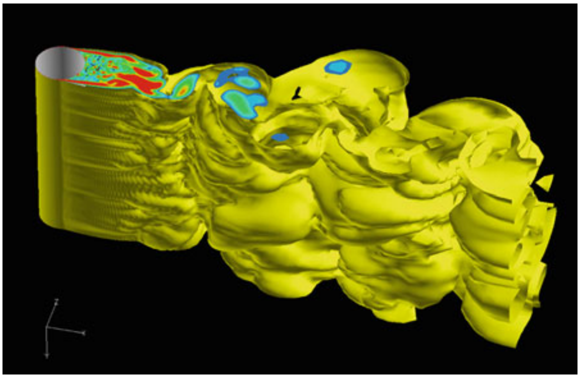

Fig. 6 Iso-vorticity surface of the flow around a circular cylinder with a diameter D of 4 m, a length l equal to 16 m and at a wind speed of 8 m/s. In the top of the figure a contour plot of the vorticity is shown to illustrate the complexity of the flow structure right behind the cylinder. Figure from [7]

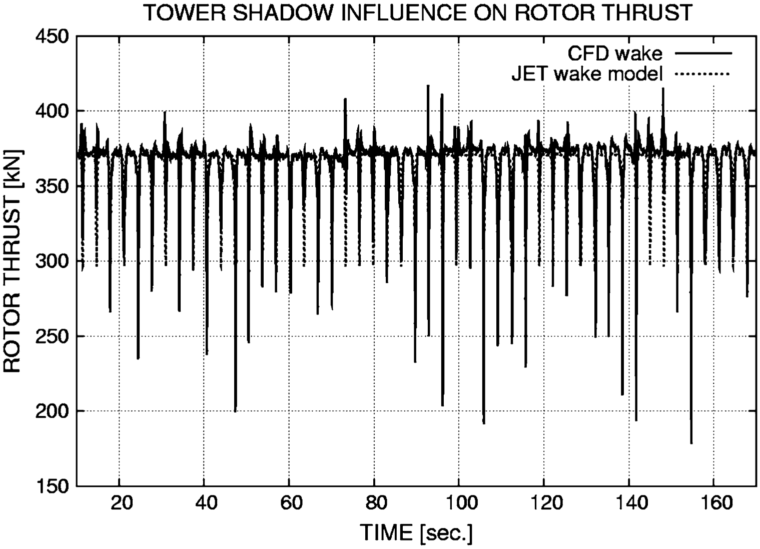

Fig. 7 Rotor thrust for a downwind, two-bladed rotor at 8 m/s. One simulation was carried out with the CFD unsteady wake data read into the aeroelastic simulation model (*solid line*). In the other simulation (*dashed line*) the tower wake deficit was simulated with an engineering steady model using a boundary layer solution for the development of a deficit in a flow. Figure from [7]

5 Loads from Wake Operation

The loads due to wake is becoming more and more important as almost all turbines now are build in wind farms or smaller clusters. Often, there will be an economic incitement to minimize the spacing between the turbines in order to save costs for land and costs for cabling between the turbines.

Based on a comprehensive analysis of measurements from wind farms, a rather simple methodology to take into account the increased loadings in wake operation

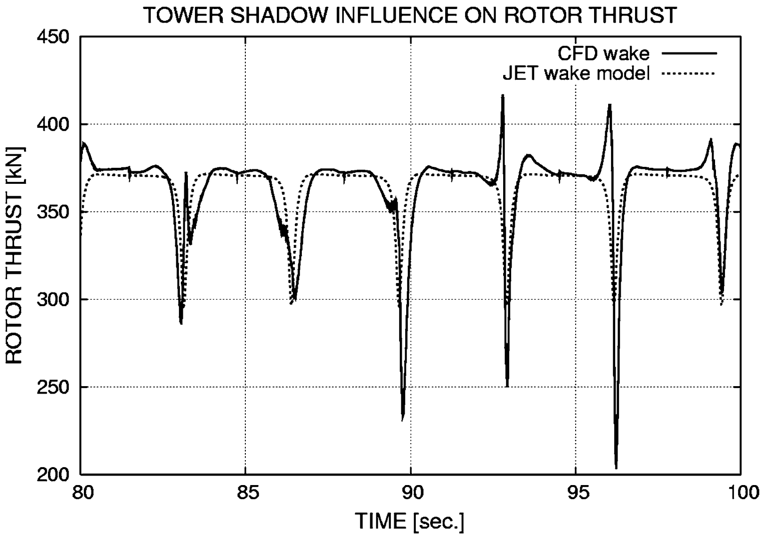

Fig. 8 Details of the variation of local lift coefficient on the outboard part of the blade from the simulation described above in Fig. 7

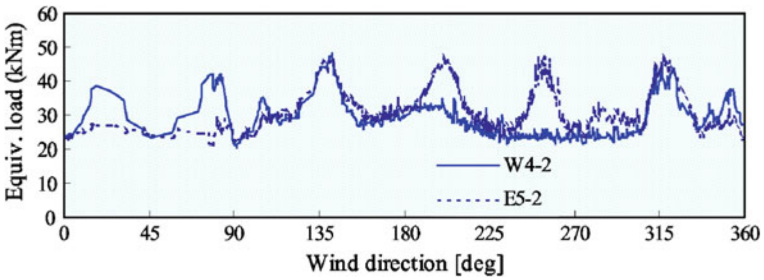

Fig. 9 Variation of the equivalent flapwise load for two turbines situated in the Vindeby Offshore Wind farm shown as function of wind direction at a wind speed between 8 and 9 m/s. Graph from [11]

has been developed [11] and now incorporated in the standard for wind turbine certification IEC61400-3 [12]. In short the basic idea in the method is that the different modifications of the flow in the wake influenced by turbine spacing, ambient wind speed and turbulence can be converted to an increase in the effective turbulence. As an example the measured increase in loading under wake operation for two wind turbines in the Vindeby Offshore Wind farm is shown in Fig. 9 [11]. Up to a 100% increase in loading is seen for the operation under wake compared with free inflow.

However, during the last few years there has been an increasing demand from the industry to have more detailed analysis models for wake operation in order to compute more accurate design loads, for example in the design of the yaw

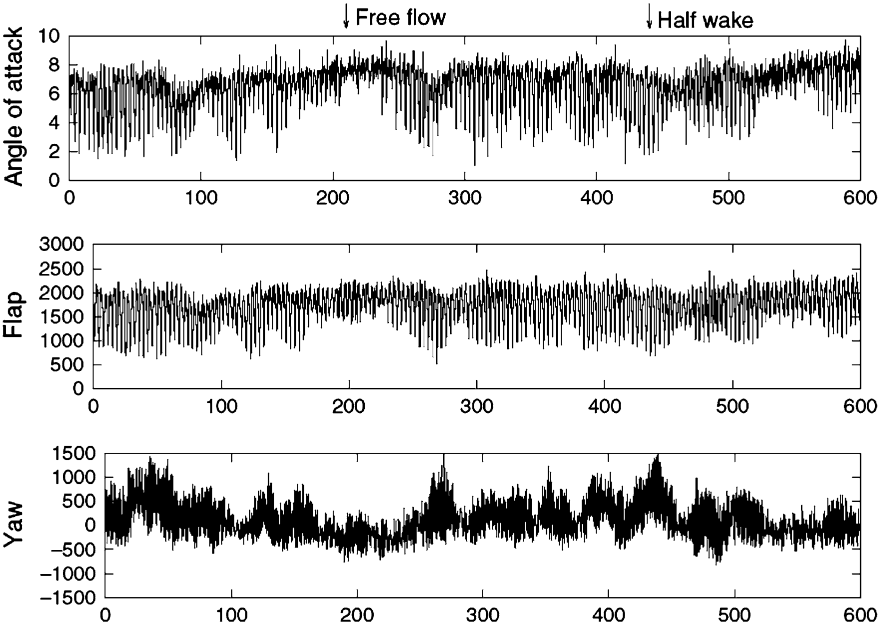

Fig. 10 Measured local inflow angle to the blade, flapwise blade root bending moment and yaw moment during half wake operation of a 2 MW turbine at 10 m/s [13]

drive systems. Also, for development of advanced control systems with individual pitch control for load alleviation, there is a need for such more detailed analysis models.

One example of a model with more detailed description of the flow mechanism in the wake has recently been presented [13]. The main elements in this model are: (1) the wake deficit (2) the meandering of the deficits and (3) increased wake turbulence. The mechanism of wake deficit meandering is considered as the most important mechanism for the dynamic loading in wake operation in this model and the influence of wake deficit meandering seems to be confirmed by measurements as illustrated in Figs. 10 and 11. The measured flapwise load and the yaw moment during a half wake operation for a 2 MW turbine is shown in Fig. 10 together with a measurement of the local inflow angle to the blade. From the amplitudes in local inflow and flapwise moment, it is seen that within one 10 min period, the wake influence changes from negligible to considerable level. This is caused by meandering of the wake deficit as indicated by variation of the yaw moment which will increase during half wake situations. The same tendencies in variations of the considered parameters are clearly seen in the simulation of the same wake operation case in Fig. 11. To summarize, the loading from wake operation is certainly an important contribution to the total loading on wind turbines operating in wind farms. Load simulation models are under further development for this important load case.

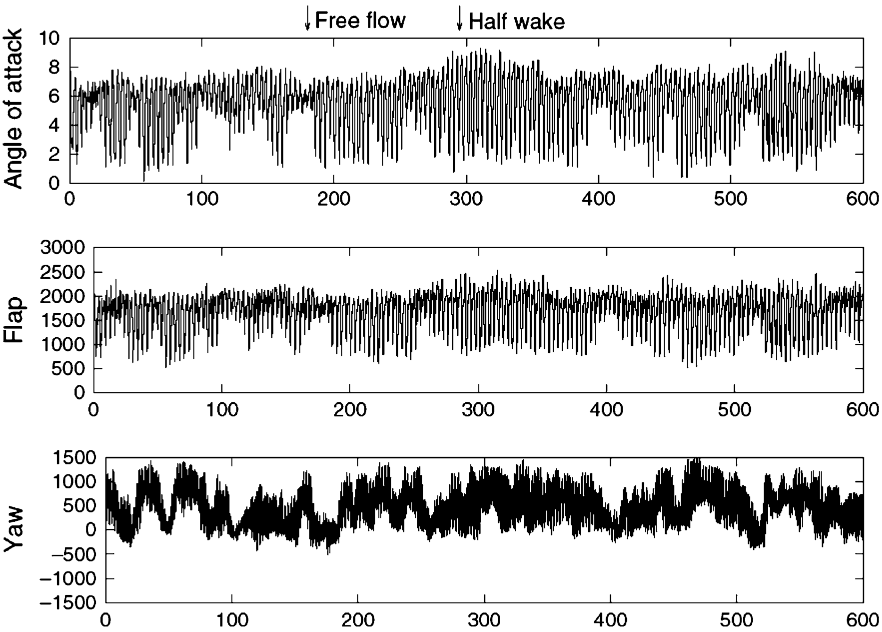

Fig. 11 Simulated local inflow angle to the blade, flapwise blade root bending moment and yaw moment during half wake operation of a 2 MW turbine at 10 m/s [13]

6 Loads from Turbulence

Turbulence in the inflow to the wind turbine rotor is the most important driver of the dynamic loads which can lead to failure of wind turbine components due to fatigue. Different models to simulate the turbulent structures have been derived among which the Mann model [8] and the Veers model [14] are the most commonly used. The Mann model is based on a model of the spectral tensor for the atmospheric boundary layer and allows the generation of all three velocity components in the turbulence. It is widely used in aeroelastic simulations. An example for the generated turbulence time series, for an average wind speed of 18 m/s over a period of 600 s (only 25 s are shown) and with turbulence intensity of 14%, is shown in Fig. 12.

The considerable difference in the turbulence at a fixed point in space and for a point on the rotating blade is illustrated in Fig. 13. At the point on the inner part of the blade, the turbulence velocity component vy is almost the same as in the fixed point coinciding with the hub center. However, at the tip of the blade vy is quite different and the mechanism is the so-called "rotational sampling of the turbulence" caused by the bladed slicing through the big structures of the turbulence. This mechanism is fundamental for the characteristics of the dynamic loading of a rotating wind turbine blade and is concentrating the aerodynamic load input

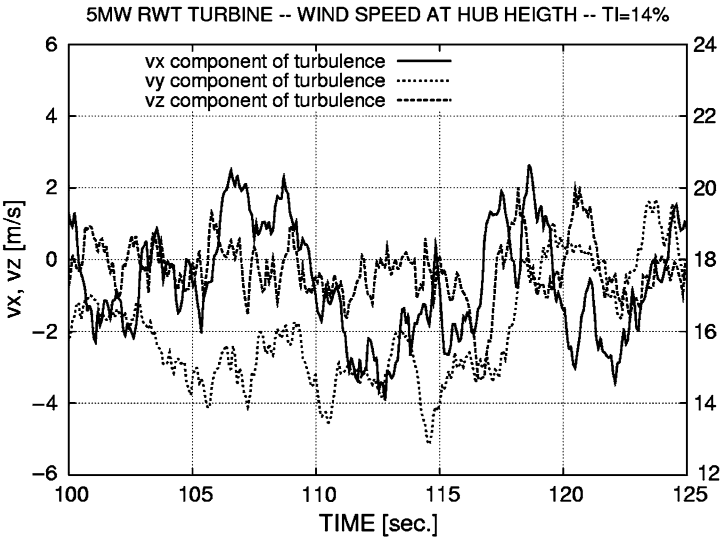

Fig. 12 Generated turbulence with the Mann model—data at hub center with a turbulence intensity of 14% and an average wind speed of 18 m/s

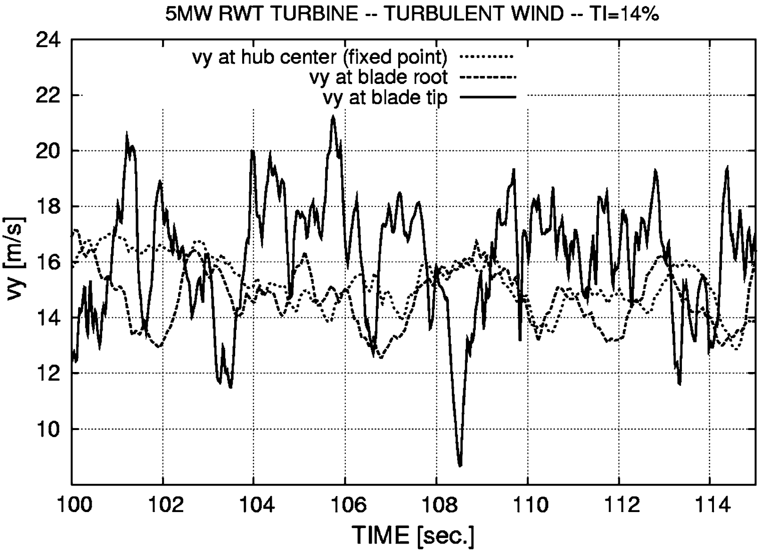

Fig. 13 A comparison of the longitudinal turbulence component *vy* at a fixed point (hub center) and with vy at a point at the tip of the rotating blade

at 1*p*, 2*p*, 3*p* etc. Finally, the dynamic flapwise blade force at the tip of the blade is shown in Fig. 14 and compared with the response of the blade in the form of the flapwise blade root moment which is seen to have a high dynamic content.

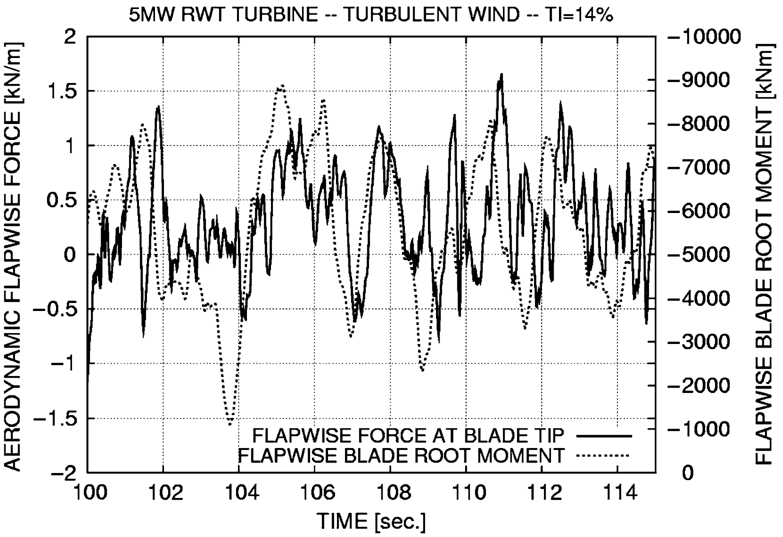

Fig. 14 The flapwise aerodynamic force at the tip of the blade and the flapwise blade root moment

7 Loads from Waves

Wave loading on the bottom of the tower is an important load type for off-shore turbines. The increased loads are mainly seen on the tower and in particular the supporting foundation submerged in the water. In the example shown in Fig. 15, the 5 MW RWT turbine is placed on a 30 m long monopile. Regular waves with a height of 3 m and a wave time of 10 s are generated and applied on the monopile. This loading is then combined with the wind turbulence on the rotor. It is seen that both load types are comparable in magnitude, though the frequency level varies.

8 Analysis of Loads for Design and Certification

The primary objective of simulation of loads for wind turbines is to be able to design the turbine components to an appropriate safety level and to ensure the structural integrity of the turbine and its sub components.

As part of the design process—and to ensure the safety level—most turbines are subjected to a certification process. Usually two different approaches are followed here: a new turbine design is often subjected to a type of certification process, while a turbine with design modification for a specific site (e.g. a new tower or foundation) can be subjected to a project certification process. The main difference between these two certification types is that, where a type certification typically is

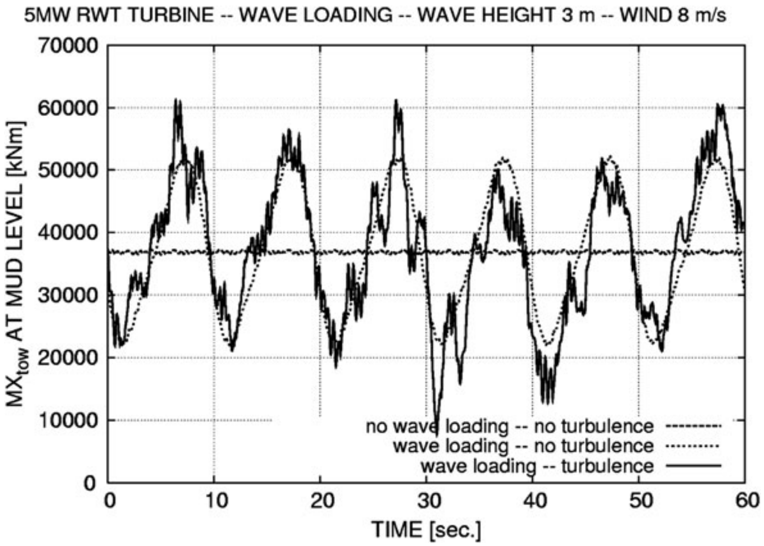

Fig. 15 The combination of wave loads on the tower and wind loads on the rotor. Turbine on a 30 m monopile and 30 m water depth

based on environmental conditions from design standards, the project certification is based on site specific conditions for the actual site.

9 Standards Used in Certification

The dominant international standard for design of wind turbines is the IEC61400-1 standard [15] for on-shore wind turbines and the IEC61400-3 standard [12] for offshore wind turbines. The latter one is often used in combination with the DNV offshore standard [16].

These standards are classification standards, meaning that they operate with a number of turbine design classes which can be chosen for a specific design. For each of these classes, a set of environmental conditions (e.g. mean and extreme wind speeds) are provided and the design of the turbine is based on these environmental conditions.

When the turbine is considered for a specific site at a later stage, a site-assessment process takes place. In the site-assessment process, the structural integrity of the turbine and the sub components must be demonstrated—based on an assessment of the site complexity and the actual wind conditions at the site. Two different approaches can be followed: It can be demonstrated that all the environmental conditions at the actual site is less severe than the design (standard) conditions used for design of the turbine and its components, or it can be

Table 1 Overview of turbine classes in IEC61400-1 [15] (ed. 3.0 “Copyright © 2005 IEC Geneva, Switzerland, www.iec.ch”)

Wind turbine class		I	II	III	S
V_{ref}	(m/s)	50	42.5	37.5	Values specified by the designer
A	I_{ref} (–)	0.16			
B	I_{ref} (–)	0.14			
C	I_{ref} (–)	0.12			

V_{ref} is the reference wind speed for the classes, corresponding to the 50-year mean value (and five times the annual average wind speed) and I_{ref} is the expected value of the turbulence intensity at 15 m/s

demonstrated that the structural integrity of the turbine components is sufficient for the site-specific conditions.

A site-assessment is often based on the last mentioned approach: the structural integrity is demonstrated for the site-specific conditions, since it is often the case that some parameters in the set of environmental conditions are more severe than the design conditions, while other parameters are less severe than the design conditions.

To exemplify the basic conditions provided in the standards, the IEC61400-1 classes are given in Table 1.

The parameters comprise of values for the 50-year extreme wind speed (and annual average wind speed) together with parameters describing the turbulence intensity as in Fig. 16. The designer can now choose a turbine class and all relevant parameters needed for establishing the design load basis as provided in the standard.

A large number of load cases and situations are given in the standards, aiming at representing the most significant conditions that the turbine may experience during its life time. The load cases consist of a combination of operational modes and external conditions. The operational modes cover normal power production, fault conditions and special modes like transport and assembly. The external conditions comprise different wind situations and other load generating conditions, for example earthquake and lightning.

The list of load cases from IEC61400-1 is given in Table 2. The load cases are combinations of turbine mode and appropriate external conditions. The turbine modes consist of normal power production, power production with faults, start-up and shut-down cases, normal parked condition, parked condition with faults and special cases representing transport, assembly, maintenance and repair. For each of the turbine modes listed, corresponding wind and other conditions are provided.

Sample time series of selected sensors are illustrated in Figs. 17 and 18, for two load cases that are extreme operating gust during normal production and extreme turbulence intensity during normal production. The first case is simulated without turbulence while the second case is a situation with turbulence.

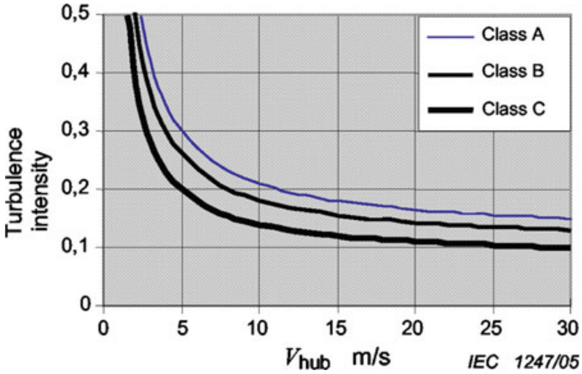

Fig. 16 Turbulence intensities from IEC61400-1 [15] (ed. 3.0 “Copyright © 2005 IEC Geneva, Switzerland, www.iec.ch”)

10 Fatigue Load Analysis

The main objective of the fatigue load analysis is to ensure the design against all load variations occurring during the life time. This means that all possible load cases must be considered and combined and the total fatigue loads are an accumulation of these load cases.

For a given component, the reference value for the fatigue loads are the SN-curve, describing the fatigue life in number of load cycles (N) as function of the stress or strain level (S) as in Fig. 19. This curve depends on the specific material used, and it is usually established using constant amplitude load cycles at different stress or strain levels. For a constant amplitude load time series, it is straightforward to evaluate whether the component will fail due to fatigue—at the correct stress/strain level it must be checked if the number of load cycles are larger or smaller than the fatigue limit from the SN-curve.

Wind turbine load time series are not constant amplitude load series and some effort must be put into converting the (often) stochastic load time series into a format where it is possible to compare with the SN-curve values.

For this a counting procedure is applied—usually the Rainflow counting method, where load cycle amplitudes and corresponding number are counted. The result of the Rainflow counting is a histogram of load cycle levels and number of load cycles at each level. Typically, the number of load levels is 30–50. An example is illustrated in Fig. 20.

The Rainflow counting can be considered as a simple rearrangement of the original load time series as in the schematic illustration in Fig. 21. A complete Rainflow cycle counting procedure includes a registration of the mean level for each load cycle, too. This is important for some materials due to the dependency of the fatigue properties (SN-curve) from mean stress/strain level.

In order to quantify the fatigue impact for a wind turbine component, the fatigue damage is introduced. For a single load range R_i the definition of the fatigue damage is: $d_i = 1/N_i$, where N_i is the acceptable number of load ranges from the material *SN*-curve. The basic assumption for this is the Palmgren-Minor

Table 2 List of load cases from IEC61400-1 [15] (ed. 3.0 "Copyright © 2005 IEC Geneva, Switzerland, www.iec.ch")

Design situation	DL C	Wind condition	Other conditions	Type of analysis	Partial safety factors
(1) Power production	1.1	NTM $V_{in} < V_{hub} < V_{out}$	For extrapolation of extreme events	U	N
	1.2	NTM $V_{in} < V_{hub} < V_{out}$		F	*
	1.3	ETM $V_{in} < V_{hub} < V_{out}$		U	N
	1.4	ECD $V_{hub} = V_r - 2$ m/s, V_r>, V_r +2 m/s		U	N
	1.5	EWS $V_{in} < V_{hub} < V_{out}$		U	N
(2) Power production plus occurrence of fault	2.1	NTM $V_{in} < V_{hub} < V_{out}$	Control system fault or loss of electrical network	U	N
	2.2	NTM $V_{in} < V_{hub} < V_{out}$	Protection system or preceding internal electrical fault	U	A
	2.3	EOG $V_{hub} = V_r \pm 2$ m/s and V_{out}	External or internal electrical fault including loss of electrical network	U	A
	2.4	NTM $V_{in} < V_{hub} < V_{out}$	Control, protection, or electrical system faults including loss of electrical network	F	*
(3) Start up	3.1	NWP $V_{in} < V_{hub} < V_{out}$		F	*
	3.2	EOG $V_{hub} = V_{in}$, $V_r \pm 2$ m/s and V_{out}		U	N
	3.3	EDC $V_{hub} = V_{in}$, $V_r \pm 2$ m/s and V_{out}		U	N
(4) Normal shut down	4.1	NWP $V_{in} < V_{hub} < V_{out}$		F	*
	4.2	EOG $V_{hub} = V_r \pm 2$ m/s and V_{out}		U	N
(5) Emergency shut down	5.1	NTM $V_{hub} = V_r \pm 2$ m/s and V_{out}		U	N
(6) Parked (standing still or idling)	6.1	EWM 50-year recurrence period		U	N
	6.2	EWM 50-year recurrence period	Loss of electrical network connection	U	A
	6.3	EWM 1-year recurrence period	Extreme yaw misalignment	U	N
	6.4	NTM $V_{hub} < 0{,}7\ V_{ref}$		F	*
(7) Parked and fault conditions	7.1	EWM 1-year recurrence period		U	A
(8) Transport, assembly, maintenance and repair	8.1	NTM V_{maint} to be stated by the manufacturer		U	T
	8.2	EWM 1-year recurrence period		U	A

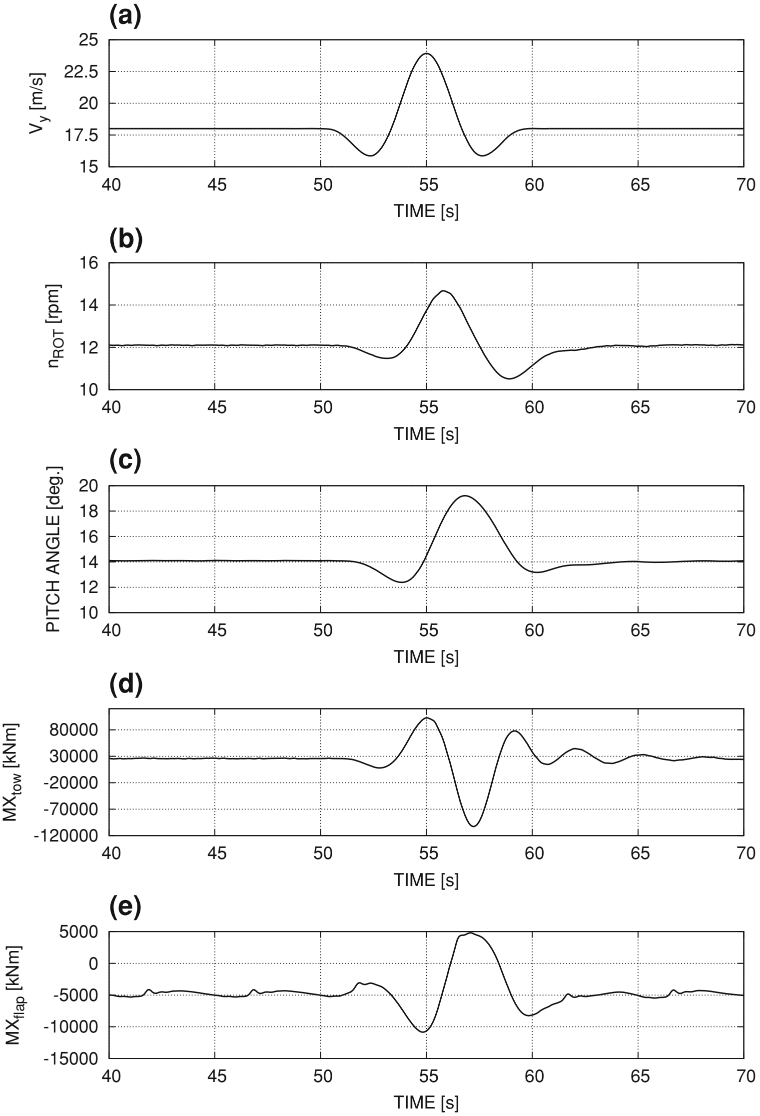

Fig. 17 Sample simulation EOG gust during normal operation. **a** Wind, **b** rotational speed, **c** Pitch, **d** tower bottom moment and **e** flapwise moment

linear damage rule, stating that the damage from several load ranges can be added linearly. The damage caused by a number of load ranges n_i, at the load range R_i is:

$$D_i = n_i\, d_i = \frac{n_i}{N_i} \tag{1}$$

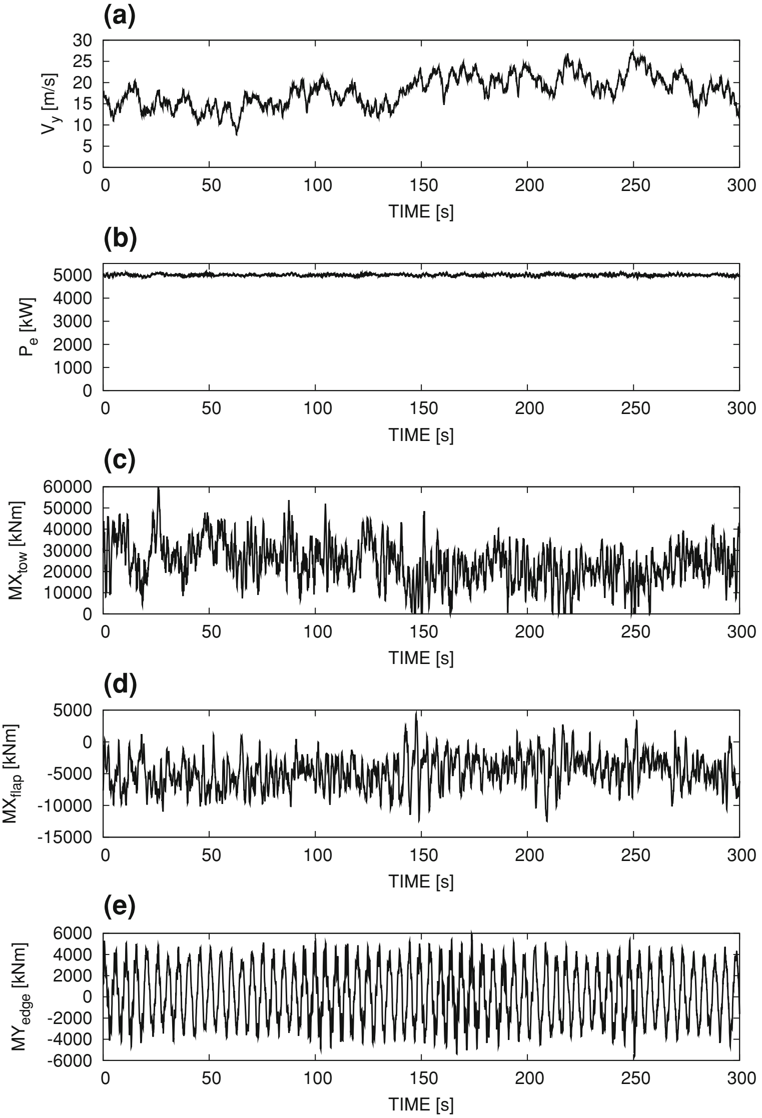

Fig. 18 Sample simulation extreme turbulence at 18 m/s. **a** wind, **b** electrical power, **c** tower bottom bending moment, **d** flapwise blade root moment, **e** edgewise blade root moment

By this definition of d_i, it follows that if $D_i = n_i\, d_i$ equals unity, fatigue failure will occur. Assuming a linear relation between the material stress level and the number of cycles in a log–log plot:

$$\log S_0 - \left(\frac{1}{m}\right) \log N_i = \log S_i \tag{2}$$

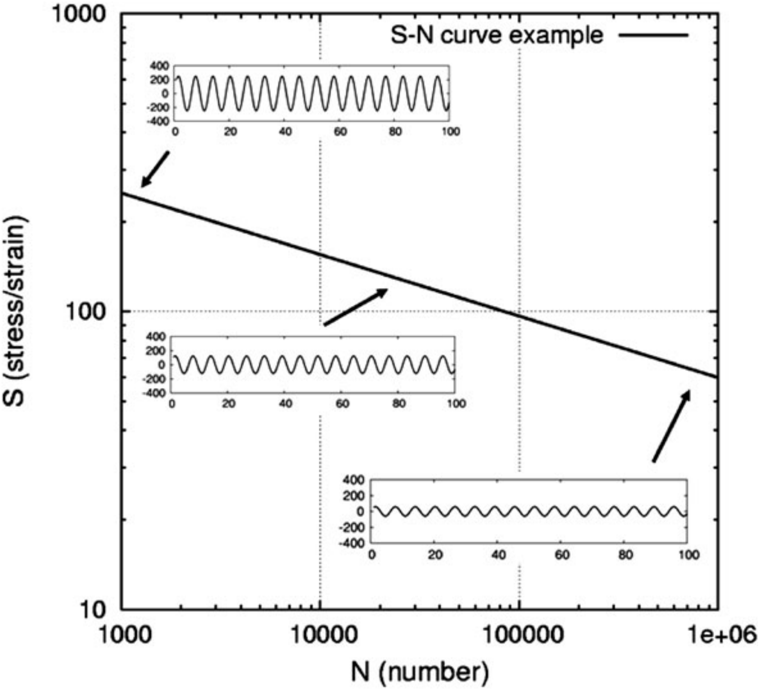

Fig. 19 Establishment of the SN-curve

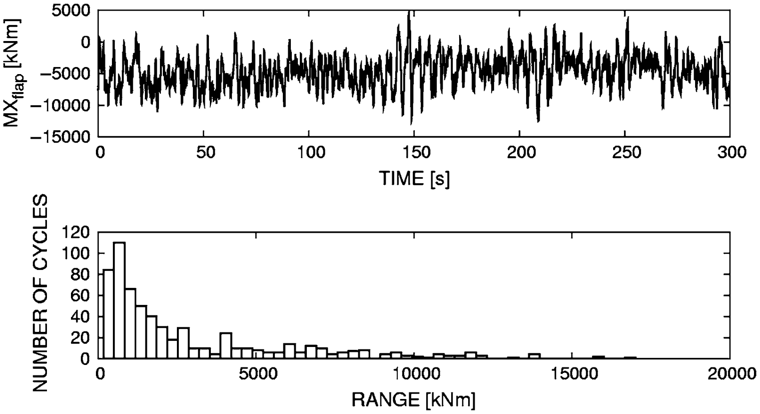

Fig. 20 Rainflow counting of a stochastic time series

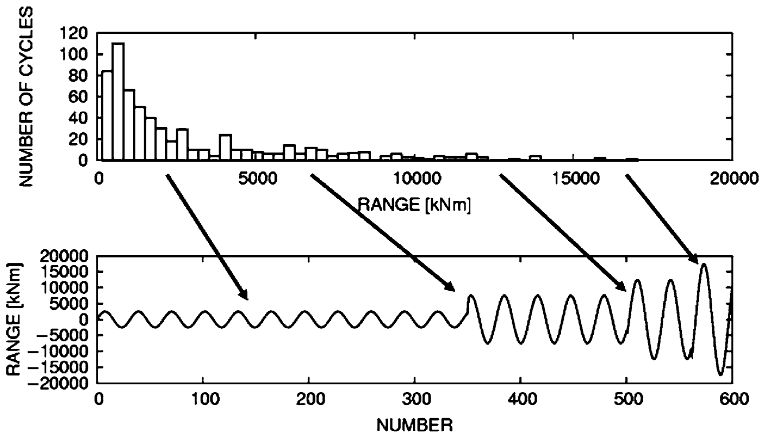

Fig. 21 Rainflow counting is a rearrangement of the original time series

or

$$N_i = \left(\frac{S_0}{S_i}\right)^m \tag{3}$$

where S_0 is the stress corresponding to $N = 1$ (the static strength), S_i is the stress corresponding to R_i and m is the SN-curve exponent, the damage can be expressed in the stress level as:

$$D_i = n_i\, d_i = \frac{n_i}{N_i} = \frac{n_i}{(S_0/S_i)^m} = \frac{n_i\, S_i^m}{S_0^m} \tag{4}$$

Since damage is usually used as a relative measure of fatigue impact, this is often simplified to (neglecting S_0^m and converting to load ranges instead of stress ranges):

$$D_i = n_i\, d_i = n_i\, R_i^m \tag{5}$$

which now express the total relative damage from load level i. The total damage is obtained by adding the relative damage contribution corresponding to several load ranges of different size, linearly:

$$D = \sum n_i\, R_i^m \tag{6}$$

The damage is a rather unphysical quantity and it is usually more convenient to evaluate the fatigue impact in more physical quantities. We now define a damage equivalent load range R_{eq} and the corresponding number of load ranges n_{eq}, which cause the same damage as the real load spectrum with several load levels, $R_i(n_i)$:

$$D = \sum n_i\, R_i^m = n_{eq}\, R_{eq}^m \tag{7}$$

which can be expressed as

$$R_{eq} = \left(\frac{\sum n_i R_i^m}{n_{eq}} \right) \tag{8}$$

This definition of the damage equivalent load range is well known in fatigue analysis and often used in wind turbine load analysis.

If several load cases are to be combined (for example different wind speeds), the number of load cycles in all load ranges can be added according to a prescribed probability of the different load cases. Afterwards, the life time equivalent load range can be calculated, as described previously. Often this is now denoted the life time equivalent load range.

11 Ultimate Load Analysis

The objective of the ultimate load analysis is to ensure the structural integrity against the largest loads experienced during the life time of the wind turbine or its components. Usually, two different approaches are applied for this.

For extreme load cases, for example with a return period of 50 years, a direct simulation method is used. Several load simulations are carried out, and the design load is the average value of the maxima for each simulation. For other load cases,

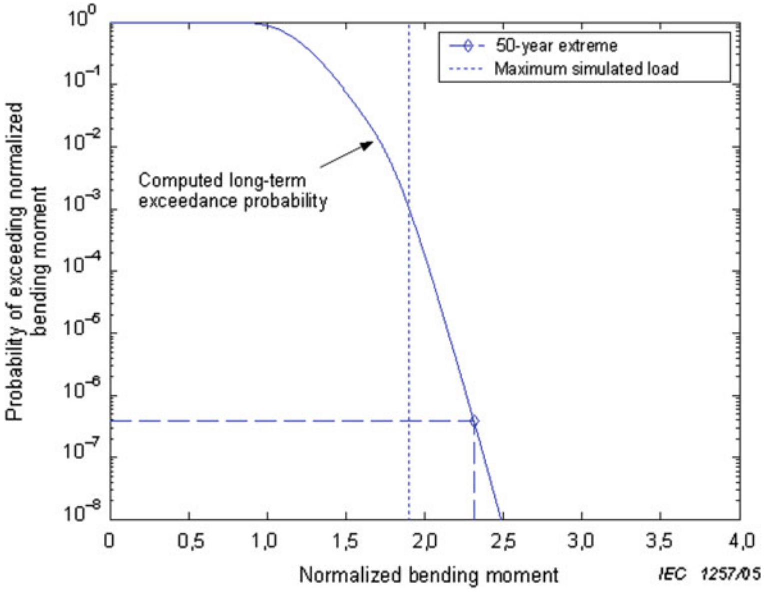

Fig. 22 Illustration of an extrapolated probability function. From IEC61400-1 [15] (ed. 3.0 “Copyright © 2005 IEC Geneva, Switzerland, www.iec.ch”)

e.g., during normal operation, the duration of the simulations is very short compared to the duration of the situations in real life. This must be accounted for in the analysis of these load cases. In the IEC61400-1 [15] standard, methods are proposed to take this into consideration.

These methods are based on the assumption that the largest load values occur at widely separated times and are statistically independent. This means that the extreme values of the load signals follow a Gumbel distribution:

$$\mathrm{Prob}(F_{\mathrm{ext}} > F \text{ given } V, T) = 1 - ((F_{\max}(F \text{ given } V)))^{E(n \text{ given V,T})} \tag{9}$$

where $F_{\max}(F \text{ given } V)$ is the short term probability distribution function of the local maxima for the load signal process, and $E(n$ given $V,T)$ it the average number of local maxima in the time T (Fig. 22).

The combination of all load cases must be considered, and this involves integration from cut-in wind speed V_{in} to cut-out wind speed V_{out}:

$$\mathrm{Prob}(F_{ext} > F \text{ given } T) = P_e(F, T) = \int_{V_{in}}^{V_{out}} \mathrm{Prob}(F_{ext} > F \text{ given } V, T) p(V) dV \tag{10}$$

where $p(V)$ is the probability of the wind speed V. The acceptable probability relates directly to the integrated probability and the return period time T_r:

$$P_e(F, T) = \frac{T}{T_r} \tag{11}$$

An example of the analysis is given in IEC61400-1 [15], where a systematic description of the procedure is given too. Once the ultimate loads are identified, the design can be checked directly to ensure the proper structural integrity.

12 Typical Design Conditions

In order to illustrate the importance of different load cases for the accumulated fatigue damage, a very simplified load basis is considered (Figs. 23, 24, and 25). In total, 38 load situations are considered, #1 to #24 being the normal operation cases, #25 to #31 being start, stop and error situations and finally #32 to #38 being stand still situations. It must be stressed that this load basis is simplified, whereas several hundreds of simulations are required in a real design situation.

In the figures, the relative damages for these load cases are illustrated for selected load sensors. The main conclusion from this is that all load cases are important. The fatigue damage for some sensors is dominated by few load cases, but for other sensors, other load cases can be the important ones. As an example there is a big difference of the relative damage distribution for the edgewise and flapwise blade root moment as depicted in Fig. 23. The reason is that the edgewise

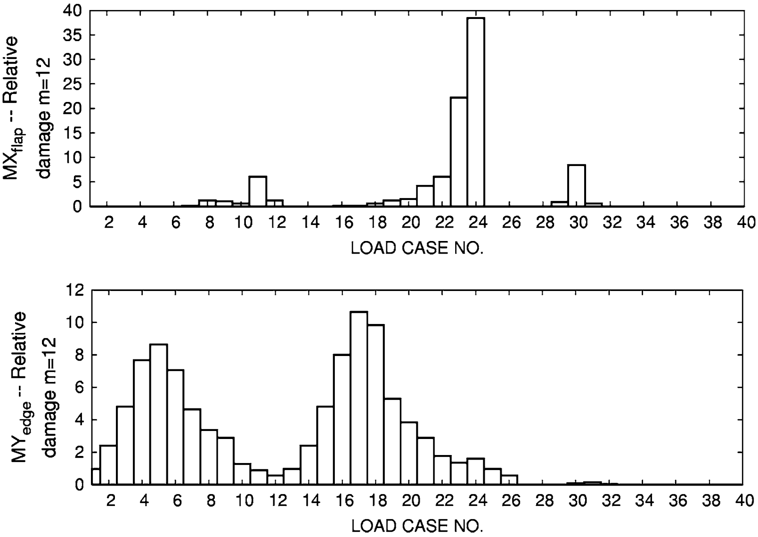

Fig. 23 Distribution of fatigue damage for a simplified load basis, consisting of 40 simulations. *Upper plot* is flapwise blade root moment and *lower* is edgewise blade root moment

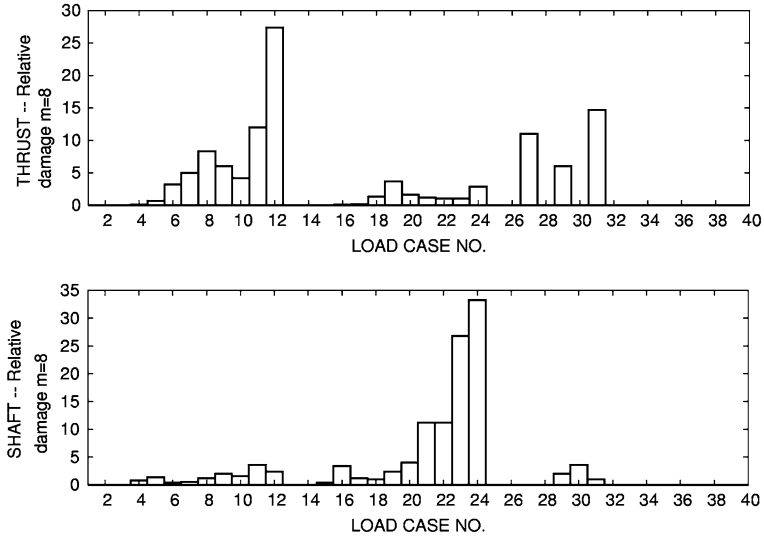

Fig. 24 Distribution of fatigue damage for a simplified load basis, consisting of 40 simulations. *Upper plot* is rotor thrust force and *lower* is shaft bending moment

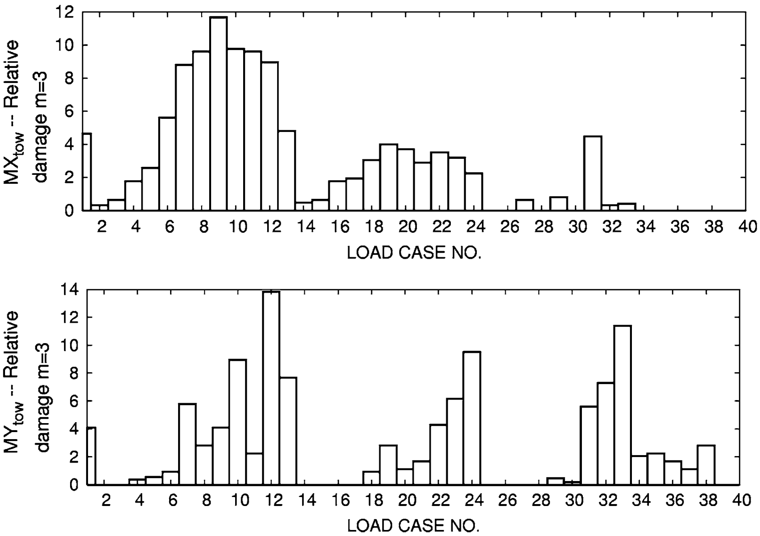

Fig. 25 Distribution of fatigue damage for a simplified load basis, consisting of 40 simulations. *Upper plot* is tower bending moment in the longitudinal direction and *lower plot* is transverse tower bending moment

dynamic loading is mainly due to dynamic loads from the gravity of the blade whereas the flapwise dynamic loading is mainly due to aerodynamic forces from the turbulence.

Acknowledgments The author thanks the International Electrotechnical Commission (IEC) for permission to reproduce information from its International Standard IEC 61400-1 ed.3.0 (2005). All such extracts are copyright of IEC, Geneva, Switzerland. All rights reserved. Further information on the IEC is available from www.iec.ch. IEC has no responsibility for the placement and context in which the extracts and contents are reproduced by the author, nor is IEC in any way responsible for the other content or accuracy therein.

References

1. Øye S (1996) FLEX4 simulation of wind turbine dynamics. In: Proceedings of 28th IEA meeting of experts concerning State of the Art of Aeroelastic Codes for wind turbine calculations, ed B.M. Pedersen, held at the Technical University of Denmark, Lyngby, April 11–12, 1996. pp 129–135
2. Petersen JT (1996) The Aeroelastic Code HAWC—model and comparison. In: Proceedings of 28th IEA meeting of experts concerning State of the Art of Aeroelastic Codes for wind turbine calculations, ed B.M. Pedersen, held at the Technical University of Denmark, Lyngby, April 11–12, 1996, pp 129–135
3. Bossanyi EA (2003) GH Bladed Theory Manual. GH & Partners Ltd, Bristol
4. Larsen JT, Madsen HA, Hansen, AM, Thomsen K (2005) Investigation of stability effects of an offshore turbine using the new aeroelastic code HAWC2. In: Proceedings of Copenhagen Offshore Wind 2005

5. Jonkman J (2005) IEA Annex XXIII document on NREL's baseline wind turbine aeroelastic model. NREL/NWTC, August 11, 2005
6. http://veaonline.risoe.dk/ (2008)
7. Madsen HA, Johansen J, Sørensen NN, Larsen GC, Hansen, MH (2007) Simulation of low frequency noise from a downwind wind turbine rotor. Presented at the 45th AIAA Aerospace Sciences Meeting and Exhibit, held at Grand Sierra Resort Hotel, 8–11 Jan 2007 Reno, Nevada
8. Michelsen JA (1992) Basis3D—a Platform for Development of Multiblock PDE Solvers. Technical Report AFM 92-05, Technical University of Denmark, 1992
9. Michelsen JA (1994) Block structured Multigrid solution of 2D and 3D elliptic PDE's. Technical Report AFM 94-06, Technical University of Denmark, 1994
10. Sørensen NN (1995) General Purpose Flow Solver Applied to Flow over Hills. Risø-R-827-(EN), Risø National Laboratory, Roskilde, Denmark, June 1995
11. Frandsen S (2003) Turbulence and Turbulence Generated Fatigue Loading in Wind Turbine Clusters. Risø-R-1188(EN), Risø, Roskilde
12. IEC61400-3 (2005) Wind turbines—Part 3: Design requirements for offshore wind turbines. IEC TG88 WG3: Committee
13. Thomsen K and Madsen HA (2005) A new simulation method for turbines in wake—applied to extreme response during operation. Wind Energy 2005, **8**, pp 35–47
14. Veers PS (1988) Three Dimensional Wind Simulation. SAND88-0152, Sandia National Laboratories, Albuquerque
15. IEC61400-1 (2005) Wind turbines—Part 1: Design Requirements. International Electrotechnical Commission. IEC61400-1:2005 (E). Current edition: Ed. 3
16. DNV-OS-J101 (2004) Design of offshore wind turbine structures. Det Norske Veritas, Offshore standard

Author Biography

Dr. Helge Aagaard Madsen has taken his Masters and Doctoral degrees from the Aalborg University, Aalborg Denmark. His PhD project comprised of developing a flow model for vertical axis turbines and led to the formulation of the Actuator Cylinder flow model which is an extension of the well-known Actuator Disc model for horizontal axis turbines. Since 1984, Dr. Madsen has been working with wind energy research at Risø National Laboratory for Sustainable Energy, Technical University of Denmark and has now a position of "Research Specialist". His major areas of expertise are aerodynamics and aeroelasticity of wind turbines. He has been the leader for a number of national and international research programmes and has carried out a large scale experimental project on aerodynamics during the period from 1987 to 1993, which was part of a joint programme on aerodynamics within the European Union. Presently, Dr. Madsen is coordinating a big national project on experimental aerodynamics "The DAN-AERO MW project" comprising blade surface pressure measurements and inflow measurements on a full-scale 2 MW turbine. He has recently participated in the development of the aeroelastic code HAWC2 developed at Risoe DTU and is presently involved in the development of the Dynamic Wake Meandering (DWM) model for aeroelastic simulations on wind turbines in wakes.

Power Regulation Strategies for Wind Turbines

Mario Garcia-Sanz, Marta Barreras and Pablo Vital

Wind energy has widely grown through the last two decades. Due to the significant increase of the number of wind turbines connected to the grid, new technologies aimed to assure power system quality and stability have become an important area for research and development [1, 2]. In particular, the design of advanced control techniques has recently emerged as a crucial issue for wind energy to penetrate into the electrical market. On the other hand, the need of more reliable control systems has become even more crucial with the increasing size of the machines and the related shift of their natural frequencies [3–5]. As wind turbines become larger and more flexible, the design of innovative control strategies with load reduction as an explicit objective turns out to be more critical [6, 7].

As a first approach, some of the main control objectives to take into account in the design of a WT controller should include some of the following aspects:

- *Reliability and availability*: The design of advanced control techniques has to improve the reliability, long-term operation and high availability of the machines [8]. These features are even more relevant for offshore turbines due to the limited accessibility [9].
- *Energy capture maximisation*: The first requirement for turbine's control algorithms is to maximise the energy capture over the low-medium operating wind spectrum. This means to optimise the conversion efficiency below rated wind speed conditions and to limit energy production above rated in order to minimise the mechanical fatigue of the turbine structure [10].

M. Garcia-Sanz (✉)
The Milton and Tamar Maltz Professor in Energy Innovation Director, Wind Energy and Control Systems CenterCase Western Reserve University, 10900 Euclid Ave. Olin 605, Cleveland, OH 44106-7071, USA
e-mail: mario@case.edu

M. Barreras · P. Vital
M. Torres Diseños Industriales, Torres de Elorz, Navarra, Spain

S. Mathew and G. S. Philip (eds.), *Advances in Wind Energy Conversion Technology,* Environmental Science and Engineering,
DOI: 10.1007/978-3-540-88258-9_6,

- *Mechanical load and fatigue attenuation*: As turbines increase in size, alleviating structural loads plays a more important role in the design of controllers [6, 11]. Thus, one of the main purposes of the control system is to keep both the maximum mechanical loads on the turbine structure and the mechanical fatigue within the design limits. The latter is usually more critical because wind turbines are normally designed for a lifetime of 20 years.
- *Provide damping*: The mentioned increase in size of wind turbines leads to bigger blades and lighter and more flexible structures. As a consequence, the tower shifts its structural modes towards lower frequencies and the blade itself provides less damping. The natural flap (out of-plane) frequency of the blades also decreases as the size increases. The control system must ensure that the dynamics of the WT are sufficiently damped to avoid resonant modes in the closed-loop system that may be excited by external disturbances.
- *Energy quality and grid stability*: In the last few years, wind power quality demand has become essential since the increase of the number of wind farms has brought a significant impact on system stability and operation [1, 2]. Thus, the controller must assure the quality of the power supplied, including the ability to: (a) react to sudden voltage dips; (b) avoid power flickers; (c) correct the power factor; (d) contribute to control the grid frequency; (e) regulate the voltage; and (f) provide low harmonics content.

This chapter introduces the main characteristics and strategies of the control system for wind turbines (WT).

1 Control Strategies

Roughly speaking, there are essentially two types of wind turbines: specifically constant speed and variable speed machines. Until the end of the 1990s, the constant speed concept dominated the market. Nowadays, it still represents a significant part of the operating wind turbines, but gradual innovation has led to the emergence of variable speed designs.

Alternatively, there are three main strategies for regulating the amount of power captured by the rotor: passive stall control or fixed pitch [12, 13], variable pitch control [14, 15] and active stall control [16]. So far, over the whole size range, no one of them has taken the lead over the others. However, as machines get larger and the loads greater there is a trend toward pitch control and active stall control.

1.1 Constant Speed Wind Turbines

The configuration of a fixed speed wind turbine is based on a gearbox and an asynchronous generator, which is usually a squirrel cage induction generator to reduce costs (e.g. NEG Micon NM72/2000, Bonus 1300). The gearbox speeds up the rotational shaft speed from the rotor to a fixed generator speed (see Fig. 4). The generator produces electricity through a direct grid connection with a set of capacitors to compensate reactive power. Due to the lack of a frequency converter, the generator speed is dictated by the grid frequency.

One of the main drawbacks of the fixed speed operation is the poor aerodynamic efficiency, particularly at partial load operation. From the electrical system's point of view, another disadvantage is that this type of operation gives only a limited power quality because asynchronous generators demand reactive energy from the grid. This is the reason why they have to be connected through a set of capacitors. On the other hand, wind gusts provoke higher mechanical load variations and these wind fluctuations lead also to fluctuations of the generated electrical power.

1.2 Variable Speed Wind Turbines

Many different options have been developed to achieve some degree of speed variation [17]: (a) dual speed generators with pole switching; (b) high slip asynchronous generators for a low range of variable speed; (c) doubly fed induction generators for a moderate range of variable speed; and finally (d) direct drive systems for a wide range of variable speed. These techniques improve sound aspects and energy capture at low winds, and power quality at high winds.

Dual speed means that, by changing the number of pole pairs, the rotor spins at two different speeds: a lower speed at low winds, which improves performance and reduces noise emission; and a faster speed (lower number of poles) at high winds (e.g. Vestas V82-1.65, NEG Micon NM900/52).

Another alternative of the popular squirrel-cage asynchronous generator is the so-called slip control method, which adjusts the slip continuously (e.g. Vestas V80-1.8, V90-2.0). In this case, a wound rotor is connected to some variable resistors through slip rings. By changing the electrical resistance of the rotor it is possible to compensate small changes in rotational speed of about 10% of variation above synchronous speed, without varying the generator output frequency. The main drawback of this design is that the slip rings wear easily due to the movement. Some companies overcomes this difficulty by using an optical fibre to avoid physical contact [18].

Another approach which has a considerable dominance in the current market is the doubly fed induction generator (DFIG), also called wound rotor induction generator [19]. In this machine the stator windings are directly connected to the grid and a partial scaled frequency converter links the standard wound rotor and the grid (e.g. Gamesa G80-2.0, General Electric GE-1.5/77, Dewind-D70-1500). This configuration allows the machine to control the slip in the generator, and so the rotor speed can vary moderately, achieving a better aerodynamic efficiency. Besides, as the converter controls the rotor voltage in magnitude and phase angle, a partial active and reactive power control is also possible. As power electronics are not rated for full power capacity, simpler and less expensive converters can be employed. The main drawbacks of this design are the difficulty to work under voltage dips, the limitation to control effectively the grid variables with such a small converter, and the high maintenance costs of the gearbox.

In some designs a synchronous generator is indirectly connected to the grid through a full-power electronic converter which handles all the energy produced (see Figs. 1 and 6). This concept, also called direct drive machine, takes advantage of the wide range speed operation allowed by the full-scale frequency converter [14, 15, 20]. The generator can operate at any rotational speed of the rotor and the rotor operates at the optimal speed for each wind condition. Among its main advantages are the low maintenance costs and high reliability due to the omission of the gearbox, the improved aerodynamic efficiency, and the ability to assist the grid stability and performance. Both, a wound rotor (e.g. MTorres TWT-1.65/82, Enercon E66-1.8, E112-4500, Lagerwey LW72/1500) and permanent magnet rotor (e.g. Eozen-Vensys 77-1.5) designs can be used in this approach.

On the whole, the power electronics used to accomplish variable speed operation are a little more expensive. However, variable speed machines are able to reduce mechanical loading and drive train fatigue and to capture more energy over a wider range of wind speeds, something that increases remarkably the annual production. Another important advantage of some of the variable speed wind turbines is the ability to control independently their active and reactive power and thus to assist the power system.

1.3 Passive Stall Control

For passive stall controlled wind turbines, the generator reaction torque regulates rotor speed below rated operation to maximise energy capture. Whereas above

Fig. 1 Direct-drive variable-speed pitch-controlled turbine (Courtesy of MTorres)

rated operation, rotor speed is controlled by deliberately inducing stall over a specific wind speed (e.g. Ecotecnia 62-1.3, Made AE61-1.3, Bonus MkIV). This way, the power delivered by the rotor is limited at high winds, thanks to a particular design of the blades that provokes a loss of efficiency. For such stalling to take place it is essential to hold the rotor speed constant, and this is usually accomplish with an asynchronous generator connected to the electrical network. Additionally, in this type of control the pitch angle is fixed and tip brakes are the only part of the blade which can rotate with the aim of spilling off the spare energy to shut down the wind turbine.

1.4 Variable Pitch Control

In pitch control, the blades regulate the power delivered by the rotor either by pitching the blades towards the wind to maximise energy capture or by pitching to feather to discard the excess of power and to ensure that mechanical limitations are not exceeded (e.g. MTorres TWT-1.65/82, Nordex S77-1.5). At rated operation, the aim is to maintain power and rotor speed to their rated value. To achieve this, the torque is held constant and the pitch is continually changed following the demands of a closed-loop rotor speed controller that optimises energy capture and follows wind speed variations. In contrast, below rated operation there is no pitch control, the blade is set to fine pitch position to yields higher values of power capture and the generator torque itself regulates the rotor speed. In this case, the way to turn off the machine is simply by turning the blade to feather position, i.e. perpendicular to the wind. Consequently, pitch control requires variable speed operation allowing slight accelerations and decelerations of the wind turbine's rotor at wind gusts and lulls [5, 14].

1.5 Active Stall Control

This technique is a combination of stall and pitch control. Active Stall was the name used by NEG-Micon, now Vestas (e.g. NM72C/1500, NM82/1650), while a similar concept is named combi-stall by Bonus–Siemens (e.g. Bonus 1.3 MW/62, Siemens SWT-2.3-82). Active stall/combi-stall control has got the same regulation possibilities as the pitch regulated turbine, but using the stall properties of the blades. The blades are designed in a similar way as stall control blades but the entire blade can be turned ninety degrees to adjust its pitch. Thus, the blade tip brakes used in passive stall are not required. In this technique the blades are rotated only by small amounts and less frequently than in pitch control [12]. The idea is to pitch the blade gradually with a negative pitch angle, "pitch to stall", in order to optimise the performance of the blades over the range of wind speeds, especially with low wind speeds. The power control method adjusts the amount of blade that is at stall to compensate the reductions of power output. It allows a more accurate control at high wind speeds, resulting in a more constant power value at rated power.

As a summary, stall controlled wind turbines are still attractive because they are relatively simple to construct and operate and therefore are much cheaper. Nevertheless, during the last few years the market interest for the fixed speed operation has decreased slightly, and the trends have pointed to variable speed wind turbines. One of the main reasons is that the latter improves the power quality and produces more energy than stall machines [21]. Alternatively, among all the possible configurations, apart from fixed speed with passive stall control, variable speed together with pitch control is being one of the most demanded machines. Recently, some manufactures have also been using active stall control in conjunction with variable speed operation because it is not as complex and expensive as pitch control. In contrast, other configurations like fixed speed with variable pitch control, although very popular in the past, nowadays are generally rejected because they produced very large transients in the power output when controlling power.

2 Control System

The control system of a WT consists of a hardware/software configuration. It handles all the necessary variables and parameters to govern the wind turbine, aiming two overall objectives: reliability and performance. This binomial has changed over the time. Availability was the unique goal in the past, but nowadays

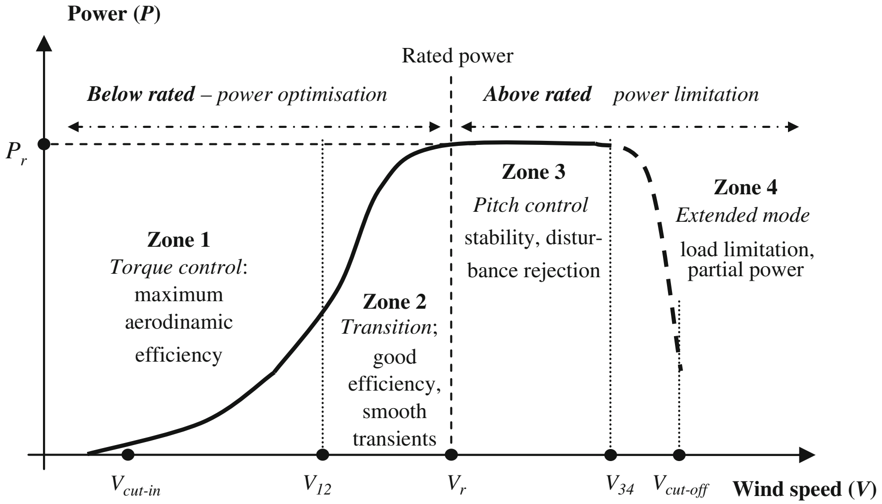

Fig. 2 Power curve of a wind turbine

that is not enough. Market increasingly requires more advanced control features. This is the reason why this section focuses on performance.

A generic qualitative power curve for a variable speed pitch controlled WT is shown in Fig. 2. Four zones and two areas are remarked. The rated power P_r of the wind turbine (i.e. the actual power supplied to the grid, which is the incoming wind power minus losses) separates the graph in two main areas: below and above rated power. Below rated the wind turbine produces only a fraction of its total design power, and therefore an optimisation strategy needs to be performed. In the other hand, above rated a power limitation strategy is required.

The four zones of the power curve present the following characteristics:

- *Zone 1. Torque control*: Lowest wind, between $V_{\text{cut-in}} = 3–4$ m/s and $V_{12} = 7–8$ m/s. The objective in this zone is to obtain the maximum aerodynamic efficiency. This is usually done by means of manipulating the electrical torque in order to get a particular and pre-fixed ratio (tip speed ratio) between wind speed and rotor speed. In that way, the maximum aerodynamic power coefficient C_p is achieved (see Fig. 3 and Eqs. 1 and 2).
- *Zone 2. Transition*: Medium wind, between $V_{12} = 7–8$ m/s and $V_r = 11–13$ m/s. In this zone it is not possible to get the desired tip speed ratio because rotor speed is near to maximum values. Torque has to be increased until the turbine reaches the rated power. This is usually done by following a high slope torque/rotor-speed reference or by implementing a closed-loop controller.
- *Zone 3. Pitch control*: High wind, between $V_r = 11–13$ m/s and $V_{34} = 20–25$ m/s. The blades have to move the pitch angle in order to limit the incoming power, control the rotor speed and minimise the mechanical loads at the same time. An important cost reduction and life operating augmentation can be achieved if load attenuation is targeted as a primary objective when designing the controller, or if a blade independent control strategy to reduce loads is performed [7].
- *Zone 4. Extended mode*: Very high wind, between $V_{34} = 20–25$ m/s and $V_{\text{cut-off}} = 25–30$ m/s. Although not very common, an extended mode in very

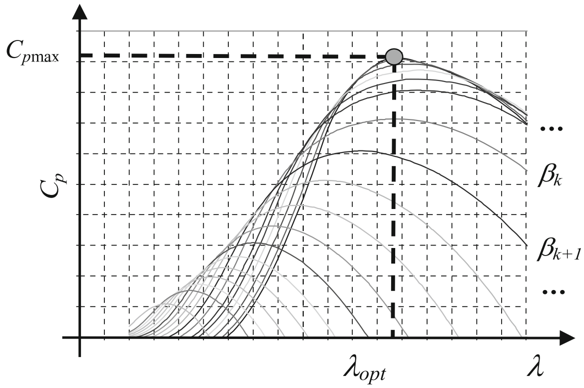

Fig. 3 C_p/λ curves, where $\beta_k < \beta_{k+1}$

high winds can be done by means of varying the pitch closed-loop performance. Through a rotor speed limitation, the extreme loads can be reduced.

To fulfil the control objectives detailed in the last sections, a complex hardware/software system has to be implemented. A certain number of sensors which provide information to the main control unit or controller are needed. This controller commands the actuators with appropriate outputs. A complementary and independent safety system is still needed to get redundancy and to guarantee the security of the wind turbine [22, 23].

2.1 Sensors

Some of the main measurements required to control effectively the wind turbine are the following:

- *Meteorological measurements*: anemometer, wind-vane, temperature. Wind speed is usually measured with an anemometer at the nacelle. The accuracy of this measurement is not good enough to be used in the controller, because of the existence of some wind acceleration due to the nacelle shape, some wind turbulences due to the rotor movement, and the fact that a single measurement is not representative enough of the mean wind speed that crosses the rotor surface. The use of wind speed estimators is sometimes proposed to improve control algorithms [24].
- *Angular measurements*: rotor speed, yaw angle, pitch speed and angle. Sometimes, an azimuth or rotor position sensor is also used to perform independent blade control.
- *Electrical measurements*: power, voltage and current on the generator, converter and grid, power factors, harmonics distortion (THD), etc.
- *Mechanical measurements*: torques, temperatures, tower vibration, nacelle acceleration, blade efforts, etc.

2.2 Controller

The controller is usually a real-time control industrial system with a dedicated microprocessor in which runs the main control software with the specific control algorithms. The principal functions of the controller are:

- Communication with the input/output system. Inputs are signals coming from the sensors whereas outputs are signals going to actuators. All these devices have an electronic interface to sample and translate physical signals to digital variables for the WT controller.
- Signal processing.

- Execution of control laws and supervision.
- Handling data acquisition for the SCADA system, for storage, maintenance and remote-operating purposes.

2.3 Actuators

- *Pitch*: The pitch system is a mechanical, electrical or hydraulic device, acting over the blade to turn it in both directions. The pitch system has a crucial role on the turbine, not only because it is the main actuator, but also because of the safety of the machine. A wrong operation of the pitch system will cause the turbine to suffer dramatic and irreversible damage. To avoid that, an autonomous and independent pitch system has to be implemented in each blade to get redundancy and reliability; if some error or malfunction occurs, the other two blades go to safety position. An energy storage device is also required to be able to move the blades during a grid loss.
- *Torque*: The generator torque is the other main actuator of a wind turbine. It is manipulated by means of a power drive or electrical converter. Its action response is fast, but smaller than the one of the pitch system. Generator torque is used below rated with the aim of maximising the aerodynamic efficiency, as explained below.
- *Yaw*: The yaw system is in charge of tracking the wind direction. It usually turns at a constant speed. Thus, a very simple configuration consisting of several motors working together is enough to position the nacelle.
- *Brakes*: The shaft brakes consist of some hydraulic devices able to actuate over the high speed shaft. Modern direct drive machines usually do not need a shaft brake, and the rotor is stopped only by means of a highly reliable pitch system.

2.4 Safety System

The safety system is a redundant hard-wired security-chain with autonomy to shutdown the WT in a secure mode under all circumstances. The safety system is capable to drive back the blades to feather position, to switch off every electrical device, to provide an emergency digital signal to the controller and to generate an appropriate alarm for the maintenance staff. Physically, it consists of a long path of contacts in series, beginning by a power supply which provides a reference voltage, and ending in a safety relay. The opening of any contact causes the loss of that reference voltage. Thus, the safety relay breaks the “OK” hard-wired signal of every subsystem (converter, pitch, yaw, brakes, etc.) causing the turbine to stop in a safe manner.

3 Main Control Loops

In the following paragraphs the main control loops of the wind turbine are described.

3.1 *Torque*

The incoming power P_v in a wind turbine is:

$$P_v(t) = T_v(t)\,\Omega(t) = 0.5\rho A C_p(t) V(t)^3 \cos^3[\alpha(t)] \tag{1}$$

where T_v is the aerodynamic torque, Ω the rotor speed, ρ the air density, A the rotor effective surface, V the wind speed, α the yaw angle error (nacelle-wind angle) and C_p the aerodynamic power coefficient, so that,

$$C_p(t) = f[\lambda(t), \beta(t)] \tag{2}$$

The aerodynamic design of the blades is such that the power coefficient C_p (as pitch angle β is kept constant) is a function of λ (tip speed ratio), defined as a function of the rotor radius R, rotor speed Ω and wind speed V, so that,

$$\lambda(t) = \frac{R\Omega(t)}{V(t)} \tag{3}$$

The electrical torque T_e is manipulated below rated power in order to get maximum aerodynamic efficiency C_p. This strategy aims to keep optimal the relation between wind speed V and rotor speed Ω as long as possible (see λ_{opt} in Fig. 3). It modifies the rotor speed by changing the electrical torque to follow the wind speed changes, and then keep $\lambda = \lambda_{\text{opt}}$.

Neglecting mechanical losses in the shaft, the aerodynamic torque T_v on the rotor is,

$$T_v(t) = 0.5\rho A C_p(t) V(t)^3 \cos^3[\alpha(t)] \Big/ \Omega(t) \tag{4}$$

Hence, for every value of rotor speed Ω, the resulting T_e (Eqs. 5 and 6) maximises the power capture at every wind speed.

$$T_e(t) = K_a \Omega(t)^2 \tag{5}$$

$$K_a = 0.5\rho A R^3 C_{p\max} \Big/ \lambda_{\text{opt}}^3 \tag{6}$$

where $C_{p\max}$ is the maximum power coefficient, obtained at λ_{opt} (see Fig. 3).

Equation 5 shows a very simple and useful expression to set up the torque below rated zone. The expression is based on the C_p/λ curves provided by the blade manufacturer (Fig. 3), which usually gives only a first approach for steady state and laminar flow conditions. For a more complete approach some improvement could be done by slightly changing Eqs. 5 and 6, taking into account some dynamic conditions. Due to the erosion and dirtiness of the blades, or due to the variation of the air density value at different weather conditions, some parameters such as C_p become time variant. A reduction of the value of the constant K_a, or the application of adaptive techniques to estimate it, could optimise the energy capture.

The electrical torque T_e obtained by Eq. 5 is not usually enough to complete the whole region below rated, because the rated rotor speed is reached before than the maximum torque. Hence, a different strategy has to be performed to increase the torque until its maximum (rated) value, usually following a high slope torque/rotor-speed reference or by implementing a closed-loop controller.

3.2 Pitch

The main purpose of the pitch loop is to control the rotor speed, limiting the incoming aerodynamic torque by moving the pitch angle. There are two possible strategies: pitch to feather and pitch to stall. The methodology to design the pitch control loop is based on the dynamic model of the aerodynamic torque (see next section for more details). As showed above, T_v can be expressed as a non-linear function that depends on the rotor speed, the wind speed and the pitch angle. A simple linear Proportional–Integral–Derivative PID controller [25] is a good starting point, although further considerations have to be observed [26]. As wind speed increases, the $\partial\Omega/\partial\beta$ ratio becomes higher. The controller will take this effect into account in order to keep the mechanical fatigue within the design limits, and to guarantee the system stability. The design can be carried out by using robust and/or adaptive control strategies [26]. Additionally, a good controller should filter the resonance modes of blades, tower, drive-train, gears, etc., as well as frequencies related to the rotor revolution (1P), blade crossing in front of the tower (3P) and some multiple (6P). The increasing size of wind turbines and the use of larger and more flexible structures result in a more demanding design of the pitch control system.

3.3 Yaw Angle

The main objective of the yaw controller is to follow the wind direction, maximising the energy capture, avoiding any dangerous gyroscopic effect, cable winding and oscillatory behaviour. As a first approach, the potential loss of energy due to yaw errors is a function of $\cos^3(\alpha)$; i.e. a yaw error of 10° means a reduction of 4.5% of power. A closed control loop is needed to compensate this effect.

A wind-vane in the nacelle supplies the reference angle to the controller, which sends a signal to the yaw actuators to move the nacelle towards the wind direction.

3.4 External Grid

As the number of wind farms increases, advanced control issues are required by the grid. Active-power/frequency and reactive-power/voltage loops can be performed to contribute to the stability, quality and reliability of the overall electrical system. The modern direct-drive gearless turbines with full power converters are in a good position to contribute to such innovative trends.

3.5 SCADA

The so-called Supervisory Control and Data Acquisition system (SCADA) is a software tool able to start-up and shut-down each turbine operation and to coordinate them in the wind farm. It usually runs in a PC independent to the one in which the main turbine controller works. It has the following functions:

- Handles warnings and alarms for preventive and corrective maintenances.
- Visualises the status and specific variables of the wind turbine for operating purposes.
- Develops reports, including performance, faults, events, production, etc.
- Provides an interface for external communication and remote operation tasks.
- Coordinates the turbines of the wind farm.

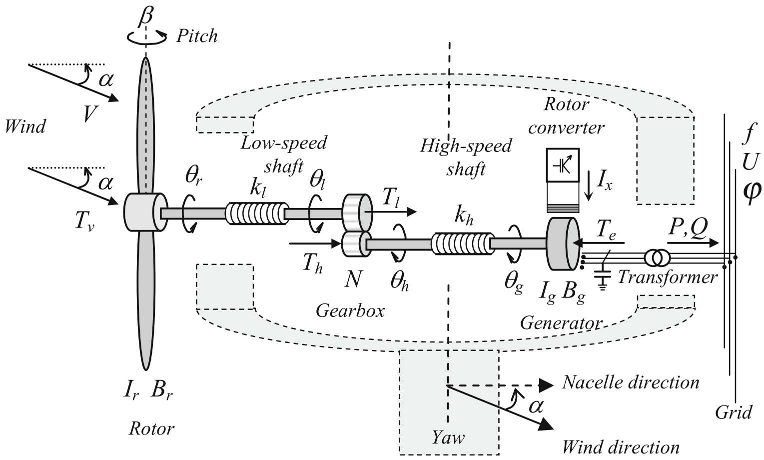

Fig. 4 Classical wind turbine

4 Wind Turbine Modelling

This section introduces a dynamic model that describes the dominant characteristics of the wind turbine, as a first step to integrate more complex elements. Figure 4 shows a classical wind turbine with a two-part horizontal drive shaft that connects, through a gearbox, a large rotor inertia at one end (blades) with a generator at the other end. The wind applies an aerodynamic torque T_v on the rotor. The grid or the power electronics applies an electrical torque T_e on the generator.

The rotor presents a moment of inertia I_r and a viscous damping coefficient B_r. The low-speed shaft has a torsional stiffness coefficient k_l. The increasing ratio between the low and high speed parts in the gearbox is N. The high-speed shaft has a torsional stiffness coefficient k_h. The generator shows a moment of inertia I_g and a viscous damping coefficient B_g. The rotor angle is θ_r, the rotor speed $\Omega = \dot{\theta}_r$, and the generator angle θ_g. The angles at the gearbox are: θ_l at the low-speed part and θ_h at the high-speed part. Two torques are applied to the gearbox: T_l by the low-speed shaft and T_h by the high-speed shaft. α is the yaw angle error (nacelle-wind angle) and β the pitch angle (blades). I_x is the rotor current excitation, P and Q the active and reactive power supplied to the grid respectively, and f, U and φ the frequency, voltage and power factor at the grid connexion point respectively. The main equations of the classical wind turbine are the following:

$$\theta_h = N\theta_l \tag{7}$$

$$T_l = NT_h \tag{8}$$

$$I_r\ddot{\theta}_r(t) + B_r\dot{\theta}_r(t) = T_v(t)\cos[\alpha(t)] - k_l[\theta_r(t) - \theta_l(t)] \tag{9}$$

$$I_g\ddot{\theta}_g(t) + B_g\dot{\theta}_g(t) = -T_e(t) - k_h\left[\theta_g(t) - \theta_h(t)\right] \tag{10}$$

$$T_l(t) = k_l[\theta_r(t) - \theta_l(t)] \tag{11}$$

$$T_h(t) = k_h\left[\theta_h(t) - \theta_g(t)\right] \tag{12}$$

Applying the Laplace Transform to Eq. 9 with $\alpha = 0$ and zero initial conditions, $\dot{\theta}_r(t = 0^+) = 0$ and $\theta_r(t = 0^+) = 0$, the rotor angle θ_r is,

$$\theta_r(s) = \frac{1}{I_r\, s^2 + B_r\, s + k_l}\left[T_v(s) + k_l\, \theta_l(s)\right] \tag{13}$$

Analogously, by applying the Laplace Transform to Eq. 10 with zero initial conditions, $\dot{\theta}_g(t = 0^+) = 0$ and $\theta_g(t = 0^+) = 0$, the corresponding generator angle θ_g is,

$$\theta_g(s) = \frac{1}{I_g s^2 + B_g s + k_h}[-T_e(s) + k_h\theta_h(s)] \tag{14}$$

From Eqs. 7, 8, 11 and 12, the low-speed shaft angle θ_l is,

$$\theta_l = \frac{1}{k_l + k_h N^2}\left[k_l\theta_r + k_h N\theta_g\right] \tag{15}$$

The dynamic transfer function $M(s)$ between the demanded pitch angle β_d and the actual one β is,

$$\beta(s) = M(s)\ \beta_d(s) \tag{16}$$

where $M(s)$ includes the pitch motor, the pith position controller and the pitch speed controller. Combining the above equations, the block diagram of the classical wind turbine is showed in Fig. 5.

A direct-drive (gearless) wind turbine is a simple and more reliable option (see Fig. 6). By applying the conditions $N = 1$, $k_l = k$, $k_h = 0$, $\theta_l = \theta_g$ and $\theta_h = \theta_r$ to the above equations, the main expressions of the direct-drive wind turbine are the following:

$$I_r\ddot{\theta}_r(t) + B_r\dot{\theta}_r(t) = T_v(t)\cos[\alpha(t)] - k\left[\theta_r(t) - \theta_g(t)\right] \tag{17}$$

$$I_g\ddot{\theta}_g(t) + B_g\dot{\theta}_g(t) = -T_e(t) - k\left[\theta_g(t) - \theta_r(t)\right] \tag{18}$$

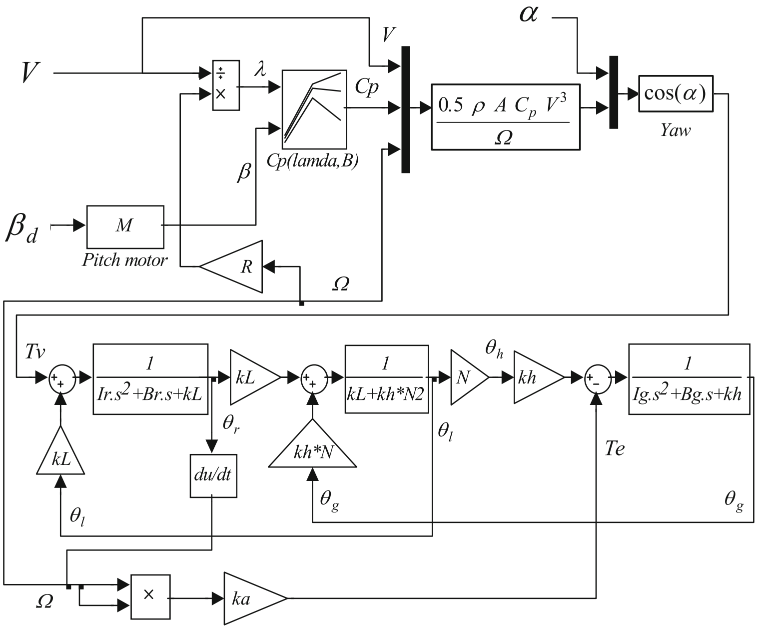

Fig. 5 Classical wind turbine block diagram

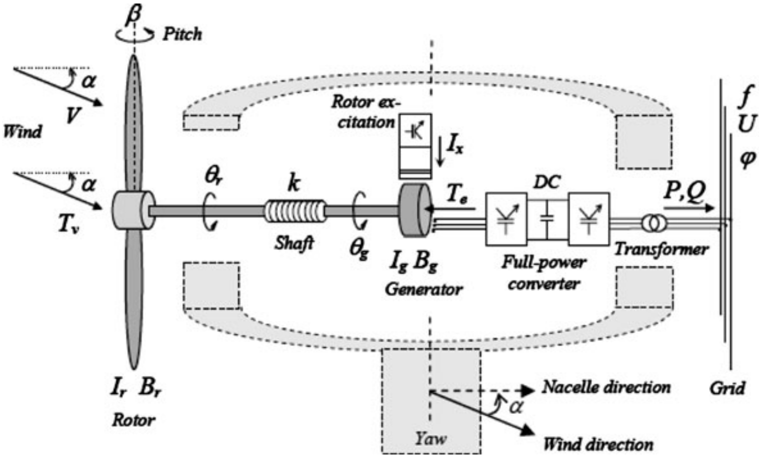

Fig. 6 Direct-drive wind turbine

Once more, applying the Laplace Transform to Eq. 17 with $\alpha = 0$ and zero initial conditions, $\dot{\theta}_r(t = 0^+) = 0$ and $\theta_r(t = 0^+) = 0$, the corresponding rotor angle θ_r is,

$$\theta_r(s) = \frac{1}{I_r s^2 + B_r s + k}\left[T_v(s) + k\theta_g(s)\right] \tag{19}$$

Analogously, by applying the Laplace Transform to Eq. 18 with zero initial conditions, $\dot{\theta}_g(t = 0^+) = 0$ and $\theta_g(t = 0^+) = 0$, the corresponding generator angle θ_g is,

$$\theta_g(s) = \frac{1}{I_g s^2 + B_g s + k}[-T_e(s) + k\theta_r(s)] \tag{20}$$

Now, using the last equations, the block diagram of the direct-drive wind turbine can be made by simplifying the diagram of Fig. 5 accordingly.

Figure 3 and Eq. 2 described the aerodynamic power coefficient C_p as a nonlinear gain. However, a more advanced analysis shows that the aerodynamic torque T_v depends nonlinearly on the pith angle β, the rotor speed Ω, the effective wind speed V, and the yaw error α, so that,

$$T_v(t) = f[\beta(t), \Omega(t), V(t), \alpha(t)] \tag{21}$$

Assuming that T_v is differentiable, and applying the Taylor series expansion theory to a specific equilibrium operating point $p_O = (\beta_o, \Omega_o, V_o, \alpha_o)$, the last nonlinear expression may be linearised as shown in Fig. 7, where the partial derivatives at the equilibrium operating point are,

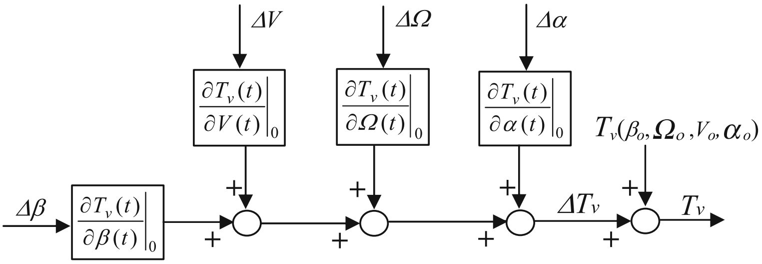

Fig. 7 Local linearisation of the nonlinear aerodynamic torque

$$\left.\frac{\partial T_v(t)}{\partial \beta(t)}\right|_0 = 0.5\rho A\,\cos^3(\alpha_0)\frac{V_0^3}{\Omega_0}\left.\frac{\partial C_p}{\partial \beta}\right|_0 \tag{22}$$

$$\left.\frac{\partial T_v(t)}{\partial V(t)}\right|_0 = 0.5\rho A\,\cos^3(\alpha_0)\frac{1}{\Omega_0}\left(3C_{p0}V_0^2 + \left.\frac{\partial C_p}{\partial V}\right|_0 V_0^3\right) \tag{23}$$

$$\left.\frac{\partial T_v(t)}{\partial \Omega(t)}\right|_0 = 0.5\rho A\,\cos^3(\alpha_0)V_0^3\left(-C_{p0}\frac{1}{\Omega_0^2} + \left.\frac{\partial C_p}{\partial \Omega}\right|_0 \frac{1}{\Omega_0}\right) \tag{24}$$

$$\left.\frac{\partial T_v(t)}{\partial \alpha(t)}\right|_0 = -1.5\rho A C_{p0}\frac{V_0^3}{\Omega_0}\cos^2(\alpha_0)sen(\alpha_0) \tag{25}$$

The partial derivatives strongly depend on the equilibrium operating point. It means that the behaviour of the wind turbine varies considerably over the operational envelope of the machine. The function $\partial T_v/\partial\beta$ provokes a variation in the plant gain. The function $\partial T_v/\partial\Omega$ induces a variation in one of the dominant poles (low frequency) of the plant and the functions $\partial T_v/\partial V$ and $\partial T_v/\partial\alpha$ affect the magnitude of the external disturbances [27].

5 Conclusions and Future Research

This chapter introduced, as a first approach, the main characteristics, objectives and strategies of the control system of a wind turbine.

The principal control objectives of an advanced wind turbine, including stability, captured energy maximization, mechanical load reduction, fatigue limitation, power-train damping, reliability optimization, availability aspects, etc. are described. The efficiency and reliability of a wind turbine strongly depends on the applied control strategy. Some typical control strategies to fulfil the previous objectives are also described.

This is followed by an analysis of the classical control loops to regulate in a coordinated way the critical variables of the machine: torque, power, pitch, rotor speed, yaw orientation, temperatures, voltages, currents, power factors, etc.

Dynamic model that describes the dominant characteristics of the wind turbine is introduced, as a first step to integrate more complex elements like the large nonlinear characteristics and high model uncertainty due to the interaction of the aerodynamic, mechanical and electrical subsystems, the large flexible structures of the machine (tower, blades, etc.), which have to work under very turbulent and unpredictable environmental conditions, and which are subject to a variable and demanding electrical grid, etc.

In the last few years increasing level of wind energy penetration in the grid has revealed new critical challenges and problems: frequency/active-power control loops, voltage/reactive-power regulation, response to grid voltage dips, restoration of grid services after power outages, control with wind prediction, etc. They demand an urgent need for new control solutions, combining robust methodologies, non-linear control, adaptive techniques, load sharing aspects, predictive laws, multi-variable strategies, etc. In addition new control strategies including independent pitch control and/or new sensors (accelerometers) to alleviate mechanical loads will be important to design larger machines (multi-megawatt) in the near future.

References

1. IEC 61400-21. Ed.1 (2001) Wind Turbine Generator Systems. Part 21: Measurement and Assessment of Power Quality Characteristics of Grid Connected Wind Turbine
2. EWEA (2005) Large scale integration of wind energy in the European power supply: analysis, issues and recommendations. EWEA, Brussels
3. Bossanyi EA (2000) The Design of Closed Loop Controllers for Wind Turbines. Wind Energy, 3:149–163
4. Quarton DC (1998) The evolution of wind turbine design analysis: a twenty year progress review. Wind Energy 1:5–24
5. Kuik G, Ummels BC, Hendriks R (2006) Perspectives of Wind Energy. Advances in New and Sustainable Energy Conversion and Storage Technologies. IUC, Dubrovnik
6. Bossanyi EA (2003) Wind Turbine Control for Load Reduction. Wind Energy, 6:229–244
7. Bossanyi EA (2005) Further Load Reductions with Individual Pitch Control. Wind Energy 8:481–485
8. Hooft EL, Schaak P, Engelen TG (2003) Wind turbine control algorithms. DOWEC-F1W1-EH-03-094/0. ECN-C-03-111, ECN Windenergie, Petten
9. Andrew CM, Henderson R, Smith B, Sørensen HC, Barthelmie RJ, Boesmans B (2003) Offshore Wind Energy in Europe—A Review of the State-of-the-Art. Wind Energy 6:35–52
10. Leith DJ, Leithead WE (1997) Implementation of wind turbine controllers. Int. Journal of Control 66:349–380
11. Torben HAM, Larsen J, Thomsen K (2005) Active load reduction using individual pitch, based on local blade flow measurements. Wind Energy 8:67–80
12. Spruce CJ (2004) Power Control of Active Stall Wind Turbines, European Wind Energy Conference, London, UK
13. Mercer AS, Bossanyi EA (1996) Stall regulation of variable speed HAWTS. European Wind Energy Conference, Sweden
14. Torres E, Garcia-Sanz M (2004) Experimental Results of the Variable Speed, Direct Drive Multipole Synchronous Wind Turbine: TWT1650. Wind Energy 7 (2):109–118
15. Garcia-Sanz M, Torres E (2004) Control y experimentacion del aerogenerador sincrono multipolar de velocidad variable TWT1650, RIAI, 1 (3):53–62

16. Risø and DNV (2002). Guidelines for Design of Wind Turbines. Det Norske Veritas (DNV) and Wind Energy Department, Risø National Laboratory
17. Carlson O, Hylander J, Thorborg K (1996) Survey of variable speed operation of wind turbines. EWEC'96
18. Vilsboell N, Pinegin AL, Fischer T, Bugge J (1997) Analysis of advantages of the double supply machine with variable rotation speed application in wind energy converters. DEWI Magazine, 11:50–65
19. Hansen AD, Lov F, Blaabjerg F, Hansen LH (2004) Review of contemporary wind turbine concepts and their market penetration. Wind Engineering, 28:247–263
20. Grauers A (1996) Directly Driven Wind Turbine Generators. International Confernce on Electrical Machines, ICEM 96, Vigo, Spain
21. Mutschler P, Hoffmann R (2002) Comparison of wind turbines regarding their energy generation. Power Electronics Specialists Conference
22. Germanischer Lloyd Certification GmbH www.gl-group.com
23. International Electro-technical Commission.www.iec.ch/
24. Leithead W E (1992) Effective wind speed models for simple wind turbine simulation. British Wind Energy Conference, pp. 321–326
25. Astrom KJ, Hagglund T (1995) PID Controllers: Theory, Design, and Tuning. 2nd edition. ISA, Research Triangle Park, North Carolina, USA
26. Houpis CH, Rasmussen SJ, Garcia-Sanz M (2006) Quantitative Feedback Theory Fundamentals and Applications. 2nd edition. Florida, USA, a CRC Press Book. Taylor and Francis
27. Leithead WE, Connors B (2000) Control of variable speed wind turbines: dynamic models. International Journal of Control, 73 (13):1173–1188

Author Biography

Dr. Mario Garcia-Sanz is Professor at Case Western Reserve University (CWRU), Cleveland, Ohio, the Inaugural Milton and Tamar Maltz Professor in Energy Innovation, and Director of the Wind Energy and Control Systems Center at CWRU. Formerly a Professor at the Public University of Navarra, Spain, and Senior Advisor for the President of the MTorres Group, he held visiting professorships at the Control Systems Centre, UMIST (UK, 1995); at Oxford University (UK, 1996); at the Jet Propulsion Laboratory NASA-JPL (California, 2004); and at the European Space Agency ESA-ESTEC (The Netherlands, 2008). He holds 20 industrial patents, has done more than 35 research projects for industry and space agencies, and is author or coauthor of more than 135 papers and the books *Quantitative Feedback Theory: Theory and Applications*, Taylor & Francis (2006), and *Wind Energy Systems: Control Engineering Design*, Taylor & Francis (2011). Dr. Garcia-Sanz served as NATO/RTO Lecture Series Director and is also a member of the IFAC Technical Committee on Robust Control, the IFAC Technical Committee on Aerospace Control, the IEEE Technical Committee on Aerospace, and Subject Editor of the International Journal of Robust and Nonlinear Control. He was awarded the IEE Heaviside Prize (UK) in 1995. Professor Garcia-Sanz's main research interest focuses on bridging the gap between fundamental and applied research in advanced control and systems engineering, with special emphasis in Energy Innovation, Wind Energy, Space, Environmental and Industrial Applications.

Grid Integration of Offshore Wind Farms

Lie Xu

Offshore wind farms tend to become bigger and far from the onshore point of connection. The developers and the system operators are facing a number of technical, economical, and environmental challenges in transmitting the bulk power developed at these offshore wind farms over long distances. In this Chapter, some of these issues are discussed, giving emphasis to the basic system requirements along with various options for transmission and grid integration.

1 Connection Requirements

The operating procedures and principles governing the relationship between the Transmission System Operator and the users of the transmission system (for example Generators, Suppliers or Non-Embedded Customers) are set out in the Grid Code. For a wind farm to be connected, it must meet the Grid Code requirements in terms of fault ride through, frequency range, frequency control, reactive range capability, voltage control etc., in order to maintain the stability and security of the grid [1, 2]. Different countries have different Grid Codes to be followed.

L. Xu (✉)
School of Electronics, Electrical Engineering and Computer Science,
Queen's University of Belfast, Stranmillis Road, Belfast, BT9 5AH, UK
e-mail: l.xu@ee.qub.ac.uk

S. Mathew and G. S. Philip (eds.), *Advances in Wind Energy Conversion Technology,* Environmental Science and Engineering,
DOI: 10.1007/978-3-540-88258-9_7,

1.1 Fault Ride Through

Under the Grid Code proposals, the wind farm, whether connected directly to the transmission system or distribution system, is required to remain connected and feeding power into the system for any solid single or multiphase short circuit fault occurring on the HV transmission system. In addition to the continuous and stable operation, the mechanical power to the wind turbines should not be deliberately reduced during this period. The minimum remaining voltage and the duration required also differ from countries. For example, a minimum voltage of 15% for 140 min is required for the GB system [2] while for E.ON system [1], zero voltage for 150 min is essential.

1.2 Frequency Range and Frequency Control

The Grid Code requires that the wind farms should operate continuously at certain system frequency range and should have the capability of providing frequency response. The wind turbines will have to be capable of operating at part load for a given wind condition and be able to continuously respond to any increase or decrease in system frequency against a target frequency by decreasing or increasing power output respectively.

1.3 Reactive Range Capability and Voltage Control

The increasing use of non-synchronous generating units that are not able to produce the same amount of reactive power as synchronous generators may cause an increasing amount of reactive power compensation devices to be required in the zones where the non-synchronous generating units are connected. The Grid Code requires that wind farms should have the reactive power control capability, for example, over the normal active power operating range of the wind farm, a predefined reactive power capability of 0.95 power factor lagging to 0.95 power factor leading based on full output power should be available at the connection point. In addition, wind farms must be capable of controlling the voltage at the point of connection to the public electricity system. Additional requirements may also have to be met in individual cases.

2 Grid Connection Methods

High voltage AC (HVAC) has been used for all the existing offshore wind farms. This is largely due to the fact that most of those offshore wind farms are relatively small in size and close to the onshore connection point. HVAC will also be used for most offshore wind farms in the near future with a connection distance of less than 50–75 km. Such HVAC solution provides the simplest and most economic connection method.

However, with the increasing offshore wind farm size, high voltage DC (HVDC) transmission may be the only feasible option for connection of a wind farm if the distance exceeds 150–200 km. HVDC transmission offers the following advantages for integration of large offshore wind farms over long distance [3]:

- Fully controlled power flow.
- Decoupled sending and receiving networks by the asynchronous connection. Faults are not transferred between the two AC networks.
- DC transmission is not affected by cable charging currents (therefore no limit on distance).
- A pair of DC cables can carry up to 1200 MW.
- Lower cable power loss than an AC cable scheme.

There are two different HVDC transmission technologies, i.e. line-commutated converter HVDC (LCC HVDC) using thyristors, and voltage source converter using IGBTs (VSC HVDC). LCC HVDC has been used for over 50 years and currently there are over 60 schemes in operation worldwide with a number of projects rated up to 3,000 MW. While for VSC HVDC, a number of transmissions up to 330 MW are in operation and higher power up to 1,100 MW are currently under development [4]. Compared to the LCC HVDC system, VSC HVDC has a number of advantages including [5]:

- It is self commutating and does not require an external voltage source for its operation.
- The reactive power flow can be independently controlled at each AC network.
- Reactive power control is independent of the active power control.

These features make VSC HVDC attractive for connection of offshore wind farms, since power can be transmitted to the wind farm at times of little or no wind and the AC voltage at either end can be controlled [6–10]. However, power loss is likely to be higher for VSC HVDC compared to a LCC HVDC system [5].

If HVDC is used, an offshore substation must be required. Currently, there is no experience on offshore LCC HVDC substations. The first offshore VSC HVDC substation was installed by ABB for the offshore Troll A platform in Norway in 2005. It is rated at 84 MW at ± 60 kV with a transmission distance of 70 km [11]. While for AC connection, unless the offshore wind farm is very small and close to the shore, an offshore substation is normally required. For example, the UK's Barrow offshore wind farm rated at 60 MW has a 33/132 kV offshore substation with a transmission distance of 26 km [12] while a larger Danish Horns Rev wind farm rated at 160 MW has an offshore 36/150 kV substation with a transmission distance of 15 km [13]. There are a number of challenges for such an offshore substation, e.g. limited space in order to minimize the cost of the offshore installation, extremely harsh and variable environment (constant exposure to the salt air, wind and water), and limited maintenance access [3].

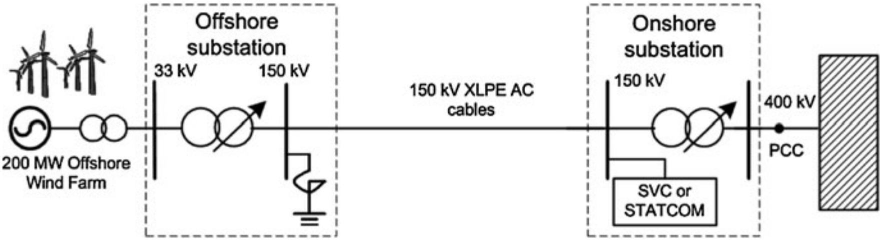

Fig. 1 A typical HVAC scheme

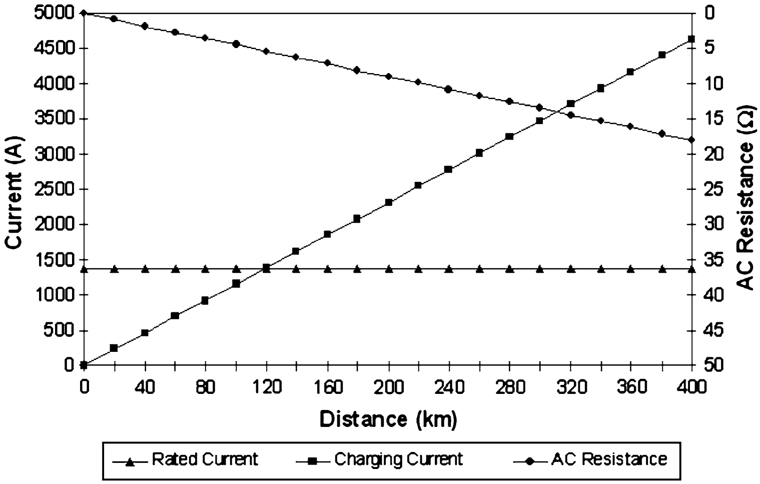

Fig. 2 Typical characteristic of an AC cable

2.1 HVAC Connection

One of the main advantages of AC connection is the low cost of substations. The layout of the transmission is also relatively simple. A schematic diagram of using HVAC for connecting a 200 MW offshore wind farm is shown in Fig. 1. Current technology limits the maximum power rating for a 3-phase AC cable to about 200 MW based on 150–170 kV and a maximum cable length of 200 km. Thus, for connecting a large wind farm, multiple cables are required which could increase the cost considerably.

With the increase in power transmission distance, long AC cables will produce large amounts of capacitive reactive power. It will reduce the cable transmission capacity accordingly. A typical characteristic for an AC cable is shown in Fig. 2. The capacitive power of the cable needs to be balanced by inductive reactive power in order not to create problems with high voltage and cable de-rating. Therefore, large reactive power compensation is required. This can be achieved by permanently connected shunt reactive power compensation at one or both ends of the onshore and offshore substation in order to balance the reactive power generated by cable shunt capacitance.

At a connection distance in excess of 50 km, it is likely that dynamic reactive power compensation using Static Var Compensator (SVC) or Static Synchronous Compensator (STATCOM) at the connection point (see Fig. 1) will be required, to meet the necessary reactive power and AC voltage controls during rapid load changes and during and after fault conditions in the grid [14].

Apart from the problems caused by the AC cables, AC connection will result in the synchronous operation between the wind farm and the grid. Faults occurring on the grid will directly affect the wind farm and vice versa. In order to meet the Grid Code requirement, the wind turbines must have fault ride through capability.

2.2 LCC HVDC Connection

A thyristor based LCC converter requires an AC voltage source to commutate. For the offshore system, such commutation voltage can be provided by either a synchronous compensator [3] or a VSC based STATCOM [9, 15]. For wind farms based on synchronous generators with full-sized interface converter, the wind farm itself may be able to provide AC voltage support and the required commutation voltage for the LCC HVDC system. Therefore, a STATCOM or synchronous compensator might not be required [16]. However, this would require very close coordination of the wind farm and the converter and the system response during onshore network fault has yet to be proved. Figure 3 shows the schematic diagram for connecting a 500 MW wind farm using LCC HVDC, in which a STATCOM is used for providing the commutation voltage.

The offshore substation of a LCC HVDC system comprises of a thyristor based LCC HDVC converter, a small STATCOM (or a synchronous compensator) rated at around 25% of the scheme rating, converter transforms and some passive filters.

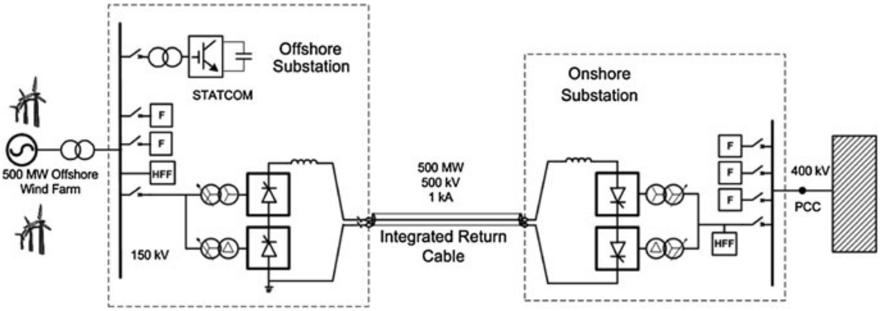

Fig. 3 System configuration of using LCC HVDC for connecting a 500 MW offshore wind farm [9]

For the onshore substation, it is identical to those used in LCC HVDC systems connecting two conventional AC systems.

The transformers for offshore convertors may not require tap changers as the offshore AC voltage can be kept constant. LCC HVDC converters absorb reactive power at both converter stations. For the offshore systems, the reactive power required by the HVDC converter is provided by the filters, the STATCOM and the wind farm. For the onshore station, conventional filters are used for reactive power compensation.

The STATCOM provides the necessary commutation voltage for the LCC HVDC converter and also reactive power compensation for the network during steady state, dynamic and transient conditions. It also provides some limited active power support to the network during transient conditions such as power changes of the wind farm output (e.g. due to gusts or ramping) and during AC fault. If a synchronous compensator is used, it can provide better active power support due to its much larger energy storage compared to a STATCOM.

Typical power loss for one end of a LCC HVDC system is around 1% including the transformer losses while the power loss for a STATCOM is between 1 and 2% depends on its configuration. Thus the overall conversion efficiency for such a LCC HVDC system is around 97–98% depends on the detailed system design.

2.2.1 Principles of LCC Converter Operation

The operation of a LCC HVDC system can be simplified by considering two DC voltage sources connected via DC cables. Thus, under steady state, the DC current is given as

$$I_{DC} = \frac{V_{dc1} - V_{dc2}}{R} \tag{1}$$

where V_{dc1} and V_{dc2} refer to the DC voltages generated by the two thyristor converters and R is the equivalent DC resistance of the cables. Under normal operation, one converter is assigned to control the DC voltage to a certain level and the other converter controls the DC current by regulating its own DC voltage.

The regulation of the converter DC voltage is achieved via the control of the thyristors' firing angles. A typical 6-pulse bridge rectifier and its generated DC voltage waveform are shown in Fig. 4a, b respectively. By varying the firing delay angle α, the DC voltage can be controlled. For $\alpha < 90°$, the generated voltage is positive and the converter works in rectifier mode which transmits active power from AC to DC. For $\alpha > 90°$, the generated voltage is negative and the converter works in inverter mode converting active power from DC to AC.

During the operation of thyristor converters, the phase current is delayed by the firing angle α with reference to the phase voltage. This indicates that the converters absorb reactive power from the network. In addition, the current commutation

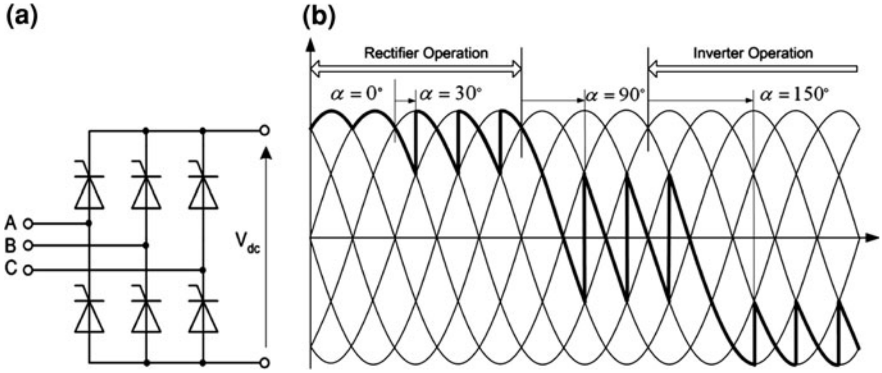

Fig. 4 Six-pulse bridge rectifier (**a**) and DC voltage control using the thyristors' firing angles (**b**)

between the thyristors relies on the terminal AC voltage and therefore, external AC voltage must be supplied in order to operate such converters.

The AC current in a 6-pulse bridge circuit contains characteristic harmonics in the orders of $6n \pm 1$ where $n = 1, 2, 3, \ldots$. In order to reduce the harmonics entering the AC network, 12-pulse configuration is normally used which comprises of two 6-pulse bridges whose DC sides are connected in series whereas the AC sides are connected in parallel through a star-star and a star-delta connected transforms respectively. The characteristic harmonics from a 12-pulse configuration are in the orders of $12n \pm 1$ where $n = 1, 2, 3, \ldots$. Passive harmonic filters are normally used to absorb the current harmonics generated by the converter. In addition, such filters appear to be capacitive at fundamental frequency, and thus compensate the reactive power absorbed by the converter.

2.2.2 Basic System Control

For the LCC HVDC system, the onshore converter (inverter) is in DC voltage control, while the offshore converter (rectifier) is in DC current control. For the offshore AC network, its voltage amplitude and frequency must be maintained and the transmitted active power via HVDC link must match with that being generated by the wind farm.

For conventional AC system, AC frequency is the indication of active power balance. However, due to the absence of synchronous generators in the offshore network (see Fig. 3) active power does not have a direct impact on AC frequency. The control system can consider the LCC HVDC converter and the STATCOM as a single unit and the offshore AC system can be controlled to resemble an infinite voltage source with constant frequency, voltage amplitude and phase angle. Thus, the active power generated by the wind farm is automatically absorbed by the combination of the HVDC converter and the STATCOM and then transmitted to the onshore converter. No extra frequency and/or active power control loops are required in such design.

The active power flow within the offshore system can be expressed as

$$P_{WF} = V_{dc} \cdot C \cdot \frac{dV_{dc}}{dt} + V_d I_d + P_{loss} \tag{2}$$

where P_{WF} and P_{loss} are the active power generated by the wind farm and the power loss in the offshore system respectively. V_d and I_d are the DC voltage and current of the offshore HVDC converter and V_{dc} and C are the STATCOM DC voltage and DC capacitance respectively.

As the DC voltage of the LCC HVDC is maintained by the onshore converter, the power transmitted from the offshore wind farm to the grid is determined by the DC current of the LCC HVDC system which is controlled by the offshore converter. Therefore, the primary aim of the active power control is to generate an appropriate DC current order for the offshore LCC converter such that the transmitted power matches the generated power. According to Eq. 2, the STATCOM DC capacitor energy/voltage is an immediate indicator of any change of the active power balance and therefore, it can be used to rapidly change the current order for the offshore LCC converter. Once active power is balanced, the STATCOM DC voltage is also controlled at the correct value.

2.2.3 System Operation

First, the system must be able to start from a complete shutdown. Before starting the system, the STATCOM DC capacitor must be pre-charged by using a small auxiliary power supply, for example an emergency diesel generator. When the DC capacitor is fully charged, the STATCOM output voltage is ramped up to give smooth energisation of the transformers and permanently connected filters. The DC capacitor has to be fed by the auxiliary power supply until the wind generators start to generate power, since the STATCOM has to provide the converter and network system losses. Once the wind farm's output active power is increased, the HVDC converter can be enabled and start to transmit power to the onshore grid.

The grid code requires the system must have fault ride through capability. When there is a fault in the onshore grid network, the onshore inverter is likely to fail commutation repetitively, causing a short circuit on the DC side. Thus, the DC voltage and the transmitted power of the offshore HVDC converter reduce to near zero. The DC voltage of the STATCOM rises rapidly as it absorbs the surplus active power. To prevent the system from tripping, the active power output of the wind turbines must be reduced immediately using high speed communication.

Thus, both the offshore AC system and the STATCOM DC voltage (active power remains balanced) are fully controlled. After the fault is cleared, the DC voltage of the HVDC system recovers and the transmitted active power increases.

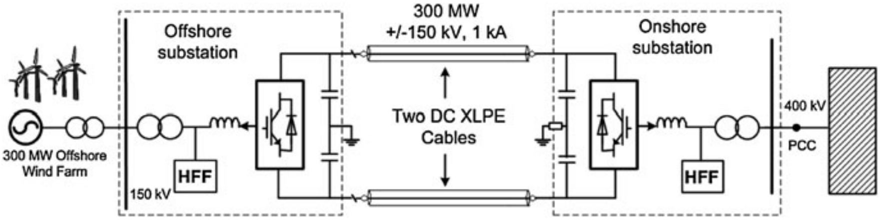

Fig. 5 Schematic diagram of connecting a 300 MW offshore wind farm using VSC HVDC

Thus, such system can achieve satisfactory fault ride through during onshore grid fault.

2.3 VSC HVDC Connection

Figure 5 shows the single-line diagram of connecting a 300 MW offshore wind farm using VSC HVDC. The VSC HVDC system transmits active power from the offshore wind farm to the main grid via two DC XLPE cables. It also provides AC voltage and frequency control to the offshore wind farm network and reactive power/AC voltage control to the onshore network, if required. A high pass filter (HFF) is connected at each side to absorb the high frequency harmonics generated by the converters during operation.

Due to the use of IGBT devices switched at high frequency (e.g. 1–2 kHz), the power loss for VSC HVDC system is much higher than the LCC HVDC system and the total conversion efficiency was quoted to be in the range of 90–95% [17].

As the harmonics generated by the VSC are in the high orders, only a small high frequency filter typically rated at around 15% of the scheme rating is required for each end.

2.3.1 Principles of VSC HVDC Operation

The fundamentals of VSC HVDC system operation may be explained by considering each terminal as a voltage source connected to the AC transmission network via a 3-phase reactor. The two terminals are then interconnected by a DC link. Figure 6a shows the equivalent circuit of one end of a VSC HVDC system and Fig. 6b shows the system vector diagram.

The output voltage vector (V_c) of a VSC may be described by:

$$V_{\mathrm{c}} = \frac{1}{2} V_{dc} \cdot M \cdot e^{j\omega t + \delta} \tag{3}$$

where V_{dc} is the DC voltage and ω is the system frequency. M is the modulation index and δ is the phase angle of the VSC output with reference to that of the AC

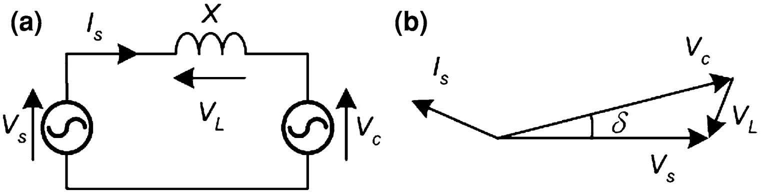

Fig. 6 Equivalent circuit (**a**) and vector diagram (**b**) of one end of a VSC HVDC system

system fundamental voltage, as shown in Fig. 6b. Both M and δ can be adjusted independently by the VSC controller.

As a result, the voltage drop V_L across the reactor X can be varied to control the active and reactive power flows. Based on Fig. 6, the active and reactive power output (P_s and Q_s), as seen from the AC system terminals, can be expressed as:

$$\begin{aligned} P_s &= \frac{V_c \cdot \sin\delta}{\omega L} \cdot V_s \\ Q_s &= \frac{V_c \cdot \cos\delta - V_s}{\omega L} \cdot V_s \end{aligned} \tag{4}$$

According to Eq. 4, by independently regulating the components of $V_c \sin\delta$ and $V_c \cos\delta$, P_s and Q_s can be controlled separately. This indicates that VSC HVDC system can operate at any power factor.

The control of VSC is achieved using Pulse-Width-Modulation (PWM) switching at high frequency, usually in the range of 1–2 kHz. This not only results in fast system response, but also produces only high order harmonics by the VSC.

2.3.2 Basic System Control

For the normal operation of a VSC HVDC system, its DC link voltage must be maintained at a constant value. Furthermore, a constant DC voltage indicates the balancing of active power exchange between the two sides. To achieve this, the onshore VSC station is assigned to control the DC voltage for ensuring the transmission of the energy collected by the offshore VSC station to the onshore AC network. The main tasks for the offshore VSC station are to collect energy from the wind farm and to control the voltage and frequency of the offshore AC network.

The onshore VSC is operated as the DC voltage controller and its functions are similar to those of a VSC HVDC system connecting two conventional AC networks [18].

Due to the absence of synchronous generator in the offshore system, the offshore VSC can again be controlled to resemble an infinite voltage source with constant frequency, voltage amplitude and phase angle. Thus, similar to wind farms connected to an infinite AC system, power generated by the wind farm is automatically absorbed by the offshore VSC and then transmitted to the grid via the onshore VSC station.

2.3.3 System Operation

Similar to LCC HVDC, the VSC HVDC systems also must have black-start capability. With VSC HVDC system, achieving this can be relatively easier. With the offshore converter blocked, the DC capacitors and the DC cables are charged via the diodes from the onshore AC system. The DC voltage is then regulated to its nominal values by the onshore VSC. The offshore VSC can then be enabled and ramps up offshore AC voltage (giving smooth energisation of the transformers and the permanently connected filters). During this period, the onshore VSC works as a rectifier and the offshore VSC as an inverter, since a small amount of active power is required to supply the power loss of the offshore equipment and network. After the establishment of the offshore AC voltage, individual wind generators can be started. As the power output from the wind farm increases, the VSC HVDC system automatically changes power direction and transmits power to the onshore grid.

To meet the fault ride through requirement, it is crucial that the active power is balanced even during onshore AC faults, otherwise the system would have to be tripped and normal operation interrupted. During a close AC fault, the power capability of the onshore VSC will be significantly reduced due to the reduced AC voltage and the converter AC current limit. Consequently, the DC voltage will increase, as the offshore VSC continues to feed energy into the cable. The wind farm power output must be reduced immediately upon the detection of DC over voltage. Similar to system with LCC HVDC, this can be achieved by applying active power limit to each wind turbine, using high speed communications. After fault clearance, the active power limit applied to each wind turbines can be removed. The wind generators' rotor speed will increase during the fault, but this is not a major concern due to the variable speed nature of the wind generators used.

2.4 Alternative Solutions

As the transmission link is built specifically for connecting the offshore wind farm which operates in a different way to conventional power stations with synchronous generators, by considering the wind farm and the required transmission link together, the system can be designed in a complete different way.

For wind turbines equipped with AC–DC–AC converters (such as those based on permanent magnet generators), one possibility is to use a local DC network in stead of AC [19, 20]. The output from the wind generators are rectified first and then converted to inter-medium DC voltage level, say 15 kV, which is then connected together to the local DC bus. The inter-medium DC is converted to high voltage DC, say 150 kV in the offshore substation, using DC–DC converters. This DC voltage is then transmitted to the onshore VSC converter via DC cables.

An alternative solution is to combine HVAC and HVDC systems. Large offshore wind farms, say above 1,000 MW, are likely to be built in different stages. Hence, it will be very difficult to economically justify the building of one single

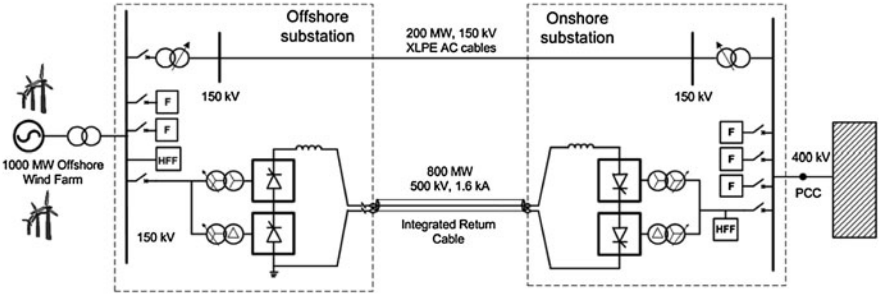

Fig. 7 System configuration of combining HVAC and LCC HVDC for connecting a 1,000 MW offshore wind farm

large HVDC converter which could take a number of years. Therefore, it may be more economical to combine HVAC and HVDC technology. Such a scheme for connecting a 1,000 MW offshore wind farm, in which 200 MW HVAC and 800 MW LCC HVDC transmission systems are used, is shown in Fig. 7. During the earlier stage of the offshore wind farm construction, the HVAC system can transmit the power generated by some of the wind turbines to the onshore grid. After the completion of the whole system, the HVAC system can provide the required commutation voltage to the offshore LCC converter. Thus, no STATCOM or synchronous compensator will be required in the offshore substation. Furthermore, when there is no wind, the HVAC system can reverse power direction and supply power to the auxiliary equipment in the offshore substation and the individual wind turbines. The LCC HVDC design can then be more economic, as operation at very low power is not required.

3 Case Studies

Dynamic simulations of using LCC HVDC and VSC HVDC for connecting a 500 MW offshore wind farm based on doubly-fed induction generator (DFIG) were performed respectively. The connection distance is 100 km. For both cases, normal wind speed variation and grid AC fault are studied and the results are shown in Figs. 8 and 9 respectively.

For LCC HVDC connection, the offshore system comprises a 500 MW wind farm, a 500 MW LCC HVDC transmission system and a STATCOM rated at ± 100 MVar. The wind speed is increased at 0.2 s and at 2.5 s, a 100 ms solid AC fault is applied to the onshore connection point. When the increased wind speed is applied to the turbine, the speed of the generator starts to increase, as does the power generated. The onshore converter controls the DC voltage, and hence its value stays almost constant throughout the operating conditions whereas the DC current increases to increase the transmitted active power. Both the AC frequency and voltage on the offshore wind farm side are well controlled.

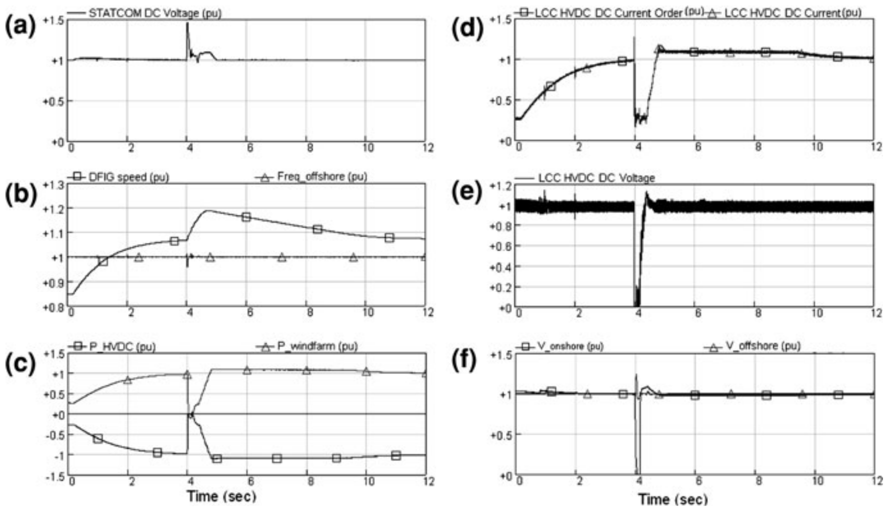

Fig. 8 Simulation of the LCC HVDC connection [9]

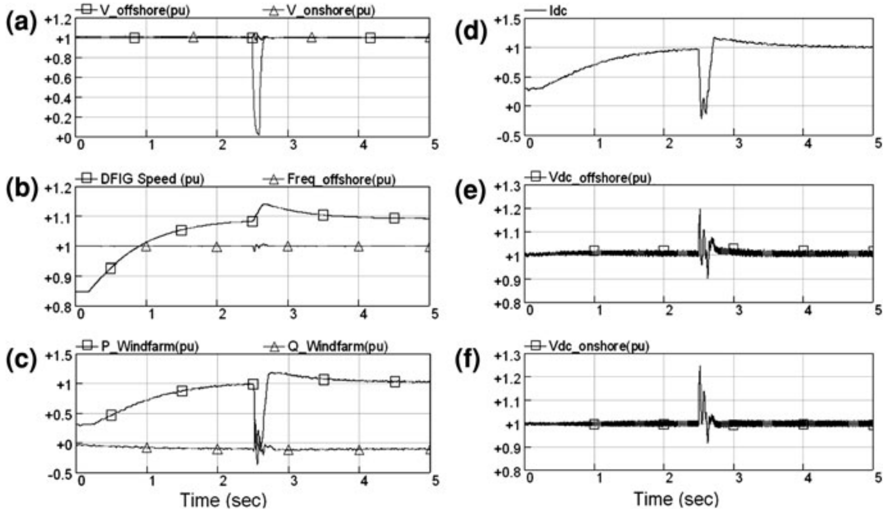

Fig. 9 Simulation of the VSC HVDC connection [9]

When the fault occurred at 2.5 s, the onshore inverter fails commutation and the power transmitted by the HVDC system reduces to zero. The STATCOM temporarily absorbs active power from the generator and consequently its DC voltage increases rapidly. The active power orders for each wind turbine are then reduced immediately via high-speed communications. The offshore AC system has been successfully maintained and after the fault clearance the system gets back to the normal operation.

For the VSC HVDC system, when the wind speed increases at 0.2 s, both the generated and transmitted active power increases accordingly. The offshore AC system is well regulated. When a solid 3-phase to ground fault is applied on the onshore network at 2.5 s, the rapid reduction of the power export by the onshore VSC causes the DC voltage to rise quickly.

Similar to LCC HVDC system, the active power orders for each wind turbine are reduced immediately via high-speed communications. Again, the offshore AC system is well maintained during such onshore AC faults. When the fault is cleared, the system gets back to normal operation. Both of the HVDC systems can be seen to be capable of providing a satisfactory solution to the connection of a large offshore wind farm.

4 Comparison of Connection Options

The three connection methods, i.e., HVAC, LCC HVDC, and VSC HVDC are compared with respect to grid code compliance, power loss, and cost.

4.1 Grid Code Compliance

Dynamic studies shown earlier indicate that both DC solutions comply with the grid code and especially fault ride through requirement. As DC connections decouple the onshore and offshore AC networks, onshore AC fault does not directly affect the offshore AC system. While for HVAC connection, onshore AC fault will directly affect the offshore AC voltage and fault ride through is mainly achieved by the proper design of the wind turbines. Thus DC connections potentially ease the requirement for the wind turbines as offshore AC voltage is maintained during onshore grid fault. For LCC HVDC solution, if precise AC voltage and reactive power control is required at the onshore connection point, a SVC or STATCOM might need to be installed at the onshore substation as the LCC converter itself has limited reactive power control capability.

4.2 Power Loss

Power loss for HVAC connection is largely dependent on the cable characteristic and transmission distance. It is possible to use conductors with a larger cross section area to reduce the cable resistance. However this will inevitably increase the AC capacitance and therefore the charging current. While for DC connections, apart from the increase of the equivalent cable DC resistance, the impact of transmission distance on power loss is less significant. However, the converters will have relatively high power loss especially for VSC HVDC system. Even after adding the power loss of the STATCOM required in the LCC HVDC solution, the power loss of the VSC HVDC solution is likely to be approximately twice that of the LCC HVDC solution [9].

The exact power losses for different connection solutions are very much dependent on the detailed system design of the individual cases. For a wind farm rated at 200 MW, it was quoted that critical distance for HVAC compared to VSC HVDC is around 100 km [17, 21].

4.3 Overall Cost

A number of factors can affect the overall scheme cost, such as the substation cost which includes both the converter cost (for HVDC) and the platform, cable cost etc. Such cost can vary significantly among different projects.

For offshore wind farm up to 200 MW and with a connection distance up to 100 km, HVAC is likely to be the most economic solution due to the high cost of DC converter station [17]. For bigger wind farms over longer transmission distances, DC solution may be economically more attractive due to the features of HVAC connections such as increased power loss, the requirement of multi-cables and dynamic reactive power compensation.

The main disadvantage of the LCC HVDC solution compared to the VSC HVDC solution is its larger weight and footprint caused by the requirement for breaker switched AC harmonic filters etc. In order to minimize the space required, special techniques could be used—for example cabling between equipment, use of oil-immersed reactors, use of GIS, etc. However, these measures will increase the cost of the LCC HVDC solution. It is likely that the capital cost of the LCC HVDC solution will be higher than for the VSC HVDC solution, particularly for lower ratings, e.g. below 500 MW.

At very high power ratings, e.g. 1,000 MW or more, the LCC HVDC solution may prove to be more advantageous because of the use of technology which is proven during many years of service. Further, the smaller number of DC cables required for the large power transmission reduce the cost and minimize the environmental impact.

5 Conclusions

Connection of large offshore wind farms to electrical grids is one of the main concerns of transmission system operators and wind farm developers. Both AC and DC solutions are technically viable and the selection is dependent on the specific project. Current experience for connecting offshore wind farm is largely limited to HVAC system with relatively short distance. Further research and development are required for developing satisfactory solutions for integrating large offshore wind farm over long distances.

References

1. E.ON (2003) Grid Code—High and extra high voltage, E.ON Netz GmbH, Bayreuth, Germany
2. National Grid (2004) Appendix 1, Extracts from the Grid Code—Connection conditions. Available online: www.nationalgrid.com
3. Kirby NM, Xu L, Luckett M, Siepmann W (2002) HVDC transmission for large offshore wind farms. IEE Power Engineering Journal, June 2002:135–141
4. ABB (2007) HVDC Light. Available online: www.abb.com
5. Andersen BR, Xu L, Horton P, Cartwright P (2002) Topologies for VSC transmission. IEE Power Engineering Journal, 16(3):142–150
6. Lu W, Ooi BT (2003) Optimal acquisition and aggregation of offshore wind power by multiterminal voltage-source HVDC. IEEE Trans. Power Delivery, 18(1):201–206
7. Skytt AK, Holmberg P, Juhlin LE (2001) HVDC Light for connection of wind farms. In the Proceeding of the second International Workshop on Transmission Networks for Offshore Wind Farms, Sweden
8. Sobrink KH, Sorensen PL, Christensen P, Sandersen N, Eriksson K, Holmberg P (1999) DC feeder for connection of a wind farm. Cigre Symposium, Malaysia
9. Xu L, Andersen BR (2005) Grid connection of large offshore wind farms using HVDC. In the Proceeding of the Fifth International Workshop of Large-Scale Integration of Wind Power and Transmission Networks for Offshore Wind Farms, Glasgow, UK
10. Xu L, Yao LZ, and Sasse C (2007) Grid Integration of Large Wind Farms Based on DFIG Using VSC Transmission. IEEE Trans. Power System, 22(3):976–984
11. ABB (2005) Troll HVDC Light. Available online: www.abb.com
12. Barrow Offshore Wind (2006), available online: http://www.bowind.co.uk/
13. Horns Rev (2004), available online: http://www.hornsrev.dk/
14. Eriksson E, Halvarsson P, Wensky D, Hausler M (2003) System approach on designing an offshore windpower grid connection. In the Proceeding of the Fourth International Workshop on Large-Scale Integration of Wind Power and Transmission networks for Offshore Wind Farms, Sweden
15. Cartwright P, Xu L, and Sasse C (2004) Grid integration of large offshore wind farms using hybrid HVDC transmission. In the Proceeding of Nordic Wind Power Conference, March 2004, Sweden
16. Xiang D, Ran L, Bumby JR, Tavner P, Yang S (2006) Coordinated control of an HVDC link and doubly fed induction generators in a large offshore wind farm. IEEE Trans. Power Delivery, 21(1):463–471
17. Ackermann T. ed. (2005) Wind power in power system. John Wiley & Sons, England
18. Thomas JL, Poullain S, and Benchaib A (2001) Analysis of a robust DC-bus voltage control system for a VSC transmission scheme. In the proceeding of the 7th AC/DC Transmission Conference, London
19. Courault J (2001) Energy collection on large offshore wind farms—DC applications. In the Proceeding of the second International Workshop of Large-Scale Integration of Wind Power and Transmission Networks for Offshore Wind Farms, Sweden
20. Lu W, Ooi BT (2002) Multiterminal LVDC system for optimal acquisition of power in wind-farm using induction generators. IEEE Trans. Power Electronics, 17(4):558–563

21. Negra NB, Todorovic J, Ackermann T (2005) Loss evaluation of HVAC and HVDC transmission solutions for large offshore wind farms. In the Proceeding of the Fifth International Workshop of Large-Scale Integration of Wind Power and Transmission Networks for Offshore Wind Farms, Glasgow, UK

Author Biography

Dr. Lie Xu received BEng. in electrical and electronic engineering from Zhejiang University, Hangzhou, China in 1993 and the Ph.D. in electrical and electronic engineering from the University of Sheffield, Sheffield, UK, in 1999. Currently, he is with the School of Electronics, Electrical Engineering, and Computer Science, Queen's University of Belfast, Belfast, UK. He has also worked with ALSTOM T&D, Stafford, UK from 2001 to 2003, where he conducted R&D on VSC based HVDC system. His main research interests are power electronics, wind energy generation & grid integration of large wind farms, and application of power electronics to power systems.

Small Wind Turbines

David Wood

The recently released revision of the international safety standard for small wind turbines [1] defines a small wind turbine as having a rotor swept area (equal to πR^2 where R is the radius of the blade tip) of less than 200 m^2. This corresponds to $R < 8$ m and a rated power below about 50 kW. The standard also makes a further division: "micro" turbines have a swept area less than 2 m^2 and rated power below about 500 W.

Small wind turbines share the basic operating principle of large turbines. However, there are some major differences in detail. Small turbines operate at lower Reynolds numbers. They usually rely on a tail fin for alignment with the wind direction and their low wind speed and starting performance are more critical. In addition, their blades rotate faster to maintain a comparable tip speed ratio, λ, for the reasons to be explained in Sect. 1 where λ is defined. Thus the blade angular velocity, Ω, of a typical turbine scales as R^{-1}. This has important implications for turbine dynamics and the loads experienced by the main components. For example, if ΩR remains roughly constant, then the blade centrifugal loads, which depend on $\Omega^2 R$, must increase as R decreases. As suggested by the example, most of the differences add to the difficulties in designing and building safe small wind turbines. On the other hand, one advantage of small size follows from their major role as battery chargers: there is no need for Ω to be kept constant to maintain synchronicity with an electricity grid.

On most large wind turbines a hydraulic yaw drive rotates the nacelle and rotor in response to changes in the wind direction. This is deemed too expensive for

---

D. Wood (✉)
School of Engineering, University of Newcastle, Callaghan, Australia
e-mail: dhwood@ucalgary.cu

D. Wood
Schulich School of Engineering, University of Calgary, Alberta, Canada

S. Mathew and G. S. Philip (eds.), *Advances in Wind Energy Conversion Technology,* Environmental Science and Engineering,
DOI: 10.1007/978-3-540-88258-9_8,

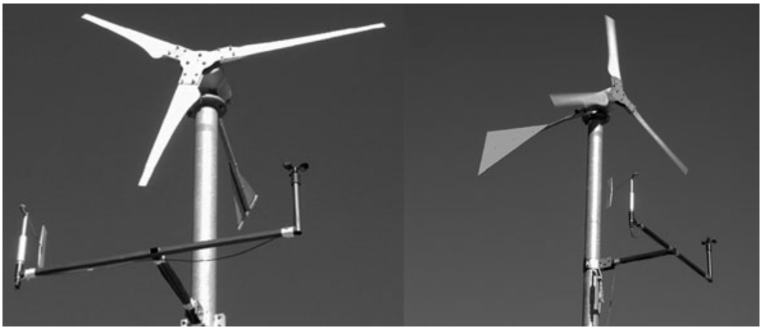

Fig. 1 Two views of a 400 W experimental turbine at the University of Newcastle. Blade radius is 0.97 m. Note the vane and cup anemometer for wind monitoring. Additional measurements include rotor shaft speed, turbine orientation, and power output. Photos by Dr. Andrew Wright

small turbines and the “free yaw” arrangement using a tail fin is the main alternative, although a substantial minority are “downwind” turbines with the blades behind the tower. Note that the wind turbine in Fig. 1 shows two tail fins of the same geometry but different size. We will see that free yaw can result in rapid changes in turbine direction which combine with high Ω to generate large gyroscopic moments on the blade roots, the main shaft, and tower. The “simple load model” of [1] suggests that these gyroscopic moments may be the highest loads on a small turbine. It is important, therefore, to consider tail fin design and yaw performance.

An obvious further difference between large and small turbines is in their purpose and siting. Small turbines are most commonly located alone near the load they supply, whether or not the turbine is grid connected. The load, such as a remote house or village, may be in a region of poor or moderate winds. It is very important, therefore, that a small turbine has good low wind speed performance but this requirement is made difficult by the corresponding low Reynolds numbers. To take an example, the blade of a 400 W turbine in Fig. 1 has a chord (the width of the blade) at the tip of approximately 45 mm. If the turbine is to perform well in low winds, then the blades should start rotating at a wind speed of about 3 m/s. The Reynolds number, *Re*, of the stationary blade is the product of the wind speed and the blade chord divided by the kinematic viscosity of air. This *Re* is less than 9,000 at the tip, which is in the range for insects (roughly 1,000–10,000) and well below the operational range for large wind turbines and commercial aircraft.

As wind turbine blades are made from aerofoil sections, low *Re* has at least three important consequences. The first is that the ratio of lift to drag usually decreases with decreasing *Re* as demonstrated in Fig. 2 for a number of aerofoils. Since the lift generates the torque on the blade but the drag reduces it, the ratio is the most crucial parameter for blade design and turbine efficiency. Secondly, a number of studies (for example [2]) have shown that the best aerofoils at very low *Re* (in terms of maintaining *L*/*D*) are only about 5% of the chord in thickness. It is

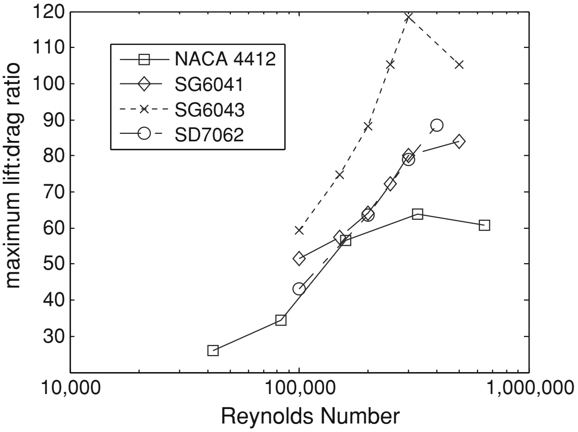

Fig. 2 Variation of maximum lift:drag with Reynolds number for several aerofoils. NACA 4412 data from [34], SG6041 and SG6043 from [35] and SD7062 from [36]

common practice for the aerofoils near the root of large wind turbine blades to be thicker than 25% of the chord, primarily for structural reasons. Such a choice would be aerodynamically disastrous for small blades. The need for thin sections, however, must be balanced against the centrifugal loads which are greater than on large blades and are maximised at the blade root. Thirdly, as implied by Fig. 2, there is very little data on aerofoil behaviour in the *Re* range of 10,000–100,000.

The final aspect of low wind performance that we will discuss is the indirect one of the resistance in the drive train and generator that opposes the aerodynamic torque on the blades. Most small turbines, particularly micro-turbines, use permanent magnet generators (PMGs) which can (but do not need to) have a resistive “cogging” torque, caused by the salient pole nature of the generator. On the other hand, induction machines offer virtually no resistance when the field is not energised, but usually need a gearbox for wind turbine use. The gearbox may have a significant frictional resistance. Furthermore, the cogging or resistive torque is usually maximised when the blades are stationary. In an example we will examine later, the 400 W turbine shown in Fig. 1 has a stationary resistive torque of 0.36 Nm, and a starting wind speed of nearly 5 m/s. In other words, the aerodynamic torque on the stationary blades is less than 0.36 Nm for any wind speed lower than 5 m/s. Once the blades have started, and the turbine is producing power, the aerodynamic torque increases significantly and the resistive torque usually decreases (to about 0.24 Nm for the 400 W turbine). For small wind turbines, the torque at rated power is between one and two orders of magnitude larger than the resistive torque. For example, the 400 W rated power of the turbine in Fig. 1 occurs at 700 rpm which corresponds to a rotor torque of 5.5 Nm.

This Chapter will describe the design and operation of small turbines with emphasis on these major differences from large machines. It is important, however, to first discuss the basic performance parameters. Only horizontal-axis turbines, such as that shown in Fig. 1, will be considered here.

1 Basic Performance Parameters

The basic performance parameters of small wind turbines are the same as for large wind turbines. The first is the power coefficient, C_P, which is defined as

$$C_P = \frac{P}{0.5\rho U^3 \pi R^2} \tag{1}$$

where P is the power produced in Watts, ρ is the air density in kg/m^3, and U is the wind speed in m/s. C_P is the ratio of the actual power produced to the power in the wind due to the kinetic energy that would pass the swept area of the rotor in the absence of the turbine. A 'perfect' turbine will operate at the Lanchester–Betz limit, $C_P = 16/27 = 0.593\ldots$, whereas real turbines, large and small, are less efficient. A modern large turbine has a maximum C_P of around 0.5, which is impressive given that the coefficient in practice includes the efficiency of converting the rotational kinetic energy of the blades into electrical energy. Because of their low *Re*, small turbines tend to be significantly less efficient.

The second important parameter is the tip speed ratio, λ, which relates Ω, measured in radians/s, to the wind speed:

$$\lambda = \Omega R/U = V_{tip}/U \tag{2}$$

where λ is the ratio of the circumferential velocity of the blade tips, V_{tip}, to the wind speed. λ controls the angle of attack of the wind on the rotating blades independently of the size of the turbine. It follows that the optimal operating point of any turbine is the value of λ at which C_P and hence P at any U, is maximised. (The plot of C_P versus λ is called the "performance curve" which is discussed later). Usually λ lies between 7 and 10 when a turbine is performing optimally. Thus the tips are moving at many times the wind speed and may reach 20–30% of the speed of sound, approximately 340 m/s at sea level and 20°C. At 70–100 m/s it is possible that compressibility of the air reduces aerofoil performance and certainly would reduce performance if λ were significantly higher [3]. The high λ has two other important consequences. The first is that the operational Reynolds number is much higher than that during starting, as can be demonstrated by extending the previous example. Since the rated wind speed (at which the rated or advertised power is produced) is usually 10 m/s or higher, the Reynolds number at rated conditions is approximately (10/3)λ times the starting Reynolds number. That factor can be in the range 20–30. Secondly, if we consider the power (in a hypothetically steady wind) as the product of shaft torque, Q, and Ω, then wind turbines, in general, can be characterised as fluid machines with high Ω and low Q.

However much the designer is concerned with efficiencies and tip speed ratio, the purchaser and user are more interested in the power produced for a given wind speed. This vital information is contained in the power curve, shown in Fig. 3 for the turbine in Fig. 1. The solid squares in the figure shows 1-min averages of the power output and wind speed. The averages of those averages—the

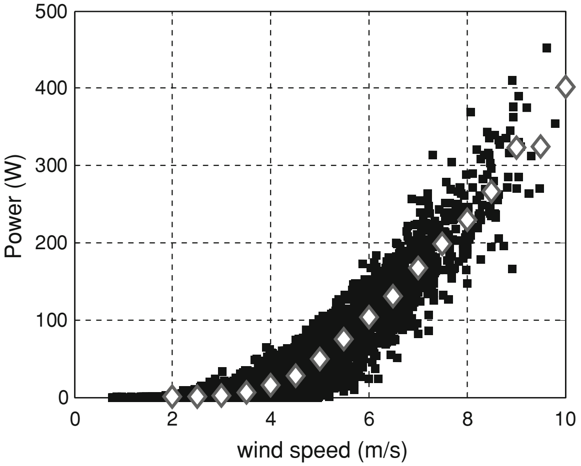

Fig. 3 Power curve for the turbine shown in Fig. 1. The *solid squares* show 1-min averages of wind speed and power. The *large unfilled diamonds* show averages of these averages. Figure from [9]

diamonds—would then be advertised by the manufacturer as the power curve. We are skipping over some very involved data handling and processing issues here as can be appreciated by the fact that there is a separate IEC standard just for power curve determination. That standard requires 10-min averaged data. One-minute averages were used simply because there was insufficient data to implement the standard procedure. Nevertheless, Fig. 3 shows another important feature of any wind turbine; a finite cut-in wind speed, below which no power is produced. For Fig. 3, the cut-in wind speed is an impressive 3.5 m/s or less. This speed is considerably less than the 5 m/s required to overcome the generator cogging torque for reasons that we will address in Sect. 2. All wind turbines have a region of the power curve where P increases very rapidly with U—a cubic dependence is implied by Eq. 1—followed by a levelling off to a maximum power, possibly followed by a reduction to zero in high winds. These regions are not apparent in Fig. 3 due to a lack of high wind data.

Well designed wind turbines are extremely quiet: one simple data correlation for the sound power level, L_P, gives [4]:

$$L_P \approx 10^{-7} P \tag{3}$$

that is one-ten millionth of the turbine's power is output as noise. Another correlation that is more accurate in some cases, at least for large turbines, is

$$L_P \approx 50 \log_{10} V_{tip} + 10 \log_{10} R - 1 \tag{4}$$

where now L_P is measured in the more common unit of decibels (dB) [5]. Very few measurements have been made of the noise from small wind turbines, [6, 7]. They show that well designed small turbines can be as quiet as large ones, in the sense that Eqs. 3 and 4 appear to be valid. L_P is the strength of the source of the sound as a multiple of the standard base level of 10^{-12} Watts. It is used, in combination with an equation for the propagation of the sound, to determine the noise level at any point around the turbine or turbines.

2 Starting Performance

A typical low speed starting sequence for the turbine in Fig. 1 is shown in Fig. 4, along with the wind speed and three predictions of the starting sequence. The rotor is stationary at the origin for the time, t. The blades begin to rotate as U increases after 6 s. They reach 250 rpm, when power extraction commences, after a further 90 s: this is the starting time. Figure 4 is typical of low speed starts in two ways. First, the starting time is long; partly because it scales as U^{-2} [8]. Secondly, starting is dominated by a long “idling time” of nearly 80 s, during which the blades accelerate slowly and the angles of attack decrease; the tip angle of attack on the stationary blade is about 86°. Somewhere after $t = 86$ s, the angles have reduced sufficiently for the final acceleration to be very rapid. The idling time is long enough for starting to be analysed using a quasi-steady blade element formulation, which has many similarities to that used for predicting the power output of turbines of all sizes. The blade is divided into a number of elements (fifteen were used for the predictions in Fig. 4) and each element is assumed to act as an aerofoil independently of the other elements.

It is assumed in the analysis that the wind does not decelerate through the blades so that the aerodynamic torque accelerates the blades rather than

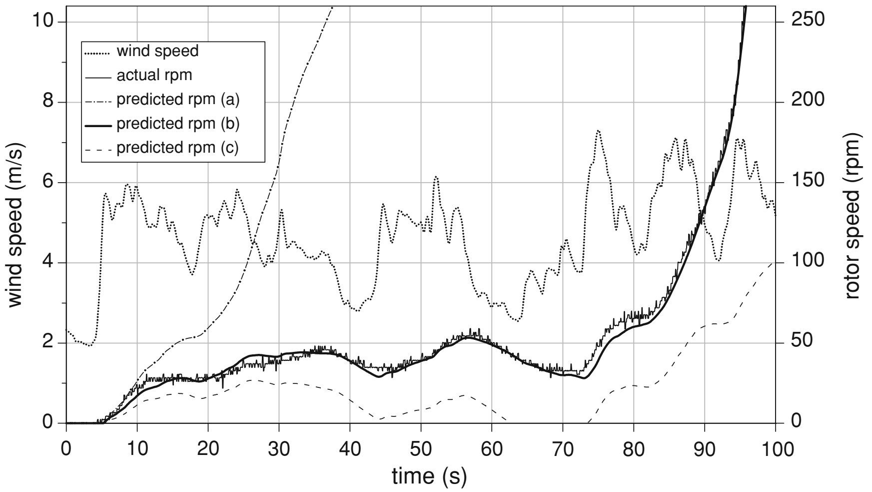

Fig. 4 Low wind speed starting sequence for the turbine in Fig. 1 [8]. *Curves a*, *b*, and *c* represent predicted starting performance with different assumptions for lift and drag [9]

produces power. The resulting autonomous ordinary differential equation for Ω can be integrated using standard techniques such as the Runge–Kutta method. We will not be concerned here with the three different predictions, apart from noting that prediction "b" shows that starting can be accurately predicted with the appropriate lift and drag values at high angles of attack. Further details can be found in [8, 9]. Starting depends on parameters that do *not* influence power production, such as the rotational inertia of the blades, J, and the resistive torque of the generator and drive train.

The discussion of starting illuminates the point made earlier that the cut-in wind speed determined from Fig. 3, about 3 m/s, is considerably lower than the starting wind speed of 5 m/s. The reason is that the standard method of determining the power curve causes the "cut-in" wind speed to be some average of the starting and the "cut-out" speed at which the blades stop turning as the wind drops. For the turbine in Fig. 1, the cut-out speed is less than 2 m/s [8], which is considerably lower than the starting speed simply because the rotating blades can maintain lower angles of attack and higher torque as the wind drops.

It is extremely significant that the starting torque is generated primarily near the hub, whereas the torque for power is concentrated near the tip. This suggests that blades may be designed for the dual purpose of fast starting and efficient power production. Optimisation of blade design for power only is reasonably straightforward. For example, it can be based on the equations for the optimum chord and twist, Eqs. 3.67 and 3.68 of [10].

Multi-objective design optimisation is usually more difficult and often does not lead to equations for the best performing blade, whatever that is. For example, numerical optimisation technique of "differential evolution" was used to design the blades for a two-bladed 3 m diameter rotor [11, 12]. Beginning with a randomly generated initial population of 2,000 blades, the design was then "evolved" for 200 generations. The blades were assumed to be solid and made from a constant density material. Figure 5 shows typical results for the approximation to the "Pareto front" in terms of the two objective functions, C_P, and the inverse of the starting time, T_s. This is the time it takes for the blades to accelerate from rest to a user-input Ω at a user-input U.

The Pareto front contains only those blades (typically 1–10% of the final population) which have at least one objective function greater than every other blade, so that every member of the Pareto front is, in some sense, optimal. The value of the parameter a given in the legend, controls the relative importance of power and starting in determining the fitness of each blade, and the left-most symbol for each of the four optimisation runs represents the so-called "superblade". Exploiting the independence of the blade elements, the superblade is assembled from the best power producing blade elements of the final population. It is shown in [11] that in all cases, the twist and chord of the superblade are very close to those for the optimum blade as defined by the equations from [10] that were referred to previously. This gives confidence in the accuracy of the multi-objective optimisation. However, the superblade is always the slowest to start, so the first important conclusion from Fig. 5 is that it is necessary to sacrifice some

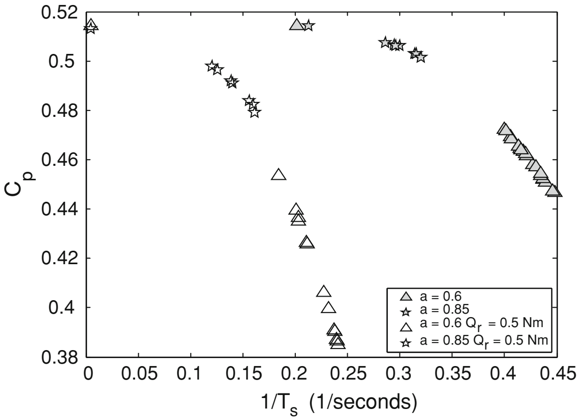

Fig. 5 Approximate Pareto front for a two-bladed 3 m diameter rotor [11]

power extraction efficiency in order to improve the starting performance. Figure 5 demonstrates that a very large reduction in starting time can be achieved for a modest reduction in efficiency. Figure 5 also demonstrates the great impact of resistive torque; the open symbols represent no resistive torque and the filled-in symbols are for a constant resistive torque, Q_r, of 0.5 Nm, which is not large for a turbine rated at 1.5–2 kW.

3 Yaw Behaviour and Gyroscopic Loads

As the wind direction changes, randomly and sometimes rapidly, the rotor must follow to minimize power loss. As a rule of thumb, the reduction in power due to a "yaw error" is $\cos^2(\gamma_t - \gamma_w)$ where $\gamma_t - \gamma_w$ is the error: γ_t is the angle of the turbine axis and γ_w is the wind direction, both measured relative to an arbitrary "earth-fixed" co-ordinate system originating at the turbine's yaw axis. A useful mnemonic is that a 20° yaw error causes a substantial 12% loss of power. On the other hand, it is not desirable for the turbine to follow the high frequency wind direction changes as these will induce high loads on the blade roots and the rotor shaft due to gyroscopic effects. The magnitude of these loads for any turbine is proportional to $J\Omega\omega$, where ω is the rate of change of turbine yaw: $\omega = \mathrm{d}\gamma_t/\mathrm{d}t$.

Gyroscopic effects are shown in Fig. 6 for the 400 W turbine in Fig. 1. Again the origin for time is arbitrary. A strain gauge was mounted on the upwind side of one blade just above the bolts which can be seen in Fig. 1 and calibrated to give the root bending moment. The top part of Fig. 6 indicates that U varies between 6 and 11 m/s, Ω is decreasing, and the yaw rate reaches 170°/s which is the maximum specified by [1] for a turbine of this size. The bottom part of the figure shows the blade root bending moment is a combination of the slowly increasing "average" component due mainly to the thrust on the blade, and the oscillating

Fig. 6 The root bending moment during rapid yaw motion of the turbine in Fig. 1. Data from [37]

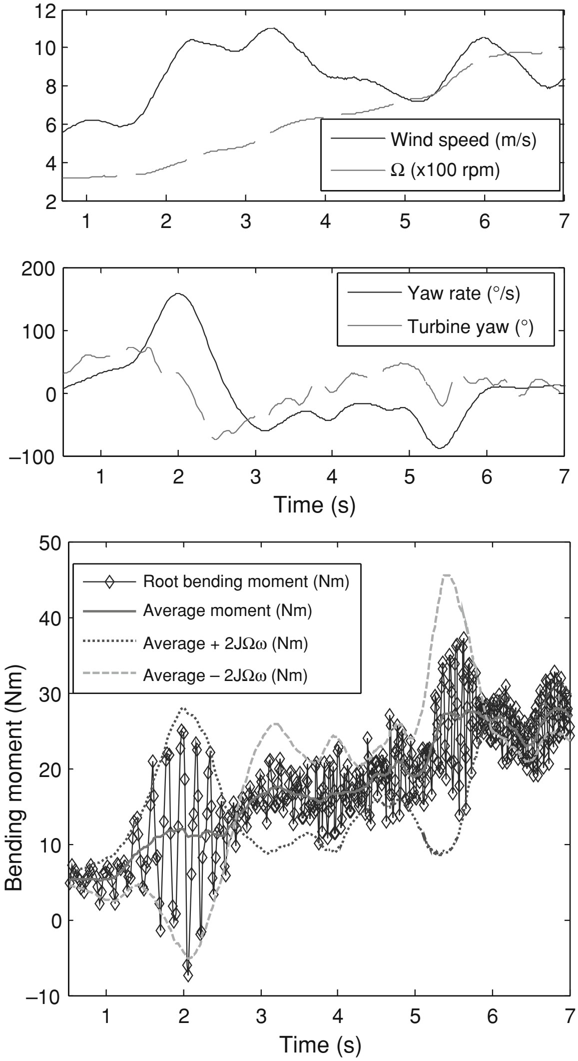

gyroscopic load, $2\,J\Omega\omega\,\cos\psi$, where ψ is the azimuthal angle of the blade. The period of the oscillations which peak at around 2 s, corresponds to one blade revolution. According to the simple load model of [1], the stress in the main drive shaft, which is dominated by the gyroscopic term, is the largest stress in any component of the turbine in Fig 1.

It is often said that a turbine with three blades is inherently smoother in yaw than two, and this is certainly true for the loads on the rotor shaft. The reason is that the azimuthal variation in the rotor moment of inertia about the yaw axis is considerably reduced by adding a third blade, as can be seen by considering the

Fig. 7 A 5 kW turbine being raised on a guyed tower using a gin pole. Photo by Ben Fox

difference in moment due to two blades being vertical rather than horizontal. This variation leads to larger variations in the gyroscopic shaft load for two blades as compared to a larger number. Nevertheless, Fig. 7 clearly shows that each *blade* is loaded gyroscopically independently of blade number and the shaft loads do not depend strongly on the number of blades, N. There is, however, an indirect effect of blade number as well: to achieve the same power output a two-bladed turbine requires blades with a higher Ω and J than does a three-bladed machine.

To better understand the gyroscopic loads, as well as the design of the tail fin, it is necessary to formulate the yaw dynamics. It will be assumed that response to wind direction changes is determined by the tail fin and not the blades. This can only be an approximation as, for example, coning of the blades, either by pre-setting or by the downwind deflection of a flexible blade under load, should improve yaw stability in much the same way that dihedral on aircraft wings improves roll stability, but the net effect appears not to be large in practice. The oldest theoretical approach to yaw response is the pseudo-static (PS) method developed for vanes which measure wind direction [13, 14]. More recently, unsteady slender body (USB) theory [15] has been applied to define the yaw response [16]. Neither is fully trustworthy; PS does not consider the aerodynamic effects of the unsteadiness, whereas USB requires the tail fin "chord" to vary in order to produce lift. In other words, USB predicts no steady lift for a rectangular tail fin, in obvious conflict with the measurements [17]. Nevertheless (within some further approximation for USB), both suggest that a yawing wind turbine is a second order linear system, and this has been found to be reasonably accurate, at least for yaw angles less than about 20°. Thus yaw behaviour can be characterised by the natural frequency, ω_n, and damping ratio, ζ. The equations for these quantities from the two analyses can guide tail fin design. For example, using wind tunnel data for the lift of delta wings [18], rectangular wings and other low aspect ratio wings [17], it is easy to see that the actual shape of the tail fin is not crucial to its performance. This is especially true for ζ which must be large enough to prevent oscillations that will add to the fatigue loading. As can be seen from the following USB equations for a delta tail fin as in Fig. 1, ω_n, is proportional to the wind speed:

$$\begin{array}{ll} \omega_n \approx U\sqrt{\frac{K_1}{I}} & \text{and } \xi \approx \frac{K_2}{2\sqrt{K_1 I}} \quad \text{where} \\ K_1 = \pi\rho b^2\left(x + \frac{2}{3}c\right)/4 & \text{and } K_2 = \pi\rho b^2(x^2 + 2xc + c^2)/4 \end{array} \qquad (5)$$

I is the total moment of inertia about the yaw axis, x is the distance from the yaw axis to the apex of the fin, b is the span (the height) and c is the chord (the length) of the fin. These equations ignore the "added mass" contribution due to the air accelerated by the moving fin, which was shown to be small [19]. They also show that the USB equation for ζ is more accurate than the pseudo-static one. The results suggest that $\zeta \approx 0.3$ provides a good compromise between following the lower frequency changes in wind direction and avoiding those of higher frequency [9, 19]. It is not necessarily easy to achieve this level of damping. Equation 5 suggests that the easiest way to increase damping is to increase b but this also increases I. To account for different tail fin shapes, Eq. 5 can be rewritten in terms of the lift-slope, K, defined in terms of the angle of attack, α, as

$$C_l = K\alpha \quad \text{where } K = \pi b/(2c) \text{ for a delta wing} \qquad (6)$$

The data in [17] and others can be used to estimate K for other tail fin shapes. It will be found that changing the shape of the fin has little effect on the damping ratio.

The initial response to a change in wind direction depends on the product of ω_n and ζ, which is proportional to U and inversely proportional to I, which suggests the need for a smaller I! In view of the dependence on U, it is not surprising that the highest yaw rates occur at high wind speed; typically around 10 m/s for the experiments on the turbine in Fig. 1, [19]. At lower wind speeds, the high frequency changes are not "seen" by the turbine, and at wind speeds greater than 10 m/s there may well be a decrease in the maximum frequency of direction changes.

A more complete treatment of yaw behaviour is unlikely to improve the design of tail fins over that based solely on consideration of the natural frequency and damping ratio as defined above. The features that so far have been ignored—the slowing down of the wind as it moves through the rotor and over the tail, the influence of the vorticity and turbulence shed from the blades, and the azimuthal dependence of the flow during large yaw—are unlikely to be easily included in the analysis.

4 Over-Speed Protection

The rapid development of power electronics over the last 20 years or so means that the generator itself can be used for over-speed control, by slowing the blades to reduce the power as the wind speed approaches and exceeds the rated value. Pulse width modulation (PWM) of the rectified generator voltage is a common method. Furthermore, the output of PMGs can be shorted provided their thermal and magnetic behaviour is adequate. For an inadequately designed PMG, a short circuit can demagnetise the magnets. However, it is always possible that electronic control will fail through "loss of load" and [1] mandates an additional over-speed protection. The three most common methods are:

1. to pitch the turbine so the rotor axis tilts from the vertical to horizontal plane,
2. to "furl" the rotor so the axis is approximately normal to the wind but remains parallel to the ground, and
3. to mechanically brake the rotor.

We will consider the three in turn. Pitching involves hinging the nacelle below, and at right angles to, the rotor axis and behind the centre of mass. As *U* increases, the thrust on the blades eventually overcomes the gravitational moment and pitches the rotor up and the tail down. Pitching is generally used only on micro-turbines for the following reason. The sign of the gyroscopic moment considered in the previous section depends on the sign of the rate of change of yaw. Thus the gyroscopic moment may act to cancel the thrust moment in a critical situation where the turbine needs to pitch or cause the rotor to pitch unnecessarily. The thrust scales as R^2 (i.e. it depends on rotor area) and the moment arm on R. If the blade density and blade shape are independent of R, and the maximum yaw rate is also independent of R (the formula used in [1] gives a weak dependence on R) then the gyroscopic moment scales as R^4, and so must eventually overwhelm the thrust moment, and invalidate pitching for over-speed protection.

Furling also relies on rotor thrust, but in this case, the rotor axis is offset in the horizontal plane from the turbine's yaw axis so that the thrust will eventually cause the articulated tail boom to collapse and turn the blades out of the wind [20]. There are a number of possible complications, such as inclining the furl axis to the vertical to introduce gravity, and inclining the rotor axis to the horizontal, but all furling methods follow the same basic principle. There are several fundamental problems with furling:

1. The yaw offset means a loss of power in normal operation. This is about 20% for the turbine in Fig. 1 [9]. The mean yaw error on the furling turbine in [21] is approximately 10°, which would cause a smaller power loss.
2. Furling can be associated with the largest gyroscopic loads on a turbine [9, 19].
3. Anecdotally, it is difficult to design a furling system that works repeatedly over a narrow range of *U* and output power.
4. Field testing of a 10 kW turbine revealed that the turbine often did not "unfurl" after the high winds had ceased and this lead to some loss of power [22].

In the light of these problems, it is interesting to note that furling is by far the most common over-speed protection method for small turbines above the micro class. This is probably because mechanical braking, which is used routinely on large turbines, can be considerably more expensive.

5 Control System

Usually the alternating current (AC) produced by the generator is immediately rectified to direct current (DC), often using PWM. Development of such a control system for an 11 kW turbine is described in [23], and for a 5 kW turbine in [24]. If the turbine is part of a remote power system, the DC is fed into a battery bank along with the DC from other renewable resources such as photovoltaic panels. Inversion to AC occurs after the batteries. DC loads such as LED lighting can be fed separately from the batteries through a charge controller.

For both remote and grid-tied turbines, it is also necessary to control the blade speed. This is for two reasons: first, and most common, it is desirable that Ω remain proportional to U over a large range of U, for maximum power generation at the optimal λ. The process to achieve this is usually called “maximum power point tracking” (MPPT) as in [25]. This reference specifically considers a 600 W vertical axis turbine but the basic control issues are the same for vertical and horizontal turbines. MPPT is invariably based on the “steady-state” power curve, as shown by the large diamonds in Fig. 3, whereas the instantaneous turbine behaviour may be quite different. There have been attempts to formulate the unsteady response of turbines to gusts etc., as in [26], and it seems a research area well worth pursuing from the perspective of control.

In contrast to large turbines which have an anemometer to measure the wind speed, small turbines usually track indirectly and this requires some ingenuity in the design. On the other hand, the use of modern aerofoils for the blades usually provides a performance curve that is flat enough around the optimum not to require very sensitive control. Possibly the easiest way to achieve MPPT is to measure the generator AC frequency and output power, P, both of which are readily available whereas the shaft torque, for example, usually requires an additional sensor. Ignoring any slip, which in most cases is small, the frequency is easily converted into Ω, and the optimal relation between Ω and P can be compared to the short-term averaged power and a decision made to speed up or slow down the rotor, or leave it alone.

The second reason to control blade speed is for safety at high wind speeds. PWM can also be used for this, so that the mechanical or aerodynamic measures discussed in that section are genuinely for “protection” rather than “control”. In other words, if the controller loses power the turbine must be protected aerodynamically and/or mechanically. On the other hand, the designer should be wary of excessive pitching, furling, or braking, so the attraction of limiting Ω primarily through the controller is obvious.

The rapid development of power electronics, particularly with the introduction and widespread use of IGBTs (insulated gate bipolar transistors), has significantly reduced the cost of controllers and inverters while improving the reliability and performance.

6 Towers and Installation

Small turbine sites vary widely from yachts to buildings to remote communication and mobile phone towers. An example is shown in Fig. 7; a 5 kW wind turbine is being erected at the Tortoise Head Lodge on French Island in Westernport Bay, Victoria, to be used in conjunction with a number of photovoltaic panels and a large battery bank. This turbine has a traditional tower with guy-wires. It is hinged at the base, and is erected using a gin pole, the narrow A-frame structure mounted close to the base.

Two of the four guy wires can be seen on either side of the tower, and there is another from the end of the gin pole to the tower. The turbine is being raised by the tractor on the skyline. Using a gin pole is one of the few ways to raise the tower and turbine from the ground, especially for sites where it would be very expensive or impossible to bring in a crane. It is easy to show that maximum tension in the tractor cable occurs when the tower has just lifted from the ground and is approximately mgl/L where m is the total mass of turbine and tower, l is the distance along the tower to the centre of mass, and L is the length of the gin pole [27]. (The ratio l/L may be termed the mechanical *disadvantage* of the gin pole as it is usually lies between two and four.) There is, however, at least one major drawback to a hinged tower with guy wires: the tower foundations cannot withstand the worst case overturning moment of the turbine thrust and wind load on the tower when they act in the direction of the tower raising or lowering. Thus the guy wires must have substantial foundations in order to resist this moment. This is one reason why some modern turbines use tubular towers that are bolted to their foundations, as do large turbines. Of course, these unsupported towers must be stronger than towers with guy wires and, therefore, more expensive.

Siting of a small turbine can be critical for its performance, but is, unfortunately, often very dependent on the micro-meteorology of the site and the presence of buildings and trees. A generally very useful guide to siting is provided by the British Wind Energy Association [28]. Siting often involves a consideration of power losses and cabling costs if the turbine must be placed at a large distance from the load. The crest of a gentle hill clear of trees is usually preferred, but the common advice that the tower height should be as high as practicable (as in [28]) needs careful consideration. In the ideal case of flat terrain with regular roughness, the increase of the mean wind speed with height is given by the logarithmic law [10]. Combined with an analytic approximation to the power curve, and data on the variation of tower cost with height, the optimum height, in terms of maximizing the power output per unit capital cost and ignoring the effect of tower height on transportation cost, could be as low as 14 m, [29]. (This analysis was based on the extensive data on towers and related issues on the web site for Bergey Windpower [30]). The optimum height increases with decreasing roughness, but in most cases the cost per unit power is fairly flat with height, so there was often very little difference between tower heights of say 20 and 30 m. The optimum is, however, very dependent on the cut-out wind speed, the speed at which the turbine shuts down by pitching, furling, or braking for safety. This speed is usually much lower for small than for large turbines because of the higher Ω, and increasing the tower height causes the turbine to experience more wind speeds above cut-out. Generally and obviously, the higher the cut-out wind speed the higher the optimum tower height. In the cases analysed in [29], the cost of a tower of optimum height was around 30% of the combined cost of the turbine and tower.

Small turbine heights are often similar to the heights of surrounding trees. The turbine in Fig. 1 is mounted on an 8 m tower on the roof of a four-story building. There are trees of height comparable to the building on all sides. The average wind speed is low, about 3.9 m/s, but the turbulence level is very high at around 40% [3]. For turbines away from buildings, a thick tree cover reduces the effective tower height. In meteorological terms this is because the "zero plane displacement" for the logarithmic law for the wind speed is often more than half the mean tree height. For example, the displacement was found to be 65% of the mean tree height of 7.5 m [31]. The turbulence level is also raised as seen in [31, 32]. If the turbine is placed in a clearing, then it should be at least five times the mean tree height from the nearest tree to avoid the "dead zone" immediately behind the trees [33].

Acknowledgments The author is grateful to all his colleagues and students who have contributed greatly to his knowledge of small wind turbines over the years. The most valuable contributions to the work described here were by Andrew Wright, Phil Clausen, Peter Freere, and Sturt Wilson, but the list is by no means exhaustive.

References

1. International Electrotechnical Commission (2006) IEC 61400-2 revision 2, Wind turbines - Part 2: Design requirements for small wind turbines, obtainable from www.iec.ch
2. Sunada S, Sakaguchi A, Kawachi K (1997) Airfoil section characteristics at low Reynolds number. J Fluids Engineering 119:129–135
3. Wood DH (1996) Some effects of compressibility on small horizontal-axis wind turbines. Renewable Energy 10:11–17
4. Lowson MV (1992) Applications of Aero-Acoustic Analysis to Wind Turbine Noise, Proc. 18th British Wind Energy Assoc. Conf., B.R. Clayton (ed.), M.E.P
5. Wagner S, Bareiss R, Guidati G (1996) Wind Turbine Noise, Springer-Verlag, Berlin Heidelberg, New York
6. Wood DH (1997) Noise measurement and prediction for small wind turbines, Paper #153, *Solar '97,* Canberra
7. Migliore P, van Dam J., Huskey A (2004). Acoustic tests of small wind turbines. AIAA Paper #2004–1185
8. Wright AD, Wood DH (2004) The starting and low wind speed behaviour of a small horizontal-axis wind turbine. J. Wind Eng'g & Indust. Aerodyn. 92:1265–1279
9. Wright AD (2005) Aspects of the Aerodynamics of Small Wind Turbines. Ph.D. thesis, Univ. Newcastle
10. Burton T, Sharpe D, Jenkins N, Bossanyi E (2001). Wind Energy Handbook, John Wiley & Sons, Chichester
11. Wood DH (2004) Dual Purpose Design of Small Wind Turbine Blades. Wind Engineering, 28:511–527

12. Price K, Storn R, Lampinen J (2006) Differential Evolution - A Practical Approach to Global Optimization. Springer, Berlin
13. Wieringa J (1967) Evaluation and Design of Wind Vanes. Journal of Applied Meteorology, 6:1114–1122
14. Kristensen L (1994) Cups, Props and Vanes, Riso-R-766(EN). Available from: http://www.risoe.dk/rispubl/vea/veapdf/ris-r-766.pdf
15. Katz J, Plotkin A (2001) Low Speed Aerodynamics: second edition. C.U.P, Cambridge
16. Bechly ME, Gutierrez H, Streiner S, Wood DH (2002). Modelling the Yaw Behaviour of Small Wind Turbines. Wind Engineering 26:223–239
17. Torres GE, Mueller TJ (2004) Low-aspect ratio wing aerodynamics at low Reynolds number. AIAA Journal 42:865–873
18. McCormick BW (1979) Aerodynamics, Aeronautics and Flight Mechanics, First Edition. John Wiley and Sons, New York
19. Wright AD, Wood DH (2007). Yaw rate, rotor speed and gyroscopic loads on a small horizontal axis wind turbine. Wind Engineering, 31:197–209
20. Bikdash M, Chen DA, Harb M (2001) A hybrid model of a small autofurling wind turbin J Vibration & Control 7:127–148
21. Corbus D, Hansen AC, Minnema J (2006) Effect of blade torsion on modeling results for the small wind research turbine. J Solar Energy Engg 128:481–486
22. Bowen AJ, Zakay N, Ives RL (2003). The field testing of a remote 10 kW wind turbine. Renewable Energy 28:13–33
23. Teodorescu R, Blaabjerg F (2004). Flexible control of small wind turbines with grid failure detection operating in stand-alone and grid-connected mode. IEEE Transactions Power Electronics 19:1323–1332
24. Sürgevil T, Akpinar E (2005) Modeling of a 5-kWwind energy conversion system with induction generator and comparison with experimental results. Renewable Energy, 30:913–929
25. Mirecki A, Roboam X, Richardeau F (2007) Architecture complexity and energy efficiency of small turbines. IEE Transactions Industrial Electronics 54:660–670
26. Rauh A, Peinke J (2004) A phenomenological model for the dynamic response of wind turbines to turbulent wind. J. Wind Eng'g & Indust. Aerodyn. 92:159–183
27. Wood DH (2007) A simple force analysis for the raising and lowering of a small wind turbine and tower. Wind Engineering
28. http://www.bwea.com/you/siting.html
29. Wood DH (2001) An improved determination of the optimum tower height for a small wind turbine. Wind Engineering, 25:191–196
30. http://www.bergey.com/
31. Irvine MR., Gardiner BA, Hill MK (1997) The evolution of turbulence across a forest edge. Boundary-layer Meteor. 84:467–496
32. Lopes da Costa JC., Castro FA, Palma JMLM, Stuart P (2006) Computer simulation of atmospheric flows over real forests for wind energy resource evaluation. J. Wind Eng'g & Indust. Aerodyn. 94:603–620
33. Lee X (2000) Air motion within and above forest vegetation in non-ideal conditions. Forest Ecol. & Management 135:3–18
34. Miley SJ (1982) A Catalog of Low Reynolds Number Airfoil Data for Wind Turbine Applications. Report DE82-021712, U.S. Dept Energy
35. Giguere P, Selig MS (1998) New airfoils for small horizontal axis wind turbines. J Solar Energy Engg 120:108–114
36. http://www.ae.uiuc.edu/m-selig/
37. Wilson SVR, Clausen PD Wood DH (2008). "Gyroscopic Moments on Small Wind Turbines Blades at High Yaw Rates", Trans IE Aust, Aus. J. Mech. Engg, 5:1–8

Author Biography

Prof. David Wood graduated with Bachelor's and Master's degrees in Mechanical Engineering from Sydney University in the 1974 and 1976 respectively, and obtained a Ph.D. in Aeronautics from Imperial College, London in 1980. From 1981 till 2004 he was a member of the Engineering Faculty at the University of Newcastle, apart from a year as a Senior Research Associate at NASA Ames Research Center in California in 1987. He resigned from the University in 2004 to form Aerogenesis Australia to commercialise the small wind technology developed by him and his colleagues through many years work. He was the Australian representative on the international committee that produced the latest version of the International Electrotechnical Commission standard for small wind turbine safety. Since 2005 he has been editor for aerodynamics and small turbines for the journal *Wind Engineering*. He has published over 50 refereed papers on wind turbine behaviour, principally in relation to the aerodynamics of small turbines, and holds patents on blade and controller design. His work covers theoretical, computational, and experimental investigations of noise, blade design and performance, yaw behaviour, wake development, and component loads. In february 2010 he took up the Enmax/Schulich chair of renewable energy at the University of Calgary

Index